An Investigation on the Hydrodynamics and Sediment Dynamics on an Intertidal Mudflat in Central San Francisco Bay

by

Stefan Andreas Talke

B.S., (University of California, Berkeley) 1996

M.S. (University of California, Berkeley) 2001

A dissertation submitted in partial satisfaction of the requirements for the degree of

Doctor of Philosophy in

Engineering – Civil and Environmental Engineering

in the GRADUATE DIVISION of the

UNIVERSITY OF CALIFORNIA, BERKELEY

Committee in charge:

Professor Mark T. Stacey, Chair

Professor James R. Hunt

Professor Stanley A. Berger

Spring 2005

The dissertation of Stefan Andreas Talke is approved:

Chair Date

Date

Date

University of California, Berkeley

Spring 2005

An Investigation on the Hydrodynamics and Sediment Dynamics on an Intertidal Mudflat in Central San Francisco Bay

Stefan Andreas Talke

Abstract

An Investigation on the Hydrodynamics and Sediment Dynamics on an Intertidal Mudflat in Central San Francisco Bay

by

Stefan Andreas Talke

Doctor of Philosophy in Engineering – Civil and Environmental Engineering

University of California, Berkeley

Professor Mark T. Stacey, Chair

On an intertidal mudflat in Central San Francisco Bay, we conducted four field experiments between February, 2001 and October, 2003 to investigate hydrodynamic and sediment transport processes. Not only tides and locally driven wind waves bring energy onto the mudflat, but also remotely forced ocean swell and infra-gravity seiching. These energy sources persist and dominate over different time scales, with variation occurring over minutes, hours, and days.

The different hydrodynamic forcing mechanisms superpose upon each other—and interact nonlinearly—in the water column, creating a dynamically varying interaction

with the sediment bed. Wind waves produce the largest stresses; however, ocean swell often determines the virtual roughness experienced by the seiche and tidal currents. The boundary layer of the tide is modulated by seiching motions, and is better described by a log-linear profile than a logarithmic profile. However, an analytical log-linear model using acceleration and stratification length scales does not explain the observed velocity structure. Instead, a k-ε turbulence closure model (General Ocean Turbulence Model, GOTM) reproduces the unsteady boundary layer structure of the seiching motion. A simple analytical solution (Smith, 1977) suffices to model the boundary layer of ocean swell. Several methods of separating wave energy and turbulence are compared; results show that TKE and dissipation vary with the total energy climate.

Sediment erosion, deposition, and transport also vary on the tidal, seiche, and wave time scales. The tidal component of sediment flux has the largest magnitude, and is often determined by the timing and strength of wind events. Notable fluxes occur at the wave and seiche frequencies. Onshore transport occurs during an ebb tide at the seiche frequency. Sediment concentrations increase when the seiche opposes the ebb current, and decrease when they are aligned. Erosion is not occurring due to a critical stress, but when flow reverses over the rippled bed and causes sediment laden vortices to be ejected. When the seiche opposes the ebb current, waves are more likely to reverse the overall flow and sediment concentration increases. The interactions of multiple frequencies of motion are clearly vital to understanding sediment dynamics on an intertidal mudflat.

Table of Contents

Acknowledgements

Many, many people are to thank for helping deploy and recover the experiments at the Richmond Field Station; this was heavy lifting under muddy conditions, and is much appreciated. These people are: Seungjin Baek, Gerald Berger, Matt Brennan, Jon Fram, Bart Forman, Kate Hucklebridge, Bryce Johnson, Maureen Martin, David Ralston, Deanna Sereno, Mark Stacey, Kurt Talke, Yusuke Uchiyama, and Shitao Xu.

Thanks also to Mark Stacey, whose class on estuarine and river dynamics inspired me to pursue this dissertation, and whose ideas and guidance helped me immensely throughout. Also thanks to Stanley Berger and Jim Hunt, whose thorough reading of the dissertation greatly improved its quality.

To Katie Ikard: Thanks for inspiring me to pursue environmental engineering, and for all your support. To my parents: Thanks for giving me the love of learning. And finally, a shout out to Anneke, my pretty little silly baby bear.

Chapter 1: Introduction

1.1. Background and Motivation

In many ways, hydrodynamic processes on an intertidal, estuarine mudflat are analogous to open shore beaches; on the other hand, estuaries are semi-enclosed basins and thus subject to hydrodynamic processes that occur for example in lakes. The intersection of these paradigms makes a unique environment. Due to its position between land and estuary, the intertidal zone plays a crucial role in the transport of land-sourced sediments and contaminants into the estuary. Intertidal flats are major sources and sinks for sediments, organic matter, contaminants, and biological scalars found in deeper water (de Jonge and van Beusekom, 1995, Schoellhamer 1996, Dyer, 1989). Local hydrodynamic conditions determine the erosion, deposition, and transport of sediment and other scalars on an intertidal mudflat. During energetic flow, sediment is eroded from the bed, while sedimentation occurs during relatively calm periods, when accretion is larger than erosion (Christie and Dyer, 1998). The mixing and transport of sediment in the water column occurs due to the action of waves and currents, which vary on the time scale of seconds to seasons (and beyond). Thus, the study of hydrodynamics and sediment dynamics on an intertidal mudflat is vital to understanding the intertidal environment and the estuary as a whole. This chapter gives a conceptual overview of the current literature on mudflats, and then introduces the specific history and current context of the field site in the Central San Francisco Bay near the city of

Richmond, CA—and details why hydrodynamic processes and sediment dynamics are particularly important there.

1.1.1 Hydrodynamics

Hydrodynamically, the intertidal zone is influenced by processes with a wide range of timescales, from freshwater flow variations to diurnal and semi-diurnal tides to surface waves and turbulent mixing. Tidal forcing sets the amount of time and the depth to which the mudflat is inundated. The bathymetry and the tidal prism at a particular location set the magnitude and direction of tidally driven currents (Le Hir et al., 2000). The timing of the tide relative to the elevation of the mudflat is critical; for example, the higher elevations of a mudflat are subject to less scour from the ebb and flood, and typically are a sink of sediment during the slack tide in calm conditions (Postma, 1961). During windy conditions, these elevations may be exposed to wave stresses and wave attack during the slack tide, causing greater erosion and inhibiting deposition (Dyer, 1998). In estuarine mudflats, waves are generally modeled as wind waves in which the fetch, the time wind blows, wind direction, and wind magnitude are the relevant factors (Dyer, 1998, Le Hir et al., 2000). On more exposed coastlines or near the entrance to harbors or estuaries, remotely forced ocean swell are important (see e.g., Whitehouse et al., 2000, de Lange and Healy, 1990, Green et al., 2001). Freshwater flow from upland watersheds or local rain runoff may also affect the mean current, as can local circulation patterns, nonlinear waves (Stokes drift), wind stress, and many other sources (Le Hir et al., 2000). During low tide when the mudflat is exposed, sunlight and wind desiccate

the mud surface while water drains through the porous sand or mud surface or drains through a network of creeks and channels (Dyer, 1998, Whitehouse et al., 2000, Anderson and Howell, 1984). Heavy rainfall may cause rivulets and other features to form on the intertidal surface (Anderson, 1981) and may decrease the erosion threshold (Dyer, 1998).

The combination of waves and tides applies a shear stress at the bed and produce turbulent vortices, which then mixes momentum and scalars such as sediment in the water column. Similarly, wind stress and white-capping waves introduce turbulence at the upper boundary. Turbulent motions in the boundary layers of waves and currents interact non-linearly to produce enhanced stresses at the bed (Grant and Madsen, 1979). Above a critical shear stress τ_{ce} the bed erodes, while sediments settle out of the water column below a critical shear stress τ_{cd} (Partheniades, 1962; Krone, 1962). Small waves exert the largest stresses on the mudflat when water is shallowest; however, large waves have their maximum effect during slack tide, when the fetch is often longest (Dyer, 1998, Le Hir et al., 2000). Bed stress is dominated by tidal currents on some mudflats (e.g., Christie and Dyer, 1998) while a combination of currents and local wind waves dominate other flats (e.g., Whitehouse and Michener, 2000).

1.1.2. Bed Characteristics

The interplay between hydrodynamic forcing, local sediment supply and biology set the composition of the bed at an intertidal flat (Le Hir et al., 2000). Areas that contain a

large amount of silt, clay, and organic matter are known as mudflats, while areas with mostly sand grains are known as sand-flats. Sand grains are inert particles with a diameter greater than ~60 micrometers and a well defined settling velocity. On the other hand, mud is chemically active (cohesive) and continually forms loose aggregates, or flocs, in the water column; as a result, settling velocity can vary several orders of magnitude (Teisson et al., 1993). Salinity and biological activity can lead to the formation of flocs (Teisson et al., 1993), while turbulent motions can both form or break flocs (Van der Lee 1998). A fluid mud layer is often formed by the currents or the cyclic loading of waves on a cohesive bed (Mehta et al., 1989, Teisson et al., 1993). Sediment transport on mudflats made of fine silts occurs either through suspended sediments in the water column or the physical advection of the fluid mud layer (Mehta, 1989). On intertidal flats with more sand content and larger grain sizes, bed forms such as ripples develop, either by currents or waves (e.g., Sleath 1984). Sediment transport occurs both in the water column and in bed-load transport, which is the advection of individual grains or sand layers along the bed.

The beds of intertidal flats are permeable to fluids and susceptible to mixing by biological activity, and form a dynamic boundary condition that affects water column hydrodynamics. As shown by Precht and Huettel (2004), gravity waves can force water into the bed at ripple troughs, setting up a subsurface circulation that is expelled at the ripple crest. In addition, groundwater discharge or seawater recirculation in coastal regions is a large source of fluid, nutrient and contaminant flux, and helps set the biogeochemical properties of the local bed (Burnett et al., 2003). Moreover, bio-

turbation by animals creates another mechanism by which sediments and water are exchanged through the bed interface.

1.1.3 Benthic Biology

Intertidal mudflats occupy an important biological niche in the estuarine environment, supporting an active food web and providing a transition zone and protective barrier between land and estuary (Dyer, 1998). The habitat provides a nursery ground for juvenile fish, and supports large amounts of shorebirds (Horne and Goldman, 1994). In addition, mudflats support large amounts of bivalves, crabs, worms, and other microbiota, which feed either directly or indirectly on the productive microalgae in the sediments and water column (Horne and Goldman, 1994). During spring and summer, diatoms and other microalgae grow in the top several mm of the mudflat surface, producing a network of long-chain carbohydrates (sugars) which strengthen the substrate and increase the shear stress needed for erosion (Holland et al., 1974, Grant et al. 1986). On an intertidal mudflat in the Dollard estuary, the critical shear stress increased from ~ 0.2 Pa to ~ 0.6 Pa during a spring algal bloom (Kornman and De Deckere, 1998). Conversely, the burrowing and feeding patterns of crabs, worms, clams, mud shrimp and other small invertebrates tends to bio-turbate and irrigate the subsurface, weakening the soil matrix (see e.g. Dyer, 1998 or Davey and Partridge, 1998). In fact, the action of benthic clams and other filter feeders cycles a large amount of fluid through the bed; for example, clams in South San Francisco Bay are estimated to filter the volume of an entire water column in less than a day (Cloern, 1982). The

benthic community can vary greatly over the scale of a ripple wave-length, reacting to—and modifying—sediment properties such as redox potential and subsurface organic matter (e.g., Meadows et al., 1998). In turn, properties such as water content, bed density, and grain size affect the critical bed stress and hydrodynamics (Mehta et al., 1989), and therefore the accumulation of subsurface organic matter and biota. In general, however, the feedback between the hydrodynamics, biology, and long-term morphodynamic change is poorly understood over both temporal and spatial scales.

1.1.4 Summary of intertidal processes

There is a growing literature related to both sandy and muddy intertidal flats; however the hydrodynamic processes governing suspension of sediments are poorly understood at water depths of less than 1 m (Christie and Dyer, 1998). Figure 1.1 shows a schematic of the muddy intertidal zone as it is typically described and modeled (see e.g. review by Le Hir et al., 2000). In this paradigm, tidal currents and wind-waves are the primary forcing mechanism and produce stresses at the bed which act to control sediment erosion and deposition of both cohesive (muddy) and non-cohesive (sandy) sediments. Thus, tidal currents and wind-waves control both bed-load transport and water column transport, the morphology of the bed (and bed roughness), and the production of turbulence. In short, tidal currents and wind waves appear to describe the physical environment that is experienced during periods of immersion by sediments, contaminants, nutrients, and biota such as clams, worms, and amphipods. However, a fundamental question frames figure 1.1 and this dissertation: are there other forcing

mechanisms and physical processes that are not being considered in this typical view of the mudflat environment?

1.2. Recent History of San Francisco Bay and field site

The environment of the San Francisco Bay and the field site at the Richmond Field Station has been greatly affected by anthropogenic activity in recent history, and is described below.

1.2.1. San Francisco Bay

In the past century, the San Francisco Bay has lost ~40 % of its tidal flats and over 90 % of its wetlands due to development. Today, the bay consists of 260 square kilometers of intertidal area and 960 square kilometers of subtidal water (http://www.berkeley.regis.edu). Over time, sediment inputs to the bay have greatly fluctuated, from an estimated 7.3 million metric tons per year during the days of hydraulic mining in the late 19th century (Gilbert, 1917) to current levels between 0.4 and 4 metric tons per/year between 1991 and 2001 (Wright and Schoelhammer, 2004). Annual sediment loads between 1957 and 2001 dropped by ~50% due to the building of dams and the end of the sediment pulse from hydraulic mining; however, other anthropogenic activities such as logging and increased urbanization form the potential to increase sediment load in the future (Wright and Schoellhamer, 2004). Thus, anthropogenic activities continue to affect the supply of sediment to the bay, and form

the long term boundary condition which likely affects the extent and location of San Francisco Bay mudflats. Over an annual scale, the storms and spring run-off events bring large pulses of sediment to the estuary, some of which is deposited onto local mudflats; wind waves during the summer tend to erode the deposits on the shoals, leading to low suspended sediment concentrations in the fall (Ruhl and Schoellhamer, 2004). The historical trends observed over the entire San Francisco estuary form the seaward boundary condition that affects the mudflat at the field site at the Richmond Field Station in Richmond, CA.

1.2.2. Richmond Field Station

On a more local scale, the geography at the Richmond Field Station has been greatly altered from its original state. In the late 19th century, open bay water and intertidal mudflat abutted a sea wall (Fig. 1.2, 'A'). In the mid 20th century, the shoreline was extended several hundred meters to the south with the addition of a railway spur ('B'), an outer breakwater ('C') and by infilling ('D'; figure 1.2). This can be seen by the remnants of an old pier ('E', built pre-1900), which now ends just to the south of the old railway spur (now a multi-use trail in the East Bay Regional Park District) at the intersection of the present tidal channel, mudflat, and marsh. Added in the 1950's (URS report, 2000), the railway and breakwater form a barrier to waves and have led to the creation of tidally forced marshland in the protected areas behind them (see figure 1.2). In addition, much of the land behind the railway was filled in, largely by the dumping of pyrite cinders (a byproduct of manufacturing sulfuric acid) from the former

Stauffer/Zeneca chemical plant, which closed in 1997 (URS report, 2000). On the margins of the marsh ('F') and to the south of the breakwater and railway, an intertidal mudflat has formed ('G') (see figure 1.2). The mudflat is bisected by two sub-tidal channels which provide the marsh with bay water and drain the small local watershed, particularly during intermittent winter storms.

Due to industrial activity throughout the local watershed in the past 135 years, the marsh adjacent to the mudflat is contaminated with pollutants such as PCB's, pesticides, and heavy metals. Analysis of soil samples in Stege Marsh found elevated levels of arsenic, cadmium, copper, lead, mercury, selenium, and zinc (URS report, 2000). In addition, pesticides including DDT, Heptachlor and byproducts, as well as PCBs were found at various locations in the marsh (URS report, 2000). Before the construction of the breakwater and railway, wave action and currents spread some of the material from the dumped pyrite cinders (including various heavy metals mentioned above) on the surface of the former mudflat; it is likely that some residue is buried in the current mudflat. Moreover, the former railway spur is porous and connects the mudflat hydraulically with the Stege Marsh area. Currently, the University of California, Berkeley and the Zeneca Corporation (formerly Stauffer) are leading an effort to clean up and contain much of the contamination behind the former railway. Occurring over several stages in the fall of 2003 and 2004, the remediation effort entailed removing large sections of contaminated soil to a consolidated site on Zeneca property. This effort opened up more land to tidal action, which is being allowed to evolve into a marsh/upland ecosystem. The implications for the long term evolution of the local

marsh and mudflat environment, the effect on flora and fauna, and the fate and transport of remaining contamination is as yet unclear; in any case, recent remediation efforts represent yet another anthropogenic change to the environment.

1.3. Structure of Dissertation

Local hydrodynamic conditions and sediment transport on the mudflat are critical to understanding the long term evolution of the mudflat/marsh ecosystem, as well as transport and mixing processes. The large amounts of contamination in the marsh area (and potentially the mudflat) highlight the importance of understanding the mechanisms that control short term—and hence long term—change. In this dissertation we present extensive hydrodynamic observations at the local mudflat on the time scale of seconds to several weeks. The hydrodynamic sources of energy and their characteristic time scales are then isolated and described. These different sources of energy superpose upon each other—and interact nonlinearly—in the intertidal water column, creating a dynamically varying interaction with the sediment bed. By modeling the observed boundary layer structure of velocity using numerical and analytical models, we attempt to describe how the bed affects the hydrodynamics (and vice versa). In addition, we investigate how parameters such as bed stress, TKE and dissipation of energy vary with changes in the hydrodynamic forcing, both by using statistical data analysis techniques and non-linear wave-current interaction theory (Grant and Madsen, 1979). Finally, we connect the variation in the hydrodynamics (for example, wave energy or bed stress) to changes in the erosion and flux of sediment. These studies provide increased

understanding of hydrodynamic forcing and scalar transport at intertidal mudflats, and form the basis for understanding the mechanisms which produce long-term change.

In summary, the purpose of this dissertation is to improve our current understanding of sediment (and scalar) transport at an intertidal mudflat (see figure 1.1) in a polluted ecosytem. Therefore it is essential to better understand the hydrodynamic sources of energy in the water column and how these forcing mechanisms interact with the sediment bed. Only then can one confidently describe sediment erosion, deposition, and fluxes. The flow of the dissertation is therefore organized as follows. Chapter 1 provides an overview of the intertidal environment and the history of the field site. Chapter 2 details the experiments, experimental methods, and data processing methods used to analyze the hydrodynamics and sediment transport. In addition, qualitative observations of the field site are described. Chapter 3 introduces the multiple frequencies of motion present on the mudflat and their relative importance over time. Chapter 4 presents the methods used to calculate Turbulent Kinetic Energy (TKE) and dissipation of energy in an environment with multiple wave frequencies. Dissipation and TKE, which indicate the amount of fluid interaction with the bed, are then presented over a typical tidal period. Chapter 5 investigates the stress imparted by the hydrodynamics on the sediment bed. To do so, the boundary layer of the tidal current, ocean swell, and the seiche are presented and compared to analytical and numerical models. In addition, the non-linear interaction between currents and waves of several frequencies is investigated. Chapter 6 looks at the effect of the multiple frequencies of motion on sediment erosion, deposition, and flux. Finally, the last chapter summarizes

the scientific contribution of this dissertation and outlines future directions for further analysis.

1.4. Figures

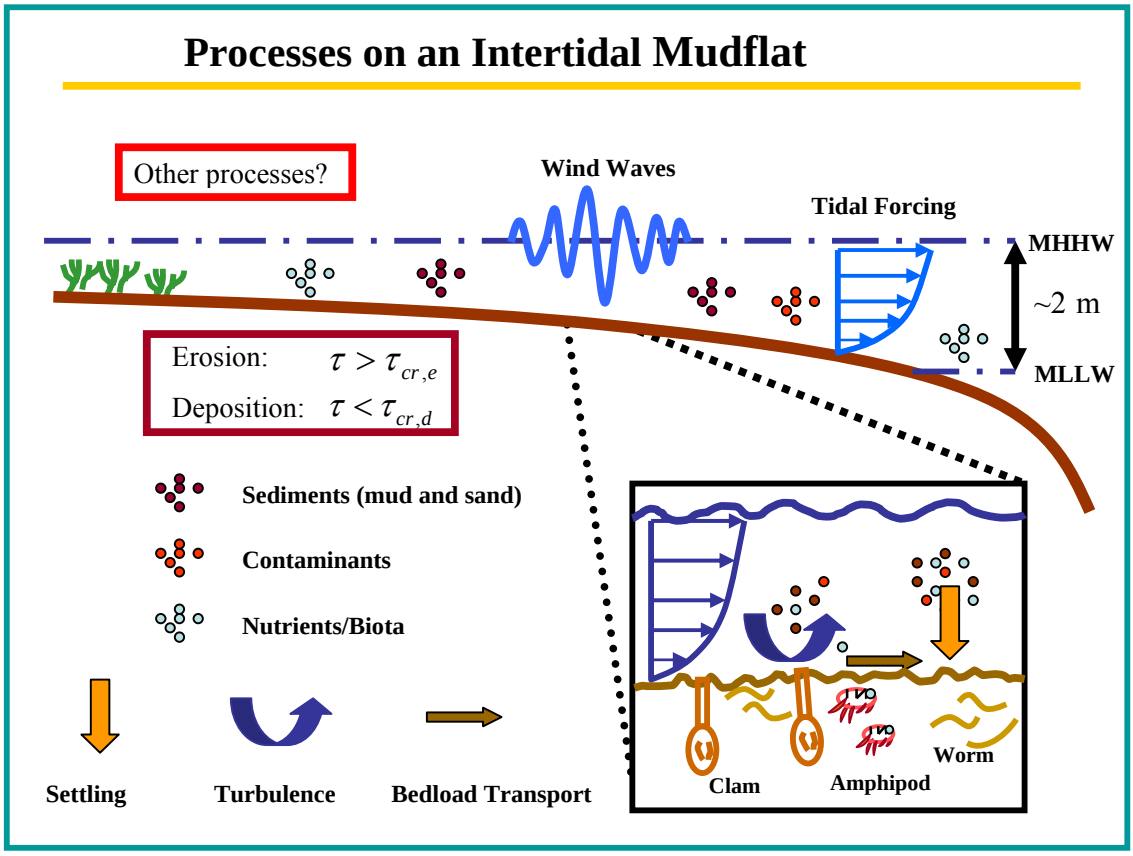

Figure 1.1: Typical view of processes on an intertidal mudflat.

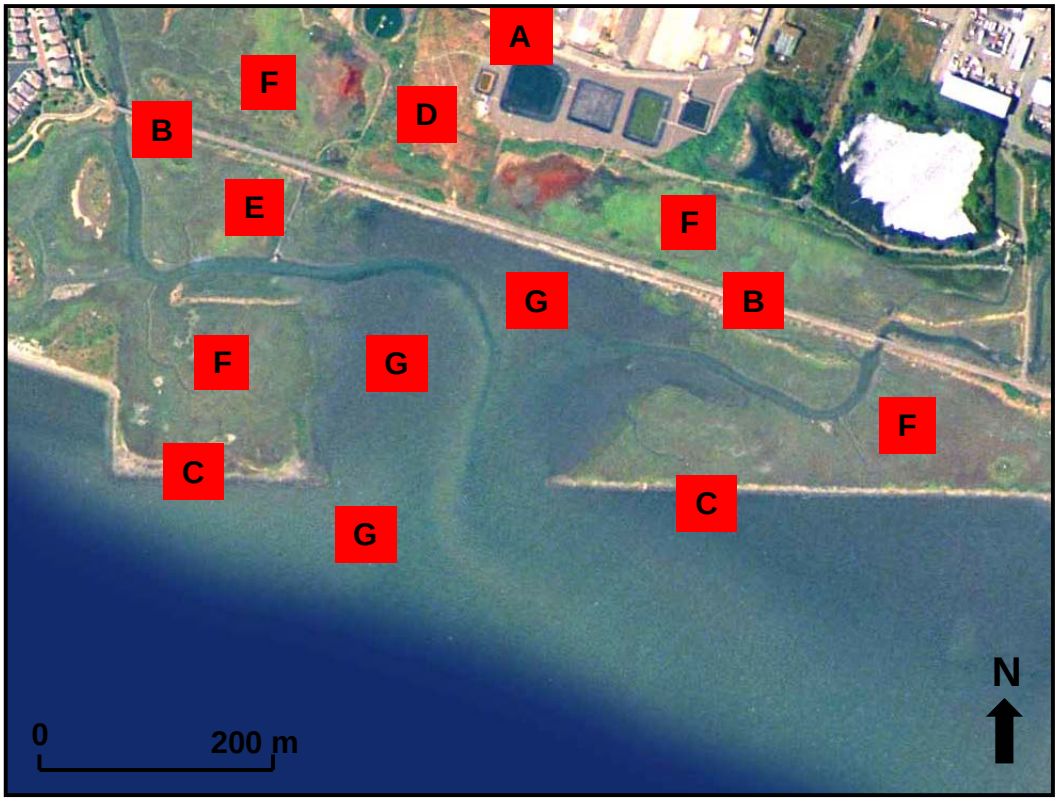

Figure 1.2: Schematic view of the field site at the Richmond Field Station. Letters 33note: A: Approximate Location of sea wall in 19th century; B: Railway spur built in the 1950's, now a trail in East Bay Regional Park District; C: Breakwater built in the 1950's; D: Location of infilling and dumping of industrial waste; E: Remnants of an old pier from the 19th century; F: Marshland that has developed in the past 50+ years; G: Intertidal mudflat that has developed in past 50+ years

Chapter 2: Experiment Description and Methods

2.0. Introduction

Over a two year period from February, 2001 to October, 2003, a series of four field experiments was conducted at the intertidal mudflat at the Richmond Field Station. The mudflat is located at 37^0 54' 31'' N, 122^0 20' 0" W on the east side of San Francisco Bay, California, near Point Isabel and the cities of Berkeley and Richmond (figure 2.1). The mudflat is tidally forced and intertidal, with a tidal range of ~2.5 m. Two sub-tidal sloughs bisect the mudflat, supply the adjacent marshland with tidal flow and drain seasonal runoff. The locations of the various experiments are depicted in figure 2.2; note that experiment 4 was spread over four locations. The frames and instruments (described below) were staged at the Richmond Field Station and manually walked out onto the flats with able-bodied volunteers (see acknowledgements). The frame and instruments used are described in section 2.1 and 2.2, followed by detailed information about each particular experiment in section 2.3.

2.1. Deployment Frames

Two types of frames were used to mount the instruments used during the field experiments—a sawhorse frame (see figure 2.3) and a lightweight frame for side-mounting instruments close to the bed (see figure 2.4).

2.1.1. Sawhorse frame

The lightweight aluminum sawhorse frame show in figure 2.3 was used in all the different field experiments. As seen in figures 2.3, 2.5, 2.6, and 2.7, various instruments are attached to the sawhorse frame along the support beams and on the crossbar. To minimize settling into the mud, the frame rests on two large, 4 foot square footpads; over all the experiments, settling of the frame never exceeded ~ 0.01 m depth except during bed failure over a stormy period (see discussion on experiment #3). Hollow structural beams are allowed to fill with water during a period of inundation, adding weight and stability to prevent lateral movement or hydroplaning due to waves or currents. In addition, as much as 75 pounds of lead bricks were attached to the base of the frame to further prevent movement. To allow mounting of instruments, the square, hollow crossbar of ~ 1 m length has pairs of ¼ inch holes drilled at 0.2 m increments along its length. The Acoustic Doppler Velocimeters (ADVs) were attached to 0.3 m long sections of 2 inch PVC pipes using pipe clamps and bolted to the crossbar in a downward facing orientation (see figure 2.5). Along the legs of the frame, Optical Backscatter Sensors (OBS) and Conductivity-Temperature-Depth probes (CTD) were attached using stainless steel pipe clamps.

The sawhorse frame is designed to minimize obstruction to the flow, and uses small aluminum tripod legs (diameter ~ 2 inches) and a crossbar that is high (~1 m) above the bed. Using simple scaling arguments, one can determine the conditions in which frame interference could occur. The frame alters the flow both by changing the potential flow

field in the water column and by adding an additional source of drag and turbulence production. Disturbances in the potential flow field can be scaled using the equation for flow around a cylindrical object:

$$u = -U\hat{x} + U(\frac{a}{r})^2(\cos\theta\hat{r} + \sin\theta\hat{\theta}) \quad (2.1)$$

where a is the radius of the cylinder, r is the distance from the center of the cylinder, and $\hat{x}$, $\hat{r}$, and $\hat{\theta}$ are unit vectors in the x, r, θ directions. For the simple case in which θ= π/2, the velocity difference between the free stream and the coordinate (r, π/2) is:

$$u = U(1 - \frac{a^2}{r^2})\hat{x} \quad (2.2)$$

Thus, the square of the ratio between the cylinder radius and the position of the measurement volume scales the effect of an obstruction on our experimental measurements. A measurement volume that is one diameter from the surface of a cylinder (r=3a) causes a deviation in velocity of ~10 %. Two diameters from the cylinder surface, the alteration in flow velocity is only 4%. To first order accuracy, then, the instruments should be located at least one diameter from an obstruction.

As seen in figure 2.4, the largest obstructions to the flow field are the side mount frame (left side of frame), the crossbeam, the downwards looking velocimeters, and the data recorders (right side of frame). For flow that is perpendicular to the crossbeam (into or

out of page), scaling suggests that the combined effect of the crossbeam (diameter= 0.1 m) and cabling (~0.1 m) is negligible on the velocity measurements, as the velocimeters are focused in the lower 0.3 m of the water column. The downward facing velocimeters and associated PVC piping (~ 0.15 m) do not extend below 0.5 m, and thus are unlikely to affect the flow in the measurement volumes.

On the outside of the frame, the combination of two data recorders and the tripod legs of the frame pose an obstruction with a width of perhaps 0.3-0.4 m. Thus, the outer velocimeter near the data-recorders, located ~0.3 m from the data recorder, is probably affected by the flow displacement around this obstruction on the order of 10%. Similarly, the side-mounted frame, with a width between 0.25 m and 0.50 m, likely affects flow on either side. The nearest downwards facing velocimeter is ~0.3 m removed from the side-mount frame, and therefore likely feels an altered flow field of ~10-20%. Because this measurement is at 0.015 m, the velocity is < 0.01 m/s. Therefore, the error associated with the obstruction is less than 2 mm/s, or less than the overall measurement error. Similarly, the error induced at 0.05 m is likely on the same order of magnitude as the measurement error.

Turbulent eddies scale with the diameter of the obstruction, and are limited by either the water depth or the distance to the bed. For unidirectional flow that is perpendicular to the frame crossbeam, the mean flow advects the turbulent eddies downstream, and disturbance of the measurement volume is unlikely. On the other hand, oscillatory waves move turbulent disturbances back and forth, allowing a disturbance to propagate

laterally by turbulent diffusion. In the absence of advection, turbulence will decay over a distance proportional to the largest eddy sizes. Because the sensors are near the bed, the largest eddy scales are small and vary between 0.01 m and 0.15 m. Since the distance between the measurement volumes and neighboring sensors or frame elements are greater than 0.2 m, it is unlikely that turbulent motions are affecting the measurements of velocity unless the mean flow is advecting flow in the crossbeam direction. Indeed, when the flow vector is primarily in the direction of the cross beam, large disturbance of the free stream velocity is possible. Therefore, in practice, any flow data in which the flow vector deviated more than 30 degrees from the perpendicular direction is flagged and used with caution.

2.1.2. Side-mount frame

In addition to using the sawhorse frame, we also built an easily transportable, wooden frame to which the ADVs (and other instruments) can be mounted in a sideways pointing configuration. As can be seen in figure 2.4, the frame consists of plywood squares (approximately 1 meter squared) to which a 2 inch PVC pipe is attached using ¼ inch bolts. Instruments are attached to the piping and frame using pipe clamps, and the distance off the bed is varied by attaching small 2x4 blocks to the frame. In experiment 3, the side-mount frame was attached to the saw-horse frame, while in experiment 4 the frame was anchored directly to the mudflat surface by driving rebar through the frame several feet into the subsurface.

2.2. Instruments

The physical quantities measured during the field experiments include velocity, pressure, turbidity, salinity, and temperature. The instruments used to measure these quantities are described below.

2.2.1. Acoustic Doppler Velocimeter (ADV) Probes

The Acoustic Doppler Velocimeter is an instrument that measures velocity using 'pulse to pulse coherent ranging' (Lhermitte, 1983). Typically, three emitters that are oriented 120 degrees apart from each other and angled from a common plane emit two time-lagged acoustic signals. These acoustic waves are focused on a control volume on the order of ~ 1 cubic centimeter, where they scatter off particles that are moving with the flow. Some of the scattered signal is reflected to the transducer at the probe tip, which then measures the average phase shift in the acoustic signal due to all the particles. This Doppler shift is then transformed into an averaged estimate of 3-D velocity within the control volume for a particular acoustic pulse set, or ping. The average over multiple pings gives an accurate estimate of velocity in three dimensions. When individual probes are close together, acoustic interference between ADV probes is possible. However, tests in a laboratory tank found no evidence of impaired signal strength, signal correlation, alterations in velocity signal, or other changes for probes placed within 0.2 m of each other. Note that for a velocity range setting of 0.3 m/s, the

velocimeter reports an error of less than 2 mm/s per measurement (Sontek 2001) when sampling at a frequency of 10 Hz.

Acoustic Doppler Velocimeters (ADVs) from two different companies were used in the experiments detailed in this dissertation. The ADV by Sontek comes as part of the watertight Hydra module, which includes a Conductivity-Temperature Probe, an Optical Backscatter Sensor, and an external data logger that takes synchronous data. By contrast, the ADV vector by Nortek is a self-contained probe with internal logging. Each ADV comes equipped with compass and tilt sensors so that the absolute orientation of the probe—and the velocity estimate—is known. In addition, each ADV comes equipped with a pressure sensor. The Sontek ADVs are also able to estimate the distance to the bed, and are capable of several simultaneous sampling schemes. While the Nortek velocimeters sampled at up to 32 Hz, the maximum sample rate for the A349 Hydra and A342 Hydra systems was 10 Hz and 25 Hz, respectively. The limiting factor of each deployment was either memory or battery power. The Hydra module was deployed with an 18 V battery, while the Nortek uses a smaller 12 V battery. Thus, while the Hydra was generally memory limited, the Nortek velocimeters were generally battery limited. Section 2.3 describes the various experimental configurations and the amount of memory available during each deployment.

2.2.2. Optical Backscatter (OBS) Probes

The Optical Backscatter Probe (OBS) by d-a Instruments, Inc. measures turbidity and optical backscatter, which is then used to estimate ambient sediment concentrations. It functions by sending out a broad cone of infrared light at ~ 875 nm and measuring how much of the light is reflected back to the sensor. As conditions become more turbid and the number of particles in the water increases, more light is scattered back to the probe—hence the term optical backscatter. For a given concentration of sediment, the intensity of backscatter increases as particle size decreases. This occurs because small particles have a greater surface area to volume ratio, and therefore present more reflective surfaces. Indeed, for a spherical particle the backscatter strength increases by a factor of 10 between 100 and 10 micrometers. Thus, the OBS preferentially measures smaller particles such as silt and mud (see Connor and DeVisser, 1992, for an overview). Because the OBS measures only relative turbidity, it must be calibrated with in-situ water samples that accurately reflect the types of sediment in a particular environment. In the first two experiments described below, water samples were taken manually by collecting 1 L samples at the approximate level of the OBS. Later experiments used a boat mounted pump to extract water from tubes located at different heights on the frame. To minimize disturbance to the local bed and obtain representative samples, the tubes were run over 50 feet from the frame and 2 inch diameter PVC pipes were used as the entrance ports at the frame (see Ralston, 2005 for more discussion).

Note that the ADV also measures backscatter intensity with its acoustic signal, and can therefore also be calibrated to estimate sediment concentrations. In general, acoustic backscatter is at a maximum when the wavelength of the sound wave is equal to the circumference of the sediment particles (Lohrmann, 2001). For the Nortek and Sontek velocimeters, this maximum occurs close to 100 micrometers; for a spherical particle of 10 micrometers, the reflectance is less than 0.01% of the maximum. Thus, the ADV preferentially measures larger grain sizes such as sand, while the OBS preferential measures smaller grain sizes such as silt or clay.

2.2.3. Other instruments: CTD, fluorometer

In addition to the OBS and the ADV, we also used two Micro-Cat Conductivity-Temperature (CT) probes and a Conductivity-Temperature-Depth (CTD) from Richard Brancker Research (RBR), as well as two combined OBS/fluorometers from Alec CKU.

2.3. Experiment Details

The instruments used in each of the four experiments, their sampling schemes, and the relative success of each experiment are described below.

2.3.1. Experiment #1

The first experiment aimed to simply test the instruments and the sawhorse frame in this environment, and gain some insight into the major forcing mechanisms over a spring-neap cycle. Thus, we deployed the sawhorse frame on consolidated sediment near the channel over a spring neap cycle (see figure 2.2), and attached an ADV, an OBS and a CT probe (see figure 2.3). Data were logged to a 48 MB capacity storage unit in a watertight HYDRA module (from SonTek), which also provides power from an 18 V battery. Attached to the center of the frame (to ensure no interference from the side of frame), the ADV was focused ~0.2 m from the bed, and measured velocity in a reference frame relative to the instrument. The OBS and CT probe were each mounted ~0.15 m from the bed at the frame supports. Data were logged in bursts of 45 seconds at a rate of 10 Hz, and repeated every 5 minutes. Data collection continued through the wet and dry periods, from 12:00 pm on February 2, 2001, to 11:00 am on Feb 15, 2001, capturing 25 wet/dry cycles in all. Unfortunately, due to a faulty connection the compass did not measure meaningful data, and pressure was not measured due to a programming error. Water samples were taken manually by collecting 1 L samples at the approximate level of the OBS. The acoustic (from the ADV) and optical backscatter results are calibrated to sediment concentration by measuring the mass retained on a filter (fiberglass filter, pore size on the order of 1-2 micron) from a known fluid volume.

2.3.2. Experiment #2

One year after experiment 1, between February 28th and March 12th of 2002, we deployed a more elaborate package of instruments in which we attached four ADVs, two OBS, and two CT sensors to the saw-horse frame. Three ADVs were attached vertically to the cross-beam of the frame at a horizontal spacing of ~0.3 m from each other, while the fourth was oriented horizontally at the base of the frame. To capture more wave activity, the experiment was approximately 50 m east of the previous location, again on consolidated sediment. As in experiment 1, water samples were taken by hand using an inflatable dinghy for transportation. To better analyze longer period waves (wave groups and ocean swell), the burst length (i.e., sample time) of each sensor was increased from experiment 1. In addition, a lower frequency sampling scheme was added to the Sontek ADVs to sample intra-tidal frequencies of motion (data set 'b'). The sampling scheme is depicted in the table 2.1.

The two Nortek ADVs measured data for 19 wet/dry periods until the batteries failed, while Sontek #342 measured 23 wet/dry cycles. Due to a firmware problem, the Nortek #4142 sensor logged data at a 10 minute offset to the other sensors. Unfortunately, Sontek #349 measured no data, either because the ADV was not configured for horizontal deployment or due to programming error.

Table 2.1: Sampling Scheme for Experiment 2; Note that the Sonteks were programmed with two sampling schemes that ran in series with each other.

	Burst Frequency	Sampling Frequency	Sampling time per burst	Height off bed
Sontek #349 (a) (Side-mount) (b)	20 minutes 60 minutes	10 Hz 0.5 Hz	150 sec 1000 sec	0.05 m
Sontek # 342 (a) (b)	20 minutes 60 minutes	10 Hz 0.5 Hz	150 sec 1000 sec	0.1 m
Nortek # 4132	20 minutes	16 Hz	210 sec	0.19 m
Nortek # 4142	20 minutes	16 Hz	210 sec	0.34 m

2.3.3. Experiment # 3

The third experiment aimed to measure larger waves than the first two experiments and to measure mean tidal flow with little cross-shore component. More instruments were added to gain resolution in the vertical direction. In addition, the experiment was run over four days in order to measure nearly continuously. Finally, each Sontek Hydra system was upgraded to a memory capacity of 128 MB. Thus, from April 11th, 2003 at

16:00 local time to April 15th at 17:00, we deployed an experiment with 14 instruments on the sawhorse frame to the west of the channel between the two outer breakwaters (see Fig. 2.2, Fig. 2.5, and Fig. 2.6). At this location the geometry of the breakwaters constrains the flow to be primarily in the north or south direction. Moreover, the exposed location eliminates the effect of the breakwater on incident waves.

An overview of the sampling scheme in experiment #3 is shown in table 2.2, while the experimental setup is depicted in figure 2.6. In total, six velocimeters, five turbidity sensors, and three CTD probes were deployed. Note that the sampling scheme for each instrument was designed to optimize battery life and available memory over a four day period. Four of the velocimeters sampled at a rate of 8 Hz, while two sampled at 16 Hz. Each velocimeter began a new sampling burst every 10 minutes. Note that the two Sontek velocimeters sampled almost continuously, allowing longer time scale processes to be measured. Four of the velocimeters were mounted vertically with a horizontal spacing of 0.2 m, while two were mounted horizontally on one side to avoid interference with the other vertical sensors. Because the compass and tilt sensor only work to within angle deviations of ~50 degrees from vertical, the orientation of the side mount probes were manually measured in the field using a compass and level. The velocimeters were focused at heights of 0.015 m, 0.05 m, 0.1 m, 0.155 m, 0.285 m, and 0.33 m.

Similarly, a vertical concentration profile was obtained by placing the OBS at heights of 0.05 m, 0.15 m, and 0.35 m and the combined fluorometer/optical backscatter sensors at

0.1 m and 0.35 m. The redundant OBS sensors at 0.35 m and velocity sensors at ~ 0.3 m allow for error checking. Each OBS was calibrated in a laboratory setting using water sampled from the mudflat area during another experiment (see Ralston, 2005). Finally, the CTD probe measured data at 0.1 m above the bed, while the two CT probes measured data at 0.5 m and 1 m. The CTD probe from RBR recorded a measurement every minute over an averaged time of 15 seconds, while the Micro-Cat CT probes attached to the Hydra system recorded 10 minute averages.

Table 2.2: Sampling scheme for all the instruments in experiment #3. All heights off bed are measured manually in the field, except for the Sontek ADVs (which measure height acoustically) . Note that instruments labeled 'borrowed' were obtained from Yusuke Uchiyama.

	Burst Frequency	Sampling Frequency	Sampling time per burst	Height off bed
Sontek # 349	10 min.	8 Hz	590 sec.	0.285 m
Sontek # 342	10 min.	8 Hz	590 sec.	0.155 m
Nortek # 4132	10 min.	16 Hz	345 sec.	0.05 m
Nortek # 4142	10 min.	16 Hz	345 sec.	0.015 m
Nortek # 4131 (borrowed)	10 min.	8 Hz	188.5 sec	0.1 m
Nortek # 4143 (borrowed)	10 min.	8 Hz	188.5 sec	0.33 m
RBR (CTD)	1 min.	1 Hz	15 sec. avg.	0.1 m
Hydra 349 CT	10 min.	8 Hz	590 sec.	0.5 m
Hydra 342 CT	10 min.	8 Hz	590 sec.	1 m
Hydra 349 OBS # 2017	10 min.	8 Hz	590 sec.	0.19 m
Hydra 342 OBS # 2018	10 min.	8 Hz	590 sec.	0.05 m
RBR OBS # 1645	1 min.	1 Hz	15 sec. avg.	0.35 m
OBS/Fluorometer # 25 (borrowed)	1 hour	2 Hz	300 sec.	0.35 m
OBS/Fluorometer # 26 (borrowed)	1 hour	2 Hz	300 sec.	0.1 m

Overall, each instrument recorded data successfully as programmed over 8 wet/dry cycles. The data from April 13th-April 15th is excellent and forms a large part of this

dissertation. Due to a storm, however, much of the data from April 11th-April 12th was compromised, as described below.

Sometime between deploying the instrument on April 11th and daybreak on April 12th, a large storm arrived at the mudflat. Large winds exceeding 10 m/s with gusts up to 15 m/s were recorded nearby at the Chevron Oil Pier in Richmond, and correspondingly large waves with velocities greater than 0.5 m/s were measured by the velocimeters. A storm surge of about 0.2 m was measured by the pressure sensors. The combined action of waves and currents weakened the bed, and caused the frame to rotate 40 degrees and sink 0.1 m into the mud on its eastern flank (see fig. 2.7). Moreover, debris such as plastic bags hindered flow to at least one velocimeter. As a result, only the data of the velocimeters at 0.15 m and 0.28 m remains viable over this time period. During low tide on the afternoon of April 13th, we manually dug out the frame and relocated it nearby.

2.3.4. Experiment 4

The fourth experiment on the mudflat aimed to look at variation in hydrodynamic properties and sediment concentrations over both spatial and temporal scales. As such, two sawhorse frames and two side-mount frames were deployed as shown in figure 2.2. To the south between the channel and the eastern breakwater we placed a sawhorse frame with a downward looking Sontek ADV focused at 0.1 m and an OBS and CT probe at ~0.2 m each. Approximately 35 m to the north, we placed the other sawhorse

frame to which we attached the other Hydra system (ADV, OBS, and CT probe) as well as two autonomous Nortek vector velocimeters. Finally, approximately 65 m and 85 m north of the southern frame we placed two Nortek vectors in the side-mount frames; as before, the orientation was manually measured using a compass and level. The sampling scheme is described below in table 2.3. Note that the Nortek 4131 and the Nortek 4143 had their memory upgraded from ~23.8 MB to ~ 79 MB.

Table 2.3: Sampling scheme for all the instruments in experiment #4. All heights off bed are measured manually in the field.

	Burst Frequency	Sampling Frequency	Sampling time per burst	Height off bed
Sontek # 349 (site 4a)	10 min.	16 Hz	520 sec.	0.1 m
Sontek # 342 (site 4b)	10 min.	8 Hz	590 sec.	0.32 m
Nortek # 4132 (site 4c)	10 min.	16 Hz	360 sec.	0.115 m
Nortek # 4142 (site 4d)	10 min.	16 Hz	360 sec.	0.115 m
Nortek # 4131 (site 4b) (borrowed)	10 min.	16 Hz	360 sec.	0.05 m
Nortek # 4143 (site 4b) (borrowed)	10 min.	16 Hz	360 sec.	0.125 m
Hydra 349 CT	10 min.	8 Hz	590 sec.	0.15 m
Hydra 342 CT	10 min.	8 Hz	590 sec.	0.20 m
Hydra 349 OBS # 1645	10 min.	8 Hz	590 sec.	0.14 m
Hydra 342 OBS # 2019	10 min.	8 Hz	590 sec.	0.19 m

2.4. Experimental Methods

The large quantities of data collected over the course of the experiment required various strategies to deal with them effectively. Raw velocity data were separated into immersed (wet) and dry periods by requiring the correlation of backscatter measured by the velocimeters to exceed 70 % (Sontek manual). Moreover, various statistical methods were used to understand the various scales of motion.

2.4.1 Calculating power spectrum

Unless otherwise mentioned, the power spectrum of velocity and other hydrodynamic properties is calculated using a fast Fourier transform (FFT) method. A hanning window is applied to reduce spectral leakage from abrupt changes at the beginning and end of each data set (for more information, see Oppenheim and Schafer, 1989). In order to compare the residual wave energy left over after calculating TKE, we calculated the power spectrum for both the Soulsby, Trowbridge, and hybrid methods. Note that the power spectrum for the Soulsby method is found using the raw, measured velocity U, while for the 'Trowbridge average' and 'hybrid' method the differenced velocities ΔU_k (Equation 4.9) and $v'(t)_{t,j}$ (Equation 4.13) are used.

2.4.2 Bandpass filtering

To look at the boundary layer development of various frequencies of motion (e.g., ocean swell or the 500 second seiche; see chapter 3), we separated the raw velocity signal into its constituent frequency bands. We applied a bandpassed, 5^{th} order buttersworth filter between 1/8 Hz and 1/20 Hz to obtain a continuous train of ocean swell. For the seiche, we bandpassed between 1/300 Hz and 1/800 Hz . By definition, signal attenuation at the cutoff frequency is equal to $\sqrt{1/2}$; thus there is some leakage of energy from outside the specified frequency range (Matlab Help, version 6.5).

2.4.3 Wavelet Decomposition

In addition to bandpass filtering, we also used wavelet decomposition to look at different scales of motion. Wavelet decomposition is similar to Fourier analysis in that it uses a series of wave forms to represent the raw signal. However, while Fourier analysis uses a series of cosine waves of different frequencies to represent the signal, wavelet analysis uses a decaying, oscillatory signal called a wavelet to represent the raw signal. These wavelets can be stretched or compressed, i.e., scaled. Depending on the scale of the wavelet, a different frequency of motion is measured (much like changing the frequency of a cosine wave). However, because the wavelet decays, multiple wavelets must be used over a particular scale of motion to represent the signal in time (or space). Thus, wavelets measure the time-varying amplitude at a particular scale (roughly, frequency); by changing the scale, it is possible to create independent, time varying signals that represent the different time scales of motion in the raw signal. Compared to Fourier analysis, which measures the rms velocity at a given frequency, this is a great advantage for identifying intermittent events. Moreover, because they are independent, there is no leakage of energy from one scale to the other; by contrast, a bandpass filter by definition contains some energy at frequencies above and below its cutoff frequencies. However, the disadvantage of wavelet analysis is that the scales only roughly translate into a frequency band, and, perhaps more importantly, there are significant errors that can occur at the edge of the data set. Thus, we discard data that is less than 10 percent of a period (reciprocal of frequency) away from the beginning or end of a data set. For example, for a wavelet decomposition with a period of 500

seconds, we discard 50 seconds of data at the beginning and end. Empirically, this minimizes error to the order of 1 mm/s. In this dissertation, we used the daubechies wavelet of order 5, known as 'db5' (for more information, see Meyer, 1990).

2.5. Experimental Error

For the most part, the instruments and setup proved reliable. However, some anomalous measurements occurred with the vertical velocity measurements and the compass measurements, as described below. In addition, there was some discrepancy between the velocity measured in the side mount configuration vs. the vertical configuration.

2.5.1. Vertical Bias

A variable downwards bias on the order of 0-0.02 m/s was measured in the vertical direction, perhaps due to frame interference or instrument error. A small error in the tilt sensors or the acoustic signal can bias the measured reading. The cross-beam of the frame may cause fluid to accelerate and push it downward; in fact, the largest downward velocities occur when the percent obstruction is largest (water level ~ 1 m). Finally, the slope of the bed will induce a legitimate negative velocity during the ebb. In all likelihood, a combination of factors leads to the downward bias; however, the vertical velocity readings of each burst must be evaluated carefully before using.

2.5.2. Compass readings

Compass readings between the velocimeters in experiment #3 varied by up to 20 degrees. Other experiments using velocimeters have also noted anomalous compass readings (D.K. Ralston and D. Sereno, personal communication). A possible explanation might be magnetic interference from frame elements (steel rods, clamps, etc) or nearby magnetic sources (e.g., subsurface piping). Fortunately, all the instruments were manually aligned and their orientation measured in the field with a hand-held compass. Thus, the internal compass error can be estimated and the error in the velocity measurements can be greatly reduced.

2.5.3. Side mounted velocimeters vs. vertically mounted velocimeters

In experiment #3, the total energy measured by the side-mounted velocimeter at 0.33 m and the vertically mounted velocimeter at 0.28 m is not always consistent. During the flood tide, the velocity generally varies by less than 0.01 m/s. However, during the ebb tide the total velocity varied by up to 0.04 m/s over some 3 minute periods. On average, the side-mount measured between 10 percent and 20 percent less energy over a tide, though some individual bursts during the ebb showed variation up to a factor of two. Wave orbital velocities measured by the two sensors differ by 10 percent to 20 percent as well. In general, the vertically mounted velocimeter measured more energy than the side-mount, though not always. Possible physical explanations include acceleration of flow through the saw-horse frame or shielding of the side-mounted frames due to the

obstruction by the various instruments and frames. It is also possible that the side-mount velocimeters did not work well (they are designed for downwards facing deployment). Interestingly, the magnitude and direction of flow for closely spaced sensors follow each other over a tide. For example, the side-mounted velocimeters and the pair at 0.155 m and 0.285 m show a great degree of internal consistency. Overall, the set of vertically mounted instruments are internally consistent, while the side-mounted instruments are similarly consistent. Use of all six instruments together, however, needs to be evaluated on a burst by burst basis.

2.5.4. Discussion of instrument errors

Most of the results presented in this dissertation focus on detailing physical processes in the intertidal zone and on developing techniques to understand them, and depend more on the relative magnitudes of velocity and turbidity in the water column than on absolute quantities. Therefore, the condition that the instruments be internally consistent (i.e., that the mean direction and magnitude of velocity follow similar trends) is sufficient to obtain confidence in the results. The profiles of velocity and sediment concentration measured under the crossbar of the frame are self-consistent and fulfill the criteria. In many calculations, however, the side-mounted instruments are not consistent with the vertical instruments and are therefore not included.

2.6. Observations of field site

While the quantitative results from the field experiments will be analyzed and discussed in the following chapters, some interesting insights about the field site can be made using qualitative observations of the wind, water dynamics, sediment characteristics, and biota. For example, meteorological conditions at the field site range from calm with barely discernable wind to quite windy (measurements are sometimes > 10 m/s), particularly during storms or when fog comes ashore on summer afternoons. Wind from the south and southwest causes large waves (0.1-0.3 m height) with intermittent, visible white-capping, though small waves are apparent even in calm conditions. The wave attack appears to be largest at the outer breakwater and on the east side of the mudflat, as waves occurring there have the largest fetch. During both receding and flooding tides at depths of less than 0.1 m, waves come ashore as slow moving bores with a height of several centimeters. The time lag between each bore is irregular and varies from approximately 2-10 seconds, indicating a varied wave climate with several dominant frequencies. As the tide recedes, water streams over the mudflat in sheet flow or in small rivulets on the flat, and appears to flow either towards the channel or towards the bay. Inside (north of) the breakwater, visual inspection suggests that bathymetry of the mudflat is concave, suggesting an accreting mudflat (Dyer, 1998). To the south of the breakwater, the intertidal area is generally convex, suggesting an erosive environment (Dyer, 1998).

The intertidal zone at the Richmond Field Station contains fine grained sand (non-cohesive) and silt (cohesive). Visual inspection shows some evidence of partition over the small ripples. An analysis of sediment cores from the mudflat shows a peak at 70-80 micrometers and a secondary peak at 5-10 micrometers in the top 0.02 m of mud (Ralston, 2005). Water samples, on the other hand, show a more defined peak at 5-10 micrometers and a secondary peak at 70-80 micrometers. Therefore, while the bed contains mostly fine-grained sands mixed with a small percentage of silt, the water column contains more silt. This suggests that the silt is being eroded preferentially and is staying in suspension longer because they have lower settling velocity. Alternatively, silt is being advected from another location. A similar difference between the grain size on the bed and in suspension was observed on some mudflats in the Humber estuary (Widdows et al, 1998). Depending on location and time of year, the distribution and dominance of the different grain sizes changes; generally, more protected areas show more organics and finer grained silt (Ralston, 2005). On the shoals, organic content varied between 2-3 percent (Ralston, 2005), which is relatively low for a mudflat (Dyer, 1998); by comparison, organic content on mudflats in the Humber estuary varied between from 4-8 percent (Widdows et al., 1998). The color of the mudflat is grayish to grayish-brown (see figure 2.8) , which indicates aerobic conditions and confirms an organic content below 5 percent (Dyer, 1998).

The bed of the mudflat at the Richmond Field Station typically exhibits an irregular pattern of small ripples that are aligned with the primary direction of wave propagation (see figure 2.8). The typical length between ripple crests is on the order of 0.05 m,

while the height is ~ 0.01-0.02 m. This bedform is ubiquitous in the non-channel portions of the mudflat, and was similar in shape and size at all measured locations over several years. Interestingly, observation suggests that the ripples are formed during periods of large waves, but persist during low wave-energy periods. For example, disturbances to the mudflat surface caused by sliding the instrument frame or walking on the surface remained readily apparent from the shoreline for many days until large waves from a storm event reworked the surface. Mean flows due to tidal variation therefore appear to have little effect. These 'relic' or 'fossil' ripples are commonly found in marine environments (Sleath, 1984), and form the primary roughness element on the mudflat. Empirical estimates of the roughness height scale as a ratio of the height squared (H^2) and wavelength (L) of the ripples (Sleath, 1984, Whitehouse et al., 2000):

$$z_0 = a\frac{H^2}{L} \qquad 2.3$$

where a is an empirical constant approximately equal to 1. This yields a roughness estimate of ~0.002 m to 0.01 m, which is consistent with the roughness estimated from the velocity measurements (see chapter 5).

Other bedform features have also been observed on the mudflat and suggest the complex forcing that shapes the local morphology. For example, a pattern of small pools (order 0.5 m-1 m diameter, depth ~0.01-0.02 m) was observed near the site of experiment 3 (see figure 2.7). On the east side of the channel, near the breakwater, a

pattern of eroded patches (0.05-0.1 m depth, 1-10 m diameter) were observed in the winter of 2002. This suggests whole scale bed erosion (e.g., Mehta 1989) in which an entire portion of the cohesive bed fails. Not coincidentally, these erosion features occurred in the area of largest apparent wave exposure. Sometime over the next year, these 'holes' were largely filled in with new sediment. Thus, there is qualitative evidence of bed variation and reworking on several different spatial scales. Bed failure also occurred at the site of experiment 3, in which large waves rotated the ~ 100 kg frame and buried one footpad under ~ 0.1 m of sediment. The probable mechanism is the fluidization of the bed due to wave action and the weight of the frame. Other observed bedforms are a series of small rills that run parallel to the channel (order of several cm tall), and the presence of small, conical mounds at random locations. Though it is unclear whether caused by biotic or abiotic forces, these conical mounds are observed to eject water during the dry period between high tides when weight is applied nearby. Finally, there are a number of man-made roughness elements, including many tires and a halfway buried boat. Our experiments were placed far from these objects so that no hydrodynamic effect would be felt.

The small biota of the mudflat is largely hidden. Bivalves and worms can be observed in sediment samples. Large amounts of shorebirds follow the receding tide back as mud becomes exposed, presumably feeding on the benthos and bioturbating the sediment surface. Other observed animals on the mudflat include a solitary salmon in the channel, a jellyfish during high tide, small fish (< 0.01 m) caught in the frame, and the remains of a dungenous crab near the frame after a storm. Protected areas of the upper

mudflat are periodically covered with mats of green algae, while there are scattered macrophytes in the channel near the breakwater.

2.7. Figures

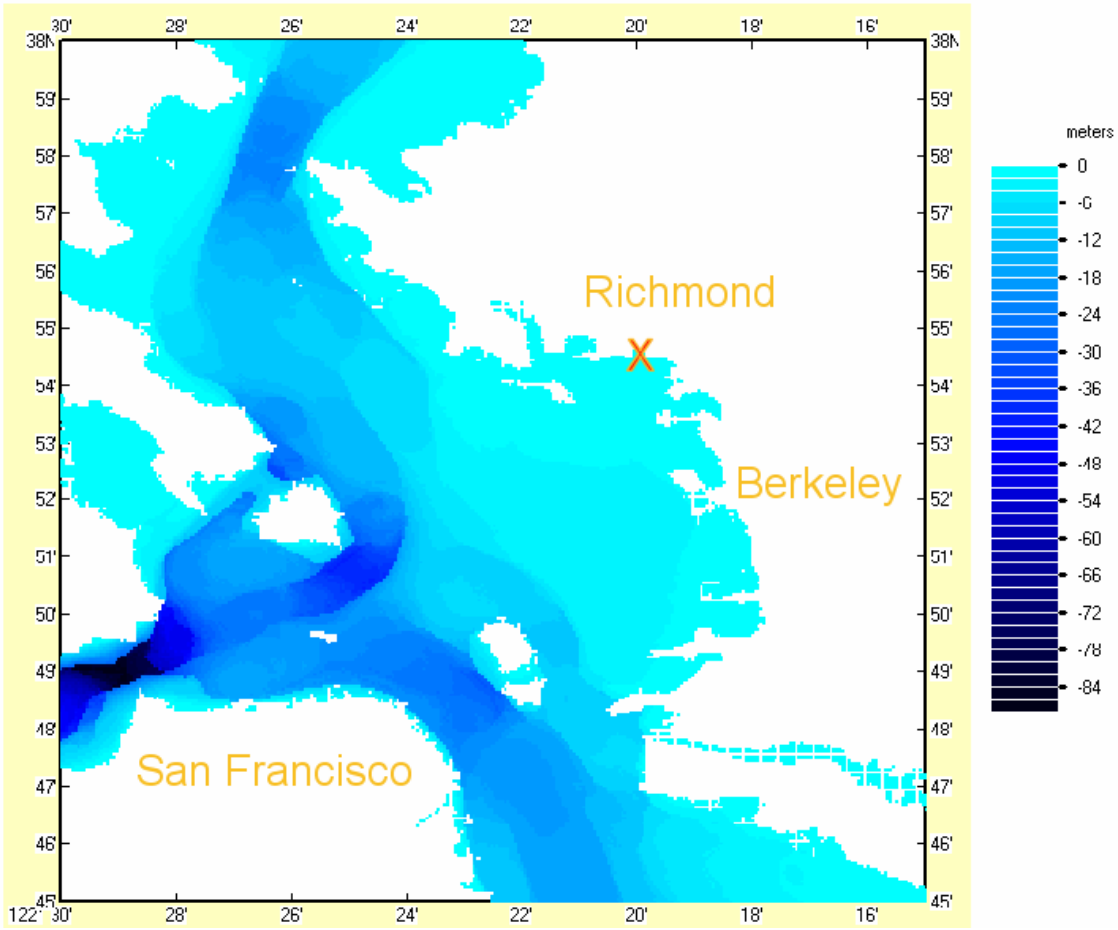

Figure 2.1: Map of Central San Francisco Bay; Location of experiment marked with an 'X'. Depths are presented in meters, while coordinates are latitudes and longitudes.

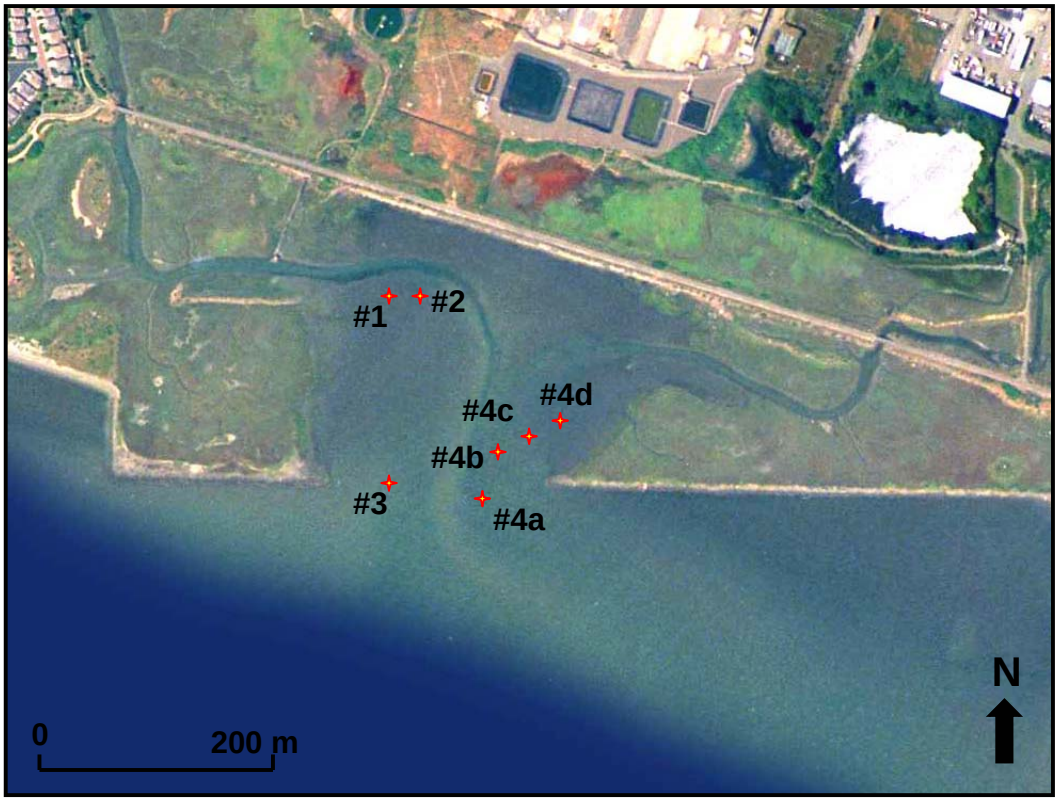

Figure 2.2: Sites of field experiments on the intertidal mudflat at the Richmond Field Station. Field campaigns are labeled sequentially; the four locations of experiment 4 are labeled a-d.

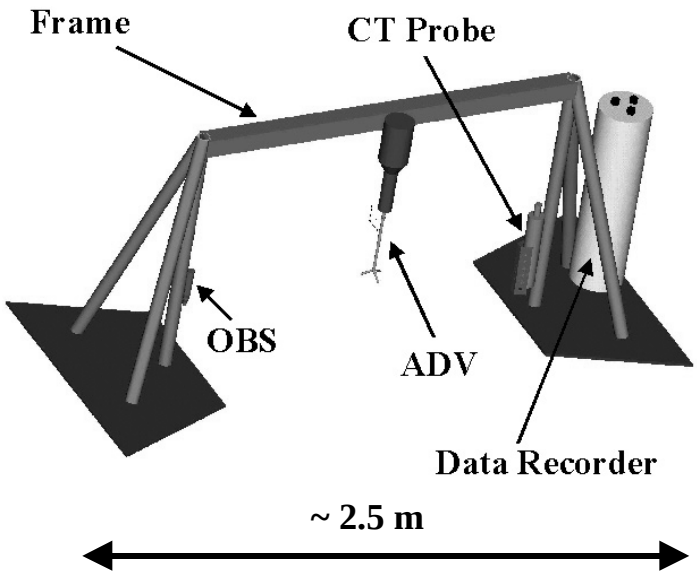

Figure2.3: Experiment # 1 setup on the sawhorse frame.

Figure 2.4: Experiment #3 on the sawhorse frame. Note the pattern of ripples overlaid on pools of water.

Figure 2.5: Photograph of the side-mount frame during experiment #4. The three transmitters of the ADV probe jut out over the mud and measure velocity in a sideways orientation.

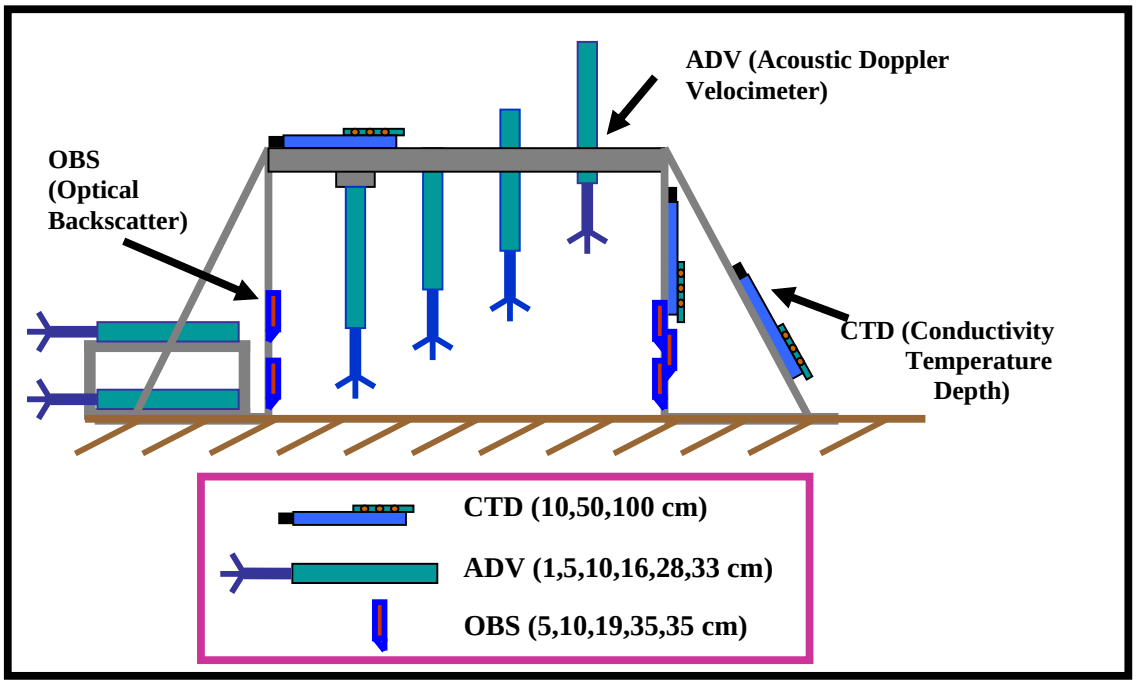

Figure 2.6: Experiment # 3 setup; Data recorder not shown. The combined OBS/fluorometer are at 0.10 m and 0.35 m.

Figure 2.7: Sawhorse frame after a major storm on April 12th, 2003. Note that the yellow data recorders have been ripped from their mooring and that the frame has sunk to the right (towards the channel).

Figure 2.8: Irregular sediment ripples formed during experiment 3; the tape measure shows a 1 ft (0.3 m) portion of the bed.

Chapter 3: Hydrodynamic Forcing and the Intertidal Environment

This chapter details the different forcing mechanisms that occur on the mudflat due to hydrodynamics, and details the time scales over which they occur and the relative importance of each to the overall energy budget. In our analysis, we find four major frequencies of motion on the mudflat: locally driven wind waves, ocean swell, infra-gravity seiching, and tidal motions.

3.1. Introduction

The hydrodynamic forcing on an intertidal mudflat is critical to determining the patterns of erosion, deposition, and transport that occur on an intertidal flat. Depending on environmental conditions, either currents (tidal or freshwater) or locally driven wind waves can dominate the resuspension of sediments. On the Skeffling mudflat in the Humber estuary, bed shear stress and suspension is dominated by the mean flow (Christie and Dyer, 1998). At this mudflat, a threshold current ranging from ~0.15 m/s to ~0.3 m/s caused sediment concentration to increase above 20 mg/L at a variety of locations (Widdows et al., 1998). By contrast, an intertidal mudflat at Portishead on the Severn Estuary alternates between wind-dominated and current dominated conditions over a tidal cycle (Whitehouse and Michener, 2000). In their study, wave stirring increased suspended sediment concentrations by a factor of three during weak neap tides, but only 10 percent during spring tides. On an intertidal bank on the river Trent, sediment supply and deposition varied on a spring-neap cycle, but was modulated by

wind-waves (Couperthwaite et al., 1998). At an intertidal mudflat in the Dutch Wadden Sea, accretion of sediments occurs during calm, current dominated conditions. Erosion occurs from a combination of tidal currents and wave action during rough conditions, while severe erosion occurs during stormy, wave-dominated conditions (Janssen-Stelder, 2000). In the Ems estuary, concentrations of mud and phytoplankton on both mudflats and channels varied with wind wave conditions (de Jonge, V.N. and van Beusekom, J.E.E., 1995). In San Francisco Bay, Krone (1979) found that wind generated waves cause the majority of sediment resuspension in shallow water. More recent studies by Bricker (2003) and Ruhr and Schoellhamer (2004) echo the importance of wave-current interaction and wave energy to erosion in the shallow waters of San Francisco Bay.

In addition to wind waves, longer frequency waves are important to the hydrodynamic and sediment transport processes of estuaries and mudflats. A cycle of offshore/onshore sediment transport can occur at infragravity frequencies due to correlation between sediment resuspension and intermittent wave groups (Shi and Larsen, 1984, Green et al., 2001). Storm surges, edge waves, and basin scale seiching accounted for approximately 5 percent of the wave energy in a shallow, mesotidal estuarine lagoon in New Zealand (de Lange and Healy, 1990). In that study, waves from the coastal ocean accounted for 70 percnet of the total wave energy, even though most wave energy was filtered by the geometry of the harbor entrance and only high frequency components (3.5 to 4 sec) entered (de Lange and Healy, 1990). Ocean waves

are the principal forcing mechanism at a sandy intertidal flat at the mouth of an estuary in New Zealand (Green et al., 2001).

However, the role of ocean swell and seiching in estuarine hydrodynamic processes is not often considered, particularly at intertidal sites well removed from the entrance to the estuary. In this chapter we consider the relative importance of ocean wave energy, wind wave energy, local seiching, and tidal currents on the intertidal mudflat in Richmond, which is located approximately 15 km from the entrance to the San Francisco bay. Though most ocean wave energy is dissipated before reaching intertidal mudflats, this chapter will show that it plays a small, but perhaps significant, role in the overall energy budget. Similarly, local seiching motions provide a small but persistent modulation to the mean tidal currents.

3.2. Forcing Mechanisms

In this chapter, we will emphasize the frequencies of motions captured in the ADV velocity record, and determine which forcing mechanisms dominate the near-bed currents over the intertidal mudflat. Our results are organized as follows. First, velocity data from the mudflat are shown and analyzed, both over a spring-neap cycle and over particular tides. Next, spectral data from an offshore buoy operated by the National Data Buoy Center (NDBC) near San Francisco (NDBC buoy 46026) is presented and correlated with the velocity data from the mudflat. Similarly, wind data from the BAAQMB (Bay Area Air Quality Management District) meteorological

station at the Richmond Field Station is correlated with mudflat data. Next, we compare the energy from various forcing mechanisms over representative wet-periods, and investigate the time scales over which the energy climate varies. Finally, variation over the time scale of seconds is quantified.

3.2.1. Velocity and frequency analysis

On the scale of two weeks, the hourly variation in velocity at the mudflat is set by tidal forcing but can be modulated by freshwater outflow, as is shown in figure 3.1. The diurnal and spring-neap variation is clearly apparent in the pressure signal (Fig. 3.1a) measured over experiment #2 (see Chapter 2 for details). The maximum depth evolves from a small height difference between tides on March 1st to a large diurnal inequality on March 5th and March 6th. On the evening of March 5th, a small high-tide leads to mean velocities of ~ 0.05 m/s for both the flood and ebb, while the large high tide on March 6th leads to large ebbing velocities greater than 0.1 m/s. Clearly, the ebb dominates the mean velocity profile except for the smallest high tides. In particular, large ebb velocities are measured during storms on March 1st-2nd and March 7th, when fresh-water flow overtops the channel and augments the flood-ebb asymmetry. Time of inundation varies between ~5.5 hours to ~10.5 hours at this location. Overall, the site for experiment #2 sees complex hydraulics in which the mean flow is set by channel shoal dynamics and changes direction and magnitude due to the spring neap cycle and storm events (see Ralston 2005).

Both the amplitude and dominant frequencies of motion vary throughout the 2-week experiment, though four distinct patterns appear over all periods of inundation. This is illustrated in figure 3.2, which shows the velocity signal measured over a period of inundation on April 13th, 2003 in experiment #3. Over the nine hours the frame is inundated, figure 3.2 (a) clearly varies from positive, onshore velocity during the flood to negative, offshore flow during the ebb. With-in the tidal signal, a distinct, repeating fluctuation occurs at a period of ~ 8 minutes, as can be seen in figure 3.2 (b). Finally, zooming in on the time scale of a minute shows that fluctuations on the order of 2 seconds occur at the beginning of the tide, and on the order of 10 seconds at the end of the tide (figure 3.2(c) and 3.2 (b)). These different scales of motion are depicted in the power spectrum shown in figure 3.3, which shows peaks at frequencies of 0.5 Hz (2 second period), 0.1 Hz (10 second period) and 0.002 Hz (500 second period).

The source of the intra-tidal, 0.002 Hz frequency is found by considering local bathymetry and external forcing mechanisms such as wind. Indeed, the 500 second motion is likely a function of the local bathymetry of the Richmond inner harbor, of which the mudflat at the Richmond Field Station is a small part (see figures 2.1 and 2.2).

Fronted by Point Isabel to the east, Point Richmond to the west and Brooks island to the southwest, the Richmond inner harbor is a semi-enclosed basin with an east-west diameter of ~3000 m and a north-south diameter of ~1500m. With-in this basin, depths are between 2-3.5 m at the mean high-high water mark (from http://sfbay.wr.usgs.gov/access/Bathy/zTool.html). Using the approximation that the

phase speed of a wave is $\sqrt{gh}$ (g = gravity, h=depth), the wavelength of a standing wave within the basin can vary between a period of ~ 250 seconds and ~670 seconds. Thus, the measured seiche, with a period of ~500 seconds, plausibly fits into the bathymetry of the Richmond inner harbor. Note that the measured pressure signal is ~90 degrees out of phase with the velocity, further suggesting a standing wave. The most likely cause of the seiche is basin-scale sloshing that occurs when the water surface relaxes after being set up by wind. Indeed, the large seiche on April 13th occurs after a storm on April 11th-12th in which winds with gusts of up to 15 m/s caused a storm surge of ~0.2 m. Because wind is common in the central San Francisco Bay, seiching is a common feature at the field site and is seen in all the experiments. Moreover, seiching appears to occur in the South Bay and San Pablo Bay as well (conversation, Phillip Williams), and is a feature of all enclosed basins. Any asymmetry in tidal propagation over flats and channels can also force infra-gravity motions, as can spatial variations in wave climate (e.g., edge waves; see Lippmann et al., 1997). Therefore, characterization of forcing at intertidal flats should consider these infra-gravity frequencies, which modulate the flood and ebb flows and provide a source of currents during the slack tide. Note that a more complete analysis of the seiche within the Richmond harbor area is outside the scope of this dissertation.

The two second (0.5 Hz) and ten second (0.1 Hz) fluctuations vary both over the time scale of a minute and on longer time scales such as hours or days. For example, the two second waves vary between groups with relatively large magnitudes (e.g., between 10-20 seconds) and small magnitudes (e.g., between 28-35 seconds). The 10 second wave

also shows variability in magnitude (figure 3.2). In order to examine the longer timescale variability and determine the source of the wave motions, we examine the velocity data from experiment # 1 over an entire spring-neap cycle. By calculating a power spectrum of each 45 second burst (sample period) and averaging the energy intensity at each frequency over all the bursts in a period of inundation, we define an average energy as a function of frequency. That is, we define average energy intensity as:

$$\overline{P_t(f,n)} = \frac{1}{T_n}\int_{t_1}^{t_2} P(f,t)dt \qquad (3.1)$$

where t_1 and t_2 are the start and end of each period of inundation, *P(f,t)* is the energy intensity for each individual burst, and $\overline{P_t(f,n)}$ is the average energy intensity as a function of frequency, *f*, for each period of inundation *n* (of duration $T_n = t_2 - t_1$, the total time for which instruments are submerged during a high tide). The results of averaging are shown in figure 3.4, which presents the energy intensity of the near-bed flows as a function of frequency (horizontal axis) and calendar day (vertical axis).

Two distinct energy bands are evident over the two weeks of the experiment, one between 0.05 Hz and 0.1 Hz and one between 0.2 Hz and 1 Hz (figure 3.4). The low frequency band persists throughout the two weeks, with a maximum energy intensity of 0.04 m^2/s^2/Hz and 0.02 m^2/s^2/Hz occurring on February 3 and February 10, respectively, at a frequency of 0.0667 Hz (period of 15 seconds). In between, less energetic motions occur at a frequency of 0.1 Hz, or a period of 10 seconds. The high frequency band of

energy primarily occurs between February 9th and February 11th, with a maximum occurring on February 11th at a frequency of 0.4 Hz and an intensity of 0.19 $m^2/s^2/Hz$. Aside from this event, the extreme calm periods of Feb. 3rd to Feb. 4th and Feb. 12th alternate with minor high frequency signals from Feb. 5th to Feb. 8th and Feb. 13th to Feb. 15th.

While the tidally averaged energy intensity $\overline{P(f,n)}$ varies at the scale of days, the individual energy spectra found in the 45-second bursts vary on the time scale of minutes or hours. We can measure the variability by extracting the maximum energy intensity in each burst for both energy bands defined by figure 3.4, and plotting the results as a probability distribution. Figure 3.5 shows the distribution of low frequency energy (0.044-0.11 Hz, Fig. 3.5a) and high frequency energy (0.2 Hz to 1 Hz, Fig. 3.5b) during the high tide on the morning of Feb. 9th. The energy intensity at low frequencies, corresponding to wave periods between 9 seconds and 22.5 seconds, is a well-defined distribution with near bed motions most commonly characterized by an energy density of ~ 0.02 $m^2/s^2/Hz$ (figure 3.5a). No discernable probabilistic distribution of energy intensity is found in the higher frequency band (0.2-1 Hz); however, several distinct bands of energy occur. This distribution and 'groupiness' is consistent with highly variable, locally generated wind waves (figure 3.5b). The maximum intensity of the higher frequency waves is an order of magnitude larger than the low frequency waves-- 0.32 $(m/s)^2$/ Hz— vs. 0.018 $(m/s)^2$/ Hz. The low frequency band's distribution closely resembles a Rayleigh distribution (figure 3.5a) with a mean value of 0.018 $(m/s)^2$/ Hz.

Frequently used to characterize the distribution of individual amplitudes of ocean waves, the Rayleigh distribution is given by (Longuet-Higgins 1952):

$$f(a) = \frac{a}{\sigma^2} e^{-\frac{a^2}{2\sigma^2}} \qquad \textbf{(3.2)}$$

where *f(a)* is the probability distribution of a wave of amplitude *a*, and σ^2 is the variance of water surface height.

In the next section, we explore an apparent coincidence between the distributions of ocean swell and spectral energy in the low frequency band. Following that, we examine the intermittent high frequency band and its apparently random distribution of energy, noting that it is most energetic during the storm of February 9th to February 11th.

3.2.2. Ocean Wave Spectrum

The spectral peak of ocean swell on the Pacific Ocean typically is characterized by a period between 10 to 20 seconds, and swell amplitude is frequently described using a Rayleigh distribution. Thus, we hypothesize that the low frequency band of energy on the intertidal mudflat is driven by surface waves from the Pacific Ocean. To establish that the low frequency energy spectrum seen in figure 3.4 is coming from ocean waves, we obtained and plotted wave climate data for February 2001 from a buoy near San Francisco (NDBC buoy 46026, located at 37.75 N 122.82 W (37°45'32" N 122°50'00" W. See website http://seaboard.ndbc.noaa.gov/station_history.phtml?$station=46026 for details). Figure 3.6 shows the amplitude intensity from buoy 46026 as a function of frequency (horizontal axis) and calendar day (vertical axis). The characteristics of these

spectra are qualitatively the same as those seen in the low-frequency band of the velocity record on the mudflat (see figure 3.4). For each graph (figure 3.4 and figure 3.6), a maximum amplitude occurs at frequencies between 0.05 Hz and 0.1 Hz, or periods of 10-20 seconds. To be more specific, we see that the largest magnitude swells occur on February 3rd and 10th, and are characterized by a frequency of 0.067 Hz, or a 15 second period. In between, the waves shift to higher frequency, but with smaller amplitude, with a period of about 10 seconds on February 6th and again on February 14th. Comparison with figure 3.4 indicates that this is precisely the same behavior as was seen in the low-frequency band of the ADV velocity record.

More quantitatively, we calculate the correlation between the ocean buoy amplitude intensity and the mudflat energy intensity for motions at different frequencies. That is, we define correlation as (see a standard reference on statistical analysis for more detail, e.g. Shanmugan and Breipohl, 1998):

$$\rho_{PS}(f) = \frac{\frac{1}{M}\sum_{m=1}^{M}(\overline{P_h(f,m)} - \mu_P(f))*(S(f,m) - \mu_S(f))}{\sigma_P \sigma_S} \qquad (3.3)$$

where $\overline{P_h(f,m)}$ is the tidally averaged power spectrum (at frequency, *f*) interpolated to the time base of *m* hours (see equation 3.1), while data set $S(f,m)$ is the variation of the ocean spectral amplitude vs. time *m* (hours) and frequency *f* (Hz). Note that μ_p and μ_s are the time averaged value of $\overline{P(f,m)}$ and $S(f,m)$ over the entire data set at each frequency *f*, respectively, while σ_p and σ_s are the standard deviation of $\overline{P(f,m)}$ and $S(f,m)$ at each frequency *f*, respectively. The total length of the data set is given by

M, and denotes the number of hours in the experiment. The variation of $\rho_{PS}(f)$ with frequency is shown in figure 3.7, and confirms the qualitative agreement observed between the ocean swell energy and the mudflat motions. At a period of 15 seconds, the correlation coefficient is greater than $\rho = 0.8$, while the correlation over the range of ocean swell (0.05 to 0.1 Hz) is greater than $\rho = 0.7$.

From this analysis, we conclude that the wave motions evident at a frequency of ~0.1 Hz on the intertidal mudflat are driven by swells from the Pacific Ocean. As such, wave motions will be evident in the intertidal zone, even when local wind forcing (as will be considered in the next section) is small. During periods of energetic ocean swells but less energetic local winds, we would expect this contribution to the dynamics of the mudflat to be significant.

3.2.3. Wind Energy

The high frequency band of energy on the intertidal mudflat is most energetic during a storm (on February 9^{th}-11^{th}) containing significant wind energy, suggesting that local winds drive these motions. Wind data were obtained from the Bay Area Air Quality Management District (BAAQMD, Meteorological Tower #2950, contact person D. Duker) located at the Richmond Field Station (< 1 km from the experimental site). Because of the breakwater, the mudflat is only exposed to significant fetch for winds directed from the south or southwest (see figure 2.2). To account for this, we have conditioned our wind forcing to be non-zero only when the orientation of the wind is

between 165 degrees and 225 degrees east of true north. In figure 3.8a, the conditioned wind forcing is illustrated in a vector format, with calendar day on the vertical axis and time of day on the horizontal. The time variability of the magnitude of this forcing is shown in figure 3.8b, and qualitatively depicts the same variability as the high-frequency band of figure 3.4: a large peak in wind forcing is evident between February 9th and 11th, with smaller events occurring on February 5th and February 14th.

To quantify the relationship between local wind forcing and the high frequency motions on the mudflat (see figure 3.4), we define a correlation between wind energy (defined as the conditioned wind magnitude squared) and near bed energy intensity at each resolved frequency, using a modified version of equation 3.3. In place of $S(f,m)$ (ocean swell amplitude spectrum), μ_s (time averaged amplitude), and σ_s (standard deviation of $S(f,m)$), we use the conditioned wind energy, $E_w(m)$, which is a function of the time increment m (hours), the time averaged wind energy μ_E, and the standard deviation of wind energy σ_E.

Using the conditioned wind data, we find that most correlation values at frequencies between 0.2 and 1 Hz are substantially greater than ρ=0.6 (see figure 3.9). Between 0.25 Hz and 0.8 Hz, correlation is larger than ρ=0.7. We conclude that the high-frequency waves, with periods between 1 and 5 seconds, are driven by local winds on the estuary coming from the south and southwest.

3.2.4. Error Estimates

The ADV reports an error of less than 2 mm/s per measurement (Sontek 2001) when sampling at a frequency of 10 Hz with a velocity range of 0.3 m/s. Using standard error propagation techniques, this results in an error in the total energy (velocity squared) of 0.0002 m^2/s^2, assuming an average velocity of 0.05 m/s (Bendat and Piersol, 1966). However, because we are averaging our results over a tidal period with typically more than 50 bursts, our error is reduced by a factor of more than 7, resulting in a conservative error estimate of less than $5* 10^{-5}$ m^2/s^2. The energy detected in the power spectrum is above the calculated error level, ranging from $\sim 10^{-4}$ m^2/s^2 to $\sim 10^{-3}$ m^2/s^2 for the low frequency band (ocean waves) and $\sim 10^{-4}$ m^2/s^2 to $\sim 10^{-2}$ m^2/s^2 for the high frequency band (wind waves). In the frequency domain, we calculate a noise floor of order 0.002 $m^2/s^2/Hz$ for the energy intensity calculations. Typical values of the energy intensity ranged between 0.005 $m^2/s^2/Hz$ and 0.05 $m^2/s^2/Hz$ for the low frequency band (ocean waves) and 0.005 $m^2/s^2/Hz$ and 0.5 $m^2/s^2/Hz$ for the high frequency band (wind waves), indicating a good signal-to-noise ratio (see figure 3.4). In practice, it appears that the error in the measured quantities may be significantly less than these estimates. Across the entire experiment, the spectra show a noise floor which is less than $1.8 *10^{-6}$ m^2/s^2, +- $1.3 *10^{-6}$ m^2/s^2. This results in a very conservative upper bound on the noise floor of $8*10^{-6}$ m^2/s^2, assuming a three-sigma deviation from the average. This suggests that the theoretical values for the error in our calculated quantities are likely to be overestimates, and that the detected signals lie well above the noise levels.

Note that with a 45 second burst sampled at 10 Hz, we can resolve a spectrum of waves with frequencies below the Nyquist criterion of 5 Hz (e.g., Oppenheim and Schafer, 1989). At low frequencies, the frequency transformation cannot resolve waves with a periods longer than Δ, where Δ is the burst length; however, conventional wisdom holds that a period of $\Delta/2$, or 22.5 seconds, is the practical limit. Thus, both ocean waves (typically between 10-20 second periods) and local wind waves (defined in our analysis with periods between 1-5 seconds) are adequately characterized by data from experiment #1. Moreover, the large correlation seen between ocean waves and the low frequency band of near bed motions, as well as between wind energy and the high frequency band, increases our confidence in the analysis. Finally, similar correspondence between ocean swell, wind, and the waves at the field site is observed in the other field experiments.

3.3. Implications of forcing mechanisms

The fact that ocean swells are, at certain times, an important contributor to the dynamics at this field site is surprising, given the geometry of the estuary and the orientation of the ocean swells. The inlet to the San Francisco Bay is a narrow strait oriented along a west-southwest/east-northeast axis. Along this axis, it is a direct line of about 15 km between the Golden Gate bridge and Pt. Isabel on the eastern edge of central San Francisco Bay (see figure 2.1). However, the direction of the dominant ocean swell at NDBC buoy 46042 in Monterey (approximately 150 km from NDBC buoy 46026) during the two-week experiment in February 2001 ranged between 300 and 320 degrees

east of true North (i.e., from the Northwest). Thus, assuming that the directional spectrum at the Monterey buoy (46042) and the San Francisco buoy (46026) are comparable, the dominant swell approaches the inlet to San Francisco bay at an angle of greater than 45 degrees. Referring to figure 2.1, the direct line of action of these waves as they enter the bay would be towards the San Francisco shoreline.

It is perhaps not surprising, however, that ocean swell undergoes extensive dispersion as it enters the Bay, given the complex bathymetry of the region around the Golden Gate. This includes a deep channel (~50-100 m deep) at the inlet, a sill approximately 2 km east of the Golden Gate, several islands, and extensive tracts (~5 km) of shallow water of less than 5m depth (figure 2.1)). All these features will likely cause refraction, diffraction, and/or reflection of incoming waves, resulting in the spread of ocean wave energy to a large portion of the central bay coastline. What is perhaps more surprising is that sufficient energy is retained in these features for them to be significant to the hydrodynamics once they reach the sheltered mudflat under consideration. Given the orientation of the incoming swell and the bathymetry of the Bay, it is highly likely that intertidal mudflats around the rest of Central Bay, particularly south of Richmond, are subjected to larger ocean swell than our experimental site.

3.3.1: Relative Importance of Ocean Swell

During the two weeks of experiment #1 in February 2001, the mudflat was exposed to a full spring-neap cycle as well as extremes of calm and stormy weather. Figure 3.10

shows an example of how the dominant source of energy varies over a tide and between tides as hydrodynamic conditions change. In this figure, three different tidal periods are displayed (corresponding to morning and afternoon of Feb. 7th , 2001 (a and b), and the night of Feb. 10th to Feb. 11th ,2001 (c)), each with different energy characteristics. Total energy is divided into a tidal component (a burst averaged, 45 second mean), an ocean wave component (oscillations with periods between 9 and 22.5 seconds), and a wind wave component (oscillations with periods between 1 and 5 seconds). During large spring tides, when the local winds are calm, the tidal current dominates (figure 3.10b). By contrast, during stormy conditions, wind waves dominate, independent of the tidal conditions (figure 3.10c). During neap tides or, at a shorter timescale, during slack tides, ocean waves become an important energy source when local winds are calm (figure 3.10a). As described below, wind wave energy is reduced at the bed during high tide, while ocean swell is unaffected. Note that the oscillation in the tidal energy in figure 3.10a suggests seiching, though the data from experiment # 1 cannot resolve this frequency.

Though ocean waves are important in the absence of other forcing, the action of wind and tidal currents clearly deliver more energy onto the mudflat. Table 3.1 shows that during the large tide at 12:00 am on Feb 11th, 2001, for example, we measured an average wind energy of ~0.0141 m^2/s^2 on the mudflat at frequencies between 0.2 Hz and 1 Hz. By contrast, ocean waves sustained an average energy of only 0.0013 m^2/s^2 between 0.04 Hz and 0.11 Hz during the maximum swell on February 2nd, 2001. However, as shown in Table 3.1, the lower limit of energy from ocean waves, wind

waves, and tidal current are comparable, and suggest that a set of conditions can occur in which ocean waves dominate the energy spectrum.

Table 3.1: A comparison of the maximum and minimum average energy loads measured per tide for wind waves, ocean waves, and tidal currents from Feb. 2 to Feb 15, 2001. Note that the average energy for wind waves and currents spans two orders of magnitude. Energy from an ocean wave is defined as the power spectrum between 0.04 Hz and 0.11 Hz, while energy from wind waves is the power spectrum between 0.2 and 1 Hz. Current is measured as the square of mean velocity.

	Max (m^2/s^2)	Min (m^2/s^2)
Wind waves	0.0141	0.0002
Ocean waves	0.0013	0.0002
Current	0.0182	0.0006

The energy climate on the mudflat becomes more varied and complex when seiching is considered, though the relative magnitudes and behavior of ocean swell, wind waves, and tidal currents described over a spring-neap cycle in February 2001 hold for the experiments in March 2002 and April 2003. Figure 3.11 shows the variation in burst averaged energy for all four primary forcing mechanisms over two periods of inundation in experiment #3, when a nearly continuous sampling scheme allowed all intra-tidal frequencies to be resolved. Note that wavelets were used to define the different scales of motion. For each scale of motion, a large frequency range was used in their definition in order to capture the effects of associated wave groups and nonlinearity. Wind waves are defined as a scale with a period between 0 and 5 seconds, ocean swell is defined as energy between 5 and 45 seconds, the seiche frequency is defined between 2 minutes and 25 minutes, and all remaining lower frequency energy is deemed a tidal velocity.

Figure 3.11a shows a situation in which wind waves dominate during the flood tide, ocean swell and seiching are dominant during the slack tide and early ebb-tide, and tidal currents become progressively more important near the end of the period of inundation. Interestingly, there seems to be a periodic fluctuation of ~ 80 minutes in the tidal signal, perhaps suggesting a bay-wide oscillation. Figure 3.11b shows a case in which tidal currents dominate during the flood but wind-waves dominate during the ebb. The seiche frequency is small throughout, while ocean swell are on the same order of magnitude as wind-waves during the flood. In terms of magnitude, the seiche—like the ocean swell—is not generally a dominant source of energy except during otherwise calm periods. However, as shown in chapter 5 and 6, the seiche has a large affect on bed stress, turbulent motions in the water column, and sediment transport.

3.3.2: Time scales of variability in forcing

The intersection of each process-tides, seiche, ocean swell, and wind wave—and the time scales they act over—creates a complex, dynamically varied environment. The perturbations in energy over a period of inundation are set by the characteristic timescales of the different intra-tidal waves; these in turn overlay the ebb/flood, diurnal and spring-neap variation in tidal currents. For example, the magnitude of the seiche appears to vary with depth; in figure 3.11a, a maximum in orbital velocity occurs at depths of ~ 1 m during both the flood and ebb tides (~ 150 min and 400 min). This suggests an optimum resonance condition within the Richmond inner harbor. Furthermore, seiching probably varies based on the amount of setup and therefore on

the local history of wind. However, a detailed analysis of the Richmond harbor is beyond the scope of this dissertation.

As shown in figure 3.6, ocean swell generally varies over the time scale of several days, though there is some variability over multiple hours. Because the time scale of variability is greater than a period of inundation (5-10 hours), ocean swell forcing is less apt to change over a tidal cycle than wind wave forcing. Indeed, ocean swell energy during flood and ebb events is fairly symmetrical over different periods of inundation (see figures 3.10b, 3.10c, 3.11a, 3.11b), with the exception of the morning of February 7th, in which ocean swell increases from ~10^{-4} m^2/s^2 to ~10^{-3} m^2/s^2 over a period of inundation. The increased orbital velocity during the flood and ebb is likely related to shoaling, in which wave heights and orbital velocities become larger as the local depth and the wavelength decreases (~ $T\sqrt{gh}$, where T= period and $\sqrt{gh}$ is the phase speed of the wave).

By contrast, wind speed—and therefore wind wave magnitude—is quite likely to vary over a period of inundation. In an estuary, locally driven, high frequency waves respond to changes in wind speed and direction on the time scale of minutes to an hour—a small time compared to the 5-10 hours of a tide. For a fetch of 5 km, for example, wind waves become fully developed over a time scale of about 30-40 minutes (Le Hir et al., 2000). Thus, the wind record gives insight into the variability of wind-driven waves and the time scales over which they vary. As shown in figure 3.8, wind may blow strongly from the south over the time scale of hours (see Feb. 1st-3rd and

February 13th-15th or on the time scale of days during large storm events (see Feb 9th – Feb 11th). The intersection of this meteorological variability with the timing of high tides produces a wind-wave climate that can vary greatly over a tidal cycle. For example, during the period of inundation on April 13th, 2003 (figure 3.11a), wind driven waves dominate during the flood tide but quickly die off over the slack tide and ebb. Conversely, wind waves are small during the flood and slack tide on April 15th, 2003 but grow greatly over the ebb (Fig. 3.11b). As shown in figure 3.10c, during storms the wind wave energy can remain large throughout the period of inundation (figure 3.10 c).

The aggregate effect of the variability seen in the ocean swell and wind-wave frequencies is apparent in the two-week average of wave energy from February 2001, which is displayed in figure 3.16. Wind waves are clearly a larger source of energy; surprisingly, though, the total ocean swell energy is ~19% of the total wind-wave energy. Thus, though ocean swell rarely dominates the energy spectrum of an individual tidal cycle, it becomes proportionally more important over the spring-neap cycle. This occurs because ocean swell is more constant in time than wind-driven waves, and varies over longer time scales. Much of the wave energy that makes it to the intertidal zone is dissipated in the mudflat or marsh area. Therefore, ocean swell is important in setting the minimum levels of turbulent kinetic energy production and dissipation, particularly during the winter months when the largest ocean swell occurs.

However, processes such as sediment erosion and turbulence production are inherently non-linear and depend critically on instantaneous processes (for more detail, see chapter

4 and 6). Thus, the short term variation of the wave climate is critical to understanding the long term effect of swell on hydrodynamic variables and sediment dynamics. For example, when bed stress due to local wind waves or current is near a critical threshold for erosion or deposition, even a small, added energy source such as ocean swell or seiching is important. In fact, the seiching motion modulates the flood and the ebb currents, and thus creates an inherent periodicity in the mean shear stress and production of turbulence (for more detail, see chapter 5). For ocean swell, extreme values in the Rayleigh distribution bring episodic bursts of greater energy onto the mudflat (see figure 3.5). Moreover, the non-linear, asymmetric ocean swell causes large onshore pulses of energy, particularly at depths below 1 m. Thus, large bed stress events due to ocean swell and/or seiching will occur episodically, particularly for shallow water (< 1 m) conditions.

3.3.3: Tidal variability in wave climate

The magnitudes of both ocean swell and locally driven wind waves vary throughout a tidal period as depth changes. During calm conditions, residual energy at the wind wave frequency is smallest during the slack tide, and largest during the flood and ebb (see figures 3.10a and 3.10b). As with ocean swell, shoaling may cause the increased orbital velocity as depth decreases. In addition, ocean swell begins to go non-linear and feeds its energy into higher frequency components within the wind-wave frequency band (see below). Finally, the water depth at slack also acts to attenuate the magnitude of high frequency waves. The ratio of orbital velocity at the bed to the orbital velocity

at the surface varies as $1/\cosh(k_w h)$, where h is the depth and k_w is the wave number, which varies by the dispersion relation for a linear wave and is approximated in shallow water as $k_w = \omega/\sqrt{gh}$. For example, the orbital velocity at the bed of a 1 Hz wave is attenuated by 96 percent over a depth of 1 m, while a 0.5 Hz wave is attenuated by 45 percent. Note that large period waves such as ocean swell (T> 5 seconds) are attenuated less than 3 percent over similar depths because of their longer wavelength.

As depth decreases in the intertidal zone, waves not only begin to shoal but also begin to vary from purely sinusoidal oscillations. This change from a linear solution to the wave equations occurs both because the ratio of wave height to depth (H/h) increases and because the ratio of depth to wavelength ($\frac{h}{\lambda} = \frac{h}{T\sqrt{gh}}$) decreases (see Komar, 1976). Physically, as the ratio of wave height to depth increases, the difference in phase speed between the trough and peak ($\sim\sqrt{gh}$) leads to a steepening of the wave face and an asymmetric wave profile (Pond and Pickard, 1983). For conditions in which the wavelength is much larger than the depth, the appropriate nonlinear solution is the 'cnoidal' wave (Fenton, 1979).

There are several semi-empirical scalings which can be used to determine the validity of using cnoidal theory over linear wave theory or higher order small-amplitude wave theory (such as Stokes theory). We use the condition suggested by Le Mehaute (1976), which requires that

$$\frac{H\lambda^2}{h^3} > 26 \qquad (3.4)$$

where H is the height of the wave, h is the depth of water, and λ is the wavelength. Rearranging, and scaling the wavelength as the wave period times the phase speed ($T\sqrt{gh}$), the approximate depth below which cnoidal theory should be applied scales as follows:

$$h \sim 0.2T\sqrt{gH} \qquad (3.5)$$

This result is graphically depicted in figure 3.12, and shows how wind waves and ocean swell require fundamentally different analytical models for the water depths and wave heights typically present in the intertidal area. For example, ocean swell with a height of 0.05 m assumes the cnoidal form below a depth of 1.4 m, while wind waves (T=2 seconds) of the same height become cnoidal at ~0.28 m depth. In fact, only the largest wind waves will be cnoidal over the slack tide (depths of 1- 1.5 m). For example, wind waves with a height of 0.4 m become cnoidal waves below 1.1 m. These wind wave heights occur only during appreciable wind conditions such as storm events. Thus, non-linearity in wind-waves is an intermittent event on the tidal flat, confined primarily to shallow conditions (< 0.5 m) and/or large orbital velocity. On the other hand, ocean swell are non-linear even at small wave heights; for example, a wave of 0.025 m height becomes non-linear at a depth of ~ 1 m.

Thus, the velocity profile of ocean swell over a tidal period is marked by asymmetry that becomes more pronounced as depth decreases. Figure 3.13 shows a wave train of ocean swell during an ebb tide with heights between 0.03 m and 0.08 m at a depth of 0.6 m. For comparison, a cnoidal wave train with a period of 9 seconds and an amplitude of 0.04 m is superposed onto the data. Though the amplitude and the period do not match perfectly, the profile of the measured and cnoidal waves are both clearly nonlinear. The non-linearity in each profile is apparent, with an asymmetric profile of sharp, shoreward peaks in velocity followed by more gentle, longer offshore sweeps. Interestingly, the period between the measured waves is not constant, but varies between 7-11 seconds. Moreover, the offshore velocity is underestimated by cnoidal theory, as can be seen for example at t=60 seconds. The observed irregularities may occur for many reasons, including small wind-waves and turbulent motions in the velocity signal, variations in phase speed for waves of different heights, wave breaking, and reflection of wave energy from the rip-rap at the former railway spur. Thus, though the cnoidal theory describes the form of ocean swell well, there is significant variability and complexity inherent in the measured results that cannot be modeled by a simple theory.

Compared to a linear wave, a non-linear wave amplifies the velocity, acceleration, and energy that is applied to the bed (Fenton, 1979), albeit over a short period of time. Thus, a non-linear swell of 0.05 m at 0.6 m depth has a maximum orbital velocity of ~0.153 m/s, while the corresponding linear wind-wave has a maximum orbital velocity of ~ 0.085 m/s. The asymmetry between onshore, positive velocity and negative,

offshore velocity becomes more marked as depth decreases, as is shown by the wave envelope for an ebb tide in which ocean swell dominates the wave spectrum (figure 3.14). The envelope basically measures the mean magnitude of the five largest orbital velocities in both the positive, onshore direction and the negative, offshore direction over 5 minute blocks, starting at a depth of ~1.4 m (t=300 min) at slack tide. The positive velocity begins to separate from the negative velocity when water depth dips beneath 1.2 m (t > 350 min). The asymmetry becomes huge at depths smaller than ~ 0.6 m (t >460 min); while the offshore velocity stays approximately constant at ~ 0.1 m/s, the largest onshore velocities exceed 0.25 m/s.

By contrast, the situation is reversed when wind-waves dominate during the ebb, as shown in figure 3.15. In this case, positive and negative velocities track each other quite well; in fact, the magnitude of the offshore orbital velocity is slightly larger than the onshore velocity, perhaps because the onshore stroke is slowed by the mean tidal current. Note that the increase in wave height and velocity over the ebb is a function of increasing wind velocity, and not due to waves becoming nonlinear (see figure 3.11b). In fact, the largest wind waves over this ebb tide (~ 0.15 m) go nonlinear at a depth of 0.5 m, which is near the lowest depth the instruments measured.

3.3.4. Implications for Modeling

Most sediment transport models apply hydrodynamic forcing and bed-stress through either a current term or a combined wave/current formulation (see review by Fredsoe,

1993), where, for estuaries, the wave climate is estimated based on local wind forcing. Usually, the type of sediment transport model depends on the individual characteristics of the study area. For example, in the Loire estuary, a sediment model using only tidal forcing found good agreement between the measured and simulated spatial distribution of the turbidity maximum and fluid mud (Le Normant, 2000). However, off channel waters and fringing mudflats may not be tidally dominated, which makes the time varying description of waves and currents important for determining sediment transport processes (Sanford, 1994). The nonlinear interaction between the wave boundary layer and currents creates an enhanced shear stress that is greater than the superposed stress from either waves or currents (see review by Soulsby, et al., 1993). In estuaries with waves in differing frequency bands, the dominant frequency may vary in both space and time, and should be considered in models. For example, in the lower Chesapeake Bay at a depth of 10-12 m, wind waves generally dominated the wave spectrum, although a persistent, small amplitude ocean swell (~0.1 m) dominated during calm, windless conditions (Wright et al., 1992). Similarly, a study in Cleveland Bay, Australia found wave-current interaction due to both swell and wind waves, concluding that at depths of ~10-15 m that ocean waves were larger sources of stress than wind and tidal currents (Jing et al., 1996). The results presented here from the San Francisco Bay suggest that ocean swell can also be important in the interior of estuaries at very shallow depths, including waters in the intertidal zone.

Nonetheless, most hydrodynamic models of the shallower regions of semi-enclosed estuaries, such as the intertidal mudflats under consideration here, include only tidal and

local wind forcing (e.g. Cheng et al., 1993, Wood et al., 1998, Zhen-Gang et al., 1999). However, ocean swell is by definition non-local, and large swell may occur during otherwise calm periods (Note the large swell of Feb. 2nd and 3rd on figure 3.4 and figure 3.6). Furthermore, ocean swell adds a small amount of energy to the total energy budget even during large local events, and is thus a source of error in current sediment models. The influence of ocean swells will not be uniform, however, and the propagation of swells into the estuary, including their refraction, diffraction and reflection by the local bathymetry, must be considered. Moreover, the nonlinearity inherent in ocean swell in the shallow water—and the resulting increases in maximum velocity, acceleration, and shear stress—must be included. To address this complexity, we would argue that a complete model of sediment dynamics in semi-enclosed coastal estuaries should include both a wave propagation model to bring ocean swell into the estuary (e.g. SWAN, see review by Booij et al., 1999) and a traditional estuarine circulation model (with tidal and local wind forcing) to define the local sediment transport that results. Moreover, both the nonlinearity of ocean swell and the occurrence of seiching motions should be parameterized into the model.

3.4. Conclusions

Ocean swell and locally driven wind waves in an estuary differ in many ways. Wind waves are forced by local meteorological conditions and are sensitive to variations in wind speed and direction. The distribution of wave heights due to local wind waves is random, and doesn't follow a prescribed distribution. Because of their short period and

wavelength, high frequency wind waves can be severely attenuated at the bed during high-tide; by contrast, ocean swell is unaffected. Most ocean swell is non-linear on an intertidal flat, particularly as depth decreases. By contrast, only at very small depths (< 0.5 m) or for large orbital velocities (> 0.4 m/s) do locally driven wind-waves become nonlinear. Observations show that local wind waves often coalesce into a series of groups of different magnitude. Ocean swell follows a Raleigh distribution and are independent of local meteorological conditions. Though large ocean swell may correspond with local storm events, they often propagate from disturbances several thousand kilometers away. As such, the energy in ocean swell varies over days. The time scale of variation for wind waves is prescribed by local geometry and nearly instantaneous wind conditions. At the field site, wind waves become well developed less than an hour after a wind event begins and persist as long as the wind continues blowing from the south or southwest. Typically, the time scale for a wind event is set by local meteorological conditions and is several hours (e.g., afternoon breeze) up to several days (e.g., storms). Finally, while ocean swell emanate from a consistent location at the mouth of the estuary, and are influenced by local bathymetry as they propagate shoreward, wind waves are constrained by the geometry and fetch for a particular wind direction.

Together, the relative magnitudes of tidal currents, seiching, ocean swell, and wind waves—which vary based on the lunar cycle, local meteorology, and swell from the Pacific Ocean—combine together to create a unique, non-repeatable hydrodynamic climate over each tide. Overall, the concept that tidal forcing and wind waves dominate

intertidal areas is simplistic and other intra-tidal frequencies such as ocean swell and basin-scale seiching are important on the time scale of seconds to weeks. Intermittent nodes of high energy are created by the superposition of these various processes.

As shown, a clear understanding of the different wave types paves the way to applying models that accurately capture the variability intrinsic in each forcing mechanism. An important further question is how these frequencies of motion interact with the sediment bed. The stress applied by the bed on the fluid flow affects the water column at different time and length scales, primarily by the variation of velocity, shear stress, turbulent kinetic energy, and dissipation in the boundary layers of each forcing mechanism. In turn the hydrodynamics acts to erode sediment from the bed and mix it into the water column, where it is transported to new locations. Chapters 4 and 5 address how to estimate and model shear stress, TKE, and dissipation of energy in the intertidal zone, as well as the boundary layer structure of velocity. Chapter 6 addresses how these processes combine to affect the erosion of sediment and its transport.

3.5. Figures

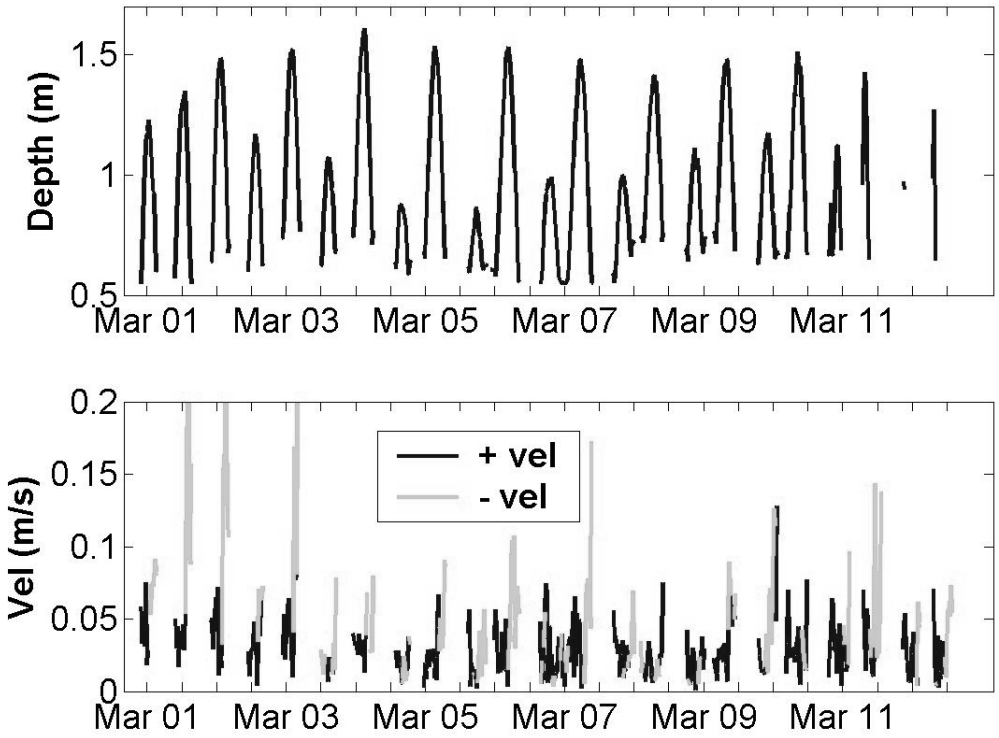

Figure 3.1: Variation in pressure (depth) and total horizontal velocity (both N-S and E-W components) over most of a spring neap cycle during experiment #2 from Feb. 28th to March 12th, 2002. Pressure measurements after March 11th are incomplete due to battery failure. Positive (+) velocity refers to northwards flow directed in the onshore direction, while negative (-) flow is directed southwards and offshore. Dates are presented at 0:00 local standard time, with each tick mark representing a 12 hour segment. March 1st is the first tickmark.

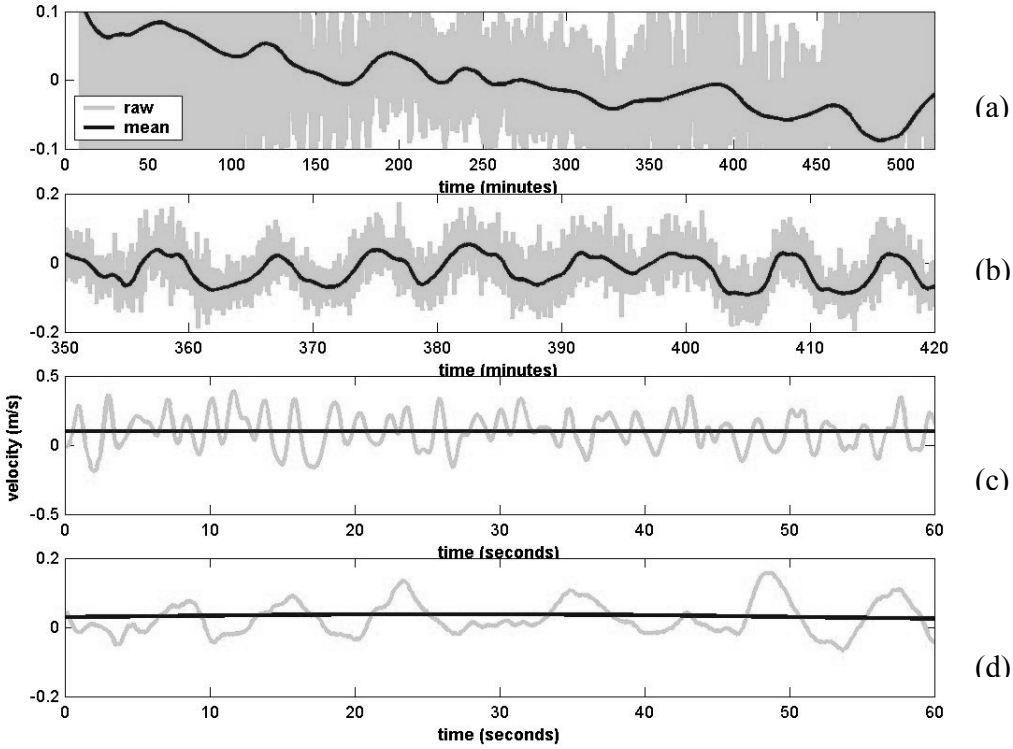

Figure 3.2: Variation in the raw, measured velocity and the mean velocity over four different time scales during a period of inundation on April 13th, 2003. The velocity is the top panel (a) is approximately a 50 minute average and depicts the variation of velocity over a tidal scale. Note that t=0 minutes corresponds to an inundation of ~0.15 m. The second panel from the top (b) depicts oscillation on the scale of 8 minutes occurring during the ebb tide, from t=350 minutes to t=420 minutes. The velocity profile is calculated by wavelets, and is approximately a 1 minute mean. Panel (c) shows a 1 minute increment during the flood tide at t=25 minutes, while the lower panel (d) shows a 1 minute snapshot during the ebb at t=357 minutes. Note that panel (c) shows fluctuations occurring at a period of 1-3 seconds, while panel (d) shows fluctuations with a period of ~ 10 seconds.

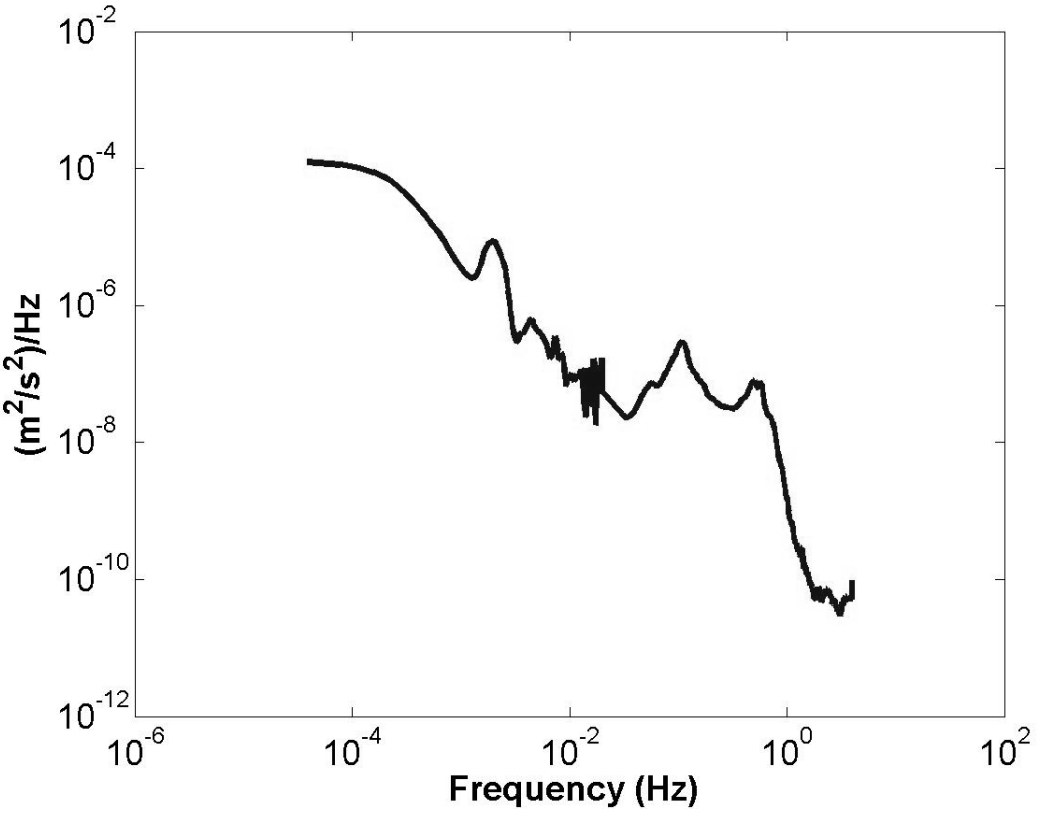

Figure 3.3: Power Spectrum of a period of inundation beginning on the evening of April 13th, 2003. Note four major frequencies of motion: At less than 10^{-4} Hz is a peak for tidal variation; other peaks occur at 0.002 Hz, 0.1 Hz, and 0.5 Hz.

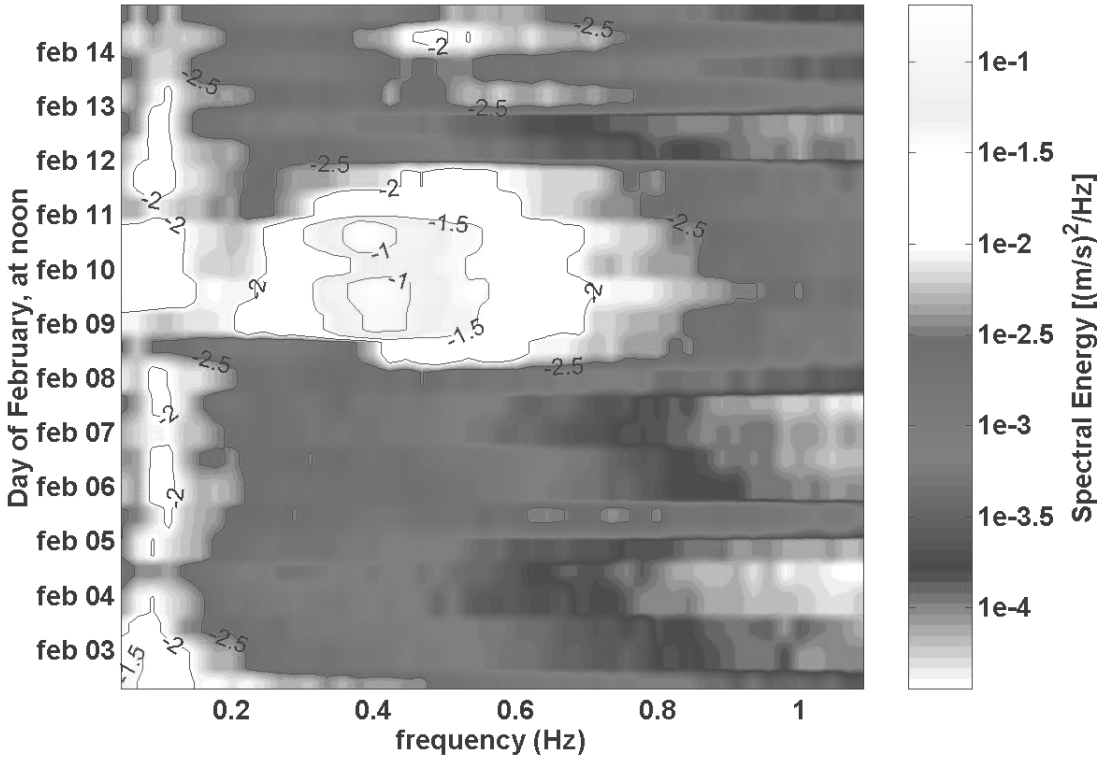

Figure 3.4: Power Spectrum obtained from ADV data at the mudflat, on a log 10 scale. Two distinct bands of energy can be seen, one between 0.05 Hz and 0.1 Hz and one between ~0.2 Hz and ~1 Hz. Contours on a log10 scale mark energy domains from $10^{-2.5}$ $(m/s)^2/Hz$ to 10^{-1} $(m/s)^2/Hz$. Note that data between periods of inundation are interpolated.

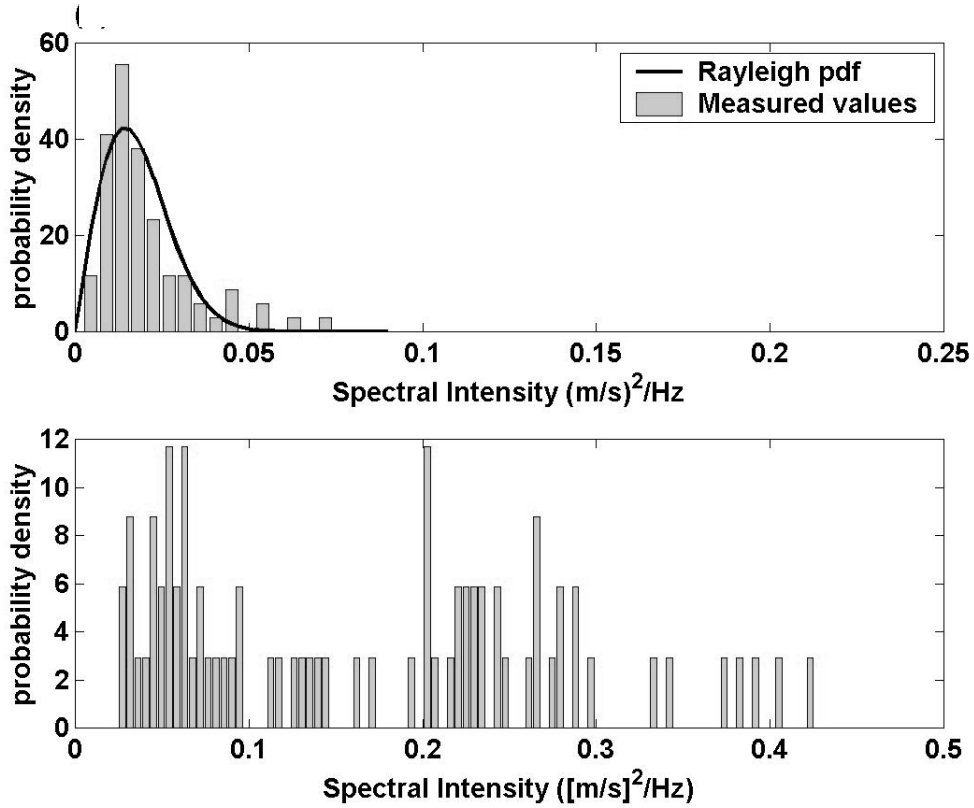

Figure 3.5: Comparison of the probability density distribution (pdf) of the maximum spectral intensity found between 0.044 and 0.11 Hz (a) and between 0.2 Hz and 1 Hz (b) for a period of inundation occurring between 10:40 pm on Feb. 09, 2001 and 4:55 am on Feb. 10th, 2001. Note that the low frequency pdf (a) resembles the Rayliegh distribution typically found in distributions of ocean waves. On the other hand, the pdf of the higher frequency band (b) is less structured, indicating a quickly changing wave climate.

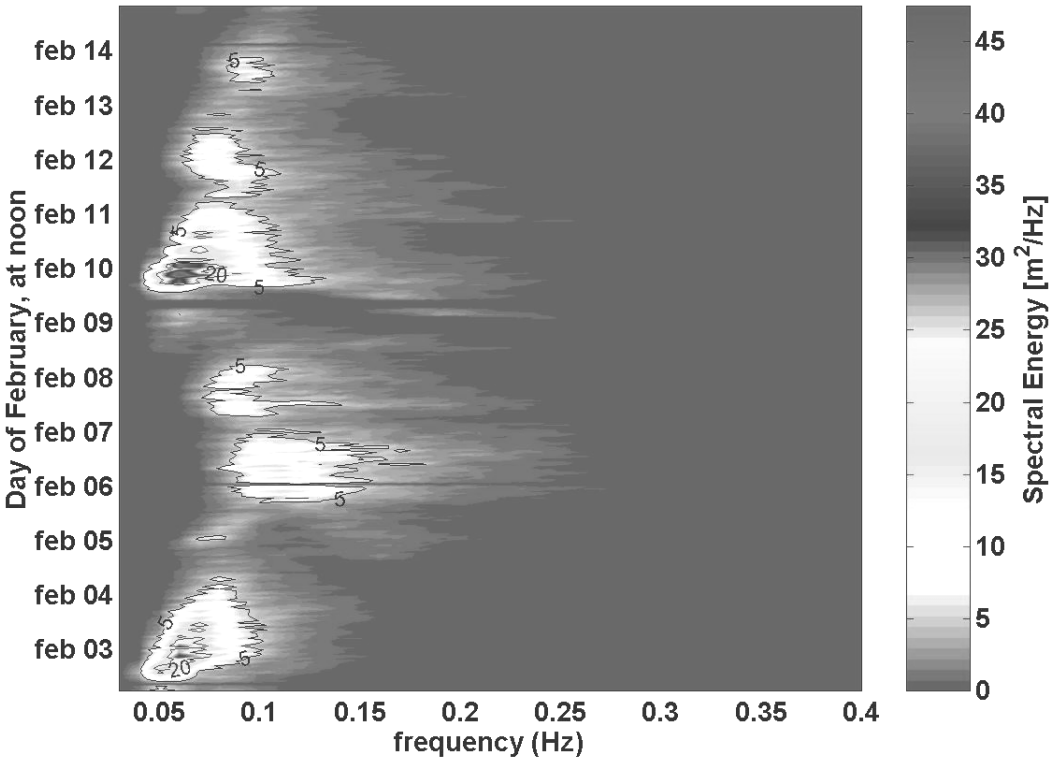

Figure 3.6: Wave amplitude spectrum from NDBC (National Data Buoy Center) buoy 46026, located just offshore of San Francisco, from Feb. 2nd to Feb 15th, 2001. Note the shift in the maximum wave period from approximately 15 seconds on February 3rd to approximately 8-10 seconds on February 6th. Contours mark energy domains of 5 m^2/Hz and 20 m^2/Hz. The maximum intensity of 47.5 m^2/Hz occurs on Feb 10th.

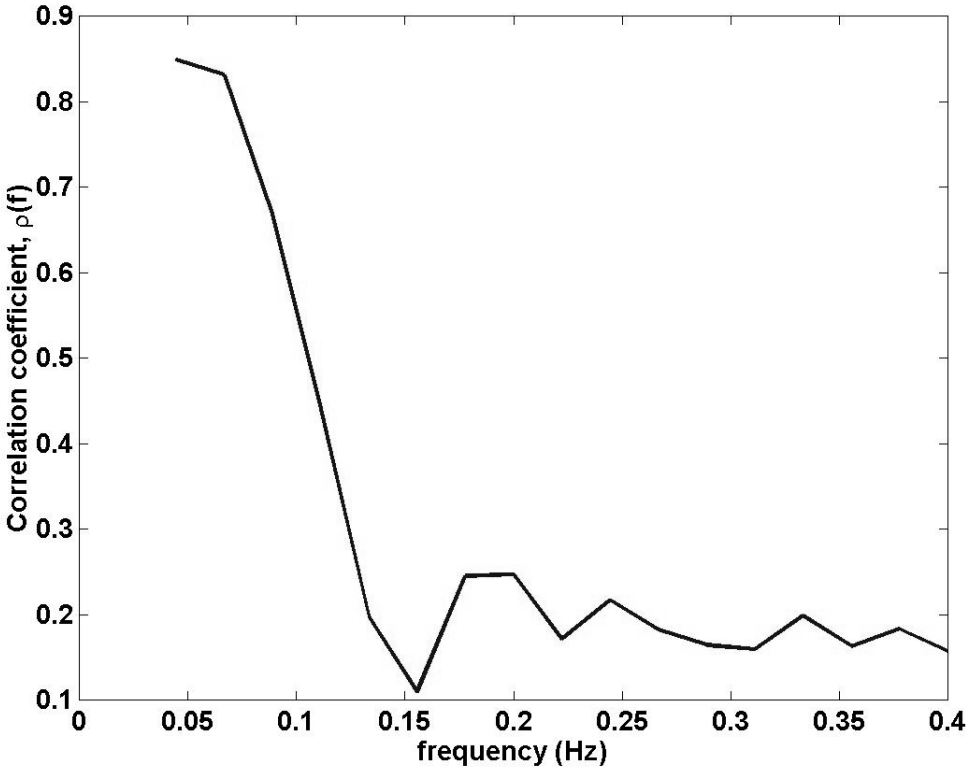

Figure 3.7: Correlation between the wave spectrum at NDBC buoy 46026 and the power spectrum from the mudflat, between Feb. 2nd and Feb 15th. Good correlation is seen at low frequencies, with a value of $\rho(f)=0.87$ at 0.044 Hz (22.5 sec period) and $\rho(f)=0.8$ at 0.067 Hz (15 sec period). Frequencies larger than 0.15 Hz have a correlation of $\rho < 0.3$, indicating that the higher frequency signals are uncorrelated with the ocean wave spectrum.

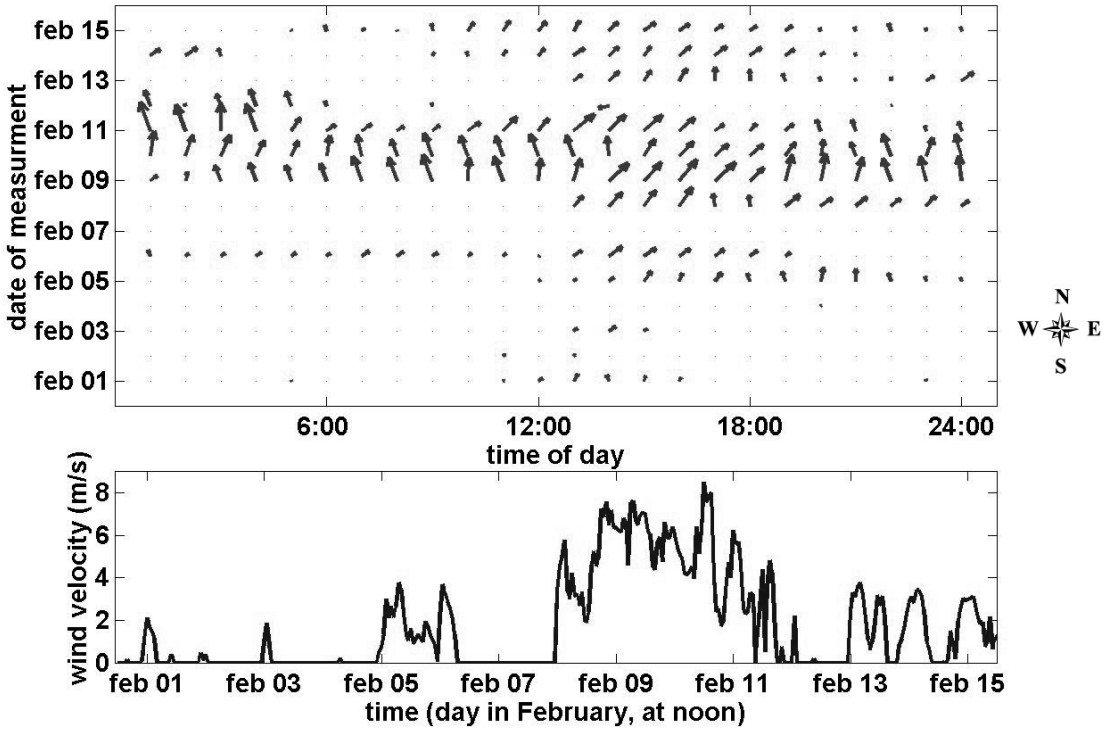

Figure 3.8: Components of wind blowing unobstructed onto the mudflat from the south from between 165^0 and 225^0 East of North. All other components of wind are set to zero. Note that the largest wind signal is seen during the storm of Feb. 9^{th} to Feb. 11^{th}, with a maximum wind speed of 8.5 m/s occurring early on Feb. 11^{th}.

.

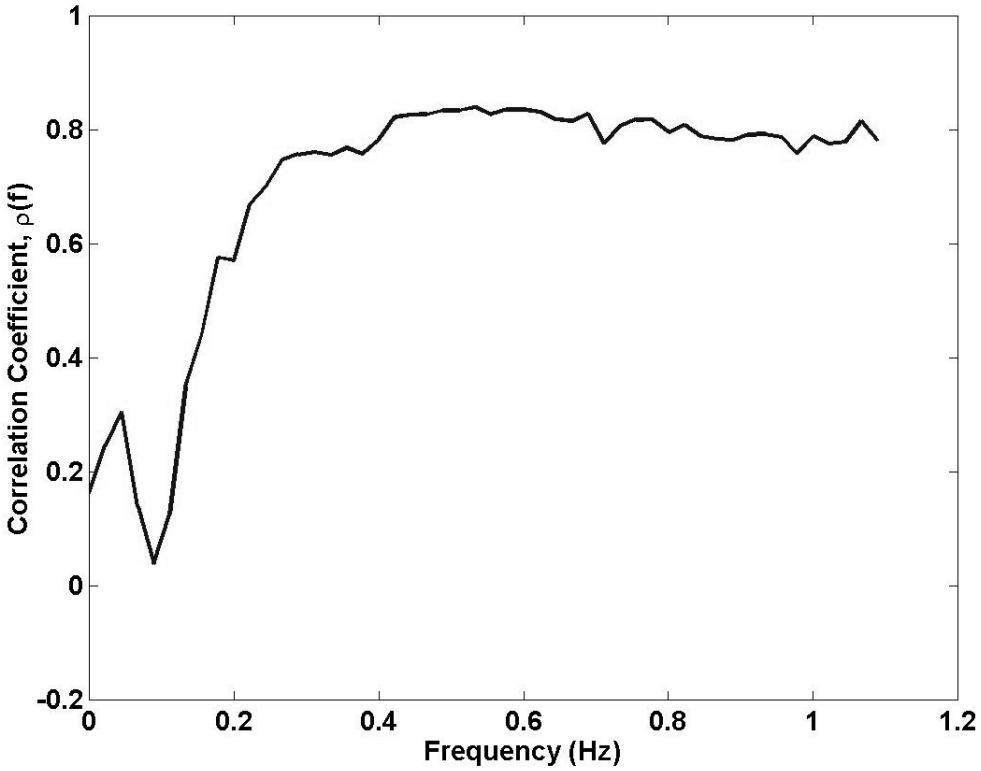

Figure 3.9: Correlation of conditioned wind energy (wind velocity squared) with the tidally averaged power spectrum over the entire, two-week experimental period. At wave frequencies > 0.25 Hz, the correlation coefficient $\rho(f) > 0.6$, indicating good correlation between wind and high frequency waves.

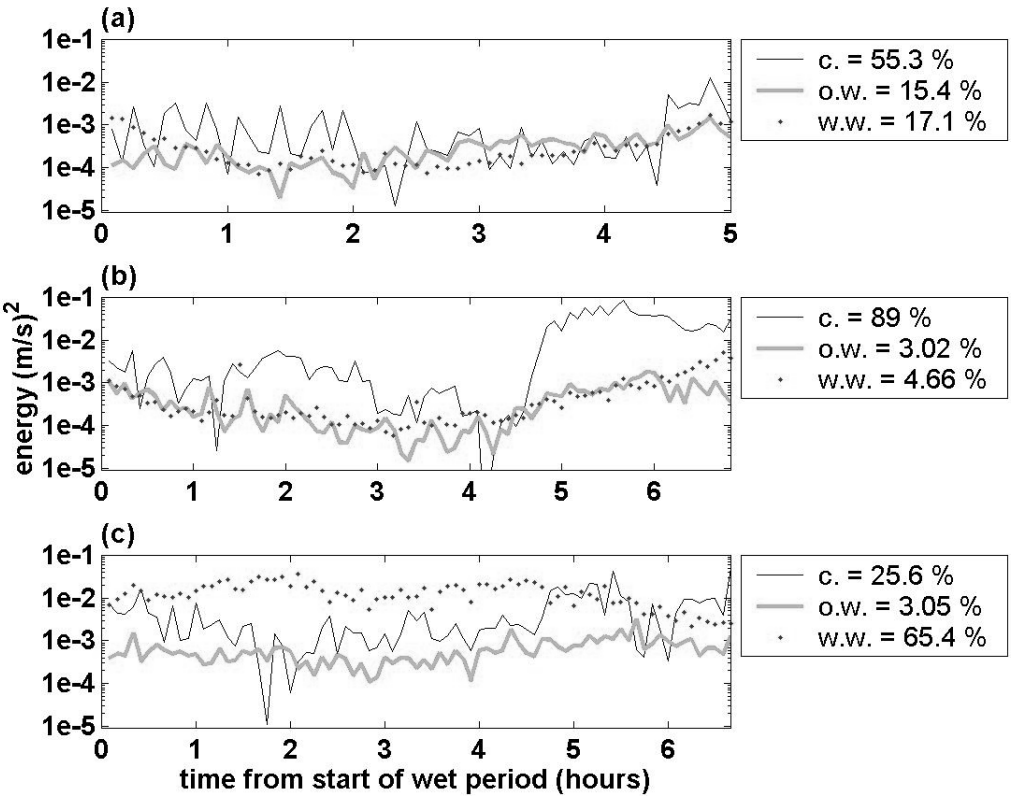

Figure 3.10: Energy incident upon the mudflat over a period of inundation during low energy conditions (a), current dominated conditions (b) and wind dominated conditions (c). The legend gives the percent of energy coming from current (c), ocean waves (ow), and wind waves (ww) for each tide. Wind waves are calculated from 0.2 Hz and 1 Hz, ocean waves from 0.044 Hz to 0.11 Hz. Note that the energy percentages do not equal unity, suggesting that there is some energy at other frequencies (e.g., seiching or high frequency wind waves and turbulence). Figure (a) shows the small high tide occurring on February 7th, and shows ocean waves becoming the largest energy source between hour 3 and 4.5. Figure (b) shows the large high tide on Feb. 7th; note the large ebb current at the end of the tide. Finally, figure (c) shows wind wave dominated conditions during the storm of Feb. 9th to Feb 11th.

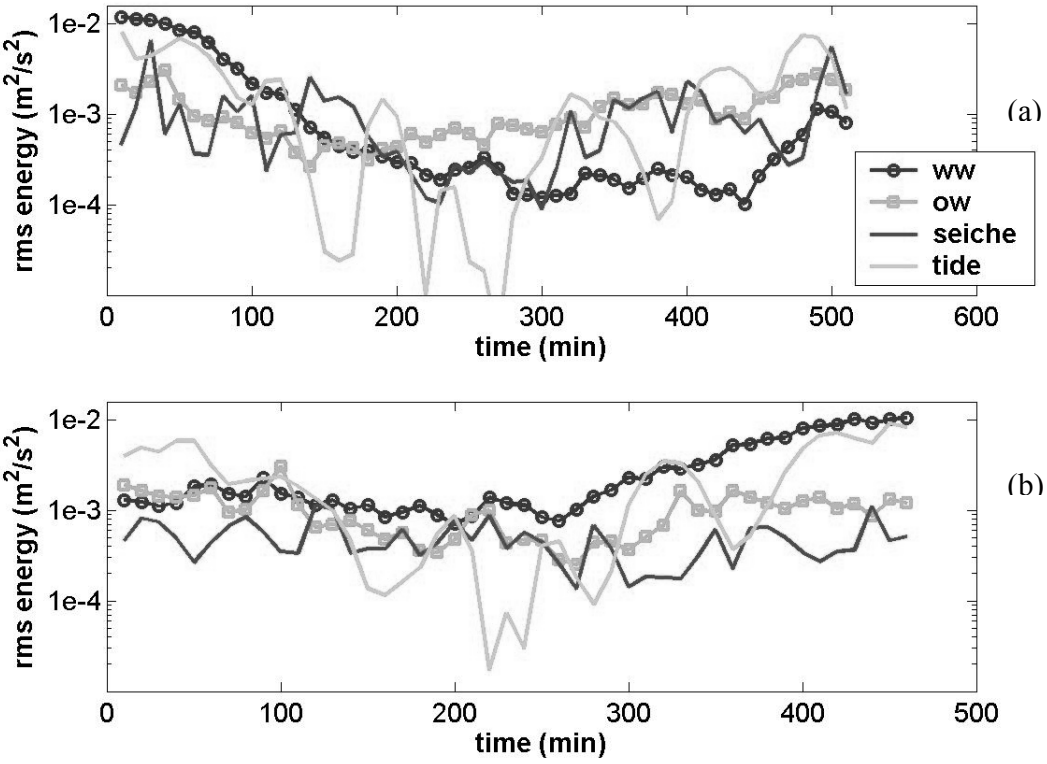

Figure 3.11: Comparison of the rms energy in experiment #3 for tide 5 (a), which begins at 6:40 pm on April 13th, 2003 and for tide 8 (b), which begins at 7:10 am on April 15th, 2003. The measured velocity at 0.285 m is decomposed into wind waves (ww), ocean swell (ow), seiche and tidal components using wavelet analysis. Wind waves correspond to scales which vary between 1/3 second and 3 seconds, while ocean swell comprises all periods between 6 seconds and 24 seconds. Seiche energy is defined as energy with a period between 1.5 minutes and 25 minutes, while the tidal component is all remaining, lower frequency energy. The rms energy is calculated from the square of velocity, in 10 minute increments.

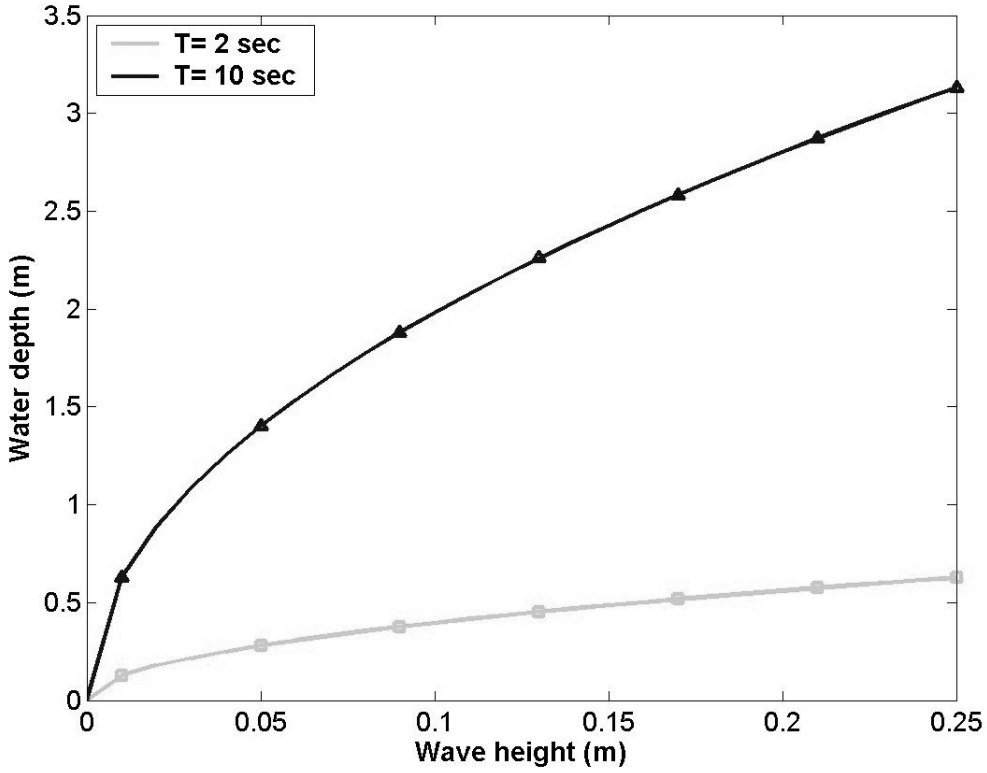

Figure 3.12: The threshold of nonlinearity as a function of wave height, wave period and water depth, calculated using equation 3.5. For local wind waves with a period of 2 seconds, non-linear cnoidal theory should be applied for wave/depth combinations below the light colored lines with square symbols. Similarly, offshore ocean swell with a period of 10 seconds should be calculated using cnoidal theory for wave/depth combinations below the dark colored line with triangle symbols. Above each of the lines, linear wave theory (or stokes theory) is adequate.

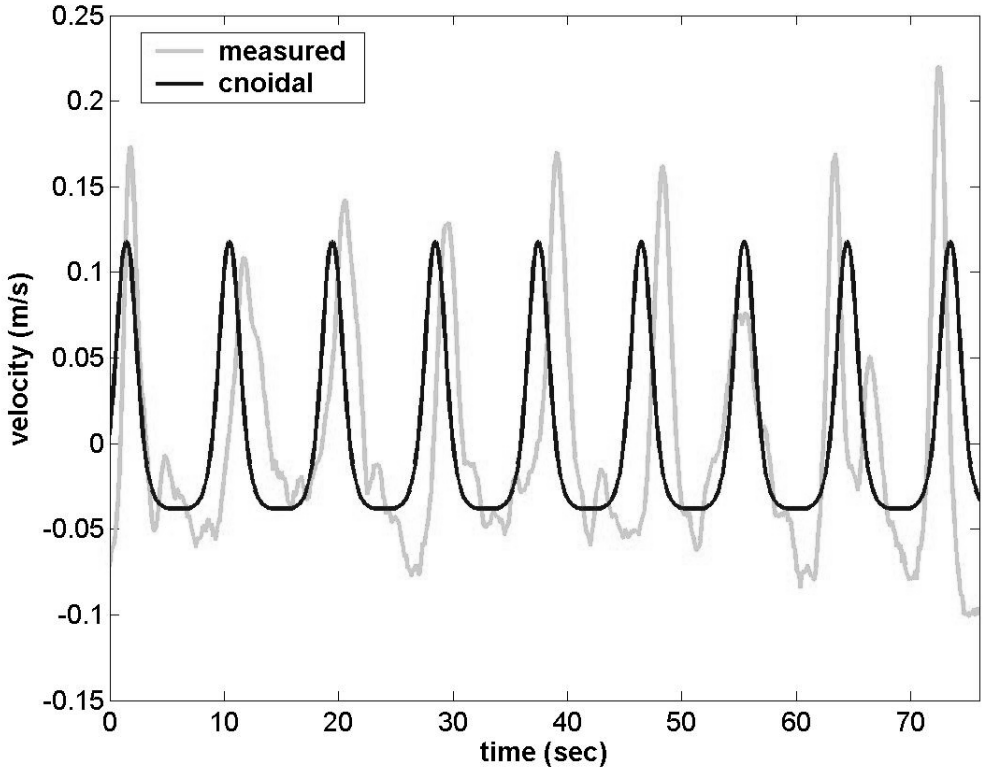

Figure 3.13: Comparison of ocean swell measured during an ebb tide (h=0.6 m) for an immersed period beginning at 6:40 p.m. on April 13th, 2003 with a cnoidal wave train using a wave height of 0.04 m and a wave period of 9 seconds. The 70 seconds presented occur 467 minutes after the start of inundation.

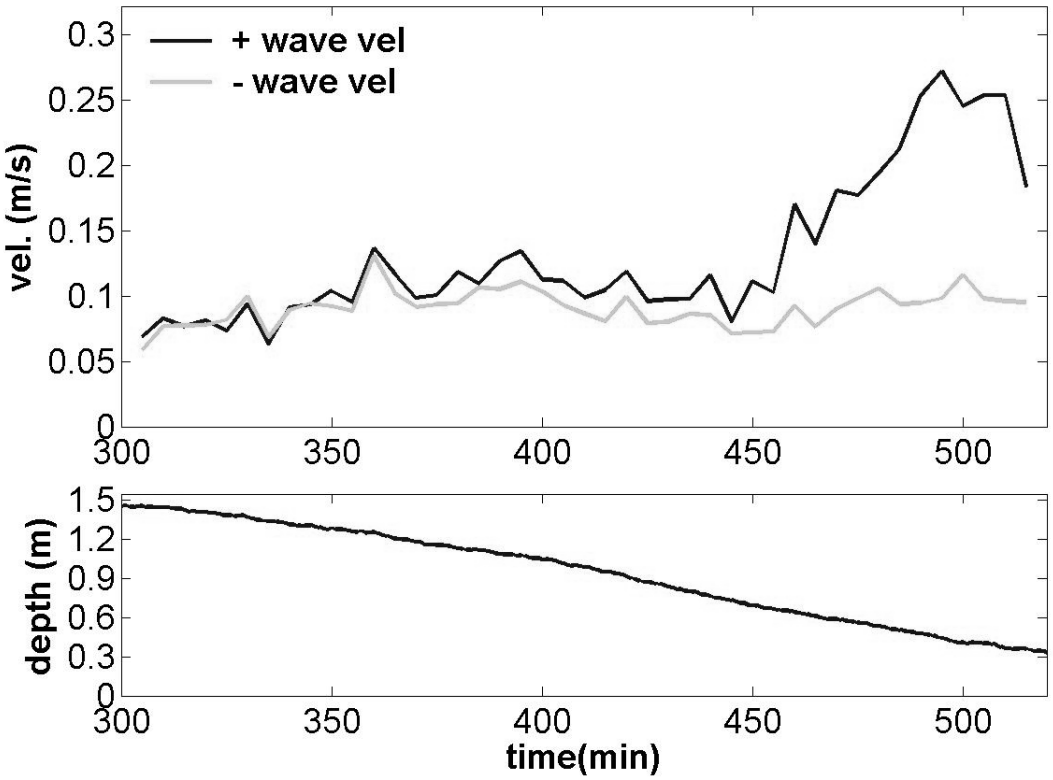

Figure 3.14: The top panel (a) shows the wave envelope for an ebb period dominated by ocean swell vs. time during an ebb tide for an immersed period beginning at 6:40 p.m. on April 13th, 2003. For comparison, the changes in water depth over the same period of time are presented in the lower panel (b). Positive, onshore orbital velocities are shown in dark color, while negative, offshore orbital velocities are shown in light color. The wave signal comprises all waves with periods between 1/3 second and 90 seconds, and is found using wavelet analysis. The wave envelope is determined by finding the average of the five largest wave magnitudes in both positive and negative directions over 5 minute blocks, then averaging.

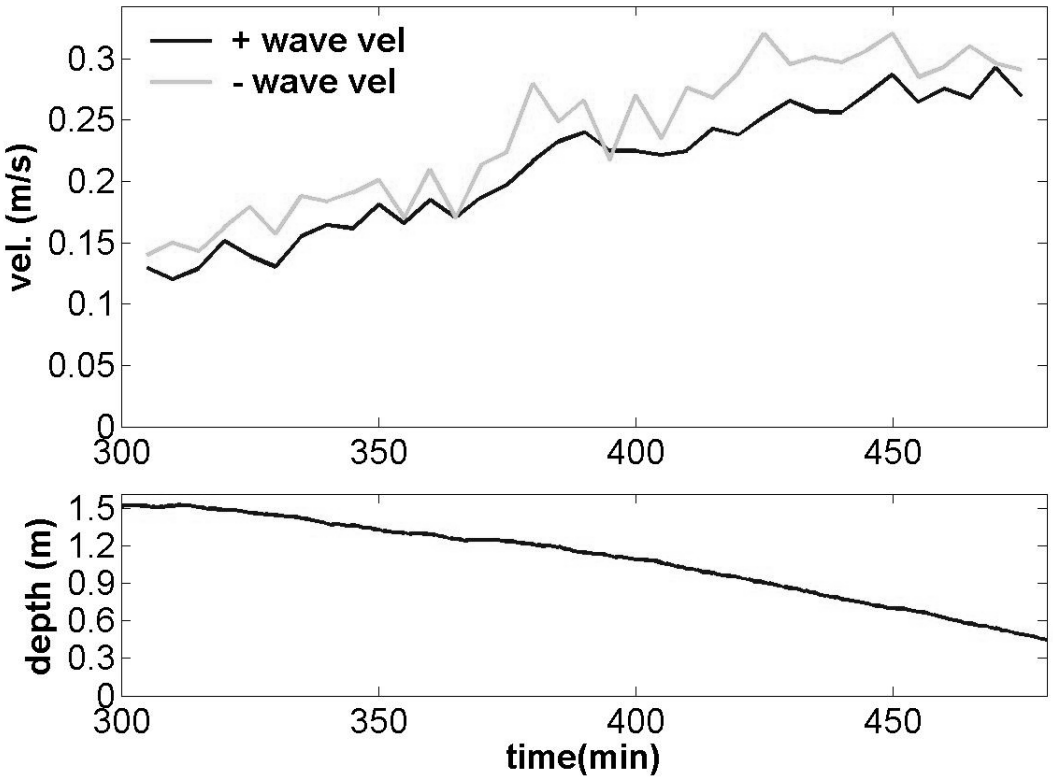

Figure 3.15: The top panel (a) shows the wave envelope for an ebb period dominated by locally driven wind waves vs. time during an ebb tide for an immersed period beginning at 7:10 a.m. on April 15th, 2003. For comparison, the changes in water depth over the same period of time are presented in the lower panel (b). Positive, onshore orbital velocities are shown in dark color, while negative, offshore orbital velocities are shown in light color. The wave signal comprises all waves with periods between 1/3 second and 90 seconds, and is found using wavelet analysis. The wave envelope is determined by finding the average of the five largest wave magnitudes in both positive and negative directions over 5 minute blocks, then averaging.

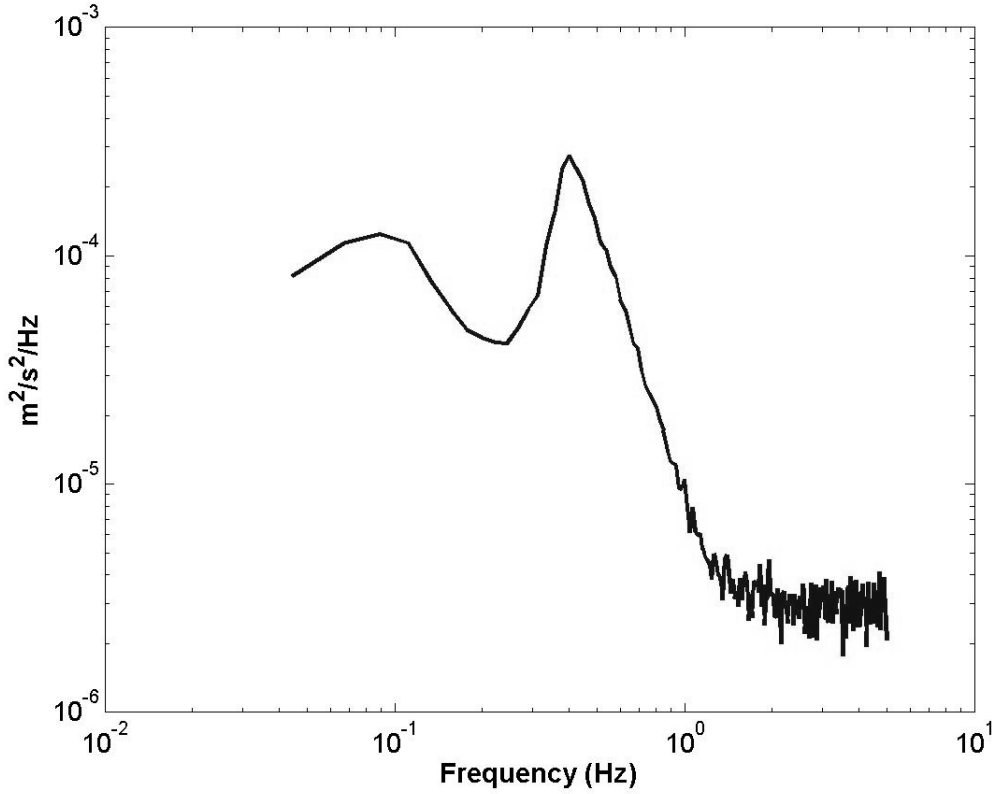

Figure 3.16: Average spectral energy of ocean swell and wind-waves over a two week spring-neap cycle from February 2nd to Feb 15th, 2001.

Chapter 4: Estimating TKE and Dissipation

4.1. Introduction

Hydrodynamic variables such as turbulent kinetic energy (TKE), bed stress, and dissipation of energy are essential for characterizing the mixing and settling of scalars such as sediment and for evaluating the effect of waves and currents on the bottom boundary. The stress acting in the near bed region is most simply calculated using the covariance of the fluctuating vertical and horizontal components of velocity, or Reynolds stress. Unless the waves are in perfect quadrature and the instrument is perfectly vertical, this method will include wave motions, and represents an aggregate of both wave and turbulent contributions. When wave motions are well-defined, linear wave theory or a statistical filter can be used to remove wave motions directly from the measured signal (e.g. Smyth et al., 2002). However, the wave climate at the field site at the Richmond Field Station contains irregular, nonlinear waves in several frequency bands. Therefore, simple corrections for waves are untenable and other, statistically based methods must be employed.

The contribution of waves to estimates of TKE and Reynolds stress can be removed by a variety of methods, for example by subtracting velocity measurements from instruments spaced such that wave motions are correlated but turbulent fluctuations are uncorrelated (Trowbridge, 1998, Shaw and Trowbridge, 2001) or through the correlation of the currents with the measured pressure record to identify wave motions

(Bowden and White, 1966, Benilov and Filyushkin, 1970, Wolf, 1999). Yet another method is to estimate TKE and shear stress based on the dissipation found in the inertial subrange of the energy spectrum (Kolmogorov spectrum), accounting for waves theoretically (e.g. Lumley and Terray, 1983, Gross et al., 1994). When multiple measurements are available, the logarithmic profile of horizontal velocity in the water column can be used to estimate the friction velocity, bed stress, and turbulence statistics (Nezu and Nakagawa, 1993). Soulsby and Humphery (1989) estimate TKE on the continental shelf by fitting a line across the base of the wave peak in the power spectrum of velocity. The extrapolated line defines the cutoff between wave energy (above) and TKE (below) in the power spectrum. By assuming a constant stress layer, bed stress can be estimated from the TKE (Soulsby, 1983).

Dissipation is most commonly measured by identifying the turbulent cascade portion of the turbulence power spectrum, first described by Kolmogorov (1941). The slope of the cascade is related to dissipation and wave number by dimensional analysis, and supported by theory (see Tennekes and Lumley, 1972). The turbulent cascade is estimated both directly from the power spectrum of velocity (e.g. Trowbridge et al., 1999, or Sanford and Lien, 1999) or indirectly using the power spectrum of a scalar (e.g. Trowbridge et al., 2001 or Lee et al., 2003). Because most instruments measure data at a point or a small volume, it is necessary to transfer from frequency space into wave number space using Taylor's frozen turbulence hypothesis (1938). However, for measurements taken at a point, estimating dissipation requires that turbulent fluctuations are much less than the mean velocity, that turbulence production balances

dissipation, and that a constant stress layer exists near the bed (Wolf, 1999, Huntley, 1988,Gross et al., 1994). Typically, only a small fraction of data in marine experiments satisfy these criteria (e.g., Wolf, 1999, Wright et al., 1992). Moreover, there is some ambiguity over what average velocity to use in an environment, and over what time scale (Lumley and Terray, 1983). For example, George et al. (1994) uses a 1/8 second average velocity over stationary segments of a nearshore swell to convert a frequency spectrum into a wave number spectrum. On the other hand, Gross and Nowell (1985) use a current averaged over 28 minutes to estimate dissipation rates in a tidal boundary layer, and Thwaites and Williams (2001) use a 440 second average on a continental shelf boundary layer. It brings to mind L.F. Richardson's question, "Does the wind possess a velocity?" (1926); in an environment with multiple forcing frequencies, it is not immediately clear what to define as a 'current' and what to define as a "wave". Error may be introduced by using a mean current and ignoring the advection of small, microscale turbulence past a sensor by a wave motion, and the fluctuations this induces in the signal; on the other hand larger turbulent eddies near the scale of the waves are missed by using a short averaging time.

Historically, most methods of calculating TKE, stress, and dissipation in the presence of waves have been developed for use on the continental shelf or the deep ocean in which one frequency of wave dominates and a large, constant stress region is formed (see e.g. Soulsby, 1983). On the other hand, shallow water is often subject to multiple frequencies of waves (see chapter 3) and a boundary layer that is potentially affected by time-varying tidal currents, seiching, wind stress, stratification, and potentially breaking

waves. These processes act over different time and length scales, making the vertical structure of shear, turbulence and dissipation highly variable and difficult to measure. Many assumptions used in more homogenous, deeper water may not hold in shallow water; for example, the assumption of a linear eddy viscosity, used to relate stress to TKE (Soulsby and Humphery, 1989) or dissipation (Kim, 2000, Thwaites and Williams, 2001), is questionable in a heterogeneous environment with multiple physical processes and must be examined. In this environment the average velocity must be defined with care. Moreover, the presence of wind waves and ocean swell at the same site (see chapter 3) makes the extrapolation used in the Soulsby method somewhat problematic; in effect, error increases as the frequency range of the interpolation increases. Similarly, a larger portion of the dissipation spectrum is obscured, making estimates of dissipation more difficult.

This chapter describes the methods and details some difficulties that are encountered when estimating turbulence and dissipation in the shallow water environment under the influence of multiple wave frequencies. In addition, we explore a new, hybrid technique for estimating the horizontal component of turbulence and dissipation. The variation of TKE and dissipation over a representative over a period in which the mudflat is immersed is shown and related to hydrodynamic flow variables.

4.2. Theory: Calculating TKE, dissipation, and stress

In this section we first present the standard methods of calculating TKE, stress, and

dissipation.

4.2.1: TKE

Turbulent flows are composed of complex, three-dimensional flow structures with a range of time and lengthscales. For a point measurement, the turbulent signal is defined as the deviation from a mean velocity:

$$v_i' = V_i - \frac{1}{T}\int_0^T V_i dt \tag{4.1}$$

where V_i is the particular component of velocity and T is an averaging time that is long compared to the largest time scale of turbulent eddies but short compared to variations in the mean velocity. To find a valid averaging period (T), one can evaluate the power spectrum of velocity and determine the lower frequency bound at which TKE drops off. In shallow intertidal water, an averaging time of 1 minute is generally larger than the largest time scale of turbulence.

Turbulent kinetic energy (TKE) is then defined as the sum of the square of the three turbulence components:

$$TKE = q^2 = v_i'^2 \tag{4.2}$$

where v_i' is the i^{th} component of turbulent velocity, and i=1,2,3. The scalar q is defined as the turbulent intensity, and has units of [m/s]. The units of TKE are energy per unit mass, or [m^2/s^2].

4.2.2: Stress

Stress and shear in the water column is often modeled by the Reynolds stress tensor, which is defined as:

$$R_{ij} = \overline{v_i' v_j'} \tag{4.3}$$

where v_i' and v_j' are orthogonal components of turbulent velocity, with i=1,2,3 and j=1,2,3. The overbar denotes a time average, using the same time T as in equation 4.1. For the case i=j, the Reynolds stress tensor reduces to the components of TKE (equation 4.2).

Stress is then defined as:

$$\tau_{ij} = -\rho R_{ij} \tag{4.4}$$

If measured near the bed in a constant stress region, the Reynolds stress becomes an estimate of bed stress. Bed stress τ_b is also commonly found using the friction velocity u_*, which is defined by the following relationship:

$$\tau_b = \rho u_*^2 \tag{4.5}$$

Friction velocity is commonly obtained from the log-linear velocity profile, which is estimated by:

$$U(z) = \frac{u_*}{\kappa} \ln(\frac{z}{z_0}) \tag{4.6}$$

where z_0 is the roughness scale, κ is von Karman's constant, and U is the horizontal velocity.

4.2.3: Dissipation rate

In a turbulent flow field, turbulent kinetic energy is transferred from larger to smaller eddies in the turbulent cascade portion of the wave number power spectrum, and is dissipated by viscosity at the smallest scales. Following Kolmogorov (1941) and Batchelor (1953), the dissipation rate ε of TKE is related to the wave number power spectrum and the wave number k_w as follows on both dimensional and theoretical grounds:

$$E(k) = C * \varepsilon^{2/3} * k_w^{-5/3} \quad (4.7)$$

where $E(k_w)$=Wave number Spectral Density [m^3/s^2], C=constant, ε= dissipation of energy per unit mass [m^2/s^3], and k_w= wave number [1/m].

In other words, the variation of the power spectrum of turbulence as a function of wave number is directly related to both dissipation and wave number. Because the field measurements are made in time and not space, equation 4.7 must be converted from a function of wave number into a function of frequency. Using the Taylor frozen turbulence hypothesis both the spectral density E(k) and the wave number k_w are multiplied by $\frac{U}{2\pi}$ to define the power spectral density in frequency space (S(f)) and the frequency f. In other words, $S(f) = \frac{U}{2\pi} E(k_w)$ and $f = \frac{U}{2\pi} k_w$. The factor 2*π converts from sample frequency (Hz) to radian frequency (radians/second). Note that to apply the Taylor frozen turbulence hypothesis, the mean current U must be much greater than the turbulent velocity v'; in addition, the change in mean velocity (ΔU) over the averaging time must be small compared to the mean velocity U (see e.g. George et al., 1994).

Combining these arguments, we arrive at an equation for energy dissipation in terms of the mean horizontal velocity U, frequency f, the inertial subrange of the power spectral density of velocity $S_I(f)$, and the empirical constant C:

$$\varepsilon = \left(\frac{1}{C} * S_I(f) * 2\pi/U * \left(2\pi f/U \right)^{5/3} \right)^{3/2} \tag{4.8}$$

Following standard practice (see e.g. Nezu and Nakagawa, 1993), we set the constant C equal to 0.5.

4.3. Separating Waves and Turbulence

In environments in which waves and turbulence occur in the same frequency range, the standard definition of turbulent fluctuations and TKE (eqn. 1 and eqn. 2) contains wave energy. Because wave orbital velocities are generally much greater than turbulent fluctuations, estimating TKE is difficult and requires first removing wave energy. In this section we detail the Soulsby (1989) and Trowbridge (1998) methods for estimating TKE and removing wave energy, and discuss how these methods can be applied towards estimating dissipation from the turbulent cascade. Then we present a hybrid method of calculating turbulence which is based on the Soulsby and Trowbridge methods.

4.3.1 Soulsby Method

The Soulsby method of calculating turbulent energy is conceptually simple and requires only one measurement location. Using multiple sensors, this method is therefore well suited to calculating a vertical profile of turbulence parameters. This method requires first identifying a wave peak in the power spectrum of a component of velocity, then interpolating a line across the base of the wave peak in log space. The portion of the power spectrum above the interpolation line is considered to be wave energy, while the energy below the interpolation line is integrated to yield the jth component of turbulent kinetic energy:

$$\overline{v_j'^2} = 2\int_{f\,\min}^{f_{\max}} (S_L - S_n)df \tag{4.9}$$

where S_L = the interpolation line $\left(\frac{m^2}{Hz \cdot s^2}\right)$, S_n is the noise floor $\left(\frac{m^2}{Hz \cdot s^2}\right)$, and

$df = \frac{s_r}{M}$ (Hz) is the frequency increment where M is the number of points in the data set and s_r (Hz) is the sample rate. The factor of two is included so that the energy in the symmetrical sides of the power spectrum is used. The calculated turbulent kinetic energy is an average over the time range used to calculate the spectrum, and is denoted by an overbar. The maximum frequency f_{max} is the Nyquist frequency (and equals half the sample rate), while f_{min} is the lower bound frequency of the largest turbulent eddies. The noise floor is assumed to be constant and is defined by the average value in the

zero-slope region in the high frequency portion (> 2 Hz) of the power spectrum. Once TKE is estimated, Soulsby estimates bed stress by assuming a constant stress layer. Then, at the continental shelf (Soulsby, 1983), total turbulence is related to the bed stress by a constant:

$$\tau = 0.19 * TKE \tag{4.10}$$

4.3.2: Trowbridge Method

The Trowbridge (1998) method requires a pair of measurement locations to remove wave energy and calculate TKE and stress. The method assumes that wave orbital velocities are strongly correlated between instrument locations, but that turbulent motions are uncorrelated. By subtracting one velocity from the other, the correlated parts of the signal (waves) are removed, leaving the residual, uncorrelated parts (turbulent motions):

$$\Delta U_i = U_{1,i} - U_{2,i} \tag{4.11}$$

where $U_{1,i}$ = i^{th} velocity component of instrument 1, $U_{2,i}$ = i^{th} velocity component of instrument 2, and i=1,2,3 is the direction of the velocity component. To avoid an offset due to the depth dependant mean current, the mean velocity at each measurement location is removed from the signal before differencing.

After applying equation 4.11 to all three velocity components, the Reynolds stress tensor is found as the average covariance between the two sensors:

$$\left\langle \overline{u_i u_j} \right\rangle = \frac{1}{2T} \int_0^T \Delta U_i \Delta U_j dt \qquad (4.12)$$

where i,j= 1,2,3 are the three components of velocity and T is the time over which the Reynolds stress is averaged. The brackets in 4.12 denote that the value is an instrument average. Evaluating the integrand in 4.12 results in an estimate that includes the Reynolds stress from both measurement locations; therefore, the factor of ½ in 4.12 is necessary to estimate the average between the two sensors. By applying linear wave theory to a vertical array of sensors, and by using a linear regression technique to obtain an estimate of the wave form at one instrument given the wave form at another, Shaw and Trowbridge (2001) are able to reduce the error in the covariance estimate. Smith et al. (2002) applied the Trowbridge method to Particle Image Velocimetry (PIV) data and minimized error by varying the separation distance between velocity pairs.

4.3.3 Hybrid Soulsby/Trowbridge Technique

In laboratory studies, wave experiments are repeated multiple times to create an ensemble of measurements at a particular location. An ensemble-averaged wave profile is defined by averaging the measured wave profile (i.e., velocity vs. time) across all experiments. The difference between the ensemble averaged wave velocity and the orbital velocity of a particular experiment is then defined as the turbulence (see e.g. Flick et al., 1981, Thais and Magnaudet, 1996; for an application to irregular waves see

Sultan and Ting, 1993 and Ting, 2001). In the field, the randomness of the wave motions makes repeatable experiments at a particular point impossible. However, a mean wave profile can be created by averaging over multiple instrument locations, provided that the wave orbital velocities are correlated and that the turbulent motions are not correlated. In analogy with the laboratory studies, the turbulent velocity component $v'(t)_{t,j}$ at a particular measurement location 'i' and direction 'j' is defined as:

$$v'(t)_{i,j} = V(t)_{i,j} - \langle V(t) \rangle_j \tag{4.13}$$

where $\langle V(t) \rangle_i$ is the spatially averaged wave profile and $V(t)_{i,j}$ is the time series of velocity at location 'i'.

The mean wave profile is defined as follows:

$$\langle V(t) \rangle_i = \frac{1}{M} * \sum_{k=1}^{M} \left(V_k(t) - \frac{1}{T} \int_0^T V_k(t) dt \right) \tag{4.14}$$

Where i=1,…M equals the set of M instruments used to define the ensemble average wave velocity for instrument "i". Instrument "i" is excluded from the ensemble average

to avoid biasing the estimate of turbulent velocity defined in 4.13. In addition, the mean velocity over an averaging time T>>wave period is removed from each velocity measurement to account for variations in mean velocity in both the horizontal or vertical direction. Note that the velocities measured from each instrument must be synchronized.

After calculating the set of turbulent velocities, the methods outlined above (section 4.2.1) can be applied to estimate TKE and/or Reynolds stress. However, the set of turbulent velocities $v'(t)_{t,j}$ which are calculated may still contain some error, particularly if wave orbital velocities between instrument locations are not completely correlated or turbulent motions between instrument locations are correlated (see e.g. Shaw and Trowbridge, 2001). There are also often quadrature alignment issues and other instrument errors. As the number of measurement locations increases, however, random error due to quadrature alignment and measurement error decreases by sqrt(1/M). Moreover, the error introduced by any correlated turbulence between two instruments is averaged and reduced by the remaining instruments. Overall, the method described here is a hybrid of the Trowbridge method and the Soulsby method. Indeed, when only two instruments are used in the calculation of stress, the method defaults into the Trowbridge method.

4.4. Practical Implementation in shallow water environment

While the theories outlined in section 4.2 and 4.3 are fairly straightforward, their implementation into the shallow water environment reveals some difficulties. Turbulent eddies are constrained by the distance to the top and bottom boundary, and a mean velocity is difficult to define in the presence of multiple frequencies of waves. Moreover, both vertical variation and spatial correlation between velocimeters needs to be considered for the Trowbridge and hybrid methods. Subjective decisions on how to define a best fit on a power spectrum, how to deal with noise, and how to determine whether the best fit indeed measures the turbulent cascade are important—but ultimately somewhat subjective—questions. Below we describe the strategy used to implement the theories for calculating TKE and dissipation into practice, and the rational used to justify it.

4.4.1: Scaling of turbulent eddies

Though the turbulent cascade is extended by the Soulsby, Trowbridge, and hybrid methods into the frequency range of wind waves and ocean swell, the question remains whether this is a realistic frequency range for turbulent energy transfer to be occurring. We test this by estimating the length scale of the largest and smallest eddies, and converting these scales into a frequency range using the Taylor frozen turbulence hypothesis. The lengthscale of the smallest eddies is given by the kolmogorov lengthscale:

$$L_k = \left(\frac{\nu^3}{\varepsilon} \right)^{\frac{1}{4}}$$

(4.15)

The largest eddies are estimated as:

$L_e \sim z$,

(4.16)

where z is the distance from a boundary. Note than in isotropic turbulence, the largest eddies scale as κz, where κ is von Karrmen's constant. However, in shallow water, turbulent eddies are often asymmetric and stretched in the horizontal direction (Nezu and Nakagawa, 1993). Because the anisotropy is unknown at our experimental location, we simply estimate the order of magnitude of the largest turbulent eddies using the local height of each measurement location.

These length scales and the characteristic horizontal velocity (U(z)) are then applied to find the frequency range:

$$f_{\min} \sim \frac{U(z)}{L_e(z)}$$

(4.17)

$$f_{\max} \sim \frac{U(z)}{L_k(z)}$$

(4.18)

At our site, typical values of L_k vary between ~0.001 m and ~0.003 m, while L_e varies between ~ 0.01 m and 0.10 m. At a typical velocity scale between 0.01 m/s and 0.1 m/s, the frequency range in which the turbulent cascade takes place is between 0.1 Hz and 300 Hz. Clearly the high frequency bound is above our sampling frequency and the frequency of locally driven wind waves (~0.3 Hz – ~1 Hz). On the other hand, the low frequency bound is smaller than the wind waves. Thus, it is valid to extend the turbulent cascade across the wind-wave peak in the power spectrum to frequencies of about 0.1 Hz, particularly when the velocity scale is small.

Significant uncertainty exists in estimating the correct velocity scale, and practical questions such as whether to include wave motions are difficult to answer satisfactorily. Rather than calculate the lower frequency bound for each instrument and each burst, we therefore assign a lower limit that is within the calculated frequency range. While this may introduce some error, the bias is fairly uniform and therefore the spatial and temporal variability of the TKE estimates should not be affected too significantly. Thus, 0.1 Hz is a reasonable compromise given the constraints of the environment, and is used as the minimum frequency value in equation 4.9 (Soulsby method of estimating TKE).

4.4.2: Line fitting methods

A practical difficulty of the Soulsby method arises when determining how to fit a line over the wave peak and how to define the floor from which to interpolate. In this chapter we examine two types of fitting methods. The first requires defining a set of points on both sides of the wave spectrum and defining a least squares fit between the points; the second involves defining an optimal fit to the high frequency side of the power spectrum (in the least squares sense), then extrapolating to 0.1 Hz. For each fitting method, the set of points on the high frequency side is found by identifying the inertial subrange (-5/3 slope) between the wave spectrum and the noise floor. For the ADVs in this environment, this typically precludes most points higher that 2 Hz and lower than 1 Hz. The low frequency points are found by finding the minimum value of the power spectrum at frequencies lower than the wave peak. This point and adjacent points are weighted so that the high and low frequency portions of the interpolation base have an equal number of points. Each method has advantages and potential limitations. The weighted interpolation method requires that a true minimum be found in the low frequency portion of the power spectrum, and not an artifact of the method used to calculate the power spectrum. The linear extrapolation method requires that an accurate slope be found that best approximates the turbulent power spectrum.

Note that the algorithm used to calculate the power spectrum introduces noise into the frequency range used to fit a least squares line. In order to reduce noisiness from the

spectral technique, we apply a wavelet filter to remove small scale fluctuations (while retaining large scale fluctuations such as the turbulent cascade or wave peaks).

4.4.3: Determining mean velocity and turbulent cascade

To estimate dissipation, we first calculate the logarithm of the power spectral density S(f) of the measured velocity signal. The inertial subrange $S_I(f)$ is then found by identifying the region in which the logarithm of S(f) has a slope of -5/3 (see equation 4.7). In practice, $S_I(f)$ is found by applying a least squares fit to the logarithm of S(f) over a range of likely frequencies. When the slope is -5/3, the inertial subrange has been identified and equation 4.8 can be calculated.

While in theory simple, there are many practical difficulties in estimating the turbulent cascade in the shallow water environment. For example, wave motions can easily overwhelm the smaller turbulent signal in the power spectrum, as can the velocimeter noise floor. In addition, noise from the spectral estimate can bias the slope, particularly from edge effects in small data sets. Noise can also bias the placing of the -5/3 line, particularly if not many points are used to fit the line. Finally, at small Reynolds numbers the flow may be viscous, in which case no turbulent cascade exists.

The choice of how to average the data set to obtain a mean velocity is not trivial. The mean velocity may vary over time, distorting the rate at which eddies are swept past a sensor over a given sampling period. In addition, the mean velocity may be small

relative to other forcing; for example, during slack tide, wave motions may be greater than the tidal current. These wave motions advect small scale turbulent eddies past a sensor, and are then captured on the ensuing velocity record and power spectrum. Clearly, using only the tidal current in this situation biases the calculated dissipation. However, using the wave orbital velocity as a velocity scale is problematic as well, since turbulent motions are aliased into the wave and because the wave is stationary over only a small period (< 1 second), requiring a high sample rate (George et al., 1994). With a maximum sample rate of 16 Hz, our sample frequency is too small to adequately resolve turbulent fluctuations over a portion of the wave. A compromise solution is to use the root mean square (rms) velocity over any given time segment (e.g., Lumley and Terray, 1983). This allows the contributions of ocean swell and local wind waves to be included in the calculation of dissipation, along with the mean current. Still, some distortion of the turbulent eddies occurs as velocity varies over the period of the wave.

4.4.4: Slope limits

Given that turbulent motions are being swept past a measurement location at various frequencies from differing forcing mechanisms, and given the inherent noise in both the measured signal and any spectral calculation technique, it is not surprising that the power spectrum in frequency space often deviates from a -5/3 cascade. Particularly at the small velocities at our experiment site (order 0.01-0.1 m/s), the distortion effects

may be large. A better standard is to obtain a best-fit slope that is close to -5/3, and clearly does not belong to the noise floor (slope=0) or to the wave spectrum (slope <-3).

To stay near the slope of the turbulent cascade, we therefore require that the slope of the line that is fit across the base of the wave peak must be between -0.9 and -2.4. Various studies have found that the measured slope in the dissipation spectrum deviates from -5/3. A study by George et al. (1994) found an average slope of -1.25 while Smyth et al. (2002) found an average slope of -1. Postulated reasons include experimental error, bubbles in the flow, aliasing of the spectral signal near the Nyquist frequency and anisotropy of turbulent motions near the bed (Smyth et al. 2002, George et al., 1994). Thus, an upper limit of -0.9 is reasonable.

4.4.5: Removing residual wave energy

In the Trowbridge and hybrid methods, the decay of orbital velocity with depth poses a source of error in the stress and TKE estimate, particularly for the vertical component. The error manifests itself as residual wave energy in the differenced velocity $v'(t)_{t,j}$ (see equation 4.13), and is easily observed as a wave peak in the power spectrum of $v'(t)_{t,j}$. While Shaw and Trowbridge's method (2001) correction for two measurement heights could be expanded to multiple heights, in practice it is easier to apply the Soulsby method for calculating TKE. Basically, any remaining wave energy in the residual velocity (equation 4.11 and 4.13) is removed by interpolating a line across the base of the wave peak in the power spectrum of $v'(t)_{t,j}$. Any energy beneath the line is

considered turbulent kinetic energy (TKE), while the energy above the line is the residual wave energy that was not removed by differencing. This approach works well for estimating TKE in the horizontal direction (see section 4.5). However, estimating the vertical component of TKE remains problematic because of the fast decay of vertical orbital velocity with depth. Often, little of the vertical wave energy is removed, making the method reduce to the Soulsby method. Therefore, we concentrate on the horizontal, streamwise component of TKE.

4.4.6: Estimating extent of spatial correlation between waves

In shallow water that contains multiple frequencies of motion, the assumption used in the Trowbridge and hybrid techniques that the wave orbital velocity of all wave frequencies is correlated may not be valid. Correlation of waves varies approximately as $\cos(\frac{2\pi}{\lambda}x)$ in the direction of propagation, where λ is the wavelength and x is the horizontal separation distance. Over the range of wave periods typical at the mudflat (T=1-15 sec), the wavelength varies from ~3 m to ~47 m at a depth of 1 m. Thus, the highest frequency wind waves (T=1-3 seconds) quickly decorrelate in the direction of propagation; for a 1 Hz wave, a separation of less than 0.4 m is a phase shift of $\pi/4$ at a depth of 1 m. Even when instruments are approximately aligned with the direction of flow, along-crest variation (e.g., diffraction) or a slight angle of wave attack on the frame will cause errors. Vertical variation in orbital velocity can be removed using linear wave theory (Shaw and Trowbridge, 2001); however, this method becomes problematic when there are many wave frequencies or waves become nonlinear.

Indeed, as shown in chapter 3, ocean swell is inherently non-linear at depths common on an intertidal flat and thus poses a problem to corrections based on linear wave theory. Determining the optimum instrument separation becomes a compromise between the different wave length-scales and the turbulence length-scale. This makes it more difficult to determine a vertical profile of turbulent kinetic energy.

In practice, the horizontal orbital velocities for most velocimeters were well correlated in the horizontal direction. An example is shown in figure 4.1, which shows the velocities of the five upper sensors of experiment #3 (see figure 2.6) overlaid on one another over a period of 60 seconds during the immersed period (high tide) of April 13th, 2003. Visual inspection shows that the horizontal velocities of all 5 instruments, which are located between 0.05 m and 0.33 m, follow each other closely, though some deviation in the signal occurs due to turbulent motions. Another source of deviation is small amplitude, high frequency waves that begin to decorrelate over the separation distance of the velocimeters (0.2m to 1 m). To avoid differences in the time recorded by each instrument, we shift each data set of velocity shown in figure 4.1 by a time lag that maximizes the correlation between different sets; typical time lags are 0-5 seconds, and are persistent throughout a period of inundation. The persistence of the time lag over a tide indicates that it is likely caused by differences in the internal clocks of the instruments, rather than phase lag affects in the oscillatory boundary layer (which would vary with wave period and amplitude).

Over the time period of a tide, the magnitude of the orbital velocities measured by the velocimeters between 0.05 m and 0.33 m are also quite similar. Figure 4.2 shows the root mean square (rms) wave orbital velocity for ocean swell and local wind waves over an entire period of inundation on April 13th, 2003 as a function of height above the bed. Measured data are first bandpass filtered into ocean swell (T=8-20 seconds) and wind wave (T=1-5 second) bands, from which the rms velocity is calculated. Note that the rms velocity at all heights is normalized by the rms orbital velocity at 0.285 m. Some turbulent kinetic energy is included in the wind wave estimate, and induces a small error. Note that the rms orbital velocity at 0.015 m is strongly attenuated because of proximity to the bed; however, all other values are within 5-10 percent of each other. Because of alignment and frame interference issues, the orbital velocity of the side-mounted instruments is biased lower than the vertically mounted instruments. In addition, the instrument error of ~ 0.001- 0.002 m/s adds to the uncertainty in our waves, which average on the order of 0.01- 0.05 m/s. However, averaging over all waves N in an inundation period reduces the error of the rms velocity by a factor of $1/\sqrt{N}$.

4. 5. Results: TKE and dissipation

The following section depicts the results of applying the Soulsby, Trowbridge, and hybrid methods of calculating TKE and dissipation. First, the methods used to obtain TKE and dissipation are compared for a few particular 1 minute segments of the

dataset. Next, the aggregate variation of TKE and dissipation over a representative tidal period on April 13th, 2003 are presented and analyzed.

4.5.1: Calculating TKE over 1 minute velocity segment

Using the five instruments from experiment #3 which are correlated, we apply the hybrid technique and calculate a spatially averaged orbital velocity over time periods in which all are recording data (eqn. 4.14). From this we construct the turbulent velocity (eqn. 4.13) which we compare to the other methods of calculating TKE and dissipation.

The power spectrum of the hybrid turbulent velocity shows that much of the original wave motion is removed, particularly at the ocean swell frequency (see fig 4.3). However, a substantial node of energy remains at a frequency greater than 0.6 Hz, and this biases estimates of TKE calculated from the hybrid turbulent velocity (equation 4.13). Most low frequency wave motion is also removed by the Trowbridge method, as can be seen in figure 4.4 by comparing the measured power spectrum and the power spectrum of the trowbridge velocity (equation 4.11). However, high frequency wave energy also remains in the Trowbridge spectrum (see figure 4.4), suggesting that high frequency waves are uncorrelated at the separation distances in the experiment (0.2 m to 1 m).

The single peak of remaining wind-wave energy (see figure 4.3 and figure 4.4) can now easily be removed using the standard Soulsby method, without the ambiguity caused by

interpolating over several wave peaks. For example, figure 4.3 shows a linear interpolation over both the measured spectrum and the hybrid spectrum using the weighted interpolation method. The hybrid spectrum is calculated from the residual velocity found using equation 4.13. Visually, both interpolations separate the wave energy from the turbulent energy. The line that is fit to the hybrid spectrum (slope = -1.55) is nearly equal to the theoretical slope of the turbulent cascade (-5/3). However, the line that is fit to the measured spectrum deviates from the turbulent cascade and has a slope of approximately –7/3. The error likely occurs because of the overlapping spectrums of ocean swell and wind-waves, which make the base of the wave spectrum more difficult to identify. There is also some ambiguity over whether to interpolate over just the wind-wave peak, or over both the wind-wave and ocean swell spectrums (see figure 4.3 and figure 4.4). The location and magnitude of the minimum lower frequency also varies depending on the technique used to calculate the power spectrum (e.g., number of points used, type of window, etc). Thus, the slope is somewhat subjective and reflects to some extent an artifact of the wave climate, spectral technique, and interpolation method rather than the spectrum of turbulent kinetic energy.

The potential errors that occur when interpolating over the measured power spectrum are reduced by techniques that remove wave energy, such as the Trowbridge method (equation 4.11 and 4.12) and the hybrid method (equation 4.13 and 4.14). When low frequency wave energy is removed (< 0.6 Hz), the remaining wave peak covers a smaller frequency range (see figure 4.3 and 4.4). Thus it is less ambiguous to define the

base of the wave peak, since the problem of overlapping wave spectrums is removed. Since there is less wave energy to remove, there is likely less error (given the same algorithm for interpolation). Finally, the turbulent cascade exists only over a finite frequency range. When the frequency range over which interpolation occurs is reduced, then it is more likely that the interpolation remains near the turbulent cascade (slope = -5/3). This is shown by figure 4.4, which shows that the slope of the Trowbridge spectrum is nearly constant (slope ~ -1.38) over the weighted interpolation, except for the residual wave peak centered around 0.6 Hz. Because less assumption needs to be made about the shape of the turbulent power spectrum that exists underneath the wave power spectrum, TKE is easier to determine. For a more complete discussion of error, see section 4.6.

4.5.2: Calculating dissipation over 1 minute velocity segment

We find that dissipation is more easily estimated from a power spectrum after removing a large portion of the wave energy using the hybrid method or Trowbridge method. Examples of fitting a -5/3 line to a spectrum using the best-fit extrapolation method are shown for the original, measured spectrum (figure 4.5) and for the calculated hybrid spectrum (figure 4.6). The best fit line over the frequency range used for calculating dissipation is presented as light-colored, while the –5/3 line is presented as a darker line. For the raw spectrum, only a narrow frequency range can be used to estimate dissipation; at frequencies below ~ 1 Hz, the wave spectrum due to local wind waves and ocean swell often overwhelms the turbulent spectrum, while the noise floor of the

instrument is often reached between 1-2 Hz. Thus, while a -5/3 line may fit onto the spectrum between 1-2 Hz (see figure 4.5), the actual best fit line to this range of data may correspond more closely to noise (~ zero slope) or to a wave spectrum (slope < -3). Even when the best fit slope fits within a range that is close to -5/3 (see figure 4.5), it is possible that the slope represents a transition between the noise floor and the wave signal, or is an artifact of the frequency range used in the line fitting.

On the other hand, the wave peak on the hybrid spectrum (figure 4.6) is spread over a smaller frequency range and is much smaller in magnitude. Moreover, it is often possible to extrapolate the -5/3 line over the wave peak for local wind waves, and extend the frequency range used for the -5/3 line and the best fit. Thus, the frequency range is extended down to ~0.5 Hz or possibly lower, and more confidence is gained in the result (larger frequency range).

4.5.3: TKE estimates over a tide

An estimate of the horizontal, along stream component of TKE over an immersed period on April 13th, 2003 is given in figure 4.7 for a height of 0.05 m off the bed. There is a factor of 3 (approximately) scatter around the 10 minute mean for the Soulsby, Trowbridge, and hybrid methods. Though some of the variation is probably due to error in the methods (see section 4.6), some of the scatter likely reflects modulation of the TKE signal by the 8 minute seiche. Unfortunately, the density of data is not good enough to obtain a good correlation between the TKE and seiche

signal. On the other hand, the ten minute moving average of the results shows that the major features over the tidal time scale are reproduced by all three methods: during the flood, TKE is large (~10^{-3} m^2/s^2), drops by several orders of magnitude during the slack tide (< 10^{-5} m^2/s^2), and increases again during the ebb (~ 10^{-4} m^2/s^2.) The behavior of the turbulent energy closely tracks the overall wave energy during this period of inundation (compare to figure 3.11a).

For comparison, figure 4.8 shows the calculated, along stream component of TKE at a height of 0.285 m off the bed over the same time period as figure 4.7. A similar pattern emerges, with large TKE during the flood (>5*10^{-4}) followed by diminished turbulent energy during the slack tide (<10^{-5}) and increased TKE during the ebb (>10^{-5}). However, the increase in TKE during the ebb is less for the measurement at 0.285 m than at 0.05 m. This indicates that TKE produced by the dominant frequency during the ebb, ocean swell, is being measured by the lower velocimeter (see figure 3.11a). On the other hand, both velocimeters show similar increases in TKE during the flood, a time of large wind waves.

4.5.4: Dissipation estimates over a tide

The measured dissipation of turbulent kinetic energy (TKE) at a height of 0.05 m over a tidal period on April 13th, 2003 follows a similar pattern as the horizontal component of TKE, as can be seen by comparing figure 4.9 (dissipation) with figure 4.7 (TKE). During the flood, dissipation of energy occurs at a rate of 10^{-4} m^2/s^3, which drops below 10^{-6} m^2/s^3during the slack and increases to 10^{-5} m^2/s^3 during the ebb. Note that the Trowbridge estimate diverges from the raw and hybrid estimate during the flood, perhaps because the Trowbridge method intrinsically measures an average between two locations while the others estimate dissipation at a point.

Dissipation scales as $\varepsilon \sim \frac{u_*^3}{\kappa z}$, while turbulent kinetic energy scales as the square of friction velocity. Thus, dissipation scales as $\varepsilon \sim \frac{{v_t}^2 u_*}{\kappa z}$. Typical values of $\frac{u_*}{\kappa z}$ are about ~0.1 (assuming friction velocity due to current is 0.01 m/s, and depth is 0.05-0.28 m). Therefore, dissipation should be about an order of magnitude less than the TKE estimate, which is consistent with measured values. Thus, the estimates of TKE and dissipation are self-consistent.

4.6. Comparisons of methods and error estimation

We use several strategies to compare the Trowbridge, Soulsby, and hybrid methods of calculating dissipation and TKE. First, we compare the total number of valid estimates found for each method, using the criteria that the slope of the best-fit line was between -0.9 and -2.4. We also compare the variance of the results for each calculation method, which gives an estimate of the relative error. Finally, the residual wave energy left by the hybrid and Trowbridge method gives an indication of how well differencing works at removing wave energy.

4.6.1 Number of valid points

Table 4.1 shows typical results for the number of 'valid' fits found by fitting a slope to a power spectrum to calculate TKE or dissipation. A valid fit occurs when the slope of the interpolated or best-fit line is close to the –5/3 slope in the turbulent cascade, i.e., -0.9 > slope > -2.4. Note that the power spectrum for the Soulsby method is found using the raw velocity U, while for the 'Trowbridge average' and 'hybrid' method the differenced velocities ΔU_k (Equation 4.11) and $v'(t)_{t,j}$ (Equation 4.13) are used.

The results clearly show that the "best fit extrapolation" method using the Soulsby method yields the smallest fraction of valid fits (0.34); in fact, the other methods yield valid estimates between 55% and 71% of the time. The "weighted interpolation" method clearly outperforms the "best fit extrapolation" method for both the Soulsby

method (0.70 vs. 0.34) and hybrid methods (0.70 vs. 0.55). The best-fit to the turbulent cascade is likely less accurate because high frequency wave energy or noise may be included in the frequency range used in the fit. On the other hand, the weighted interpolation method explicitly removes wave energy over the lower frequency (< 1 Hz) portion of the power spectrum, which is generally above the noise floor. This makes it less likely that the interpolation line is fit to the wave spectrum or the noise floor, and less invalid estimates occur.

Table 4.1: Fraction of valid estimates for each method of calculating dissipation and TKE. The number of valid points for each method is normalized by the total number of possible estimates for a representative immersed period on April 13th, 2003.

Estimate type	Soulsby best fit extrapolation	Hybrid best fit extrapolation	Hybrid weighted interpolation	Soulsby weighted interpolation	Trowbridge average method
Dissipation	0.34	0.55	0.70	0.70	0.71

4.6.2. Variance estimates

The variance in any data set consists of components due to error and natural variation in the signal. Any given data set X can be decomposed into mean ($\overline{X}$), fluctuating (x_s), and error components (x_e):

$$X = \overline{X} + x_s + x_e \qquad (4.19)$$

Applying the definition of variance, and assuming that error and natural variation are not correlated, we find that:

$$\sigma_x^2 = \sigma_s{}^2 + \sigma_e^2 \tag{4.20}$$

where σ_x^2 is the total variance in X, $\sigma_s{}^2$ is the variance due to the fluctuating component x_s, and σ_e^2 is the variance due to measurement error x_e.

From our estimates of dissipation and TKE, we estimate the total variance σ_x^2 for each of the different interpolation methods and spectrum types. Because the signal variance $\sigma_s{}^2$ is a property of the underlying physical process, it remains the same regardless of interpolation method or spectrum type. Therefore, variations in the total variance σ_x^2 reflect differences in the variance due to error (σ_e^2). Thus, the method with the least variance also has the least error.

Though the variance captures random noise in the signal, it cannot capture any persistent bias in the signal with zero variance. Therefore, one must check the magnitudes of the TKE and dissipation estimates and determine whether they (a) are consistent with each other and (b) are a reasonable magnitude given scaling estimates. Comparison of figure 4.7 and 4.8 shows that in general the TKE estimated using the Trowbridge, Soulsby, and hybrid methods are of a comparable order of magnitude,

though the Trowbridge method appears to be biased slightly lower. Similarly, the estimate of dissipation in figure 4.9 shows that all three methods of estimating dissipation are consistent with each other, with no persistent bias throughout the tide. Scaling estimates in show that the order of magnitude of the TKE intensity estimates are between 5-10 percent of the total mean and/or rms velocity. This is a reasonable estimate: larger would not make sense physically, while much lower would approach the noise floor of 10^{-6} m^2/s^2 . Similarly the estimates of dissipation are of a reasonable order of magnitude (see section 4.5.4).

4.6.2a. Variance in Dissipation Estimate

The variance in the dissipation estimate in Table 4.2 shows that the "weighted interpolation" method contains more error than the "best fit extrapolation" method. The most error is found in the raw, weighted interpolation, followed by the weighted interpolation over the hybrid spectrum. Overall, the hybrid best-fit extrapolation method has the least variance, followed by the Trowbridge method. All five methods contain >100 data points, and are a representative sample of natural variation; therefore, the differences in total variance reflect differences in measurement error.

Qualitatively, these results make sense. It is better to fit a line to the dissipative spectrum directly (as the best fit method extrapolation does) than to estimate its extent by interpolation over a wave peak (which the weighted interpolation method does). Moreover, because the turbulent, hybrid data set and the Trowbridge data sets have

removed much of the wave energy, it makes sense that there is less error associated with these methods than the Soulsby method. Finally, differencing (Equation 4.11 or 4.13) extends the frequency range in which the dissipative spectrum can be found, due to decreased wave peak and breadth. Therefore, it is possible to calculate significantly more valid fits above the noise floor.

Table 4.2: Relative variance of the different methods of estimating TKE and dissipation. The variance is taken on the log10 of data (to remove bias by outliers) for all velocimeters and all methods. The variance calculations are normalized by the method with the maximum variance for a particular velocimeter. Next, the normalized variance is averaged by method using the data from each velocimeter. Results from tide 5 for experiment #3 on April 13th, 2003.

Estimate type	Soulsby best fit extrapolation	Hybrid best fit extrapolation	Hybrid weighted interpolation	Soulsby weighted interpolation	Trowbridge average method
Dissipation	0.83	0.52	0.82	1.00	0.55
TKE-v	1.00	0.72	0.57	0.70	0.55

4.6.2b. Variance in Turbulent Kinetic Energy (TKE) estimate

In contrast to calculations of dissipation, the "weighted interpolation" method for calculating TKE results in less error than the "best fit interpolation" method (see table 4.2). The least error is seen using Trowbridge method and the hybrid using the weighted interpolation method (normalized variance of 0.55 and 0.57), while the most error is measured by the Soulsby method using the best fit extrapolation (normalized variance equal to unity).

Qualitatively, these results make sense; extrapolating over the wave peak based solely on data from one side of the peak is error prone, and leads to both over- and underestimates of the turbulent kinetic energy. Moreover, the slope of the turbulence spectrum becomes flatter at frequencies lower than the turbulent cascade; thus, extrapolating a line based on the slope in the dissipative region (turbulent cascade) will overestimate the TKE. Because the hybrid method and Trowbridge method remove much of the wave energy, it is easier to identify the minimum value on the low frequency side of the wave spectrum. Basically, there is less uncertainty that the minimum picked using the raw data is truly a minimum, and not a point between waves or an artifact of the technique used to calculate the spectrum.

4.6.3 Residual Wave Energy Comparison

In theory, both the hybrid method and the Trowbridge method separate all ocean swell and local wind waves from turbulent fluctuations. In practice, some residual wave energy remains due to experimental error and reduced correlation of high frequency waves between instruments. We quantify the residual wave energy by subtracting TKE from the total energy across the wind wave (1-3 Hz) and ocean swell (0.05-0.125 Hz) frequency band in a power spectrum. In other words the residual wave energy E_w is:

$$E_w = 2\int_{f_1}^{f_2}(S_M - S_L)df \qquad 4.21$$

where S_M is the measured power spectral density and S_L is the interpolated (or extrapolated) line using the Soulsby method. The variables f_1 and f_2 define the frequency range over which integration occurs, while the factor of '2' accounts for the symmetry in the power spectrum. Note that the interpolated (or extrapolated) line which defines TKE is set to zero at frequencies less than 0.1 Hz, based on scaling arguments that suggest turbulent eddies occur only at frequencies greater than 0.1 Hz (see section 4.4.1).

Equation 4.21 is applied to the power spectrums defined by the measured velocity and by the residual velocities from the Trowbridge and hybrid methods (equation 4.11 and 4.13).

Table 4.3 shows the residual ocean swell energy and wind wave energy left in the hybrid and Trowbridge spectrums for a representative tidal period. These results are an average over all data for that period, and are normalized by the total wave energy calculated using the measured velocity (Soulsby method). Thus, table 4.3 shows the fraction of wave energy that remains after differencing using equations 4.11 and 4.13.

Table 4.3: Mean ratio of residual energy to original energy in the wind wave (1-3 Hz) and ocean swell (0.05-0.125 Hz) frequency bands.

Wave type	Hybrid Method	Trowbridge
Local wind wave	0.09	0.10
Ocean swell	0.14	0.18

As seen in Table 4.3, the residual local wind wave energy for the hybrid and Trowbridge average methods are nearly identical, while the hybrid method removes slightly but not significantly more energy at the ocean swell frequency. Therefore, both methods give about the same answer.

4.6.4 Scaling of TKE to flow

To check that the estimates of TKE are reasonable and to gain insight into what drives turbulent motions and dissipation in this environment, we scale the turbulent kinetic energy to flow variables such as mean flow and the root-mean-square (rms) flow. For unidirectional, steady currents in open channel flow, Nezu and Nakagawa (1993) report that the horizontal, stream-wise component of TKE scales as the square of friction velocity over smooth beds:

$$\overline{v_{tx}^{\,2}} = 5.3u^{*2}\exp(-2z/H) \qquad (4.22)$$

where H is the total depth of the flow and $\overline{v_{tx}^{\,2}}$ is the horizontal component of TKE. The factor of 5.3 is an empirical constant derived from laboratory experiments. The definition of the log profile (equation 4.6) is now used to determine an equation for the friction velocity, which is substituted into equation 4.22. The turbulence intensity (defined as the square root of mean TKE) is then expressed as follows:

$$v_{tx} = \frac{2.3\kappa U \exp(-z/H)}{\ln(\frac{z}{z_o})} \qquad (4.23)$$

Thus, for any given height 'z' above the bed, turbulent intensity scales as a proportion of the mean velocity for open channel flow. Figure 4.10 shows a comparison between the ratio of $\frac{v_{tx}}{U}$ predicted by equation 4.23 and the ratio of $\frac{v_{tx}}{U}$ measured using the hybrid method. A mean depth of H= 1 m is used in equation 4.23, and roughly corresponds to the median depth of the results from the hybrid method (range from 0.5 m to 1.5 m). The horizontal component of TKE intensity for all 6 velocimeters in experiment #3 over the immersed period on April 13th, 2003 is used. The turbulent intensity is normalized by using the 1 minute mean velocity measured throughout the immersed period at each particular height above the bed. Note that outliers in the measured distribution have been removed and that the Soulsby method is used for the measurement at 0.015 m because the hybrid method is not valid at that height. The Trowbridge method is not depicted because it estimates an average between instruments.

As seen in figure 4.10, the ratio of $\frac{v_{tx}}{U}$ predicted by Nezu-Nakagawa for open channel flow with a depth of 1 m exceeds the measured ratio, with the exception of the upper two velocimeters. Though the standard deviation is large, the measured order of magnitude of the turbulent intensity varies between 11-14 percent of the total mean velocity (1 minute mean), indicating that a large portion of the energy due to the mean

current and wave fluctuations has been removed. Note that the TKE intensity also appears to scale well with the rms velocity (including all waves and currents), with a ratio that varies between 5-10 percent with a standard deviation of 2-5 percent. In fact, visually the profile of TKE (figure 4.6) closely follows the evolution of wind wave energy (see figure 3.11, top panel), suggesting that either (1) the rms velocity helps set the turbulence profile or (2) that residual wave energy is included in the estimate of TKE. However, the profile suggested by Nezu and Nakagawa predicts large turbulent intensities as the bed is approached. Thus, if anything, the turbulent intensities are under-predicted by the methods applied in this chapter, confirming that most wave energy is removed.

The difference between the predicted ratio of $\frac{v_{tx}}{U}$ and the measured ratio of $\frac{v_{tx}}{U}$ may be explained by unsteadiness in the boundary layer, for example from the seiching motion or the acceleration and deceleration of the tides. Therefore, a well developed vertical profile never develops, but rather the profile exhibits a large variance (see large standard deviation shown in figure 4.10). Moreover, other processes such as wind stress, white capping by waves and the interaction between waves and currents may push the boundary layer away from idealized open channel conditions.

4.6.5. Summary of error analysis and method performance

The error analysis presented in section 4.6 compares the line-fitting techniques used with the Soulsby method (interpolation vs. extrapolation) as well as the efficacy of three

different methods for calculating TKE and dissipation—the Soulsby, Trowbridge, and hybrid methods. Overall, interpolation is better at estimating TKE, while extrapolation is better at estimating dissipation (table 4.2). In general, however, interpolation yields a larger number of valid fits (table 4.l).

The hybrid method and the Trowbridge method of calculating TKE and dissipation have approximately the same variance (see Table 4.2), indicating similar levels of error. In addition, they exhibit virtually the same residual wave energy (Table 4.3), indicating they are equally effective at removing wave energy from the measured velocity. This is perhaps not surprising, since the hybrid method reduces to the Trowbridge method when only two instruments are used. However, by using many measurement locations, the hybrid method in theory reduces the effect of error produced at a particular measurement location. Practically, however, our experimental setup allowed only 5 instruments to be used in the spatial average; moreover, measurement discrepancies between the side-mounted instruments and the downwards facing instruments introduced error into the measurements (see Chapter 2). Therefore, the Trowbridge and hybrid method show comparable levels of error.

Overall, the Soulsby method has the most variance and is the most error-prone (Table 4.2). Because they reduce the size of the wave peak in the power spectrum, the Trowbridge and hybrid methods result in less overall variance and error. Though there is no direct way of quantifying bias, all estimates of TKE and dissipation are self consistent and of a reasonable magnitude. Overall, though, the ratio of turbulent

intensity to mean velocity ($\frac{v_{tx}}{U}$) measured using the hybrid method is less than the ratio predicted from open channel flow results. This suggests either that TKE is underpredicted, or that the velocity U is greater than in the well developed open channel flow case.

4.7. Conclusions

In this chapter, three different methods of calculating TKE and dissipation in the presence of waves are presented, and compared using field data collected in experiment #3. While the Soulsby method is conceptually simple and requires fewer theoretical assumptions than the Trowbridge or hybrid methods, results show that this method is more prone to error in a shallow water environment. This is because the interpolation scheme of the Soulsby method is somewhat arbitrary. However, the presence of multiple frequencies of waves means that both the Trowbridge and hybrid methods retain some residual high frequency wave energy. Obtaining measurements close to each other reduces wave decorrelation, but runs the risk that turbulent eddies are correlated. As a practical matter, the residual high frequency wave peak is easily removed using the Soulsby method. Because the residual wave peak found in Trowbridge and hybrid spectrum is not as large as the raw velocity spectrum, less error is generated when removing it. Note that the Trowbridge and hybrid methods are conceptually similar; in the limit of two measurement locations, they are equivalent.

Results over a tidal period show that TKE and energy dissipation follow a trend that is similar to both the mean current and to the overall energy climate. TKE and dissipation are smallest during the slack tide, when the mean tidal current and the orbital velocities of near bed wave motions are smallest. During a flood tide with large wind waves, the 10 minute mean TKE and dissipation are two orders of magnitude larger, while during an ebb tide with large ocean swell TKE and dissipation are increased by an order of magnitude. This indicates that the magnitude of fluid friction on the bed—as measured by the production and dissipation of turbulent energy—varies by several orders of magnitude over the time scale of a tide. Overall, the ratio of turbulent intensity to mean velocity is relatively constant between heights of 0.015 m and 0.33 m off the bed, in contrast to steady state, open channel flow conditions which show a large increase in the same ratio near the bed. Large scatter is observed in the TKE and dissipation estimates. While measurement and calculation errors play a role in the large variance, the results presented in this chapter suggest that the underlying variation in the flow conditions (e.g., wind waves, ocean swell, seiching, and tidal currents) push levels of TKE away from steady state values. Clearly the highly variable levels of the production and dissipation of TKE —both on tidal time scales and on smaller time scales—must interact with waves, seiching motion, and tidal currents to create highly variable boundary layers. In the next chapter we use analytical and numerical models, as well as experimental results, to investigate the structure of velocity in the boundary layers. Moreover, we also explore the non-linear interaction that occurs between waves and currents in the wave boundary layer. The accurate description of how velocity varies in

the boundary layers of waves and currents gives another indication—in addition to TKE and dissipation—of how the hydrodynamics forcing interacts with the bed.

4.8. Figures

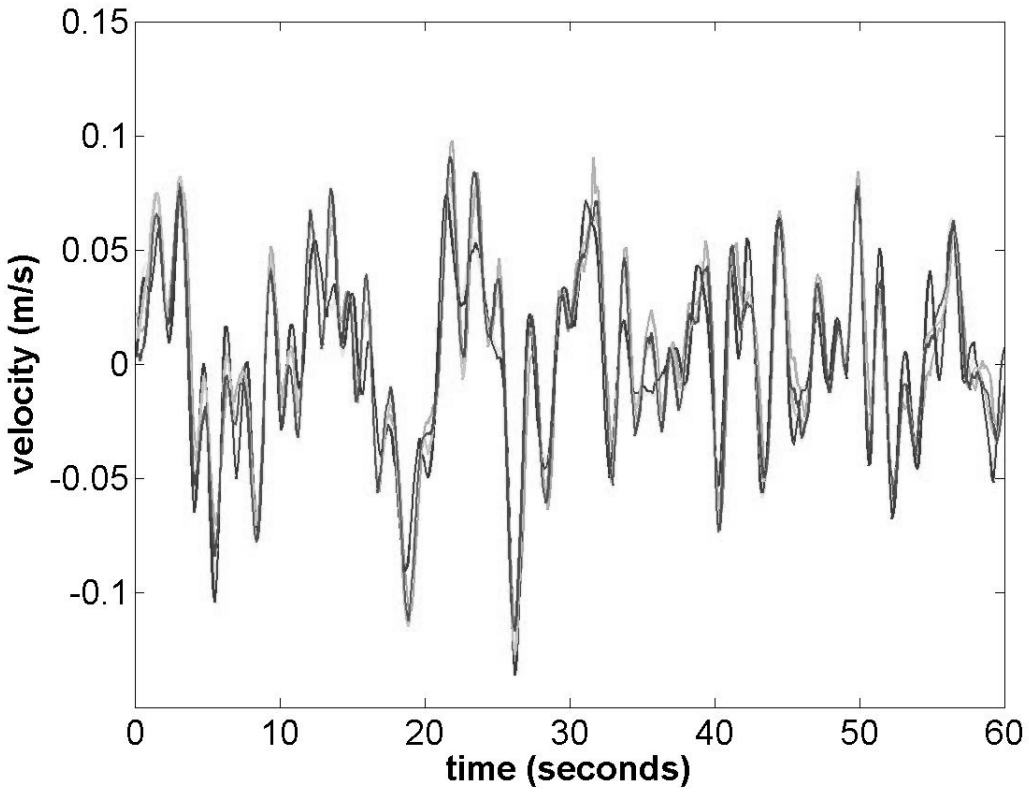

Figure 4.1: Velocities of five velocimeters during an immersed period beginning at 6:40 p.m. on April 13th, 2003 (experiment #3) overlaid on one another; x-axis is time (seconds), y-axis is velocity (m/s). The 60 second data set was logged at 9:20 p.m. The individual data sets have been shifted by 0-5 seconds so that correlation is maximized.

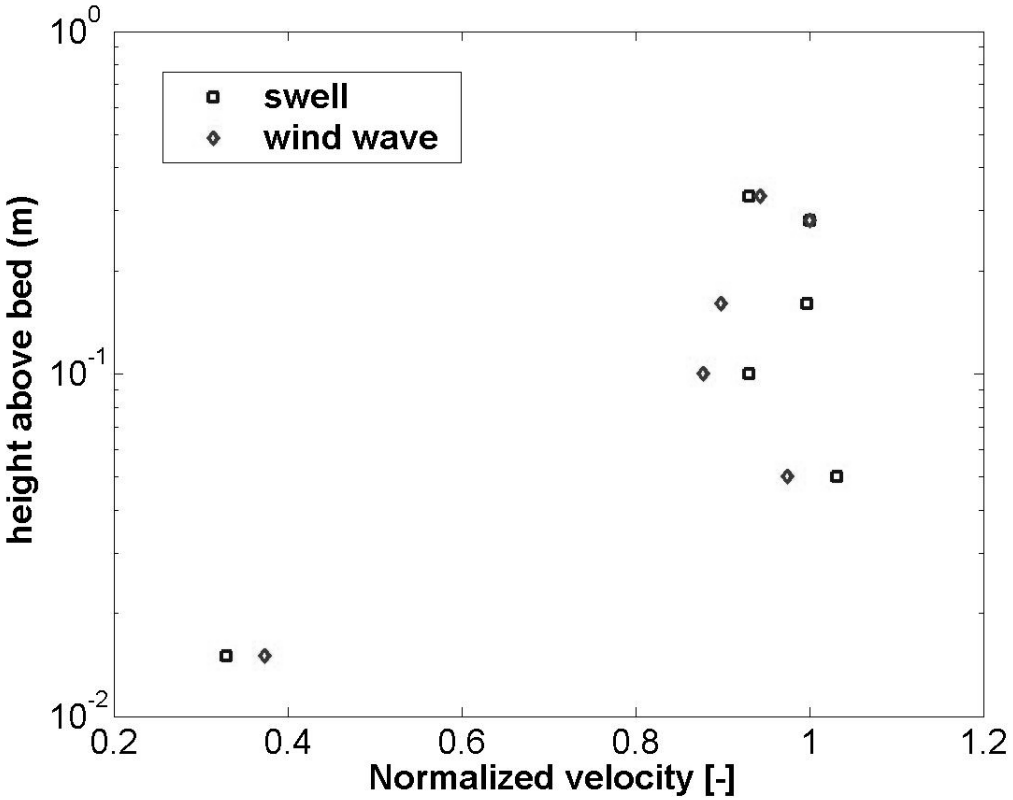

Figure 4.2: Normalized rms orbital velocity of ocean swell and wind wave vs. height above bed (m) for an immersed period beginning at 6:40 p.m. on April 13th, 2003. Note that the velocity is normalized by the rms orbital velocity at 0.285 m. Wave motions are separated from the measured signal by bandpass filtering with a buttersworth filter. Ocean swell is bandpassed between 8-20 seconds, while wind waves are bandpassed between 1-4 seconds.

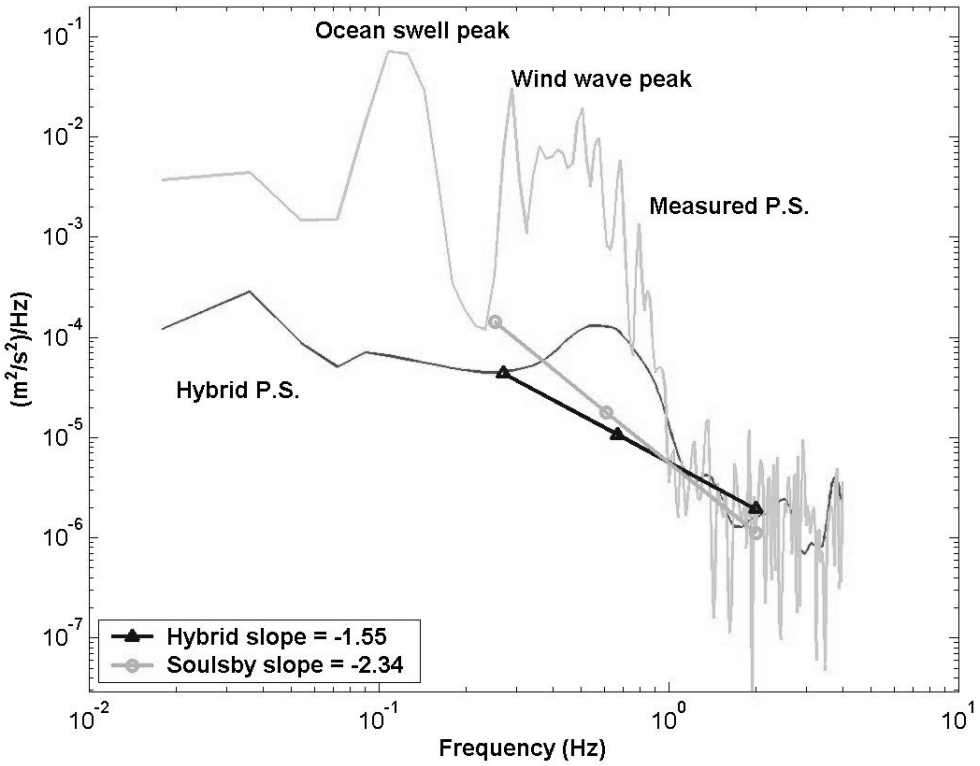

Figure 4.3: Comparison of interpolating a line across the wind wave peak for power spectrums calculated using measured velocity data (light-colored, labeled "Measured P. S.") and the residual, differenced velocity from equation 4.13 (dark colored, labeled "Hybrid P.S."). Velocity data is measured at 0.155 m at 9:20 p.m. on April 13th, 2003 (tide 5). The light-colored line with circle symbols is a weighted interpolation across the wave peak of the measured power spectrum, while the dark colored line with triangle symbols is a weighted interpolation across the hybrid power spectrum. The slopes of the respective interpolations are given by the legend. P.S. = Power Spectrum.

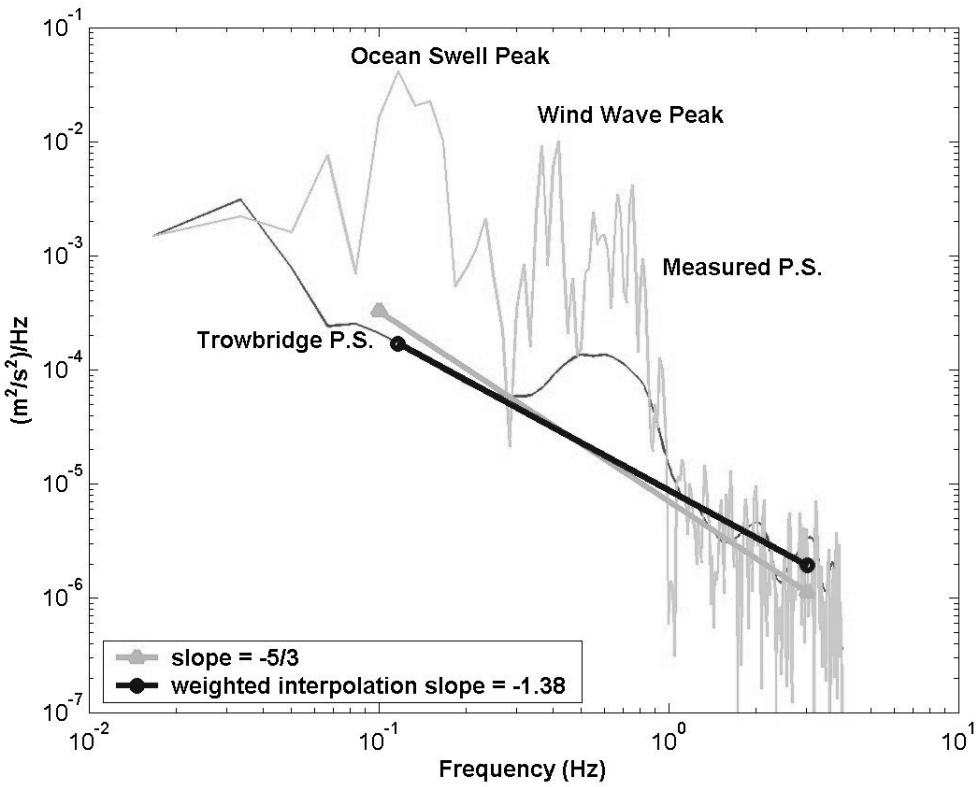

Figure 4.4: Comparison of a power spectrum calculated using the measured velocity at 0.155 m for a 1 minute time segment at 9:23 pm on April 13th, 2003 (labeled 'Measured P.S.') and a power spectrum calculated using a residual turbulent velocity (equation 4.11) calculated with the Trowbridge method (labeled 'Trowbridge P.S.'). For comparison, a weighted interpolation (light colored lines with triangle symbols) and a slope of -5/3 (dark colored line with circle symbols) are fit to the Trowbridge power spectrum, which was constructed from the difference of 1 minute velocity measurements at 0.05 m and 0.155 m. The Trowbridge power spectrum is smoothed using a wavelet filter.

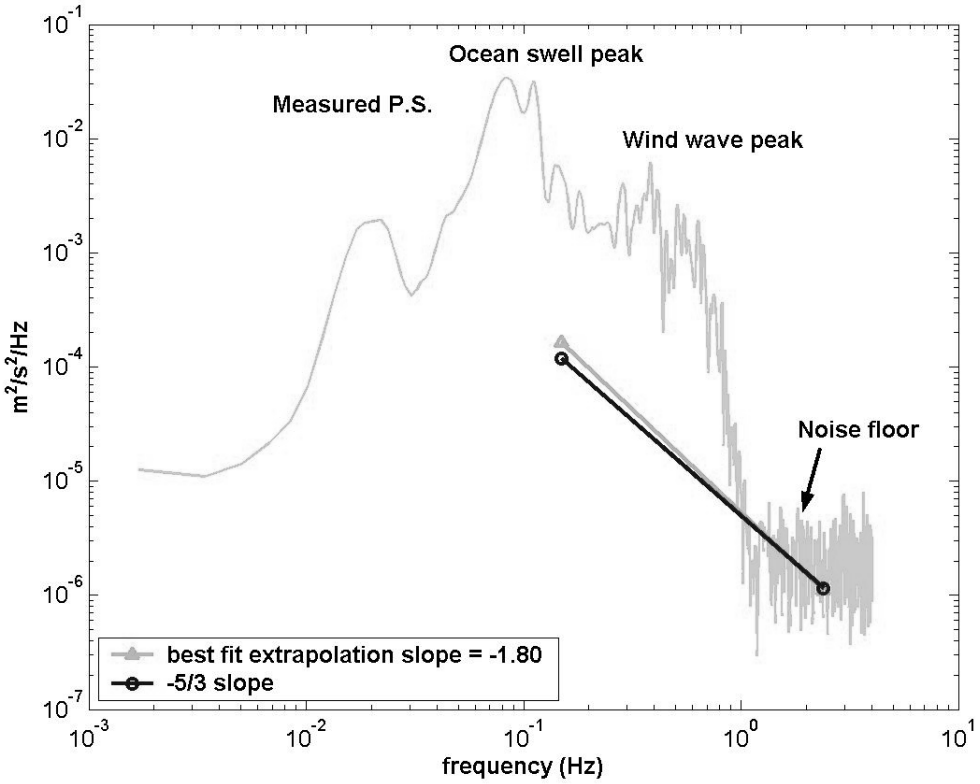

Figure 4.5: Best fit extrapolation method applied to a power spectrum (labeled 'Measured P.S.') calculated using a 1 minute segment of velocity measured at 10:13 p.m. on April 13th, 2003 during a flood tide at a height of 0.285 m. For comparison, a slope of -5/3 (dark colored line with circle symbols) is fit to the same frequency range (1-2 Hz) as the best fit extrapolation line (light colored line with triangle symbols). Note that the noise floor and the wind wave peak intersect near a frequency of 1 Hz.

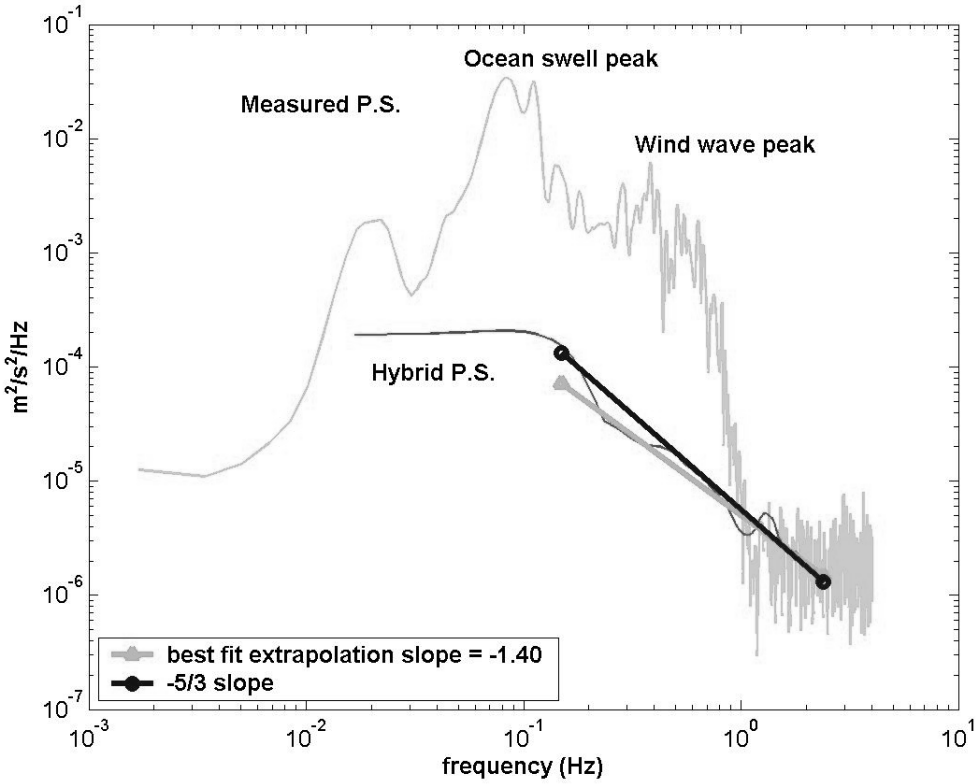

Figure 4.6: Best fit extrapolation method applied to a power spectrum (labeled 'Hybrid P.S.') calculated using a 1 minute segment of residual velocity calculated using the hybrid method (equation 4.13). The data were measured at 10:13 p.m. on April 13th, 2003 during a flood tide at a height of 0.285 m. For comparison, a slope of -5/3 (dark colored line with circle symbols) is fit to the same frequency range (1-2 Hz) as the best fit extrapolation line (light colored line with triangle symbols). The power spectrum from measured data is also shown (see figure 4.5). The hybrid spectrum has been smoothed using a wavelet filter.

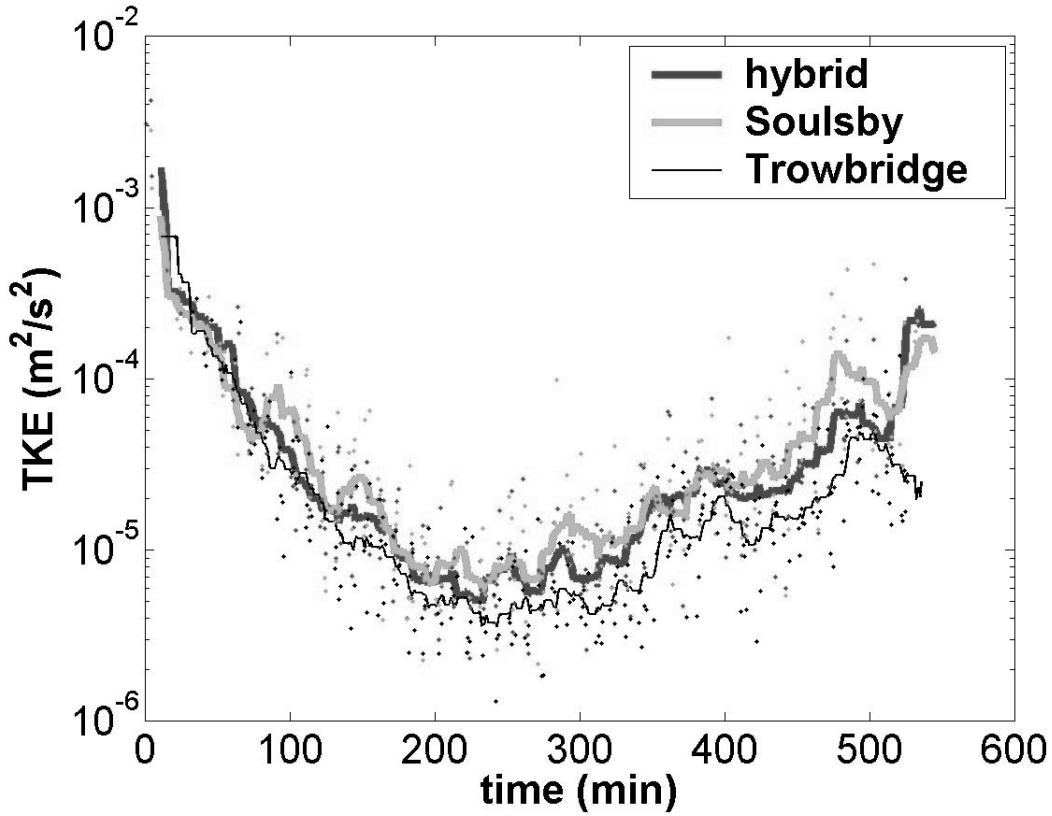

Figure 4.7: The stream-wise component of TKE during an immersed period beginning at 6:40 p.m. on April 13th, 2003, at a height of 0.05 m off the bed, estimated using the different calculation methods. The weighted interpolation method is used to remove residual wave energy for the Soulsby method, the hybrid method, and the Trowbridge method. Individual estimates calculated over 1 minute segments are shown as dots, while the solid lines denote 10 minute moving averages.

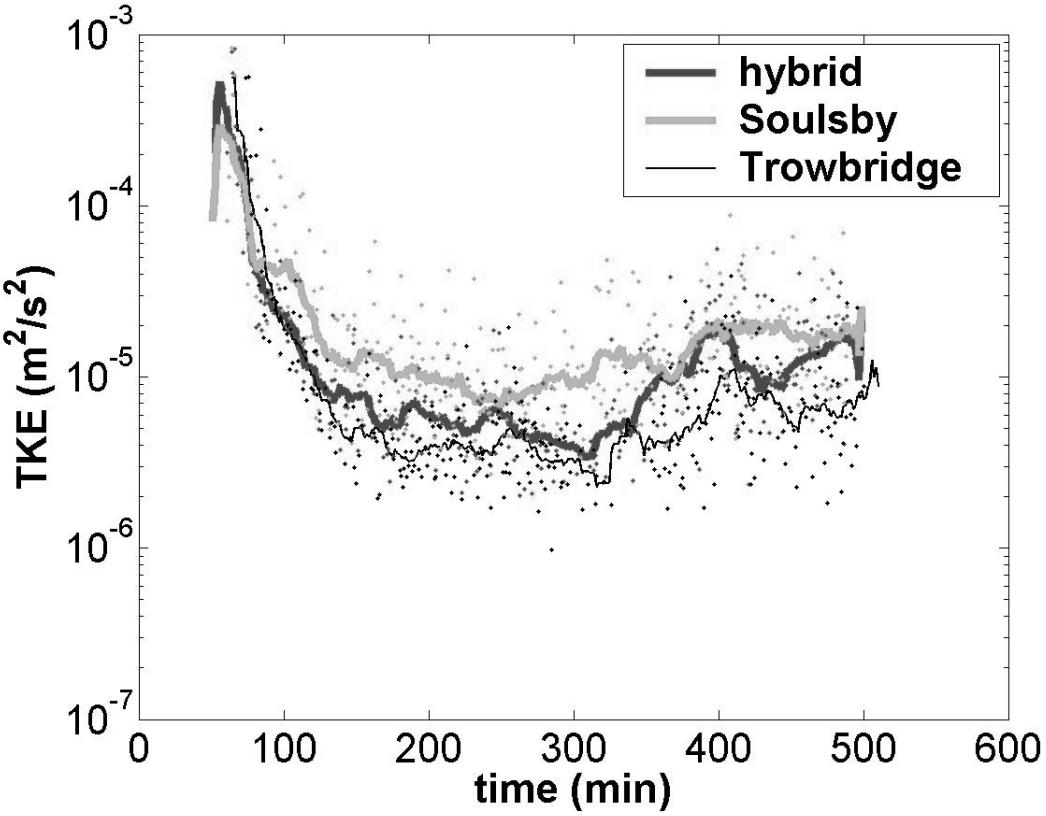

Figure 4.8: The stream-wise component of TKE during an immersed period beginning at 6:40 p.m. on April 13th, 2003, at a height of 0.285 m, estimated using the different calculation methods. The weighted interpolation method is used to remove residual wave energy for the Soulsby method, the hybrid method, and the Trowbridge method. Individual estimates calculated over 1 minute segments are shown as dots, while the solid lines denote 10 minute moving averages.

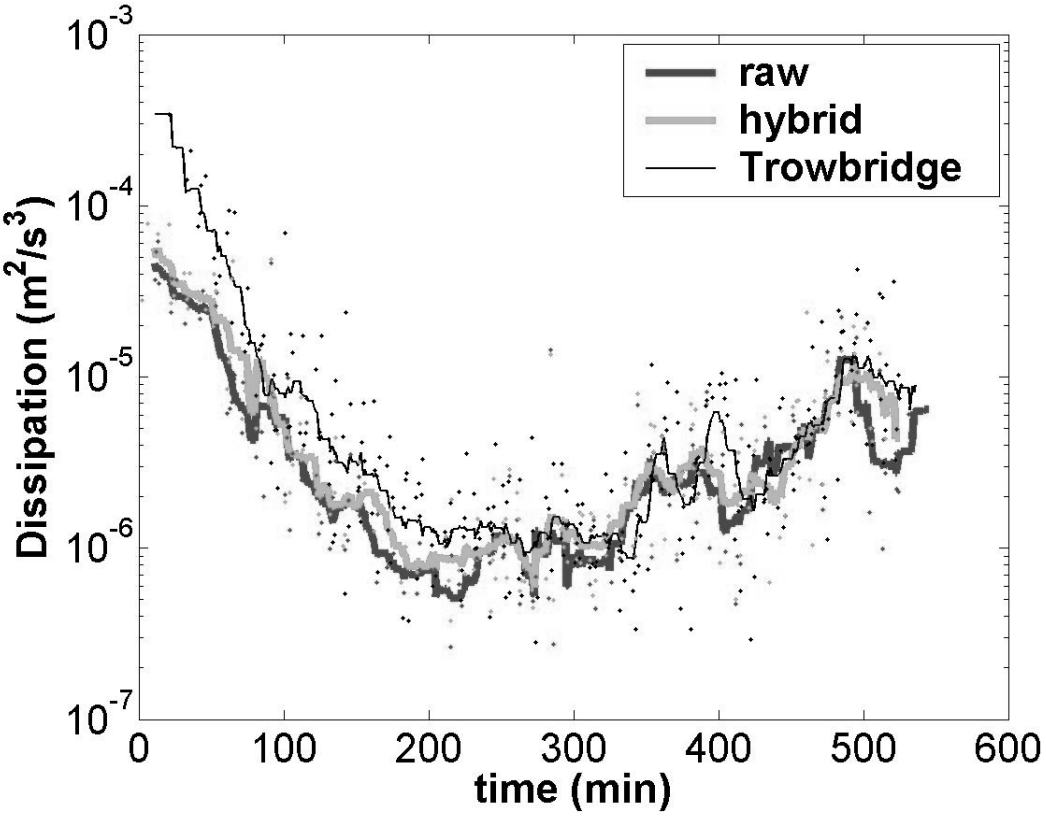

Figure 4.9: Dissipation measured over an immersed period beginning at 6:40 p.m. on April 13th, 2003 at a height of 0.05 m off the bed using the measured spectrum and the spectrums calculated using the residual Trowbridge and hybrid turbulent velocities (Eqn. 4.11 and 4.13). The solid lines are 10 minute moving averages of the calculated dissipation, which was calculated in 1 minute segments and is shown as individual points.

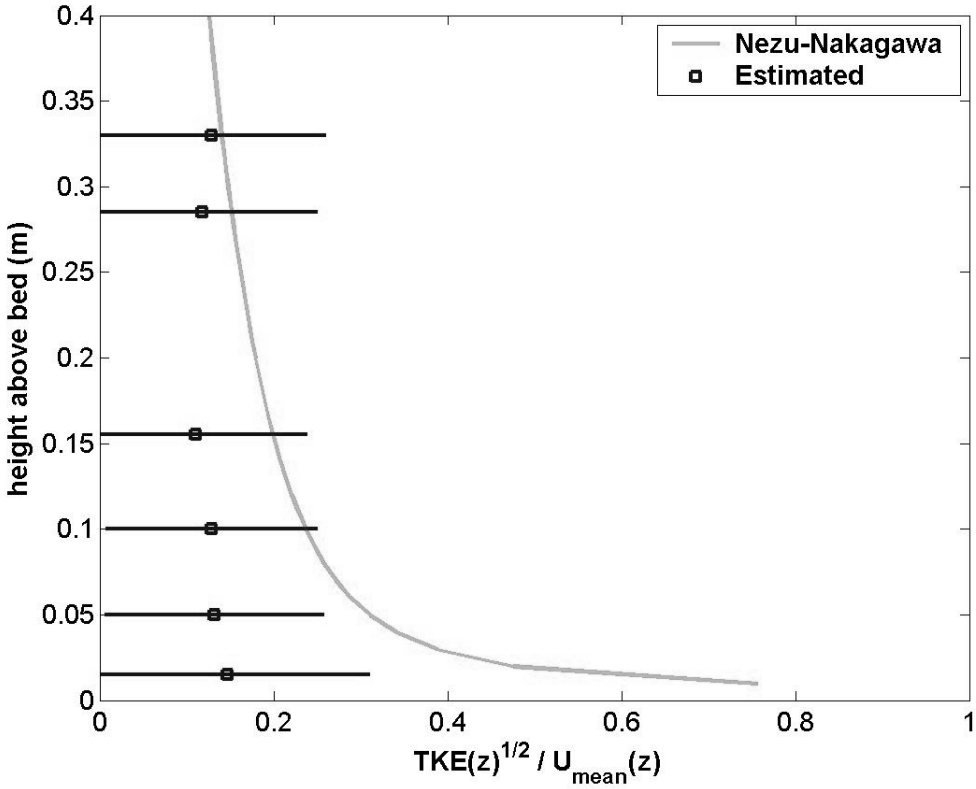

Figure 4.10: The ratio of the turbulent intensity in the stream-wise direction to the mean flow, calculated using the hybrid method and estimated using the relation of Nezu and Nakagawa, 1993. Error bars indicate standard deviation, and show large scatter in the data. However, the order of magnitude of the ratio is reasonable above 0.1 m. Nezu and Nakagawa (1993) assume steady, fully developed open channel flow, whereas the boundary layer at the mudflat is unsteady and developing. Note that the estimated ratio at 0.015 m (lowest data point) is estimated using the Soulsby method; all other data is estimated using the hybrid method.

Chapter 5: Wave and Current Boundary Layers

5.1. Introduction

As described in previous chapters, multiple frequencies of motion occur on an intertidal flat, including tidal currents, seiching motions, ocean swell, and wind waves. These motions produce turbulent motions and stress at the bed, which can be estimated using statistically based methods (as shown in chapter 4). The turbulent eddies bring slower, near bed flow up into the water column, causing water motion to slow and forming a characteristic velocity profile, or boundary layer. However, because of constantly changing conditions at all frequencies of motion, Chapters 3 and 4 suggest that steady state conditions of both forcing and TKE are likely not the norm. Therefore the boundary layer structure is likely to be complex, variable in both space and time. The objective of this chapter is to characterize the boundary layer of velocity—and the resulting bed stresses—in the intertidal zone at various timescales that correspond with the different forcing mechanisms. Moreover, nonlinear interaction between waves and current in the boundary layer is also investigated.

In hydrodynamic flows, the boundary layer is often modeled as either a steady current or as an unsteady wave. Steady flow is often modeled as a logarithmic profile, while slight deviations are modeled as a log-linear profile (see e.g. Soulsby and Dyer, 1981; Kawanisi, 2004). To estimate a wave boundary layer, the momentum equation is solved using various assumptions for pressure and eddy viscosity (see review by Sleath, 1990).

Near the bed, however, many models for wave boundary layers reduce to the logarithmic velocity profile; in fact, some wave formulations explicitly leave a logarithmic term in the equation (see Sleath, 1984). Moreover, in the free stream above the current boundary layer, flow also deviates from logarithmic (see e.g. Mathisen and Madsen, 1996). Thus, while generally treated separately, wave boundary layers and current boundary layers have some of the same theoretical underpinnings.

Shallow water is subject to a variety of forces that affect the vertical structure of the boundary layer. For example, Collins et al. (1998) points out that wind stress, wave motions, secondary flows, and unsteadiness caused by rotary flow can distort the logarithmic profile of velocity. Similarly, stratification and acceleration in the flow also distort the boundary layer structure, often within the same tidal period (Kawanisi et al., 2004). In addition, the non-linear interaction of waves and currents in the wave boundary layer alters the slope of the logarithmic profile and results in a greater dissipation of energy (Grant and Madsen, 1979, Soulsby et al., 1993). Similarly, the current also affects the wave boundary layer. Thus, the wide variety of forcing and interaction—from both the top and bottom boundary layer—makes the water column in shallow water very complex.

This chapter is organized as follows. First, the boundary layer structure of the mean velocity is investigated by fitting log and log-linear profiles to the measured data over a tidal cycle. We attempt to explain deviations from the logarithmic profile using length scales derived from acceleration and stratification. Next, the stress applied by the mean

currents on the bottom boundary is investigated, and compared to the results of a non-linear wave-current interaction model (Grant and Madsen, 1986). The roughness height and the maximum stress from waves are also investigated. Finally, the boundary layers for the seiche and ocean swell frequencies are isolated and modeled using an analytical model (Smith, 1977); in addition, the seiche is modeled using a numerical model (General Ocean Turbulence Model, GOTM).

5.2. Current Boundary Layer

In this section we describe the theory of current boundary layers and present experimental results.

5.2.1. Theory on current boundary layers

Assuming steady, uniform, unstratified flow and a linearly increasing eddy viscosity above the bottom, dimensional analysis shows that the vertical velocity profile depends on the friction velocity u_* and the roughness z_0 . Given two or more measurements of horizontal velocity at different depths, a simple linear regression in log space is used to estimate u_* and z_0:

$$U(z) = \frac{u_*}{\kappa} \ln(\frac{z}{z_0}), \qquad (5.1)$$

where κ= von Karman's constant. Typically, the value of κ is equal to 0.41. Many intertidal studies assume a log-profile (e.g. Whitehouse et al., 2000, Van der Lee, 1998).

In unsteady or stratified flow conditions, the velocity profile with depth deviates from equation 5.1. The effects of stratification or acceleration are often modeled by adding a linear term to the log profile:

$$U(z) = \frac{u_*}{\kappa}(\ln(\frac{z}{z_0}) - \frac{(z - z_0)}{L}) \qquad (5.2)$$

where L is a length scale that essentially introduces curvature into the standard log profile, as is shown in figure 5.1. When the lengthscale 'L' is positive, velocity is reduced by a linear factor; by contrast, a negative 'L' results in velocities that exceed the logarithmic velocity profile. Known as the log-linear model, equation 5.2 contains three unknown parameters when velocity measurements are known for at least three different heights: the friction velocity u_*, the roughness height z_0, and the lengthscale 'L'. An optimization routine calculates $U_{calc}(z)$ for the measurement heights 'z' and different sets of the parameters u_*, z_0 , and L. An optimized set of parameters is found by minimizing the least squares error between the measured velocity $U_{meas}(z)$ and the calculated velocity $U_{calc}(z)$. To obtain a statistically meaningful log-linear fit, the optimized least squares fit is only applied during times in which there are four valid measurements. Therefore, there are fewer log-linear estimates over a tide than simple logarithmic fits.

The optimized length scale L can then be compared to semi-empirical length scales developed for the log-linear equation from stratified and accelerating flows. For accelerating flows, Soulsby and Dyer (1981) define an acceleration length scale using the friction velocity u_* and its acceleration $\dot{u}_*$:

$$L = L_{acc} = \frac{\gamma u_* \mid u_* \mid}{\dot{u}_*} \tag{5.3}$$

where γ is an empirical constant derived from the data of Soulsby and Dyer (1981) and equal to 0.04. In an accelerating flow, the upper velocity is decreased relative to the log-profile, while in decelerating flows the velocity is increased relative to the log-profile. Soulsby and Dyer (1981) show that the change in friction velocity due to acceleration propagates up into the boundary layer in a finite amount of time. This time delay shows up as curvature in the log profile, with points higher in the boundary layer adjusting to a past friction velocity with a time lag

$$\Delta t = \frac{z}{\gamma u_*}. \tag{5.4}$$

For stratification, Monin and Obhukov (1954) (see Turner, J.S., 1973) show that the length scale L in equation 5.2 can be modeled as a ratio of the production of turbulence and buoyancy flux B:

$$L_{strat} = \frac{u_*^3}{\alpha \kappa B} = \frac{L_{mo}}{\alpha} \tag{5.5}$$

where α is a scalar constant equal to ~ 5.5 and $L_{mo} = \frac{u_*^3}{\kappa B}$ is the Monin-Obukhov length scale and B is the buoyancy flux and is defined below. Note that the sign of equation 5.5 is opposite of convention in order to be consistent with the definition of the log-linear profile (eqn. 5.2); thus, a negative length scale indicates stable stratification, while a positive length scale indicates unstable stratification. In stratified conditions, flow is increased relative to the logarithmic profile, as turbulence is damped by buoyancy. The buoyancy flux is defined as a function of gravity g, density of water ρ_0, and turbulent mass transport $\overline{\rho' w'}$ (where ρ' and w' are the fluctuation of density and vertical velocity from their respective mean values) :

$$B = -\frac{g}{\rho_o} \overline{\rho' w'} \tag{5.6}$$

In experiment #3, density is measured no more than once a minute and vertical velocity measurements are unreliable (see chapter 2). Thus, the quantity $\overline{\rho' w'}$ is not easily calculated directly. However, it can be parameterized as:

$$\overline{\rho' w'} = -K_\rho \frac{d\overline{\rho}}{dz} \tag{5.7}$$

where K_ρ is the mixing coefficient of mass and $\frac{d\bar{\rho}}{dz}$ is the vertical density gradient.

In practice, K_ρ is of the same order of magnitude as the mixing coefficient for momentum ν_T (eddy viscosity). The mixing coefficient for momentum is approximated analogously to the mixing coefficient for mass:

$$\nu_T = -\frac{\overline{u'w'}}{\frac{d\bar{u}}{dz}} \tag{5.8}$$

In fully developed channel flow, the Reynolds stress varies as a function of height (Nezu and Nakagawa, 1993). However, a developing boundary layer exhibits a region of constant stress (see e.g. Soulsby, 1983). Assuming a constant stress layer in the seiche and swell boundary layers considered in this chapter, the Reynolds stress can be estimated as $\overline{u'w'} = u_*^2$. Essentially, this is similar to the assumption that Soulsby (1983) makes in relating TKE to bed stress (equation 4.9). Moreover, the velocity gradient $\frac{d\bar{u}}{dz}$ can be estimated using either the log equation or the log-linear equation (Equation 5.1 and 5.2). Assuming that $K_\rho \sim \nu_T$ and using the definition of the buoyancy frequency N^2, one can parameterize the buoyancy flux and the stratification length scale as follows:

$$N^2 = \frac{-g}{\rho_o}\frac{d\rho}{dz} \tag{5.9}$$

$$B = K_p N^2 \tag{5.10}$$

$$L_{strat} = \frac{u_* \frac{d\bar{u}}{dz}}{\alpha \kappa N^2} \tag{5.11}$$

Because there are only three density measurements in experiment #3, the density gradient is approximated as linear in the lower 0.5 m, and the buoyancy frequency varies only in time. The quantity $\frac{d\bar{u}}{dz}$ is a function of height above the bed, z. To obtain a constant value of L_{strat}, we therefore calculate $\frac{d\bar{u}}{dz}$ near the midpoint of the seiche boundary layer (i.e., at 0.155 m).

Note that in estuarine conditions, periodic stratification often occurs due to the differential advection of fresh water over denser sea water (Simpson et al., 1990). In addition to strain induced salinity stratification, the Monin-Obhukov length scale L has also been modeled for suspended sediment induced stratification by (Soulsbyand Wainright, 1987; see also Winterwerp, 2001).

5.2.2: Results: Logarithmic vs. Log-linear

The mean profile of current that occurs on the intertidal mudflat typically varies between linear in log space (eqn. 5.1) and log-linear (eqn. 5.2). Figures 5.2 and 5.3 show the velocity profile in the water column as it varies over a five minute period for

two measurement bursts separated by 30 minutes during the flooding tide on April 13th, 2003. In addition, the least squares fit of the log-profile (eqn. 5.1) and the least squares optimization of the log-linear profile (eqn. 5.2) are shown in each of 15 panels separated by increments of 20 seconds. A panel without a log-fit or log-linear fit indicates that the fit failed, usually due to differing signs in the water column as the boundary layer collapses and changes directions. Note that the mean velocity is calculated using wavelet decomposition, which results in a smoothly varying mean profile that is approximately equivalent to a 60 second moving average (see Ch. 2 for description of wavelets).

In figure 5.2, the log-profile and the log-linear profile are approximately the same, though some curvature is introduced into the profile between 230 and 310 seconds; this coincides with an acceleration from ~ 0.02 m/s to ~ 0.07 m/s at a height of 0.28 m over the bed. Interestingly, the deceleration between 0 and 200 seconds introduces little curvature into the vertical profile of velocity. On the other hand, the velocity profile in figure 5.3 shows persistent curvature over the entire time period. The evolution from positive to negative current shows the boundary layer breaking down and being reformed, but causes little variation in the underlying curvature. As such, the log-linear profile clearly represents the measured data better than the simple log-fit in figure 5.3.

The patterns that these examples show—periods in which the vertical profile is linear in log space alternating with periods in which the log-linear profile dominates—persists throughout the period of inundation. The likely cause is the seiching motion and other

variations in the mean tidal current (see Chapter 3), which cause the boundary layer for current to alternate between developing and well developed. During times when the variation due to the seiche exceeds the mean tidal current, it appears that simple log profiles do not occur. For example, in figure 5.3 the seiche frequency has an amplitude of ~ 0.05 m/s (see bottom panel in 5.3b), and clearly dominates over the flood velocity of 0.006 m/s (non-fluctuating velocity component in the bottom panel of 5.3b) . Thus, the profiles are marked by large curvature. On the other hand, in figure 5.2 the seiching motion (with a velocity of ~ 0.025 m/s) simply modulates the flood current (with a velocity of ~0.05 m/s) and an approximately log profile develops. Indeed, for the immersed period beginning during the evening of April 13th, 2003, about 80 percent of the log profiles with negligible curvature (L> 1 m) occurred when the seiche velocity was less than 50 percent of the mean current. Under these conditions, the well-developed tidal boundary dominates over the seiche boundary layer and a logarithmic profile can occur.

As shown in figure 5.4a, however, the measured length-scale 'L' only rarely exceeds 1 m over an immersed period; instead, most of the values of this length scale are banded between 0.1 m and 0.5 m, indicating that a log-linear profile is the dominant feature throughout a tidal period. Note that the sign of the log-linear profile is always positive, indicating that the curvature is always in the direction of acceleration or unstable stratification (see figure 5.1). It is clear that the intertidal boundary layer is more complex than implied by the simple logarithmic boundary layer. In other intertidal environments, the canonical logarithmic velocity profile occurs only intermittently as

well; for example, Collins et al. (1998) found that only 22 percent of profiles are actually logarithmic. Similarly, using the criteria that the length scale 'L' in the log-linear profile be greater than 1 m, only 22 percent of velocity profiles could be considered logarithmic during the immersed period on April 13th, 2003. As Kuo et al. (1996) point out, acceleration, stratification, and suppression of the constant stress layer conspire to reduce the validity of using the log-profile. Moreover, Collins (1998) points out that rotary flow, wind action, wave activity and secondary flows from channel flow can alter the boundary layer profile. Another potential reason is non-uniform bed roughness upstream of the experiment (see e.g. Chris and Caldwell, 1982). At the Richmond mudflat, variation from the simple model may occur because assumptions such as a constant stress layer and well-developed conditions break down when there are multiple forcing frequencies occurring on different time scales.

5.2.3: Modeling the log-linear profile using acceleration

Using equation 5.2, an acceleration length scale is constructed and displayed in figure 5.4.b. Unfortunately, the acceleration length scale L_{acc} poorly represents the observed length scale L (see figure 5.4a). The acceleration length scale varies between ~ 1 mm and 1 m; moreover, the length scale alternates between positive and negative throughout the period of inundation. This is consistent with a boundary layer that both accelerates and decelerates (see figure 5.1). Therefore, the order of magnitude and the sign of L_{acc} agree only intermittently with the measured, positive length scale L. Note that L_{acc} was calculated using the friction velocity calculated using the Grant-Madsen wave-current

interaction model (1979; see section 5.3 for more information). Because the seiching motion dominates local acceleration and deceleration, the acceleration length scale varies from positive to negative over a seiche wave-cycle. This can be seen in figure 5.5, which shows all three calculated length scales (L, $L_{acc,}$ and L_{strat} , which is discussed below) as well as the local mean velocity over a 40 minute time scale that coincides with figure 5.2 (130-135 minutes) and figure 5.3 (160-165 minutes). The mean velocity is greatly modulated by the seiche frequency. During decelerating phases of the mean velocity, L_{acc} is negative, while during accelerating flow L_{acc} is positive. By contrast, the length scale L is always positive, and varies between log-linear (which occurs approximately for L < 0.5 m) and logarithmic (L >0.5 m).

5.2.4: Modeling the log-linear profile using stratification

Another explanation for the log-linear profile is the large stratification that occurs from the fresh water input after a storm. Salinity differences of > 0.4 ppt occur on April 13th, 2003 between 0.1 m and 0.5 m, resulting in density stratification of greater than 0.4 kg/m^3 (see figure 5.6). The vertical variation of salinity and density throughout the immersed period (figure 5.6) reflects runoff from the major storm that occurred on April 11th-12th, 2003. After the storm, fresh water runoff continues to flow over the more saline bay water, causing stratification. Note that density fluctuates at the seiche frequency during the ebbing tide (t > 300 minutes). Below 0.1 m, concentrations of suspended sediment are large—during the flood concentrations greater than 600 mg/L are measured, while up to 300 mg/L are measured during the ebb (for further

exposition, see Chapter 6). This modifies the density profile and potentially the water column dynamics. Thus, curvature in the boundary layer for current from stratification provides an alternate (or complimentary) explanation for the length scale 'L' in the log-linear formulation.

The large magnitude of the stratification is made clear by calculating the buoyancy frequency N^2 between the measured densities at 0.1 m, 0.5 m, and 1 m (see figure 5.7a). Note that no correction due to sediment concentration has been added, as most sediment is concentrated below 0.1 m. In the absence of more data, the density gradient is assumed to vary linearly between sensors. The results show that stratification increases during the ebb tide, resulting in a larger buoyancy frequency. In fact, there is enough stratification to support internal waves at frequencies less than 0.01 Hz ($f_{\text{int}\,ernal} = \frac{\sqrt{N^2}}{2\pi}$) throughout the period of inundation.

In theory, the flood tide should act to reduce stratification, as surface bay water is advected in the upper water column over less dense water on the mudflat (due to differential water velocity in water column), causing convective mixing (see for example Stacey and Ralston, 2005). However, stratification remains constant between 0.4-0.45 kg/m^3 in the lower 0.5 m of the water column as the depth increases during the flood (see figure 5.6), perhaps because the decreasing production of TKE (see chapter 4) counteracts the increasing likelihood of convective mixing. On the other hand, as water deepens, the buoyancy frequency between 0.5 m and 1 m is reduced—evidence that isopycnals are becoming less strained in the upper water column (less horizontal,

more vertical). During the ebb (t> 300 min), the buoyancy frequency N^2 begins to increase, in particular above 0.5 m—evidence of strain induced stratification, as fresh water advects faster in the upper water column and increases the density difference. However, the background level of stratification—0.4 kg/m^3, corresponding to a buoyancy frequency of 0.01 s^{-2} – remains throughout the tide.

Another indication of the strength of stratification is the buoyancy flux, B, which is shown in figure 5.7b. Over the period of inundation, the buoyancy flux fluctuates around a mean magnitude between 10^{-6} m^2/s^3 and 10^{-5} m^2/s^3, but increases towards 10^{-4} m^2/s^3 at the end of the ebb tide as stratification increases. From the buoyancy flux and buoyancy frequency one can construct the length scale L_{strat} based on the Monin-Obhukov length scale L_{mo} ,a measure of the physical length over which density effects become significant in the boundary layer (see equation 5.6). A positive lengthscale indicates heavy fluid overlaying a lighter fluid, and predicts convective overturning; by contrast, a negative length scale indicates that mixing is inhibited over the water column due to stable stratification. As might be predicted from the graph of buoyancy frequency (figure 5.7a), the predicted length-scale is always negative, or stably stratified. The magnitude varies greatly over a tide, from as much as 0.5 m during the flood to less than 0.01 m over portions of the slack and ebb tides. In the shallow water environment, any absolute value of L_{strat} which is less than the depth (0-1.5 m) suggests that stratification plays a role in the boundary layer dynamics. Thus, scaling suggests that stratification should be important, particularly during the slack tide and over portions of the ebb, when straining of the salt field by the ebb increases stratification.

However, the stratification length scale predicts that the curvature in the boundary layer will be opposite of that observed in figure 5.2 and 5.3; instead of reducing upper velocities relative to a log profile, stratification increases the velocity. In theory, turbulent mixing is damped by the stratification and the upper layers do not 'feel' the effects of friction as much, and therefore grow larger. However, as shown in figure 5.4a, in practice most of the length scales measured using a three parameter optimized fit to the log-linear equation are positive and banded between 0.1 m and 0.5 m. In fact, approximately 60 percent of the values of 'L' are between 0.1 m and 0.5 m, compared to ~ 22 % greater than 1 m and only 3 percent less than zero. Therefore, the stratification length scale (eqn. 5.5) does not explain the observed boundary layer structure of velocity.

5.2.5: Discussion of current boundary layer

The length scale L obtained from the log-linear boundary layer profile has fundamentally different characteristics than either $L_{acc,}$ and L_{strat}, as is shown in figure 5.5. The length scale L varies from small (large curvature) to large (no curvature). As velocity decelerates to zero the length scale L appears to increase from about 0.2 m towards values where the velocity profile is logarithmic (> 0.5 m). After a zero crossing, the length scale L is decreased to about 5-0.1 m. Thus, during the flood tide the largest curvatures (smallest L) are seen just as the boundary layer is reconstituting itself after a reversal in velocity. By contrast, L_{strat} becomes small as velocity

approaches zero. In theory, stratification effects should then produce a large curvature in the opposite sense from observed (see figures 5.1, 5.2, and 5.3). For conditions in which the velocity decelerates but does not reverse, as occurs between 130-135 minutes, a logarithmic profile is possible—as is indicated by the occurrence of scales greater than 1 m. Thus, observationally, the curvature is tied to zero crossings, and the formation of a boundary layer. By comparison, L_{acc} becomes small (indicating curvature) when acceleration is large or when friction velocity is small (see equation 5.3). Therefore, the Soulsby and Dyer (1981) formulation suggests that large curvature should occur on both sides of the zero crossing—which doesn't happen.

An interesting conundrum thus occurs, since neither the acceleration length scale nor the stratification length scale predicts the observed behavior. As Wood et al. (1998) point out, the acceleration length-scale as applied to the intertidal mudflat may need to include the spatial component of acceleration, not just the time derivative. Another potential reason might be the time scales involved; if the time scale for acceleration and deceleration is fast compared to the mixing time, perturbations to the flow that occur due to acceleration or stratification may not have time to propagate throughout the water column. By contrast, Soulsby and Dyer (1981) assume the boundary layer acceleration is long compared to the mixing time.

In the intertidal water column, acceleration changes by several orders of magnitude (and direction) over the cycle of a seiche. Using equation 5.4 and assuming a friction velocity on the order of 0.01 m/s, the time for a change in friction velocity to propagate

to 0.15 m and 0.28 m scales as 375 and 700 seconds, respectively—far greater than 120 seconds, or the approximate time that flow will be accelerating over a quarter phase of the seiche. Presumably, variations in the stratification length scale (see figures 5.4 and 5.6) will also take more than a couple of minutes to be felt by the entire water column. Thus, the length scales of stratification and acceleration developed to explain the log-linear boundary layer are not applicable in this shallow water environment.

5.3. Bed Stress

In this section, the two empirical methods used to estimate bottom stress from the mean current profile (equations 5.1 and 5.2) are compared to the results of a non-linear wave-current algorithm which considers ocean swell and wind waves separately. In addition, the case for no wave motion is also presented for comparison. Finally, estimates of bed roughness and the maximum stress due to waves are also presented and analyzed.

5.3.1: Bed Stress: Log-linear vs. log method

The stress imposed by the mean current onto the bottom boundary varies over the tidal time scale, as tidal currents vary between the flood, slack, and ebb tides. This underlying pattern is strongly modulated by the 8 minute seiching motion throughout the period of inundation, as is shown in figure 5.8. Bed-stress measured by the log-linear method varies from greater than 0.5 N/m^2 during the flood to less than 0.05 N/m^2 during the slack back up to 0.4 N/m^2 during the ebb. The bed stress estimated by the

log method follows a similar trend over the tidal cycle, though the measured value is more than 50 percent less than the log-linear value over some 1 minute segments. This occurs because applying the log-linear optimization generally results in a greater $\frac{dU}{dz}$ at the bottom boundary than the log-fit (see figure 5.2 and figure 5.3)—and therefore, results in an increased estimate of bed stress (figure 5.8). Note that when only two velocity measurements are available, a bed roughness of 0.008 m is assumed, based on the roughness calculated from times when three or more velocity measurements are available. This increases the accuracy of the friction velocity estimate, but implicitly ignores any increased roughness due to wave-current interaction. Thus, estimates using only two points are used only to compare friction velocity, and not bed roughness.

5.3.2 Non-linear interactions--Theory

The estimates of shear stress shown in figure 5.8 occur in a dynamic environment in which multiple frequencies of motion—wind waves, ocean swell, seiching and tidal currents—all interact with the bed. Thus, it is reasonable to wonder how the wave motions alter the boundary layer structure of the mean current in the intertidal environment.

Laboratory observations and theory suggest that currents and waves interact non-linearly in the wave boundary layer (see e.g. Mathisen and Madsen, 1996, Soulsby et al., 1993, Grantand Madsen, 1979), causing an enhanced friction velocity in the current boundary layer. The mean current feels the effect of waves as an increased, virtual

roughness. Turbulent motions caused by waves affect the mean current, and in turn the current boundary layer alters the wave dynamics. Thus, the stress caused by waves and currents cannot be linearly combined, but must rather be modeled using the equations of motion and informed assumptions about how the mean turbulence (i.e., eddy viscosity) can be parameterized in the wave and current boundary layers. For example, Grant and Madsen (1979; hereafter, GM'79) assumed a time invariant, piecewise eddy viscosity that varies linearly with depth. In the wave boundary layer, eddy viscosity is assumed to be proportional to u_{*cw}, the combined friction velocity from waves and currents. Above the wave boundary layer, eddy viscosity varies linearly with u_{*c}, the friction velocity due to current only. A matching condition at the top of the wave boundary layer ensures that the profile of mean velocity is continuous. Practically, the non-linear interaction between waves and currents results in a two-layer current structure, in which the slope of the upper (current only) layer is proportional to u_{*c} and the slope of the lower layer (wave-current layer) is proportional to u_{*c}^2 / u_{*cw}. Thus, the current boundary layer takes on a 'kinked' profile, with the lower layer approaching the physical roughness height at zero velocity and the upper layer approaching an apparent, virtual roughness set by the wave-current interaction in the wave boundary layer. In this chapter we use the Grant and Madsen (1986) formulation, which simplifies the original algorithm (hereafter GM'86) but builds on the theory discussed above.

Because only one measurement (z=0.015 m) is consistently in the wave boundary layer (see section on scaling in 5.4 for more information), it is difficult to verify directly that

non-linear interaction is occurring between waves and currents. As shown in figures 5.1 and 5.2, there is little evidence of an abrupt change in the slope of the current profile near the top of the wave boundary layers, as predicted by GM'79. However, one can indirectly confirm non-linear interaction by comparing the friction velocity and roughness predicted by the GM'86 model with the results of the logarithmic curve fit. To apply the GM'86 model, we separate ocean swell and wind waves from the measured signal using the wavelet decomposition technique (see chapter 2). The orbital velocity of each component is then defined as $\sqrt{2}V_{rms}$, where the rms velocity is defined over a 1 minute segment of data. The wave period is set to the dominant period of 2 and 10 seconds for wind waves and ocean swell, respectively. The angle between current and waves is approximated to be zero. Finally, the mean current is defined by using a 1 minute block average at a height of 0.15 m, and the physical roughness height is estimated as 0.0035 m, using a semi-empirical scaling technique (see section on roughness below).

5.3.3 Bed Roughness

The theory on nonlinear wave-current interaction (see Grant and Madsen, 1979, Soulsby et al., 1993) predicts that the turbulent motions in the wave boundary layer are felt by the mean current as an increased, virtual roughness z_0^*. Thus, evidence of non-linear wave-current interaction is found if the roughness height measured by the log-linear method is consistent with the virtual roughness predicted by the GM'86 method. This entails accurately estimating the physical roughness height z_0 used in the GM'86

model. Semi-empirical scaling (see Sleath, 1984) suggests that when ripples are present, the roughness is parameterized as $z_o = K_b / 30$, where K_b is the Nikaradse roughness parameter and is parameterized as $K_b = 25h^2 / L$, where h is the height of the ripple and L is the wavelength between ripple crests. Using the median values of h=0.015 m and L=0.05 m (see Ch. 2), the roughness height scales as $z_0 \sim 0.0035$ m.

Figure 5.9 shows the roughness height z_{opt} measured by the log-linear fit to the velocity profile and the virtual roughness for ocean waves and wind waves ($z_0^*{}_{,ow}$ and $z_0^*{}_{,ww}$, respectively) over the immersed period on April 13th, 2003. The virtual roughness is found by separately applying the rms orbital velocity of ocean waves and wind waves into the Grant and Madsen non-linear wave-current model (1986), using a physical roughness height of 0.0035 m. The results in figure 5.9 clearly show that the roughness height z_{opt} measured by the log-linear fit correlates well with the virtual roughness set by the ocean swell ($z_0^*{}_{,ow}$). Both are banded within a similar range throughout the tide, with z_{opt} varying between 0.008 m and 0.02 m and $z_0^*{}_{,ow}$ varying between 0.007 m and 0.02 m. By contrast, only the largest wind-waves cause an apparent, virtual roughness that approaches 0.01 m, and $z_{0*,ww}$ approaches the physical roughness height of 0.0035 m as wind energy decreases over the tidal period (see figure 3.11a). The correlation between $z_{*,ow}$ and the measured roughness z_{opt} suggests that the log-linear method is measuring a virtual roughness which is set primarily by the non-linear interaction between ocean swell and the mean current. Thus, the boundary layer of ocean swell has a proportionally greater affect on the mean current than the boundary layer of wind

waves. This is reflected not only in the friction velocity but also in the measured virtual roughness. Because ocean swell forcing is fairly constant over an immersed period (see chapter 3), the roughness measured by the log-profile remains approximately constant. Wind wave forcing is much more intermittent, and results in a more variable virtual roughness prediction (see chapter 3). The roughness predicted by using wind waves is ~ 0.01 m only for wind waves with an rms velocity greater than 0.1 m/s in figure 5.9. This occurs only occasionally at the field site during large wind events or storms (see figures 3.10 and 3.11). As wind waves decrease, the roughness $z_0^*{}_{,ww}$ quickly collapses. Therefore, the roughness predicted by velocity measurements at this intertidal mudflat is often set by ocean swell.

Though the similarity between measured bed roughness z_{opt} and predicted roughness $z_0^*{}_{,ow}$ is encouraging, it should be interpreted as illustrative rather than absolute. On the experimental side, there is ambiguity in assigning the height of 0.015 m to the lowest sensor, given that the control volume in which velocity is measured is on the order of 1 cubic centimeter and that the bed height may change throughout a tide; thus, the height of 0.015 m is only an estimate. Moreover, the ripples are irregular and of varying height and wavelength (0.01-0.02 m height, 0.04-0.06 m wavelength), and cause variation in the physical roughness estimate z_0. For example, calculating the roughness height z_0 using a ripple height of 0.01 m and a wavelength of 0.06 m results in an estimated physical roughness of 0.0014 m, while using the other extreme of 0.02 m height and 0.04 m wavelength results in an average estimated physical roughness of 0.0083 m—almost an order of magnitude difference. However, the relative magnitudes

of the virtual roughness due to ocean swell and wind waves remain the same. Thus it is valid to conclude that ocean swell sets the apparent roughness that the mean current measures for all but the most vigorous wind-wave conditions.

5.3.4 Friction Velocity

Figure 5.10 compares the GM'86 model results with the friction velocity u_{*_c} found using velocity data and the logarithmic profile (equation 5.1) over the period of inundation beginning during the evening of April 13th, 2003. Because there are two distinct wave frequencies, friction velocity is separated into estimates considering either ocean waves ($u_{*GM,ow}$) and wind waves ($u_{*GM,ww}$) only; in addition, the case of pure current (no wave action) is also included ($u_{*GM,c}$). A least squares fit of the GM'86 friction velocities to the logarithmic friction velocity u_{*_c} is presented in figure 5.10a. To make the presentation of the GM'86 results vs. u_{*_c} easier, we bin-average with an increment of 0.001 m/s and plot the resulting points in figure 5.10a. Good correlation is seen between the bin-averaged results and the least squares fit, suggesting that the GM'86 results are proportional to the friction velocity u_{*_c}. Over the time period of inundation, the estimates found using the GM'86 algorithm follow the pattern of the logarithmic estimate, with the mean friction velocity u_{*_c} estimate being modulated by the seiche frequency (see figure 5.10b). However, the magnitude of the friction velocity estimated by GM'86 differs from the logarithmic fit to data. Indeed, the slope of the $u_{*GM,ow}$, $u_{*GM,ww}$, and $u_{*GM,c}$ lines in figure 5.10a are not equal to unity, but are 0.89,

0.78, and 0.44, respectively. Therefore, the GM'86 algorithm predicts values of friction velocity that are less than the measured values. On aggregate, applying the ocean swell orbital velocity to the GM'86 algorithm results in estimates that are closest to the measured friction velocity.

Clearly, the action of waves is critical to determining the friction velocity of the current boundary layer; when waves are ignored, the predicted friction velocity is less than half of the measured value. Moreover, because the effect of ocean swell and wind waves are considered separately, the aggregate effect of waves on the mean current is likely greater than either considered by itself. To test this, we combine ocean swell and wind waves ($V_{combined} = \sqrt{V_{ow}^{\ 2} + V_{ww}^{\ 2}}$, where V_{ow} and V_{ww} are the orbital velocities of ocean waves and wind waves) and use a period of 10 seconds (ocean swell) to calculate a combined friction velocity ($u_{*GM,combined}$) using the GM'86 algorithm. Then, a least squares line is fit to the scatter plot of $u_{*GM,combined}$ vs. u_{*_c} , as in figure 5.10a. The resulting slope is 0.99, or nearly unity, which suggests a 1:1 correspondence between u_{*_c} and $u_{*GM,combined}$. This suggests that the combined rms orbital velocity is a better measure of the effect of waves on current.

While using a combined rms orbital velocity in the GM'86 model is promising, other factors (e.g., roughness and acceleration) may have an equally large affect on the estimated friction velocity. For example, the log-linear fit to the measured velocity data predicts friction velocities that are on average 16 percent greater than the friction velocity found using the logarithmic fit (see figure 5.8). Moreover, the GM'86 results

are sensitive to the estimate of physical roughness. As described in section 5.3.3, estimates of physical roughness vary between 0.0014 m and 0.0083 m. Doubling the physical roughness from 0.0035 m to 0.0070 m increases the slope of the fit between $u_{*GM,ow}$ and u_{*c} from 0.89 to 1.06. Finally, the GM'86 model also assumes a well developed current; since the boundary layer is often accelerating or decelerating, the stress applied to the bed is likely to vary from the well-developed case.

An interesting observation is that non-linear theory predicts that ocean swell will have a larger effect on the mean current than the wind waves. Over the tidal period in figure 5.10, it is clear that $u_{*GM,ow}$ is larger than $u_{*GM,ww}$. Indeed, for the combination of waves and currents generally present on the mudflat, the GM'86 theory predicts that wind wave orbital velocities need to be between 2x to 5x larger than ocean swell to have the same effect on the friction velocity of the mean current. This ratio is graphically shown in figure 5.11 over an immersed period on April 13th, 2003 as wind waves, orbital velocity and the 1 minute mean velocity vary. The largest ratios occur during slack tide, when the current is smallest (see figure 3.11a); thus, ocean swell has a proportionally larger effect on weak currents. For comparison, the actual, measured ratio of wind waves to ocean swell is plotted on the same graph. Only intermittently during the flood tide, when wind velocities ranged from an average of 5 m/s with gusts up to 10 m/s, do wind wave orbital velocities cause a larger friction velocity in the mean current. In fact, over the entire immersed period, only 2.5 percent of wind waves exceeded the importance of ocean swell on the mean friction velocity. This difference between ocean swell and wind waves occurs because the boundary layer of ocean swell

grows to a larger height than wind waves, and thus impinges into the mean current to a greater extent.

5.3.5: Maximum wave stress

Though the friction velocity and bed stress displayed in figures 5.8 and 5.9 show stress caused by the 1 minute mean current, a complete characterization of stress must include the oscillatory shear imparted by wind waves and ocean swell in their respective boundary layers. Directly measuring the bed stress of waves is difficult in the field, but can be estimated using wave friction factors calculated from semi-empirical formulas in the non-linear wave-current theory (see Grant and Madsen, 1979). Figure 5.12 shows the maximum friction velocity predicted by GM'86 for wind waves and ocean swell over an immersed period beginning during the evening of April 13th, 2003. During the flood tide wind waves cause a maximum friction velocity of 0.08 m/s, which quickly drops off to < 0.02 m/s as wind wave energy decreases (see figure 3.11a). The maximum friction velocity due to ocean swell also drops off as depth increases during the flood, from perhaps 0.03 m/s to 0.015 m/s. Interestingly, the maximum friction velocity from the ocean swell boundary layer is comparable to or larger than friction velocity from the wind wave boundary layer during the slack and ebb tide (t> 200 minutes). This indicates that remotely forced waves can create the largest instantaneous stresses on this mudflat. At the end of the tide, the maximum friction velocity of both wind waves and ocean swell increases, both from small wind-waves and increasingly

non-linear ocean swell, which increases the maximum orbital velocity at both the swell and wind wave frequencies.

Note that ocean swell and wind waves are treated independently of each other, and are input into the wave/current model as the only source of wave motions. However, that fundamentally subverts the primary observation of GM'86—namely, that turbulent motions of one type of motion affect the flow dynamics of another. Thus, it is likely that the boundary layer for wind waves affects the boundary layer of ocean swell through an increased, virtual roughness. Since there is likely some non-linear interaction between wave frequencies, the magnitudes shown in figure 5.12 should be considered a first-order approximation.

5.4. Wave Boundary Layers

The length scales of stratification and acceleration developed to explain the log-linear boundary layer are not applicable in this shallow water environment. Rather, a different approach must be taken to explain the observed water column profiles and gain a more accurate description of fluid interaction with the bed—namely, modeling the boundary layer as a wave process.

To isolate the effect of the seiche frequency from the tidal motions, we next evaluate the contribution that the seiche makes to the vertical structure of velocity and friction velocity. An analytical wave boundary layer model based on Smith (1977) is used, as

well as an open-source numerical model (General Ocean Turbulence Model--GOTM). The models are described in section 5.4.1, followed by an overview of the data processing techniques used to separate the boundary layers of ocean swell and the seiching motion from the measured data stream. Finally, the results of the numerical and analytical model are compared to the measured results and to the log-linear model (equation 5.2).

5.4.1 Theory of Wave Boundary Layer

5.4.1.a: Boundary Layer scaling

The maximum height of a boundary layer for a wave, δ_w, scales as a ratio of the friction velocity u_* and the frequency of motion ω, and is determined by the intensity of turbulent motions (which sets u_*) and the time over which the boundary layer develops (set by ω) :

$$\delta_w = \frac{\kappa u_*}{\omega}, \tag{5.14}$$

where κ is von Karman's constant. Substituting ω=2π/T, the wave boundary layer height then scales as:

$$\delta_w = \frac{\kappa u_* T}{2\pi} \tag{5.15}$$

where the dependence of the boundary layer height on wave period T is made explicit. In practice the effect of the boundary layer is observed above the height δ_w, typically in an overshoot region. Therefore one can argue that free stream, potential flow conditions are reached only between 2-4 δ_w (Grant and Madsen, 1979). For example, in mixed wave and current conditions, Mellor (2002) defines the wave boundary layer height as $2\delta_w$.

Table 5.1 shows the order of magnitude of the boundary layer heights found by scaling the boundary layer for wind waves, ocean swell, seiche, and the tidal current. By definition, tidal currents are well developed over the entire water column. The boundary layer height of waves is small, and therefore difficult to measure in the field; only the bottom instrument, at 0.015 m, is consistently within the wave boundary layer. For larger ocean swell, the instrument at 0.05 m intermittently captures the ocean swell boundary layer. Because the boundary layer for wind waves is small, it will not be considered in the following analysis. By contrast, the seiche boundary layer height corresponds well to the instrument locations in the field, which are placed between 0.015 m and 0.33 m height. Thus, a detailed analysis of the seiche boundary layer is possible.

Table 5.1: Scaling the boundary layer heights of the different wave types.

Wave Type	Wind Wave	Ocean Swell	Seiche	Tidal
Range in friction velocity	0- 0.08 m/s	0-0.04 m/s	0- 0.015 m/s	0-0.015 m/s
Period	2 seconds	10-15 sec	~ 500 sec	~12.4 hours
Boundary Layer Height	0-0.01 m	0 – 0.04 m	0-0.5 m	Entire water column

5.4.1.b: Smith model

The Smith (1977) model for a wave boundary layer starts with the governing equation for a wave in the presence of friction at the bed:

$$\frac{Du}{dt} = \frac{dU_\infty}{dt} + \frac{d}{dz}(K(z)\frac{du}{dz}) \qquad (5.16)$$

where u is the velocity of the wave as a function of height and U_∞ is the free stream potential flow of the wave. Smith assumes a constant stress region within the boundary layer, which yields an eddy viscosity K(z) that varies linearly with height, i.e., $K(z) = \kappa u_* z = K_o z$. The boundary conditions are that $u(z \to \infty) = U_\infty$ and $u(z \to z_o) = 0$. Assuming a sinusoidal, monochromatic wave of form $U_\infty = U_o \Re(\exp(i\omega t))$ and $u = U_0 \Re(\exp(i\omega t)(1 - Z(z))$ leads to the following solution for the boundary layer of a monochromatic wave:

$$u = U_o(\cos(\omega t) - Y) \qquad (5.17a, 5.17b)$$

$$Y = \frac{(\ker(\xi)\ker(\xi_o) + kei(\xi)kei(\xi_o))}{(\ker^2(\xi_o) + kei^2(\xi_o))}\cos(\omega t) + \frac{\ker(\xi)kei(\xi_o) - kei(\xi)\ker(\xi_o)}{\ker^2(\xi_o) + kei^2(\xi_o)}\sin(\omega t)$$

where $\xi = 2\sqrt{\omega z / K_o}$, $\xi_o = 2\sqrt{\omega z_o / K_o}$, ω= radian frequency, $K_o = u_* \kappa$ (eddy viscosity), and ker and kei are Kelvin functions, which are linear combinations of Bessel functions (see Zhang and Jin, 1996).

The assumption of a linear eddy viscosity and a constant stress layer is commonly made in oceanographic analysis (see e.g. Soulsby, 1983), and is critical to solving this equation analytically. Other analytical models choose a different variation of eddy viscosity with height, and several models introduce a time varying eddy viscosity to account for the change of ustar with time (see review by Sleath, 1990). More complex parameterizations of eddy viscosity require a numerical model to solve for the wave boundary layer.

5.4.1.c: GOTM Model

The General Ocean Turbulence Model, (GOTM) described by Burchard and Baumert (1995) is a 1-D, finite volume numerical model used to investigate shear, turbulence, stratification, and other physical processes in estuarine and oceanographic environments.

Essentially, the numerical model solves for the turbulent eddy viscosity υ_T, which allows for closure of the fundamental equations governing fluid motion (Navier Stokes Equation). This is accomplished using the Turbulent Kinetic Energy (TKE) equation which is defined as:

$$\frac{\partial k}{\partial t} = \frac{\partial}{\partial z}(\nu_T \frac{\partial k}{\partial z}) + P + B - \varepsilon \tag{5.18}$$

In a 1D model such as GOTM, turbulent kinetic energy (k), dissipation of turbulence (ε), production of turbulence (P), and buoyancy B are defined as follows:

$$k = 0.5(u'^2 + v'^2 + w'^2) \tag{5.19}$$

$$\varepsilon = \nu \left\langle (\frac{\partial v_i'}{\partial x_j})(\frac{\partial v_i'}{\partial x_j}) \right\rangle \tag{5.20}$$

$$P = -\frac{\partial \bar{u}}{\partial z}\langle u'w' \rangle = -\nu_T \left(\frac{d\bar{u}}{dz} \right)^2 \tag{5.21}$$

$$B = -\frac{g}{\rho_o}\overline{\rho' w'} = -\frac{g}{\rho_o} K_\rho \frac{d\bar{u}}{dz} \tag{5.22}$$

where ν= molecular viscosity, u'^2, v'^2, and w'^2 are the three components of turbulent kinetic energy, v_i' is the ith component of turbulent velocity ((i=1,2 3), x_j is the jth direction (j=1,2,3), K_ρ = mixing coefficient of mass, g= gravity and ρ_0 = background density. Note that the definition of mass diffusivity and eddy viscosity (eqns. 5.7 and 5.8) has been applied to the production and buoyancy terms. Also note that the buoyancy flux (B) is previously defined by equation 5.6.

In the so called k- ε model that we use in this dissertation, dissipation is modeled by the following equation:

$$\frac{\partial \varepsilon}{\partial t} + \frac{\partial \varepsilon}{\partial x_i} = c_1 (P + c_3 B) \frac{\varepsilon}{k} - c_2 \frac{\varepsilon^2}{k} \tag{5.23}$$

Various boundary conditions and further assumptions are used to solve for the constants c_1,c_2, and c_3, as well as Production (P) and Buoyancy (B). A more thorough discussion of the k- ε model used in GOTM can be found in Burchard and Baumert, 1995. Together, the TKE equation and the dissipation equation (eqns. 5.18 and 5.23) form a so-called 2 equation model for solving for turbulent eddy viscosity, which scales as the turbulent intensity ($k^{1/2}$) and the lengthscale of energy containing eddies (L_T). For the k- ε model, the turbulent length scale L_T is defined by:

$$L_T \propto \frac{k^{3/2}}{\varepsilon} \tag{5.24}$$

The length scale for turbulence can be calculated in GOTM using 10 different methods, including parabolic and triangular profiles, the Mellor Yamada relation, the dynamic dissipation rate equation, and others. From this the dissipation ε is calculated, which is then used to solve the TKE equation (see Burchard and Baumert, 1995). The numerical solution scheme can be varied from fully implicit to fully explicit. The user can chose between several turbulent closure schemes, including the Mellor-Yamada and k- ε models.

In addition to choosing the length scale equation, the user also selects from ~ 14 different stability functions. Either flux (Neumann) or prescribed (Dirichlet) boundary conditions are applied to the top and bottom of the 1D model. A roughness height is used to produce turbulence at either boundary. Finally, the user can define initial conditions for temperature, salinity, buoyancy, pressure, and/or velocity, and can update these parameters throughout the model run. In this way an oscillatory wave can be produced, a salinity gradient can be enforced, or intermittent, experimental data can be used to constrain the result. In short, GOTM gives the user the flexibility to reproduce experimental data or simulate idealized test cases. From the results, quantities such as shear, production, dissipation, buoyancy flux, mixing, etc. can easily be investigated.

In general, GOTM and k- ε turbulence models have limitations in resolving fluctuating boundary layers on time scale of a seiche. For example, Juesteson (1988) showed that

though the k- ε model shows good agreement with ensemble averaged velocity profiles, the fit for turbulence characteristics in oscillatory flow near the bed is poorer (Juesteson, 1988 in Sleath 1990). A possible reason is that the eddy viscosity calculated by using the instantaneous value of shear velocity is quite different from that measured by experiments (Sleath, 1990). There is also uncertainty over how to best treat the interaction between turbulence and stratification in a k- ε model (Burchard and Baumert, 1995 from Rodi, 1987).

5.4.2 Methods and Data Processing

In the following sections we describe the methodology used to estimate the wave boundary layer from our data at the ocean swell and seiche frequencies.

5.4.2.a: Ocean swell

To define the phase structure of bandpassed ocean swell data, we use a search algorithm to determine the local maximums, local minimums, and zero up-crossings in a burst. The minimum value of a particular wave cycle is defined to be zero degrees, the maximum is set at 180 degrees, and the zero up-crossings and down-crossings are assigned values of 90 degrees and 270 degrees, respectively. The beginning of the next wave cycle is defined as 360 degrees. Phases between these values are found using interpolation in time (e.g., the time halfway between 0 and 90 degrees is 45 degrees). Using phase angles defined relative to maximum, minimum, and zero up-crossings

allows waves with slightly different periods to be compared to each other (see figure 3.13 for an example of variable wave periods). However, some error is introduced when wave forms are irregular and asymmetric.

To account for a slight drift in start times between instruments, we used a lagged correlation algorithm to shift each burst velocity such that correlation was maximized between instruments. Typically, each data set was shifted between 0-5 seconds. By shifting the data, we implicitly lose any phase shift that may be occurring in the boundary layer. For ocean swell, that applies to the instruments at 0.01 m and 0.05 m (the other instruments are not in the boundary layer). However, the error introduced by retaining a 0-5 second offset is larger.

To allow comparisons between waves of different heights and orbital velocity, each wave form is normalized by the velocity at 180 degrees using the data from 0.285 m in height. If the maximum orbital velocity is < 0.01 m/s, the wave is discarded. The normalized velocity of each wave form is saved in increments of ~6 degrees from 0 to 360 degrees. The wave forms from each burst in a period of inundation are concatenated and averaged, yielding the progression of normalized ocean swell over a wave cycle.

Neither the bandpass filtering nor wavelet decomposition is able to capture the non-linear profile of ocean swell at the beginning and end of each tide. Instead, the bandpassed profile explicitly consists of only the primary signal, not the higher

harmonics. While this certainly introduces some error, the non-linearity in the swell becomes acute only below 0.6 m (see chapter 3). These time periods can be removed from the data set. Moreover, because of the paucity of data in the ocean swell boundary layer (2 points), we consider only the rms boundary layer profile over an entire period. Therefore there is no need to model the asymmetry in the ocean swell over its cycle, but rather estimate the rms velocity at each height. For this purpose, the bandpass filters are adequate (see section 5.4.4 for results).

5.4.2.b: Seiche

Defining a seiche boundary layer proves more difficult than the ocean swell, primarily because its period (~ 500 seconds) is greater than the burst length of the instruments at 0.015 m and 0.05 m, which is 345 seconds (memory limitation). Therefore, 4.25 minutes (255 seconds) of each 10 minute burst are unaccounted for, and the seiche frequency cannot be extracted without further data processing. To make the data set continuous, we extrapolate a trend line backwards and forwards from the edge of each burst for 1 minute. The remaining time gap (135 seconds) is bridged by linearly interpolating between the endpoints of the forward and backwards trend line. Note that the trend line is defined using a 1 minute subset of data. A 1 minute trend line allows the effect of ocean swell to be averaged out of the raw data while preserving variation from the 8 minute seiche wave. To verify the accuracy of the interpolation scheme, we test it on the two velocimeters (0.155 m and 0.285 m) for which nearly continuous data is available (590 seconds out of 600 seconds). Using the band-passed filtering

described below, we create two data sets, one using the interpolation scheme and one with the complete data set. Subsampling over the data range that is used in the boundary layer analysis, we find an average rms difference of 1.5 mm/s between the interpolated and continuous data sets. This is the same order of magnitude as the velocimeter error (see chapter 2), and is therefore acceptable. Moreover, because the amplitude of velocity measured at 0.015 m and 0.05 m is less than at 0.155 m and 0.285 m, the interpolation error is likely to be smaller. Note that we also interpolated over the missing 10 seconds for the instruments at 0.155 m and 0.285 m; however, not much error is introduced there.

After interpolating, we constructed a continuous data set over each period of inundation for each instrument. From the combined data, we applied a buttersworth filter (see chapter 2.) with limits set between 300 and 800 seconds to determine the seiche wave-train. Though somewhat arbitrary, these limits allow the seiche period to vary somewhat, while preserving the essential feature of a seiche set around an average period of ~500 seconds. An example of the seiche velocity over an entire period of inundation after filtering is shown in figure 5.13a, along with a comparison in figure 5.13b of the seiche generated from nearly continuous data (z=0.28 m) with the seiche estimated after interpolation (z= 0.05 m). In general, the phase of the two wave trains follow each other well, and the magnitudes of the wave motions are of the same order. Thus, the interpolation appears to work reliably, though there is some scatter in the relative magnitudes of the motions. Note that the maximum seiche velocities in figure 5.13a occur between 150 minutes and 200 minutes on the flood, and 350 minutes and

420 minutes on the ebb. At slack tide the orbital velocity decreases and the period becomes less coherent, with other frequencies (perhaps seiche harmonics) appearing. For our analysis, we manually appraised the data and discarded any wave forms that include sub-harmonics or do not follow an approximately sinusoidal shape. In addition, wave forms with an amplitude of less than 0.01 m/s are discarded. Using these criteria, about 40 wave forms (of ~60 total) were deemed usable over the immersed period on April 13th, 2003.

In order to minimize error, we do not use interpolated data in our calculation of the wave boundary layer. In addition, we excise the first and last minute of each burst of measured data to avoid edge effects that occur due to the filtering. Thus, we are left with a 3.5 minute window for each 10 minute segment from which to sample the wave boundary layer, and are able to use only a portion of each particular seiche. Since there are only approximately 40 usable seiche waveforms in a period of inundation, this means that each phase angle contains only 10-15 data points. Data density is improved by concatenating the results from several different periods of inundation together. As with the ocean waves, we normalize each seiche by the maximum velocity at 0.285 m over a wave period. We construct the development of the boundary layer by averaging the normalized profile at a particular phase.

5.4.3 Ocean Swell Boundary Layer

Figure 5.14 shows the normalized root mean square (rms) profile of the boundary layer for ocean swell measured during a period of inundation on April 13th, 2003. For comparison, the rms profile predicted by the Smith (1977) boundary layer model is plotted. Note that to generate the boundary layer profile, we apply the median measured orbital velocity of 0.026 m/s and a roughness of 0.01 m, which is within the range of experimentally derived values (see figure 5.9). To compare with the other normalized boundary layer results, we normalize the profile using the velocity at 0.285 m.

Overall, the analytical model matches the major characteristics of the observations. Close to the bottom boundary at 0.015 m, both the measured and analytical have similar normalized velocity magnitudes of about 0.3 In addition, at 0.05 m the analytical model and the measured results both show an overshoot in rms velocity that is ~ 5 percent greater than the rms orbital velocity in the free stream. Note that the overshoot region predicted by the Smith model and observed at the intertidal mudflat are typical for both laboratory and field environments (see for example Soulsby et al., 1993 and Fredsoe et al., 1999). Above 0.15 m, the effect of the boundary is no longer present in both the analytical model and the results.

The sparseness of vertical velocity data in the water column means that we cannot definitively verify any analytical model of an ocean swell for shallow water, estuarine

conditions (only two measurement locations are in the boundary layer of ocean swell). However, it is encouraging that the major features of the Smith (1977) model are followed in an rms sense. This suggests that the assumption of linear eddy viscosity that Smith made in developing his model is valid at least to a first order approximation in the wave boundary layer. In addition, it shows that a model derived using monochromatic, single period waves can be applied to a real environment with irregular, nonlinear waves and varying wave period. Therefore, the Smith (1977) model (and modifications of the Smith model, such as Foster et al. (2000)) can be used to parameterize the friction velocity and bed stress from waves, at least in an rms sense.

5.4.4 Seiche Boundary Layer

In this section the measured boundary layer for the seiche is compared to results of the log-linear curve fit, the Smith (1977) boundary layer model, and General Ocean Turbulence Model (GOTM).

5.4.4a. Measurements

Figures 5.15a and 5.15b show the normalized boundary layer of a seiche as a function of phase angle. In addition, a curve fit using the log-linear profile (equation 5.2) is also presented, as well as the Smith (1977) estimate of the boundary layer. At zero degrees, the measured seiche boundary layer is well developed in the negative (offshore) direction; as time progresses, the boundary layer decelerates, with each panel showing a

similarly shaped vertical velocity structure. At 90 degrees, the boundary layer breaks down and is re-formed in the positive (onshore) direction. Again, the shapes of the boundary layer in each panel are similar to each other. At 180 degrees, the boundary layer again reverses and decelerates towards zero velocity. Note that the normalized velocity at 0.285 m lags the normalized velocity measurement at 0.155 m, which creates the curvature that is measured by the log-linear profile. The overall form of the seiche boundary layer is consistent with the 5 minute snapshot of the mean current boundary layer shown in figure 5.2; because the mean velocity was less than 0.01 m/s and variation was dominated by the seiche, this is not surprising.

The curvature in the upper water column is produced by a difference of 10-20 percent between the sensor at 0.285 m and 0.155 m. Given maximum orbital velocities for the seiche ranging from 0.01 m/s to ~ 0.07 m/s, this translates to a velocity difference of between 10^{-3} m/s and 0.015 m/s. Thus, the velocity differences for small seiching motions approaches the noise floor, which is on the order of 10^{-3} to $2*10^{-3}$ m/s. Though the persistence of the curvature and the repeatability over many instances of the seiche suggest the results are real, experimental error cannot be completely ruled out.

5.4.4.b Log-linear model

As with measurements of the tidal boundary layer (e.g., figures 5.2 and 5.3), the log-linear model fits the measured seiche boundary layer very well (see figure 5.15). This is perhaps not that surprising, given the three parameter fit of u_*, z_0, and the length scale

L to four data points. Results for fitting a log-linear profile to the normalized seiche profile are shown in figure 5.16. Friction velocity is periodic with the seiche, while roughness is banded between 0.008 m and 0.015 m and the lengthscale L is banded between 0.05 m and 0.2 m for much of the seiche. The friction velocity over a representative seiche is calculated by assigning an orbital velocity to the normalized profile. Interestingly, the bottom friction velocity in figure 5.16a shows a marked asymmetry, with the maximum at 180 degrees being about 20 percent greater than the maximum at 0 degrees. Possible reasons include interaction of the seiche with waves, currents, or stratification, or perhaps measurement and processing error. However, more research is needed to investigate this result.

As with the tidal boundary layer analysis (see section 5.2), there are major problems interpreting the length scale L over the time scale of a seiche; for example the Soulsby-Dyer model (Equation 5.3) predicts both negative and positive length scales, whereas the optimized length scale shown in figure 5.16 stays rigidly positive in the range of +0.05 m to +0.2 m. Under the Soulsby-Dyer model, the measured length scale suggests that the seiche is accelerating on all phases of the wave, which is clearly not true. However, the goodness of fit using the log-linear model suggests that this is a good way of estimating roughness and friction velocity due to the seiche. The estimates of roughness z_0 and length scale L are consistent through most phases of the seiche. This produces vertical velocity profiles that exhibit similar curvature (set by L) and are forced to zero at a similar height (roughness height). Therefore, the boundary layer structure is self-similar on both positive and negative strokes of the seiche (see figure

5.15), except when velocity reverses and the boundary layer structure breaks down. Then, the apparent increase in roughness and Length scale may occur because the log-linear model breaks down during velocity reversal, and the goodness of fit decreases; other explanations are non-linear interaction between the seiche and waves (which could increase the apparent roughness) and the greater effect of measurement and processing error as velocity approaches zero.

5.4.4.c: Smith Model

As shown in figure 5.15, the Smith (1977) model does not fit the measured seiche profile well, except perhaps over the bottom few centimeters when both the measured profile and the Smith model approach the roughness height of 0.01 m with a logarithmic profile. Since the Smith model is constrained to go to zero velocity at 0.01 m, this is not surprising. Though the Smith model predicts an overshoot region before returning to a steady orbital velocity, this occurs much higher in the water column. For example, the panels at 0 degrees and 180 degrees in figure 5.15 show that the overshoot region in the Smith model occurs at ~0.5 m, while the measured (and log-linear) overshoot occurs at ~0.2 m. The magnitude of the overshoot in Smith is much smaller as well. A possible reason for the discrepancy is the assumption of a linearly varying eddy viscosity that is constant in time. As the seiche evolves, bottom stress, friction velocity, and turbulence production vary significantly, which affects the eddy viscosity. Moreover, the mixing length and eddy viscosity may be suppressed by stratification in the water column, and eddy viscosity may be modified by the upper boundary (e.g.

wind stress or white capping), particularly in the early and late phases of the period of inundation. Thus, the Smith model likely does not capture the complexity of the seiche boundary layer, and therefore a numerical model which includes more physics (such as time varying eddy viscosity and stratification) needs to be used.

By contrast, the boundary layer for ocean swell would not feel the effects of the upper boundary or stratification; moreover, the time scales for turbulent decay are likely greater than the ~10 second ocean swell period. As a result, mean turbulent energy may be closer to constant over the ocean swell boundary layer, which makes the assumption of a linearly varying eddy viscosity plausible. Sleath (1990) notes that though experimental evidence shows that the eddy viscosity varies over a wave cycle, the velocity profile may be adequately modeled by a mean friction velocity for rough conditions. Hence, the Smith model may be applicable to smaller period waves in an intertidal zone with ripples.

5.4.4.d: GOTM Model

For simplicity, the GOTM model presented below applies only a sinusoidal, external pressure gradient with a period of 480 seconds to a water column of 1 m depth, producing a wave with a maximum orbital velocity of ~ 0.06 m/s. We explicitly assume no shear stress due to wind and no horizontal salinity gradient. To attain the vertical resolution needed to resolve a boundary layer of the seiche, a water column of 1 m depth is divided into 200 segments with 5 mm spacing. Small time steps of 0.1 seconds

are used, and the model is run for 12 hours in model-time to allow transient effects to die down. Drag at the bed is defined using a user-defined roughness height H, which is related to the physical roughness height in the logarithmic equation (equation 5.1) by $z_o = 0.03H$. The logarithmic boundary layer equation is then used to define a friction factor at the bottom bin. Drag, defined as a friction factor times the square of velocity in the first bin, is then input into the momentum equation as a source term (bottom boundary condition). For simplicity, surface drag is set to zero. Turbulence closure is fulfilled by using the k- ε model (see section 5.4.1.c), which solves the turbulent kinetic energy equation to calculate the evolution of shear stress and the velocity gradient. In turn this defines the eddy viscosity as a function of time and wave phase.

Figure 5.17 compares the seiche boundary layer from a GOTM model run with the measured results, using both unstratified and stratified conditions. Stratification is defined by assigning the values of 25, 24.2 and 23.8 ppt to the heights of 0.1 m, 0.5 m, and 1 m, and linearly interpolating between them. These salinity values roughly correspond to measured values. Step function changes in salinity were also considered, but caused no significant change in the velocity profile. The salinity is forced to remain constant over all phases of the wave; while realistic during the flood, salinity—and therefore density—does fluctuate with the seiche during the ebb (see figure 5.6) and this introduces some error. Density is calculated using the UNESCO equation of state.

Over a wave cycle both the stratified and unstratified simulations fit the observed velocity profile fairly well, though there are time periods when the predicted and

measured profiles diverge (see for example 90 degrees and 112.5 degrees). Only below 0.05 m, near the roughness height of 0.01 m, does the numerical model consistently fail; this is because the numerical model does not deal well with the large velocity gradients near the bed. Note that the height of the overshoot region is generally well represented by the numerical model (see the inflection points at ~0.15 m for the profiles at 22.5 and 157.5 degrees, for example). Interestingly, many of the numerically modeled profiles contain two inflections—one between 0.05-0.15 m, and one between 0.15 m to well above the highest sensor at 0.28 m (see the panel at 180 degrees and 270 degrees, for example). In fact, though the data is sparse, there are several times when the measured data are consistent with a double inflection (see panel at 270 degrees and 292.5 degrees). Given the data-processing in creating the 'observed' velocity profile and the assumptions inherent in the numerical model, it is remarkable that there is this degree of agreement as the seiche progresses between positive and negative velocities.

Overall, the stratified boundary layer appears to fit the data slightly better, as for example at 45 degrees and 67.5 degrees. Moreover, the stratified boundary layer better predicts the interesting double curvature that is seen at 270 degrees, for example, perhaps because stratification appears to amplify the curvature in the double inflection. The curvature occurs because of the time-lagged propagation of turbulence through the water column, which is shown in figure 5.18. During times of maximum orbital velocity (e.g., at 0 degrees and 180 degrees), large stresses produce turbulence at the bed. This turbulence propagates through the water column, such that some depths experience the largest TKE when velocity is smallest (i.e., at 90 degrees, the maximum

TKE is centered between ~0.10-0.15 m). Interestingly, the time lag inherent in the propagation of turbulence up into the boundary layer confirms that the effect of acceleration and stratification, as parameterized in the log-linear boundary layer (equations 5.2-5.5) does not have enough time to take effect.

As turbulent energy propagates up the water column, it quickly loses energy due to dissipation; concomitantly, the mixing length increases with height. Eddy viscosity, which scales approximately with the turbulent intensity ($k^{1/2} = \sqrt{TKE}$) and the mixing length scale, will therefore be at a maximum somewhere amongst these competing trends. Indeed, as can be seen in figures 5.19 and 5.20, the maximum eddy viscosity occurs at a height of ~0.1 m at a phase of 90 degrees, i.e., when the flow is reversing. Throughout a seiche cycle, the TKE and eddy viscosity vary with depth and phase angle, with the maximum of TKE and dissipation propagating up through the water column (see figure 5.19). In fact, a new maximum of TKE and eddy viscosity begins propagating from the bottom before the old maximum vanishes, giving rise to a double inflection (see figure 5.20 at 0 degrees and 135 degrees). The double inflection in TKE and eddy viscosity may explain the double inflection that is observed in velocity. Clearly, the numerical model suggests that the assumption of linearly varying eddy viscosity with depth is erroneous. To conclude, many of the analyses presented here—from the logarithmic velocity profile to the non-linear wave-current interaction theory to the analytical wave boundary layer (Smith, 1977)—are more properly modeled with a more complex, non-linear model of eddy viscosity.

5.5. Discussion and Conclusion

This chapter investigates the effect of multiple frequencies of motion—wind wave, ocean swell, seiching, and tidal currents—on the boundary layer structure and resulting bed stress of an intertidal mudflat. Through non-linear interaction in the combined wave/current boundary layer, ocean swell and wind waves increase the friction experienced by the current-only boundary layer. Because of its larger boundary layer, ocean swell interacts more with the mean current than wind waves. On this intertidal mudflat, only when the orbital velocity of wind waves are 2-5 times the magnitude of ocean swell do they have a comparable effect on the mean current. The critical ratio depends on the relative magnitudes of the mean current, ocean swell and wind waves, which vary based on tidal stage, forcing and the random distribution of wave orbital velocities (which differ between wind waves and ocean swell; see chapter 3). Indeed, as the ratio of orbital velocity to mean current increases during slack tide, the relative importance of ocean swell increases. Over a period of inundation at the mudflat, ocean swell dominates both the virtual roughness and the friction velocity experienced by the mean current above the wave boundary layers, except during windy and stormy conditions. On the other hand, the instantaneous stress exerted by wind waves on the bed is much greater than ocean swell (due to the larger accelerations in the thinner wind wave boundary layer).

Though steady state, open channel theory predicts a logarithmic boundary layer profile for the mean current, the observed boundary layer requires a correction term to add

curvature in all but ~20 percent of the cases in a particular period of inundation. In theory, fluid unsteadiness or density stratification defines a length scale that determines the magnitude of the correction (see equations 5.3 and 5.5). However, neither the acceleration nor stratification length scale models the observed behavior, possibly because the time scale for mixing in the water column is less than the time scale of variation in the motion, which is set by the 8 minute seiching motion. Indeed, as shown in figure 5.19, a k-ε numerical model (GOTM) demonstrates that mixing to a height of 0.3 m takes longer than half a wave cycle($t > 180$ degrees= 4 minutes), which is longer than the time scale for the boundary layer to develop to its maximum height ($t \sim 90$ degrees= 2 minutes).

Therefore, the current boundary layer in the intertidal zone needs to consider the unsteadiness in the flow that occurs because of the seiching motion. As shown, simple analytical models such as Smith (1977) do well to approximate the boundary layer of ocean swell and other gravity waves. However, the seiche boundary layer is not well represented by an analytical wave model, likely because the simplifying assumption of a time invariant, linearly varying eddy viscosity inadequately captures the physics. Instead, a more complex, physically realistic eddy viscosity needs to be modeled by a two equation (k-ε) numerical model such as GOTM. By not assuming steady flow, well developed conditions, and a linear variation of eddy viscosity, the GOTM is able to more closely simulate the observed boundary layer than either the analytical current or wave boundary layer models. In fact the GOTM analysis shows that eddy viscosity and

TKE varies significantly over a seiche time period, and therefore greatly affects the structure of velocity in the water column.

The variation of bed stress, TKE and eddy viscosity as a function of both the phase of the seiching motion and height off the bed (as predicted by measured results and GOTM) suggests that the erosion of sediment and its mixing in the water column is also likely complex. Moreover, non-linear wave current interactions add another layer of complexity, by increasing both the instantaneous and mean stress felt by the bed. Finally, tidal currents represent another source of near bed energy. These multiple frequencies of motion interact over different characteristic time scales, causing shear in the boundary layer over different time and length scales. Thus, the overall interaction of hydrodynamics with the bed is a complex function of tidal currents, seiching motions, ocean swell, and wind waves. Results also show that bed roughness caused by ripples affects how fluid interacts with the bed. Chapter 6 explores sediment erosion and transport at the intertidal mudflat and how it is related to variations in the primary forcing mechanisms.

5.6. Figures

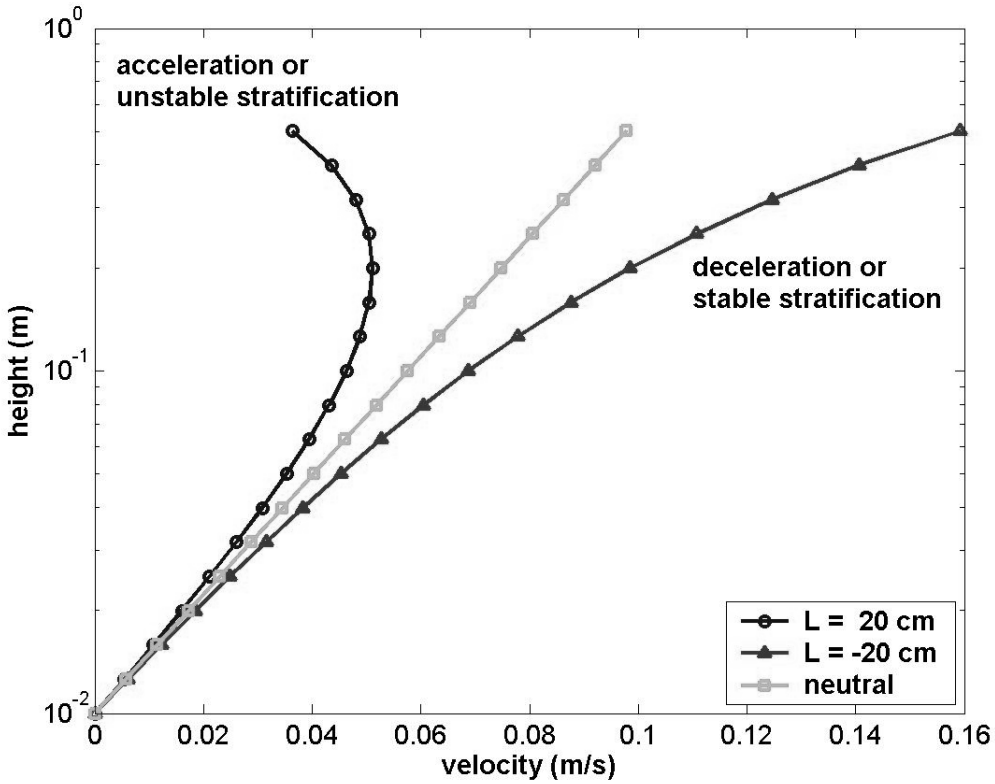

Figure 5.1: Graphical depiction of equation 5.2, using a friction velocity of 0.01 m/s, a roughness height of 0.01 m, and an arbitrary length scale of ± 0.2 m. These values are typical orders of magnitude on the intertidal mudflat at the Richmond Field Station. Neutral conditions refer to a length scale of ± ∞, in which case equation 5.2 reduces to equation 5.1.

(5.2a)

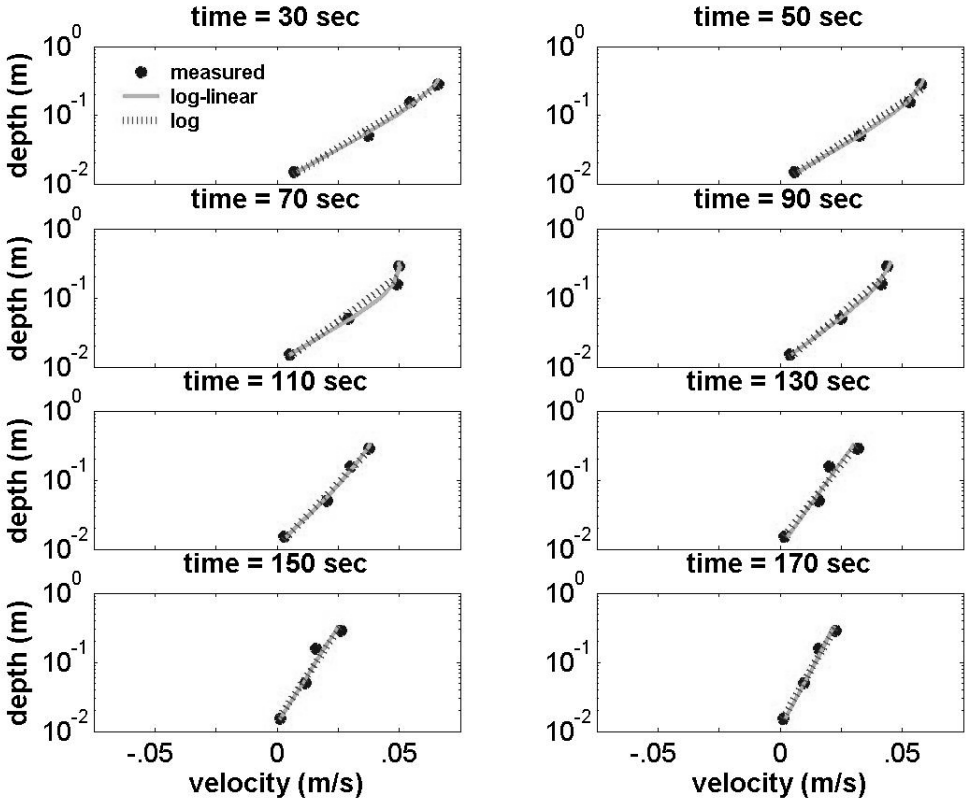
time = 30 sec
time = 50 sec
time = 70 sec
time = 90 sec
time = 110 sec
time = 130 sec
time = 150 sec
time = 170 sec
measured
log-linear
log
depth (m)
velocity (m/s)
-.05
0
.05

(5.2b)

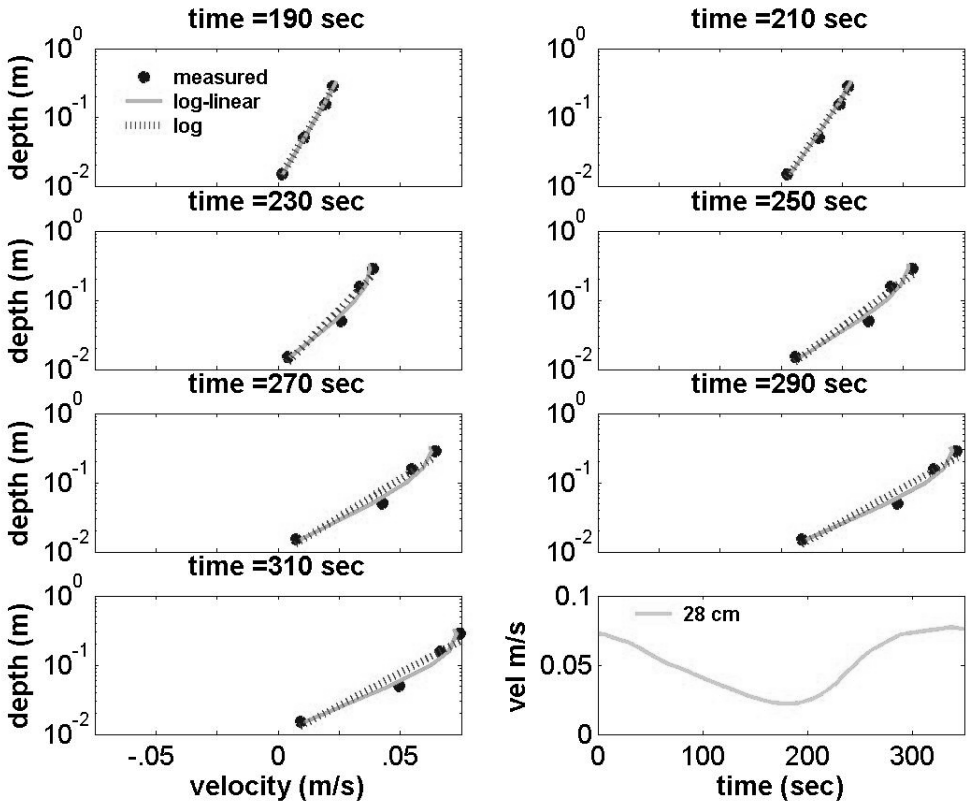

Figure 5.2: Example of fitting the log-profile and the log-linear profile to horizontal velocity over a 5 minute period during the flood tide starting in the evening of April 13th, 2003 at 6:40 p.m. (tide 5). Measured velocity data are shown by solid circles, while the log-linear profile and log profile are shown by a solid line and a dashed line, respectively. Each frame shows a snapshot of the velocity profile, separated from the previous profile by 20 seconds. For comparison, the velocity at a height of 0.285 m is shown in the bottom right frame of (b). Note that both the log profile and the log-linear profile model the data fairly well over this 5 minute period. The measured data points correspond to the velocimeters at 0.015 m, 0.05 m, 0.155 m, and 0.285 m.

(5.3a)

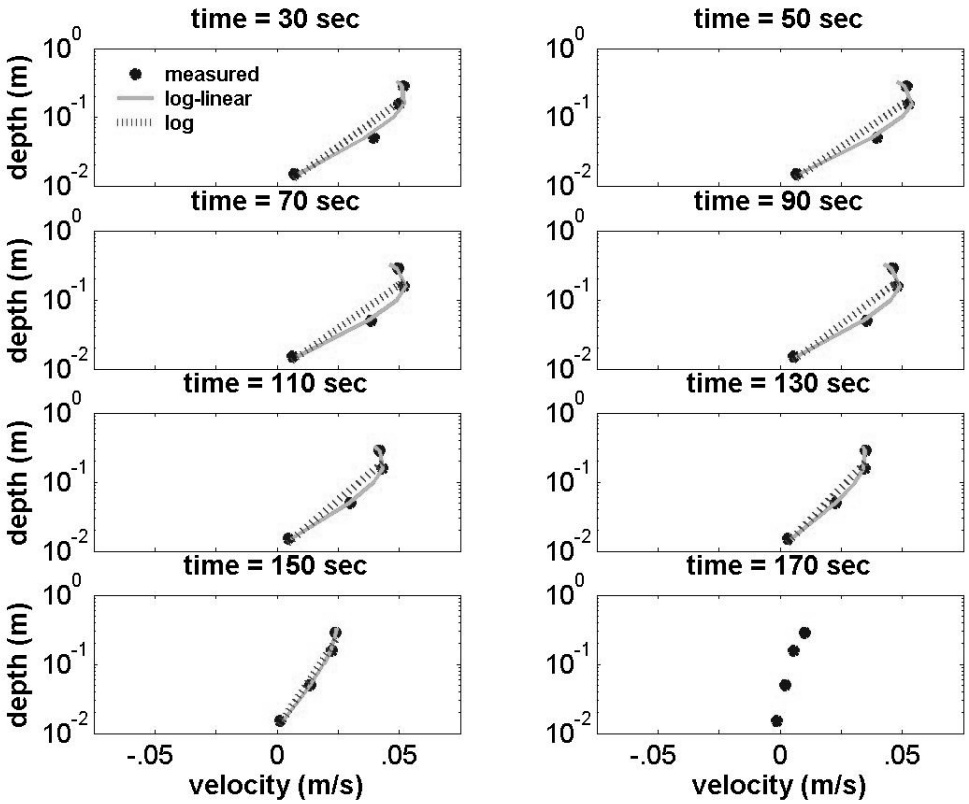
time = 30 sec
time = 50 sec
time = 70 sec
time = 90 sec
time = 110 sec
time = 130 sec
time = 150 sec
time = 170 sec
measured
log-linear
log
depth (m)
velocity (m/s)
-.05
0
.05

(5.3b)

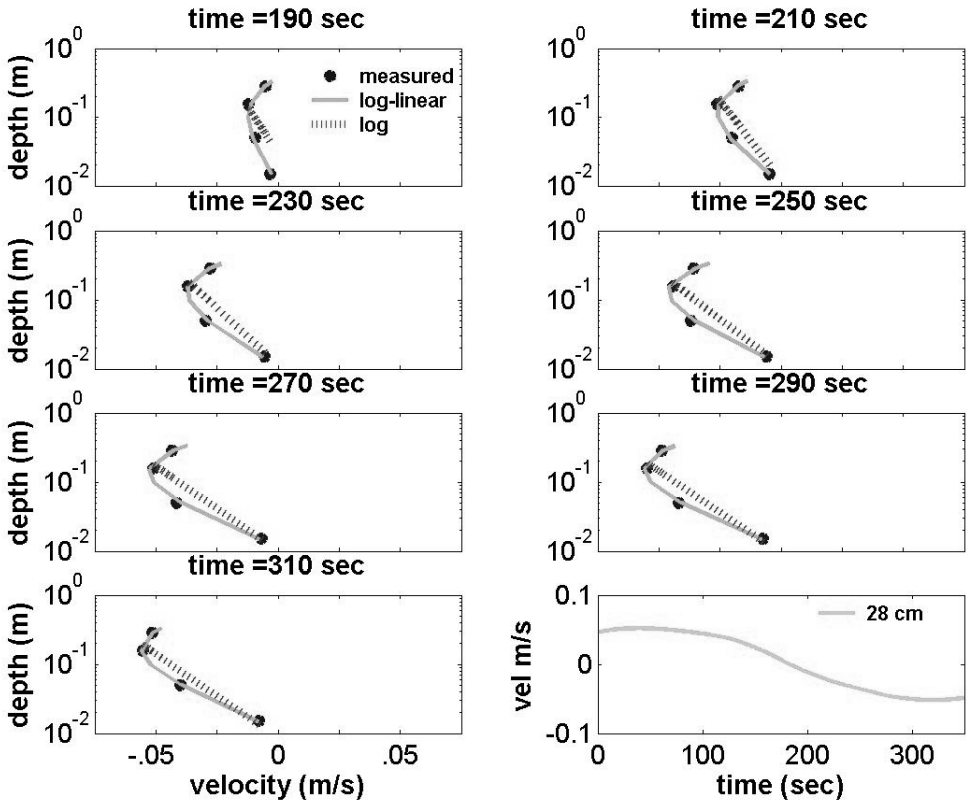

Figure 5.3: Another example of fitting the log-profile and the log-linear profile to horizontal velocity over a 5 minute period during the floodtide starting at 6:40 p.m. on April 13th, 2003 (tide 5). Measured velocity data is shown by solid circles, while the log-linear profile and log profile are shown by a solid line and a dashed line, respectively. For comparison, the velocity at a height of 0.28 m is shown in the bottom right frame of (b). Note this time period occurs only 30 minutes after the figure shown in 5.2, but displays quite different behavior. In particular, the log-linear profile is a much better fit to the data than the logarithmic profile. The measured data points correspond to the velocimeters at 0.015 m, 0.05 m, 0.155 m, and 0.285 m.

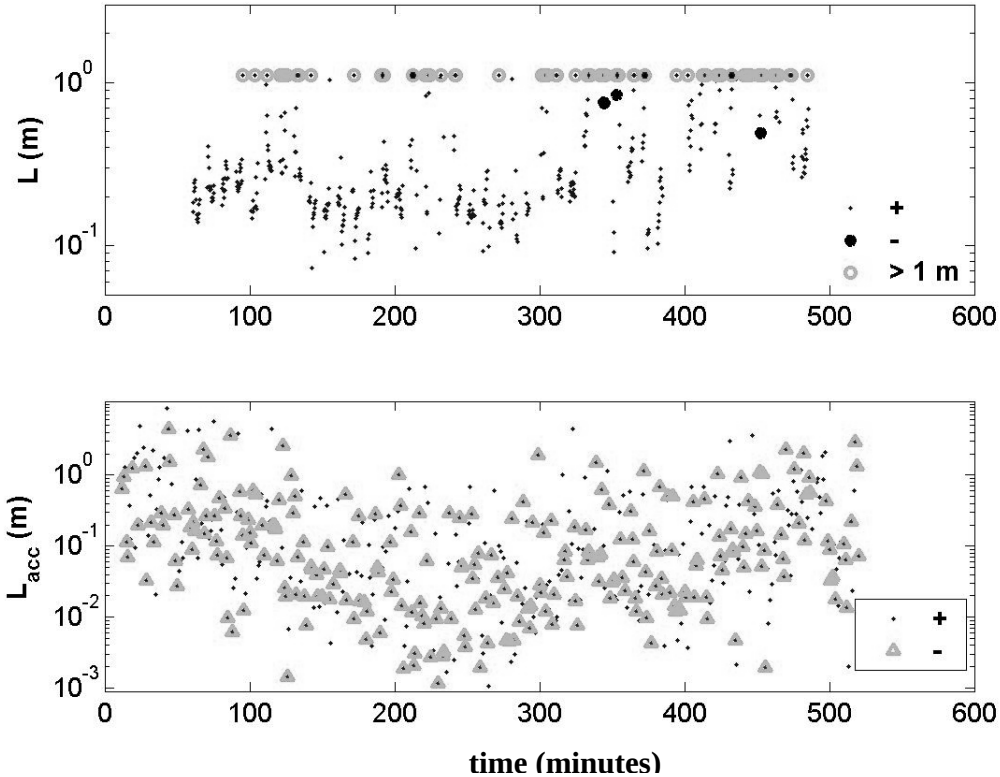

Figure 5.4: Comparison of the lengthscale 'L' calculated using an optimized, three parameter fit to data (top panel) vs. the acceleration length scale L_{acc} calculated using equation 5.3 (bottom panel) for a period of inundation beginning at 6:40 pm on April 13th, 2003. In each panel, '+' refers to a positive length scale, while '-' refers to a negative length scale. Virtually all of the observed velocity profiles are fit with positive length scales (top panel), indicating that velocity magnitudes are less than predicted by a logarithmic fit (see figures 5.2 and 5.3). By contrast, the acceleration length scale is both positive and negative, and reflects accelerating and decelerating conditions (see figure 5.1).

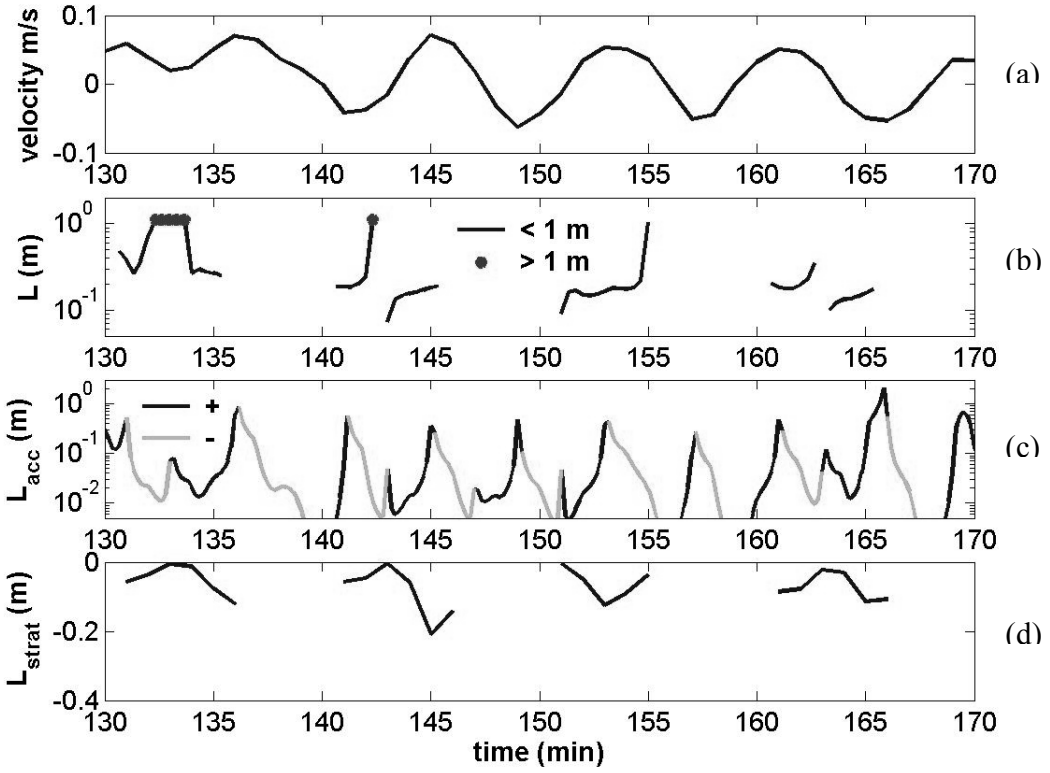

Figure 5.5: Comparison of the measured lengthscale 'L' (panel 'b) with the acceleration lengthscale (panel 'c', from equation 5.3) and the stratification lengthscale (panel 'd', from equation 5.5) over a 40 minute period of time on April 13th, 2003. For comparison, the 1 minute mean velocity over the same time period is shown in panel 'a'. The time from 130-135 minutes corresponds with figure 5.2, while the time from 160-165 minutes corresponds with figure 5.3. In panel 'b', any measured lengthscale greater than ~1 has been arbitrarily set to '1' for visualization purposes. Panel 'c' is the absolute value of L_{acc}, but is separated into positive (dark) and negative (light) colors.

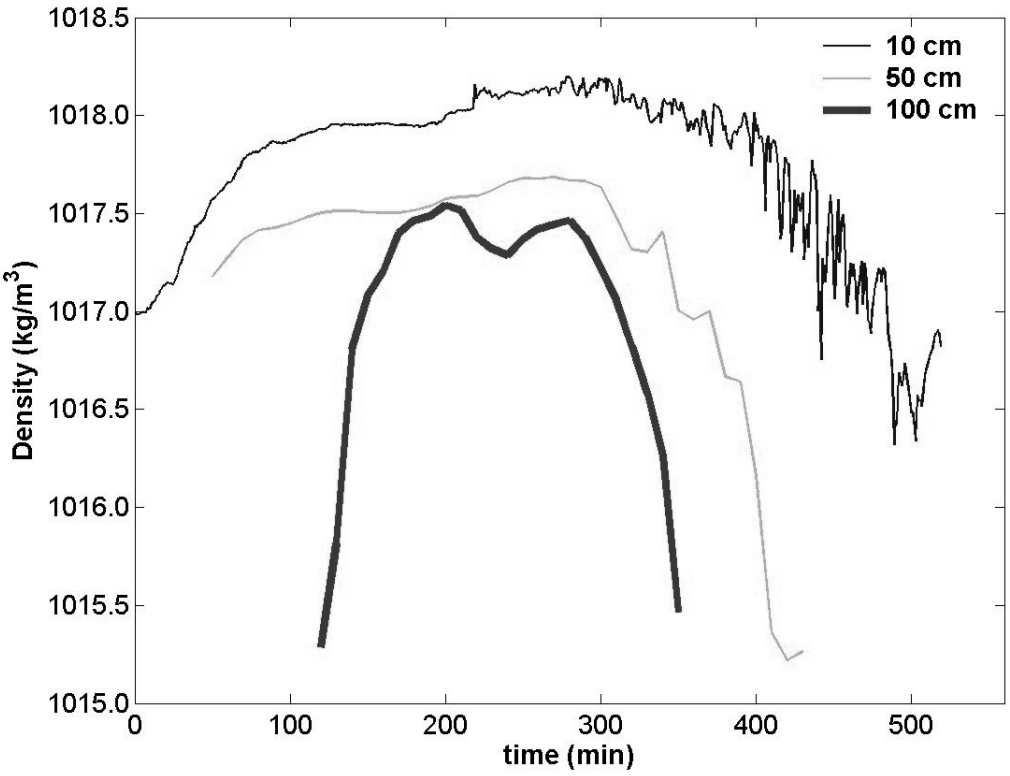

Figure 5.6: Profile of density over an immersed period beginning at 6:40 pm on April 13th, 2003, calculated using measured salinity and temperature data at three different heights off the bed. Note that the CTD at 0.1 m measured once every minute, allowing it to measure fluctuations on the seiche time scale. On the other hand, the CTDs at 0.5 m and 1 m measured only once every 10 minutes.

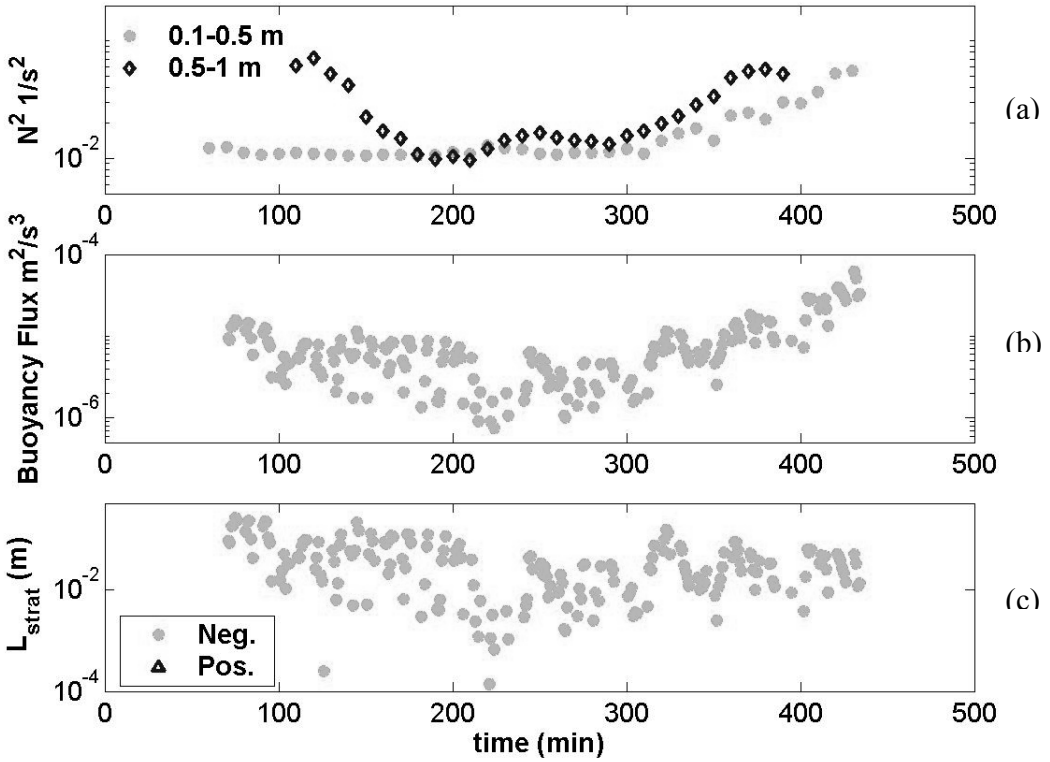

Figure 5.7: Calculations of buoyancy frequency N^2 (panel 'a'), buoyancy flux B (panel 'b'), and Stratification length scale L_{strat} (panel 'c', based on the Monin-Obhukov length scale L_{mo}) over an immersed period beginning on April 13th, 2003. A time of zero minutes corresponds to 6:40 p.m. Note that all values of the buoyancy flux are positive (stable) and that all L_{strat} (and L_{mo}) are negative, indicating stable stratification. The buoyancy flux and L_{mo} are calculated using the buoyancy frequency between 0.1-0.5 m.

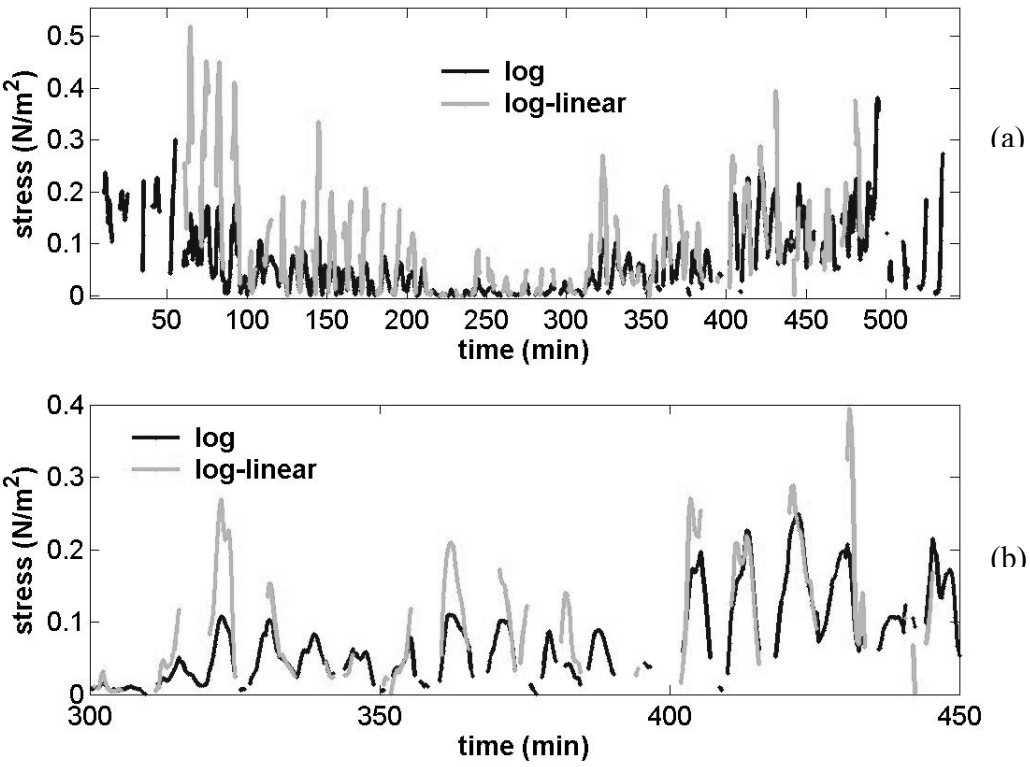

Figure 5.8: Comparison of the bed stress calculated using the log method and the log-linear fit over a completer period of inundation (upper panel, labeled 'a') and over the ebb (lower panel, labeled 'b') of a period of inundation beginning on April 13th, 2003 (tide 5). A time of zero minutes corresponds to 6:40 p.m.

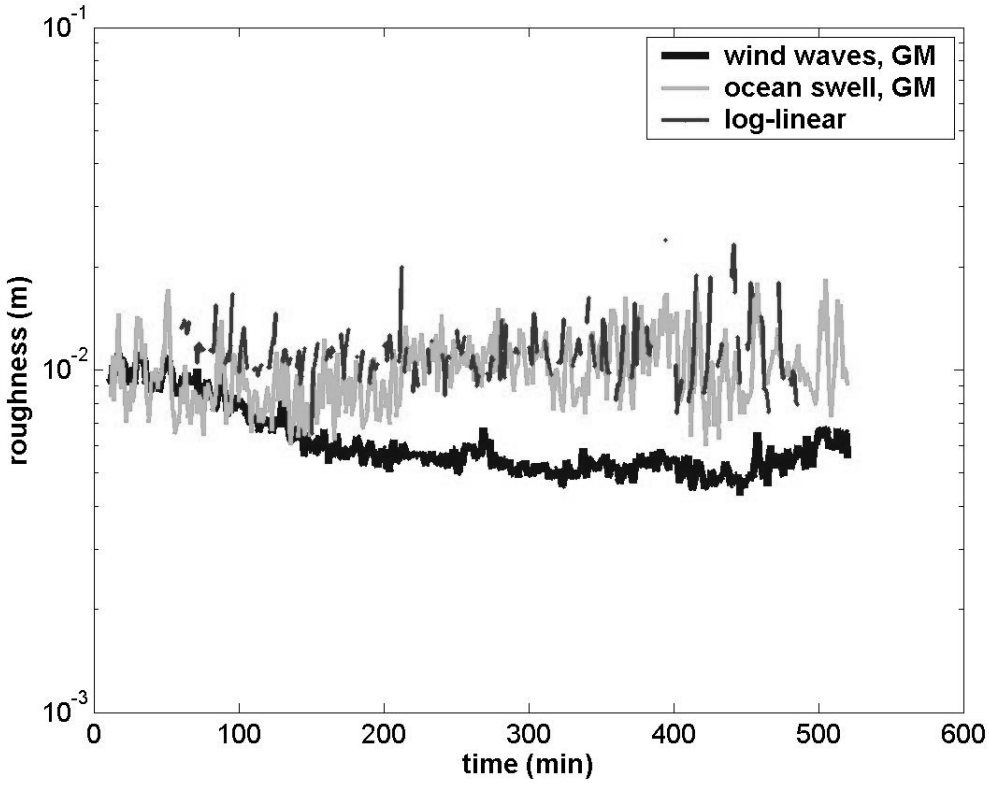

Figure 5.9: Comparison of the roughness height z_{opt} measured using the log-linear fit and the virtual roughness height calculated by the Grant and Madsen (1986) method using both wind waves ($z_0^*{}_{,ww}$)and ocean swell ($z_0^*{}_{,ow}$). A physical roughness height z_0 of 0.0035 m is input into the GM'86 model. All data is from the period of inundation beginning on April 13th, 2003 at 6:40 p.m. (t=0). As can be seen, the roughness predicted by the GM'86 method with ocean swell agrees well with experimentally measured data. By contrast, only the largest wind waves cause a virtual roughness that agrees with the experimentally measured roughness height.

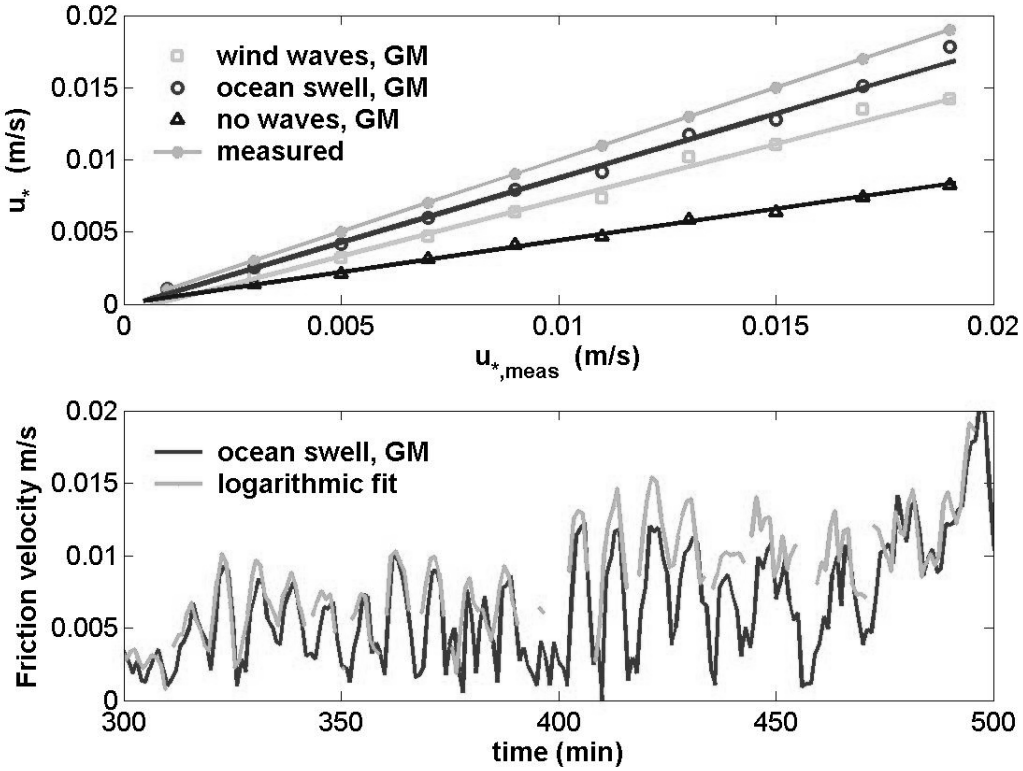

Figure 5.10: The top panel shows the least squares fit to a scatter plot of friction velocity calculated using the Grant-Madsen (GM) non-linear wave-current interaction algorithm vs. the friction velocity measured using a logarithmic fit (labeled 'measured'). For visualization purposes, the scatter plot data is bin-averaged and presented as points. The bottom panel compares friction velocity found using a logarithmic fit to velocity data and using the GM algorithm with ocean swell. Both panels refer to the period of inundation starting on April 13th, 2003. A time of zero minutes corresponds to 6:40 p.m. Note that the measured friction velocity is also plotted against itself to give a reference 1:1 slope in the top panel. Using ocean swell as the wave parameter in the GM model comes closest to matching the measured friction velocity.

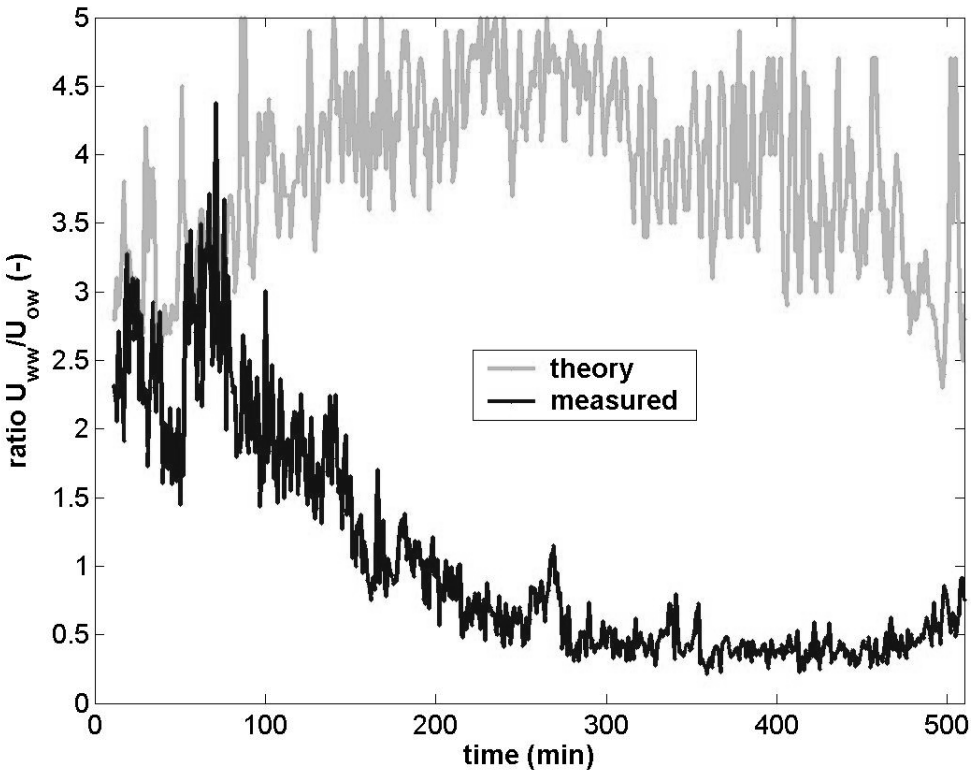

Figure 5.11: Comparison of the ratio of wind wave orbital velocity to ocean swell orbital velocity over an immersed period beginning on April 13th, 2003. A time of zero minutes corresponds to 6:40 p.m. The theoretical ratio shows the factor that wind waves would need to be greater than the measured ocean swell in order to produce the same friction velocity in the mean current (u_{*c}). For comparison, the actually ratio of wind-wave to ocean swell orbital velocity is displayed. Over this particular tidal period, ocean swell has a greater effect on the mean current than wind waves (except before t=80 minutes).

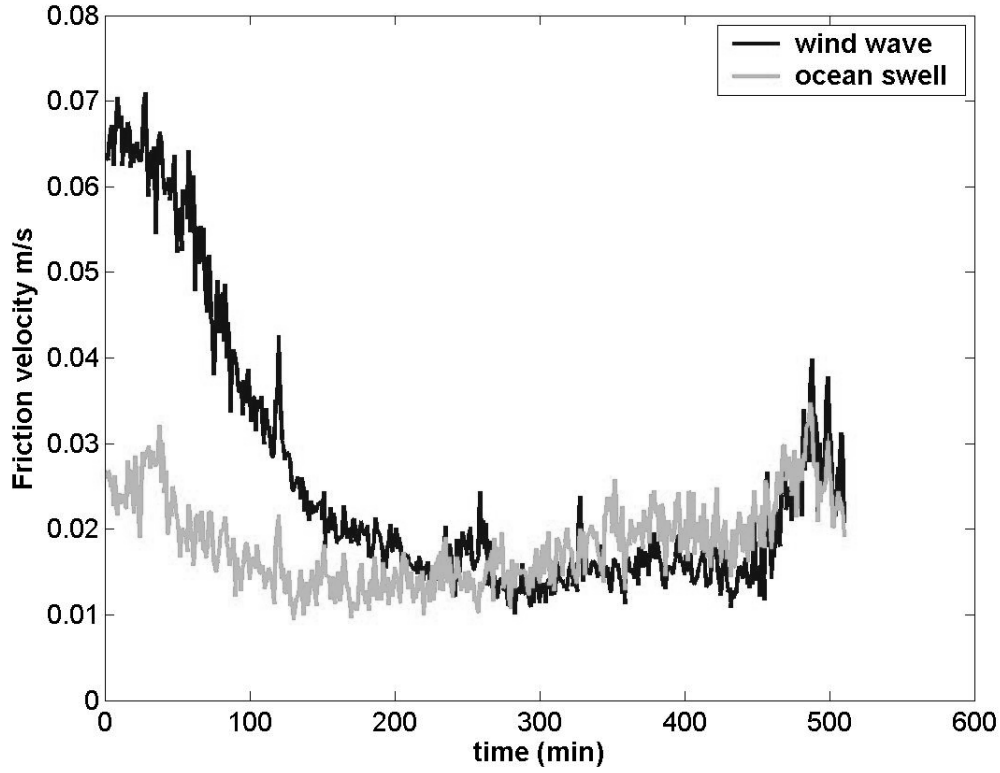

Figure 5.12: Maximum friction velocity in the boundary layer for wind waves and ocean swell calculated using the GM'86 method for a period of inundation on April 13th, 2003. A time of zero minutes corresponds to 6:40 p.m. During the flood (0-200 minutes), large wind waves cause large friction velocities; during the ebb (300-500 minutes), waves at the ocean swell frequency and wind wave frequency apply approximately the same maximum stress on the bed.

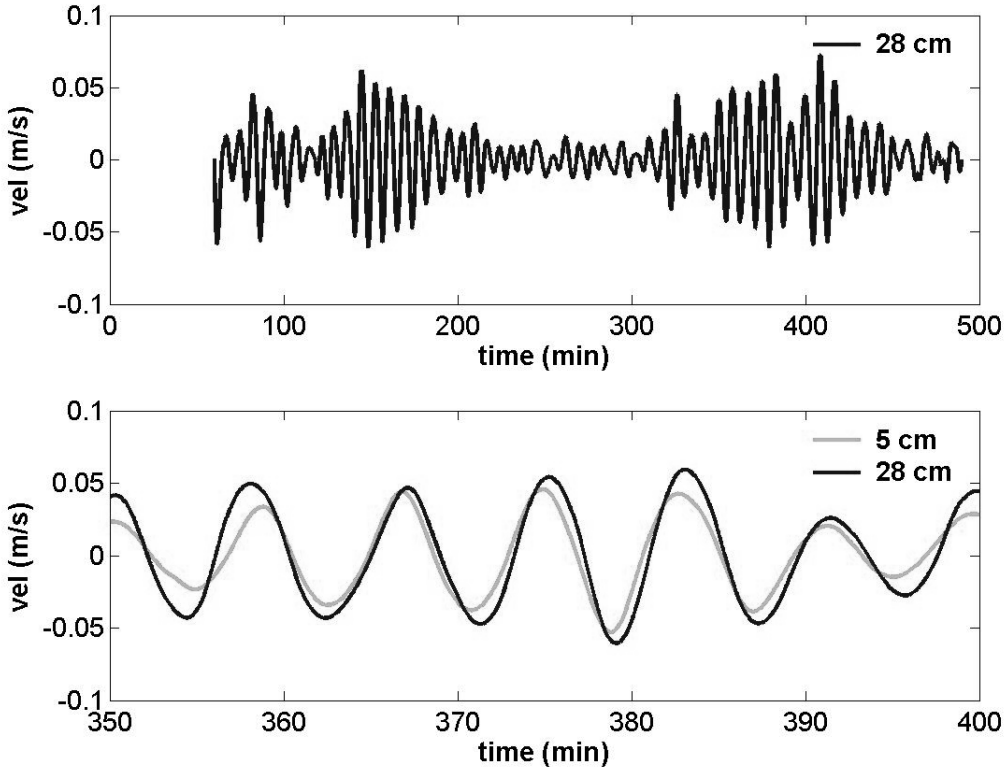

Figure 5.13: Example of bandpassed filtered seiche velocity over a period of inundation on April 13th, 2003. A time of zero minutes corresponds to 6:40 p.m. The upper and lower limits of the filter were 800 seconds and 300 seconds, respectively. The top frame ('a') follows the seiche at 0.28 m over the entire period of inundation, while the bottom frame ('b') compares the seiche at 0.28 m and 0.05 m. Note that while the seiche at 0.28 m is (nearly) continuous, the set at 0.05 m has been interpolated over 245 out of 600 seconds. Thus, only un-interpolated portions of the data at 0.05 m are used.

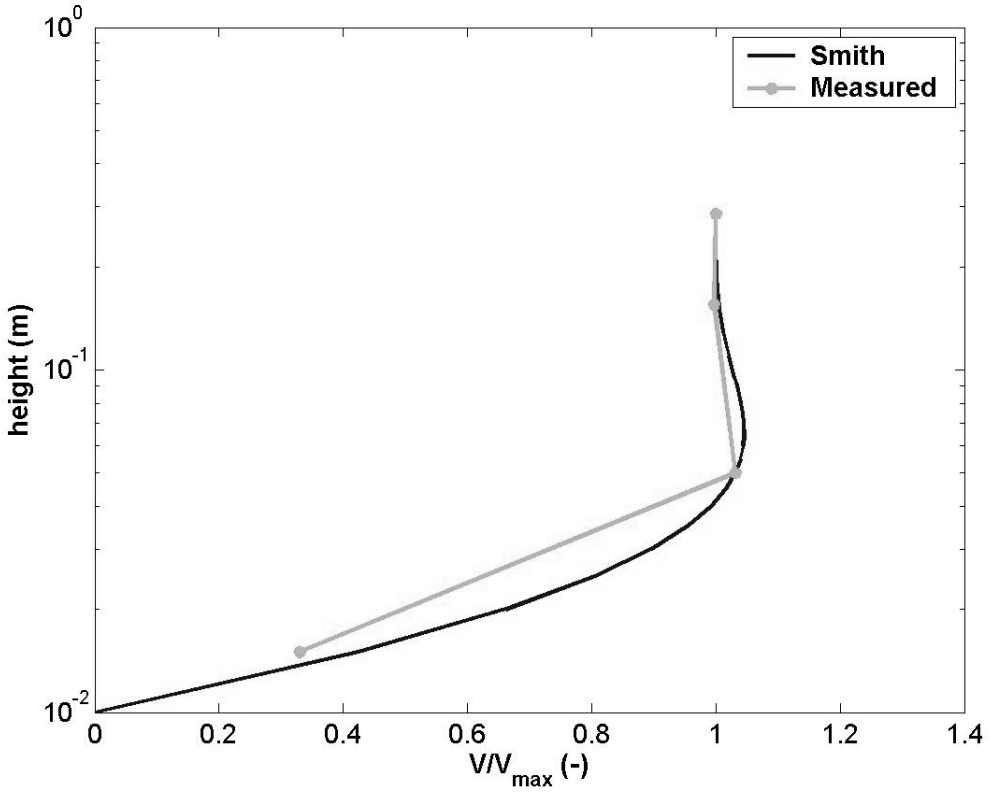

Figure 5.14: Rms (root mean square) boundary layer structure of ocean swell using the Smith (1977) model and measured ocean swell. Each profile is normalized by the velocity of the upper measurement at z=0.28 m. A wave amplitude of 0.026 m/s and a roughness of 0.01 m are input into the Smith (1977) model, giving a rms amplitude of 0.019 m/s over a wave cycle at a height of 0.020 m. This corresponds well with the measured, median rms velocity of ~0.019 m/s at a height of 0.285 m.

(5.15a)

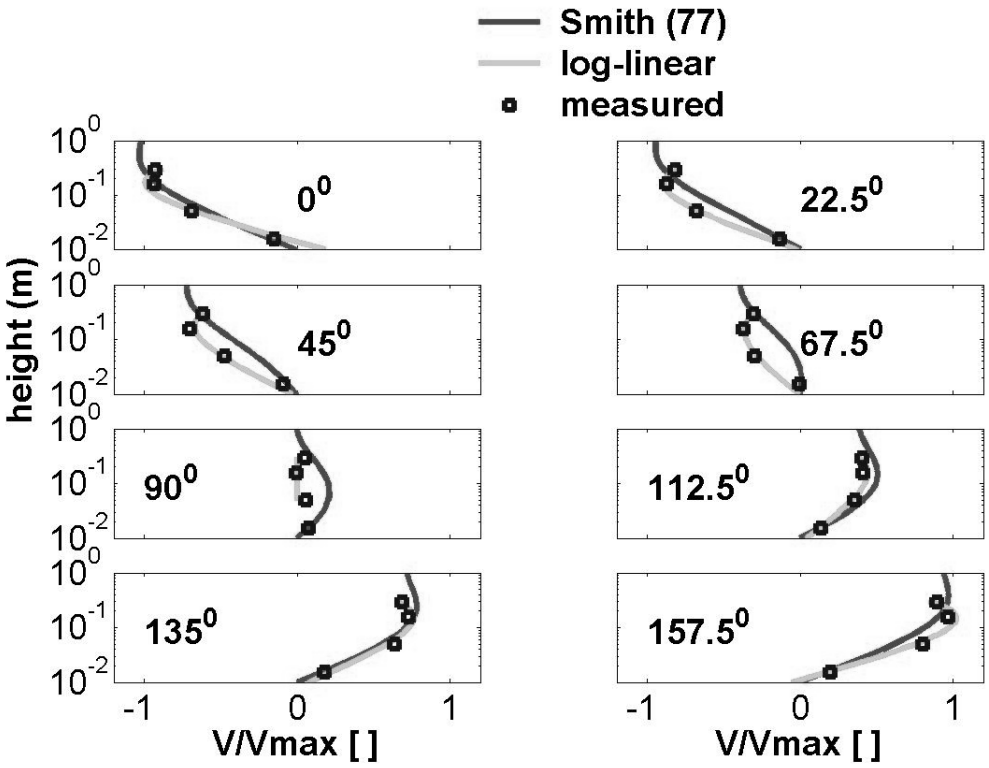
Smith (77)
log-linear
measured
height (m)
10^0
10^{-1}
10^{-2}
0^0
22.5^0
45^0
67.5^0
90^0
112.5^0
135^0
157.5^0
-1
0
1
V/Vmax [ ]

5.15(b)

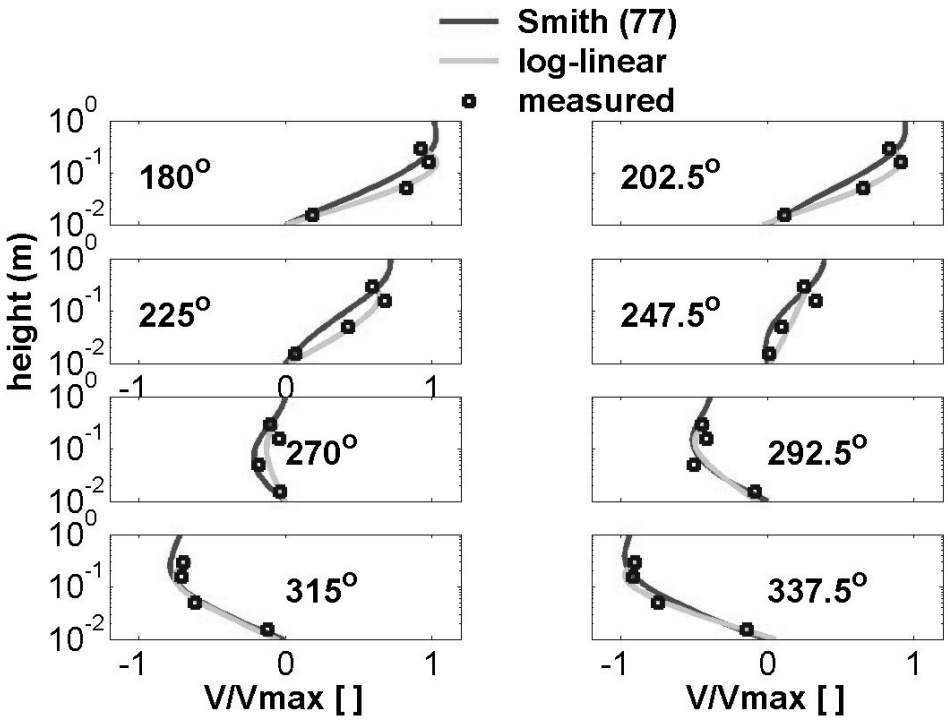

Figure 5.15: Measured profile of seiche boundary layer over all phases of the seiche (T=500 seconds) compared to the log-linear optimization and the Smith Boundary layer model. The measured profile is the average of many seiche cycles over the immersed period beginning on April 13th, 2003. Each individual seiche is normalized by the maximum velocity at z=0.285 m before averaging. The measured data points correspond to the velocimeters at 0.015 m, 0.05 m, 0.155 m, and 0.285 m.

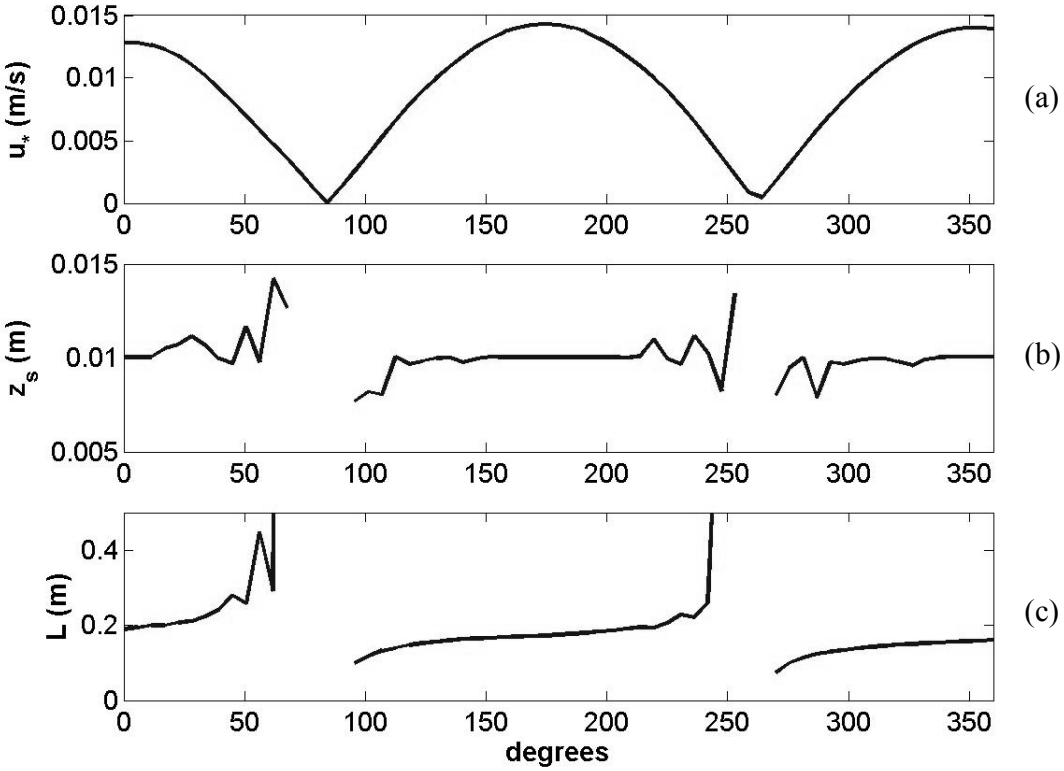

Figure 5.16: Friction velocity u_* (labeled 'a'), bottom roughness z_s (labeled 'b'), and length scale L (labeled 'c') as a function of phase angle of the normalized seiche. The values are found from the log-linear equation (see equation 5.2). The normalized seiche is found from the set of seiche wave cycles with an orbital velocity between 0.05 m/s to 0.08 m/s, in the manner described in section 5.4.2. To obtain a dimensional u_* estimate, we scale the normalized seiche profile by a factor of five, yielding a seiche amplitude of ~ 0.05 m/s at the height of z= 0.285 m/s.

5.17(a)

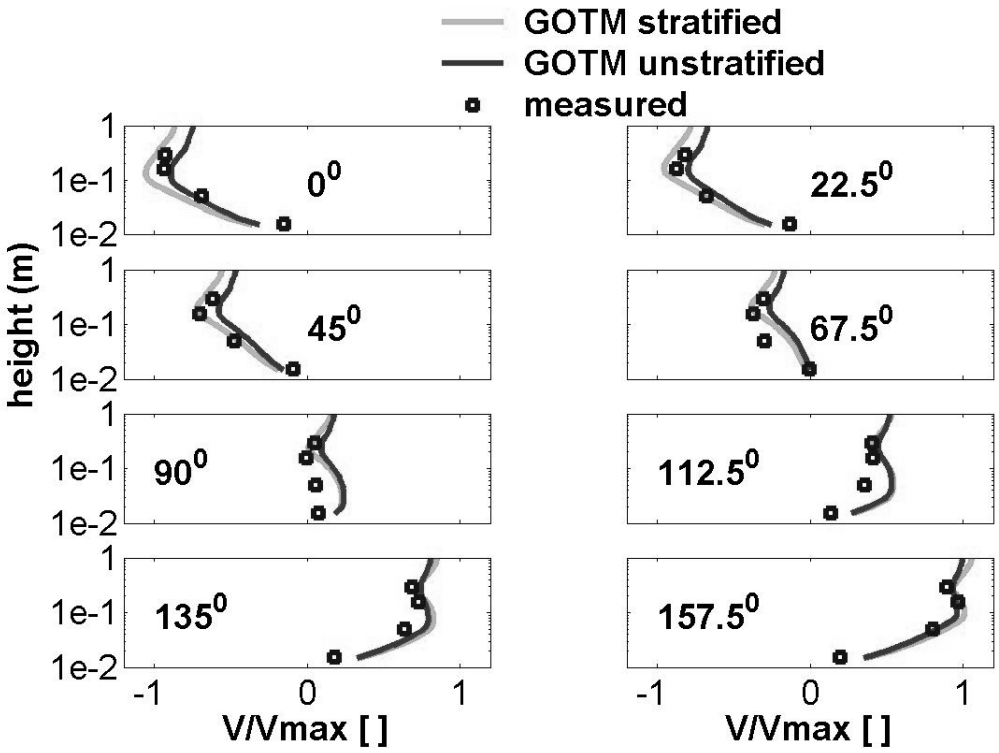
GOTM stratified
GOTM unstratified
measured
height (m)
1
1e-1
1e-2
0⁰
22.5⁰
45⁰
67.5⁰
90⁰
112.5⁰
135⁰
157.5⁰
-1
0
1
V/Vmax [ ]

5.17(b)

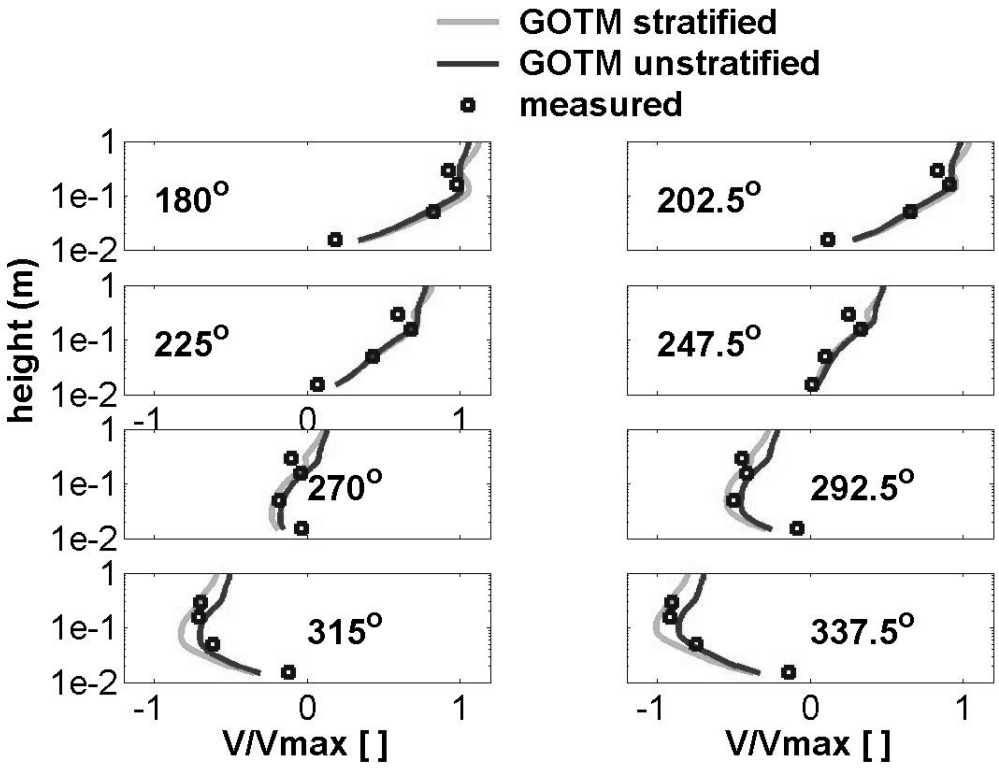

Figure 5.17: Comparison of measured seiche boundary layer over a wave cycle to the results of GOTM (General Ocean Turbulence Model) using both a stratified and unstratified boundary layer. The measured profile is the average of many seiche cycles over the immersed period beginning at 6:40 p.m. on April 13th, 2003. Each individual seiche is normalized by the maximum velocity at z=0.285 m before averaging. The measured data points correspond to the velocimeters at 0.015 m, 0.05 m, 0.155 m, and 0.285 m. Linear stratification from a salinity difference of 0.8 ppt is applied between a height of 0.10 m and 0.50 m.

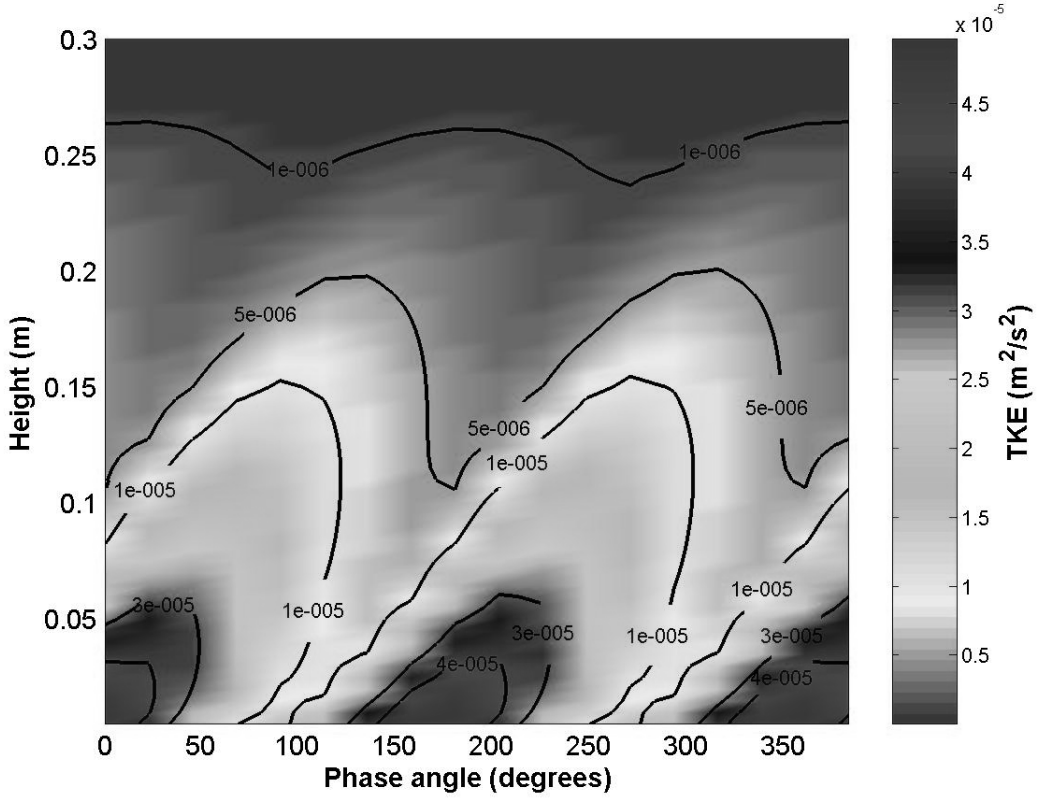

5.18: Evolution of TKE as a function of phase angle and height over an 8 minute (480 second) seiche using GOTM. Zero degrees is defined as the maximum, offshore (negative) seiching motion. As can be seen, maximum production occurs at 0 and 180 degrees (at maximum velocity) and then propagates up through the water column. Though the stratified case is depicted, unstratified conditions yield a similar behavior.

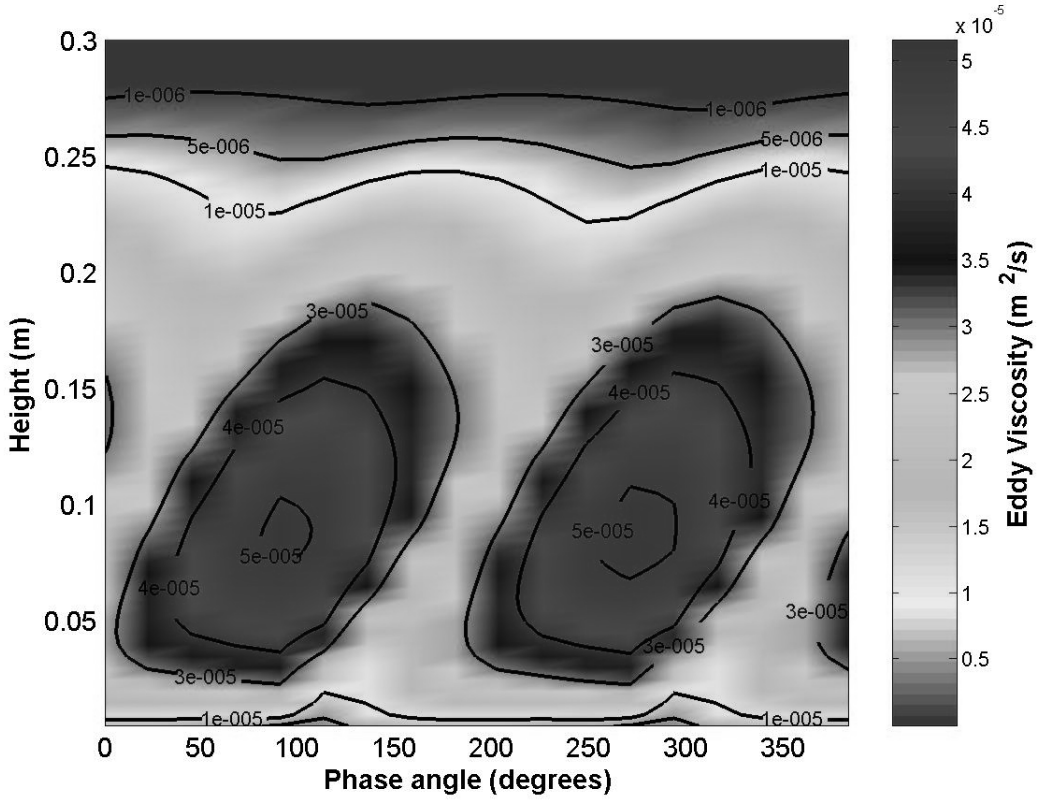

Figure 5.19: Eddy viscosity predicted by GOTM as a function of phase angle and depth. over an 8 minute (480 second) seiche wave for the stratified case. Zero degrees is defined as the maximum, offshore (negative) seiching motion. The eddy viscosity is a function of two competing scales—the lengthscale of turbulence, which increases with height, and the TKE, which decreases with height and is shown in figure 5.18. Note that the unstratified case yields a similar behavior.

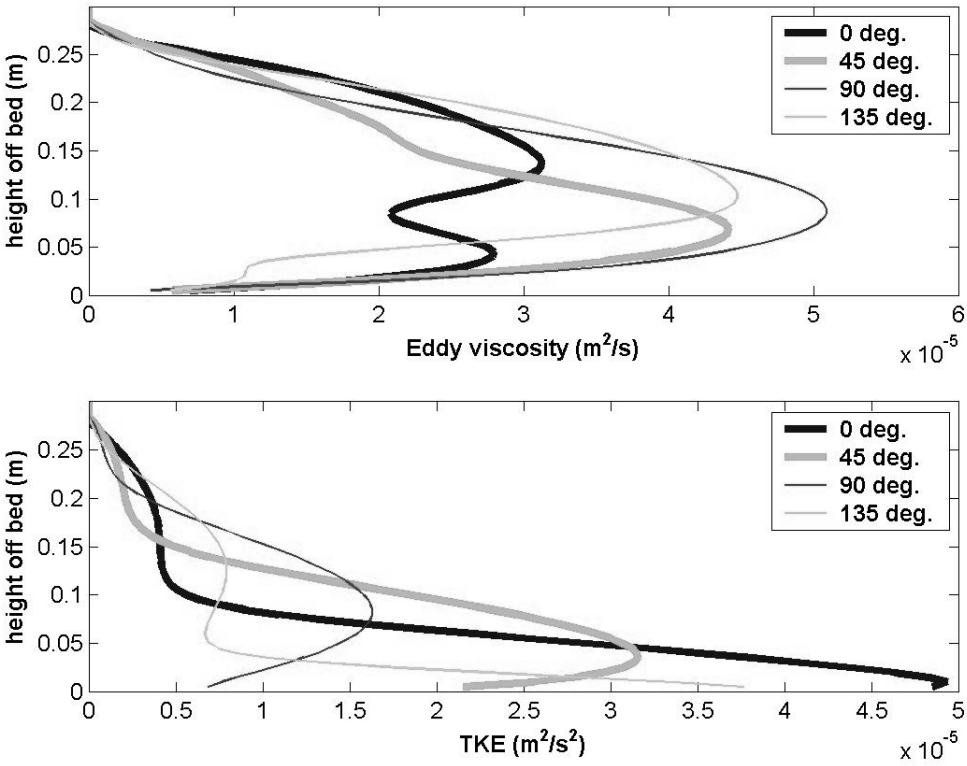

Figure 5.20: Eddy viscosity and TKE vs. depth and phase of the seiche. TKE is at a maximum at zero degrees near the bed, while eddy viscosity is largest at 90 degrees at a height of ~0.1 m. Note the double maximums of eddy viscosity at zero degrees and 135 degrees. Similarly, TKE shows a double inflection at 135 degrees.

Chapter 6: Sediment Transport

The Richmond inner harbor area is subject to waves of several frequencies, including locally driven wind waves, ocean swell, and an 8 minute second seiche (see chapter 3). Overlaid onto tidal velocities, these forcing frequencies create a continuously varied environment with intermittently large and small stresses occurring over the time scale of seconds to hours (see chapter 5). The turbulent eddies produced by the flow determine the boundary layer structure and the characteristic mixing of scalars such as sediment throughout the water column (see chapters 4 and 5). Sediment transport occurs by the various frequencies of motion, mediated by resuspension and deposition processes. In this chapter we separate the fluctuations of sediment concentration into wave, seiche, and tidal components, and investigate how these motions contribute to sediment erosion, deposition, and flux.

6.1. Introduction and Theory

Well-established theory holds that consolidated sediment erodes above a critical stress for erosion ($\tau > \tau_{crit}$) and is held in suspension above a critical bed stress for deposition (Partheniades, 1962, Krone, 1962). As a result, many intertidal studies focus on characterizing the critical shear stress for erosion and deposition; these field and laboratory studies show increases in sediment concentration due to fluid shear stress exceeding a critical value (see e.g. Amos et. al, 1998 , Mitchener et al. 1998, Christie and Dyer, 1998, Christie et al., 1999, Widdows et al., 1998, Houwing, 1999). Critical

shear stress varies based on the bulk density, water content, and grain size of the sediment (Mehta et. al, 1989, Williamson and Ockenden, 1996), and on the areal coverage of benthic algae (e.g., Paterson 1997, Kornman and De Deckere, 1998). Thus, both physical and biological factors must be considered when estimating critical shear stress (Houwing, 1999). Though many models exist, the simplest holds that the erosion rate is proportional to the amount that the critical stress threshold is exceeded (see e.g. Teisson et al., 1993). Once in the water column, vertical mixing of sediment is controlled by turbulent motions, which are modeled either as a diffusive process or by convective motions such as vortices (Smyth et al., 2002, and Sleath, 1990; see chapter 5 for discussion of mixing). The combination of erosion and mixing into the water column sets the conditions for the net advection of sediment in suspension. On intertidal mudflats, the residual, net sediment flux on an intertidal mudflat is attributed in general to the action of waves and currents. For example, Christie et al. (1999) found that in calm conditions, tidal currents brought sediment onshore, whereas during windy conditions erosion occurred.

Though the critical shear stress is undoubtedly an important physical parameter, many other processes are important and lead to erosion, resuspension, and sediment transport. Physical processes such as cyclic vertical loading by wave pressure can soften the bed or cause fluidization and erosion (Mehta, 1989, Teisson et al.,1993); once fluidized, the concept of a critical stress that causes resuspension and transport is ambiguous, since by definition an unconsolidated fluid mud layer is essentially a non-Newtonian fluid with no shear strength, and can flow or oscillate due to applied shear. Resuspension of fluid

mud into the water column is poorly understood, though laboratory experiments describe oscillations at the water/fluid mud interface that lead to entrainment of sediment into the water column through vortex shedding (Mehta and Maa, 1986). Once suspended, shear from currents, ocean waves, and wind waves not only interact with the bed on the mudflat through bed stresses, but play a role in both the aggregation and breakage of flocs (Van der Lee 1998), thus modifying the depositional dynamics of cohesive sediments.

For environments in which sand or larger grained silt dominates, a different suite of physical processes occur. For example, over the cycle of a wave, flow separates at the crest of a ripple, leading to the growth of a low pressure region; when pressure reverses, this bubble is ejected into the flow (Fredsoe 1993). The interaction of these vortices with ripples and dunes leads to the erosion and ejection of sediment into the water column (e.g., Sleath and Wallbridge, 2002, Fredsoe 1993, Black and Vincent 2000). In addition to resuspending particles into the water column, the skin drag exerted by the flow on a sandy bed can cause grains to roll along the bed either as independent grains or as sheet flow (Fredsoe, 1993). Sheet flow occurs during high stress conditions and consists of the advection of layers of sediment. As stress decreases below a Shields parameter of ~1.0, sand waves (dunes or ripples) are formed and individual grains are transported over the wavy bedforms. In some conditions, sand grains actually migrate counter to the mean current (e.g. Inman and Bowen, 1962). Collectively, transport of sediment along the bed is described as bedload transport (Fredsoe, 1993). Though ripples are commonly considered to occur only in sandy environments (e.g. Fredsoe,

1993), these bedforms are also observed at mudflats in which silt predominates over a small sand fraction (Whitehouse et al., 2000).

Thus, there are many mechanisms that can affect sediment transport on a bed containing both sand (non-cohesive, grain size > 62 micrometers) and silt (cohesive, grain size < 62 micrometers) components, as occurs at the field site at the Richmond Field Station (see chapter 2, or Ralston, 2005). For example, on mudflats in the Dutch Wadden Sea in which sand dominated (< 20 % silt), Houwing (1999) found that the critical erosion threshold applied only to the silt portion of the bed, which eroded in a floc by floc manner; by contrast, the sand portion was moved as bed load. In San Francisco Bay, Krone (1962) found that fine grained silt will settle out of the water column below a shear stress of 0.06 Pa when sediment concentrations are below 300 mg/L. When multiple grain sizes are present, the critical deposition stress varies as a function of grain size. As a result, grains often deposit in layers, with sand being covered by layers of silt (Dyer, 1998). Thus, for sediments and water columns in which several grain size fractions are present, interactions between them become complex and current practice is to analyze them separately (Mehta et al., 1989). To simplify, models often assume the bed is non-cohesive (sand) when the cohesive (silt) portion is less than 30 percent by volume (e.g. Knaapen et al., 2003).

In sandy conditions, Sleath and Wallbridge (2002) point out that bed flow over ripples is controlled by the acceleration parameter 'S' and the Shields parameter ψ :

$$S = \frac{\rho U_o \omega}{(\rho_s - \rho) g} \tag{6.1}$$

$$\psi = \frac{\tau_o}{(\rho_s - \rho) g D} \tag{6.2}$$

Where ρ_s is the density of the bed, ρ is the density of water, ω is the wave frequency, τ_o is the bed stress, D is the grain size and U_o is the orbital velocity. Sleath (1994) shows that below an acceleration parameter of 0.2 ($S < 0.2$), the height of the mobile layer is proportional to the grain size and Shields parameter. Above this value, acceleration and the horizontal pressure gradient becomes more important than the restoring force of gravity, and the height of the mobile bed increases greatly. Given that small grained sand (with a density of 2650 kg/m^3) predominates, but also considering the burrowing action of biota and the lesser density of the smaller silt fraction, a reasonable order of magnitude estimate for the bed density is 2000 kg/m^3, or roughly twice the density of water. Using this value of density results in an acceleration parameter below 0.2 for all conditions (wind wave or ocean swell) measured on the mudflat. Therefore, the height of the mobile bed layer is controlled by the Shields parameter ψ, which varies primarily with bed stress. Thus, as waves become larger as depth decreases, bed load transport increases. Above a Shield's parameter of 1, sheet flow can occur (Fredsoe, 1993). For a median grain size of ~ 80 micrometers, and a bed density of ~ 2000 kg/m^3, this gives a critical friction velocity of ~ 0.04 m/s. As shown in figure 5.11, large wind waves can exceed this stress, though ocean swell typically does not. Above this critical friction

velocity, ripples disappear, and are replaced by a flat bed. Therefore, the interaction of fluid with the bed fundamentally changes, and fluid motions induced by the ripples (e.g., the ejection of vortices) disappear as well.

6.2. Sediment Transport

The hydrodynamic forcing at the intertidal mudflat determines the resuspension and movement of sediment, and thus determines long-term morphological change. A complete analysis of sediment transport requires a mass-balance approach that considers both the landward and seaward boundary conditions and the patterns of sediment reworking within the mudflat domain. The field site for experiment #3 is ideally located between the outer breakwaters at the Richmond Field Station, which restricts lateral (east-west) movement of sediment and water. The OBS and ADV sensors thus measure sediment transported to and from the embayment behind the breakwater. Sediment fluxes measured at experiment #3 form a boundary condition that help determine whether the mudflat is exporting or importing sediment. The following analysis focuses on the immersed periods between April 13th and April 15th, 2003, immediately following the large storm of April 11th-12th. These periods of inundation are labeled tides 5-8; tide 5 corresponds to the immersed period displayed in figure 3.11a, while tide 8 corresponds to the immersed period in figure 3.11b.

6.2.1 Analysis technique

To investigate the different frequencies of motion and their effect on net sediment transport, we split both the concentration signal and the velocity into wave, seiche and tidal components using wavelet decomposition:

$$C = C_{tide} + C_{seiche} + C_{wave} \tag{6.3}$$

Similarly, we define velocity as follows:

$$V = V_{tide} + V_{seiche} + V_{wave} \tag{6.4}$$

Note that for simplicity, wind waves, ocean swell and long waves bound to these frequencies (e.g., wave groups) are lumped together into V_{wave}. This allows most energy associated with gravity waves (e.g., ocean swell or wind waves) to be included in the same data set, including non-linear harmonics and wave groups. Therefore, any wave oscillation with a period less than 90 seconds is categorized as a wave. Seiching motion is defined as any fluctuations between 90 seconds and 25 minutes, and thus accounts for higher harmonics of the 8 minute second seiche, as well as lower frequency variation in the seiche amplitude. Tidal fluctuations are defined as anything with a period greater than 25 minutes.

Assuming that dispersion and diffusive fluxes are small, the total sediment flux $\Phi_{sediment}$ over a period of inundation is then:

$$\Phi_{sediment} = C*V = C_{wave}*V_{wave} + C_{seiche}*V_{seiche} + C_{tide}*V_{tide} + \Phi_{cross-terms} \quad (6.5a.\ 6.5b)$$

$$\Phi_{cross-terms} = C_{wave}*V_{seiche} + C_{wave}*V_{tide} + C_{seiche}*V_{wave} + C_{seiche}*V_{tide} + C_{tide}*V_{wave} + C_{tide}*V_{seiche}$$

Wavelet decomposition separates a raw signal into independent scales that roughly correspond to different frequency ranges, which are then linearly combined to obtain concentration and velocity signals that contain those scales. Because the estimates at each scale are independent, leakage between frequency bands is avoided. By contrast, bandpass filters are leaky and include some energy from outside the specified frequency range. This leakiness increases the error in the estimates of flux, and shows up as residual flux in the cross-term components. The wavelet decomposition, on the other hand, minimizes the contribution of cross-terms to the total flux budget. Some error does occur, primarily because of distortion at the edge of the data sets. This is minimized by padding the beginning and end of each scale with a linear interpolation of the raw data set. Because the profile of the mean concentration is not symmetric between flood and ebb (i.e., the magnitudes of concentration are not the same), some residual cross-term flux (particularly between the seiche and the tidal components) may occur.

6.2.2: Sediment flux results

Applying equation 6.3 to the data sets of sediment and velocity over four tidal periods from April 13th to April 15th, 2003 results in the sediment fluxes shown in table 6.1. The sediment fluxes are measured at one location in the water column over the time period in which the instruments were immersed, which is listed in table 6.1. The concentration measurements are taken from the OBS at 0.05 m, while the velocity measurement at 0.155 m was used in order to obtain a continuous data set. Therefore, the flux estimates are from near the bottom. A logarithmic profile with an assumed roughness of 0.01 cm (see chapter 5) was used to extrapolate the seiche velocity and tidal velocity from 0.155 m to 0.05 m. Because horizontal wave orbital velocities are approximately constant between these heights (see chapters 4 and 5), no correction was applied.

Table 6.1: Net sediment flux due to different frequencies of motion at z= 0.05 m. Units are 10^{-3}* kg/m^3 * m/s. The begin date of each immersed period, as well as the begin and end times, are also shown.

Name	Begin Date	Begin time	End time	Wave Flux (C_{wave}*V_{wave})	Seiche Flux (C_{seiche}*V_{seiche}	Tidal Flux (C_{tidal}*V_{tidal})
Tide 5	April 13, 2003	18:40 pm	3:10 am	0.014	0.023	0.31
Tide 6	April 14, 2003	5:20 am	14:10 pm	0.005	0.001	0.132
Tide 7	April 14, 2003	19:00 pm	3:10 am	0.0024	0.001	0.15
Tide 8	April 15, 2003	7:10 am	15:00 pm	0.069	0.012	-0.26

The largest component of sediment flux on the mudflat is due to fluctuations in velocity and sediment concentration that occur on a tidal scale. By comparison, the seiche frequency makes notable contributions to the sediment flux for tide 5 and tide 8 (~7 percent and 5 percent of tidal flux), while sediment fluxes due to waves are largest during tide 8. Because the mudflat samples only a portion of each tidal period, asymmetry in the timing of sediment resuspension events and variations in the mean velocity play a large role in the direction of transport over an immersed period, as will be shown in section 6.2.3. The seiche flux represents the aggregate flux over 50 seiche periods, while the wave flux is the aggregate of thousands of waves. Therefore, though the tidal contribution to the sediment flux budget is much larger than either wave or seiche transport, the effect of aggregating over multiple tides has not been considered. The difference in sign between tide 5 and tide 8 suggests that some canceling will occur.

The noise level in the estimates of seiche and wave flux is calculated by adding an artificial phase lag to the data and estimating the resulting flux. The phase lag must be different than the periods of the ocean swell, wind waves, and the seiche. Since the phases of velocity and sediment concentration are then random, the resulting estimate measures flux due to experimental and numerical noise. Some correlation between velocity and concentration likely still occurs, though, for some phase lags. Therefore we take the average flux of many different phase lags and call it the noise floor. For the four immersed periods under consideration, a phase lag of 10-40 minutes resulted in wave and sediment flux estimates with a rms value of $4*10^{-6}$ kg/(m^2s), a median value

of $1.7*10^{-6}$, and a standard deviation of $2.7.*10^{-6}$ kg/(m^2s). A sample size of 36 was used, and estimates ranged from 10^{-5} to 10^{-7} kg/(m^2s) . Therefore, the wave and seiche fluxes estimated for tides 5 and 8 are above the noise floor, while the wave and seiche fluxes estimated for tides 6 and 7 are at the noise floor. Thus, in the following analysis we concentrate on tide 5 and tide 8.

Analysis of the cross terms in the flux calculation gives another indication of the amount of error in the estimations, as shown in table 6.2. While some cross-term flux is possible in nature, it is likely small; therefore, the cross-term fluxes are likely due numerical or experimental noise (e.g., edge effects in wavelets). In general, the largest cross-correlation terms occur between the seiche and the tidal terms; in fact, for tide 6 and tide 7 the cross terms $C_{seiche} * V_{tide}$ and $C_{tide} * V_{seiche}$ are between 4x and 20x larger than the actual flux estimate $C_{seiche} V_{seiche}$. This underscores how small the contribution of $C_{seiche} V_{seiche}$ is in these immersed periods. On the other hand, $C_{seiche} V_{seiche}$ is at least 7x larger than $C_{seiche} * V_{tide}$ and $C_{tide} * V_{seiche}$ for tide 5 and at least 3x larger than the same cross terms for tide 8. Moreover, the seiche flux term for these tides is an order of magnitude larger than tide 6 and tide 7. Thus, the sediment flux estimates at the seiche frequency are above the noise floor for tide 5 and tide 8. By contrast with the seiche/tide cross terms, the cross terms containing waves are never more than 12 percent of the flux term $C_{wave} * V_{wave}$ for tides 5,6, and 8. Only for tide 7—which has the minimum wave flux of all sampled tides—does the cross-term $C_{tide} * V_{wave}$ approach the order of magnitude of the flux $C_{wave} * V_{wave}$. Therefore, all wave flux estimates

except tide 7 are probably reliable, though tide 6 is at the upper-bound of the noise floor (see above discussion).

Table 6.2: Table of cross-term sediment fluxes measured for tides 5-8 in experiment #3 in April, 2003. Units are 10^{-3}* kg/m^3 * m/s.

Name	C_{wave} * V_{seiche}	C_{wave}* V_{tide}	C_{seiche}* V_{wave}	C_{seiche}* V_{tide}	C_{tide} * V_{wave}	C_{tide} * V_{seiche}
Tide 5	-10^{-7}	$4 * 10^{-9}$	$8 *10^{-7}$	10^{-6}	$1.7 *10^{-6}$	$-3.2*10^{-6}$
Tide 6	$3*10^{-8}$	$-4 * 10^{-8}$	$2 *10^{-7}$	$-4.4*10^{-6}$	$6*10^{-7}$	$3.6*10^{-6}$
Tide 7	-10^{-7}	$4*10^{-8}$	$-2*10e^{-7}$	$-2.0*10^{-5}$	$-1.7*10^{-6}$	$-3.6*10^{-6}$
Tide 8	$-6*10^{-7}$	$2*10^{-7}$	-10^{-7}	$-4.4*10^{-6}$	$-1.1*10^{-6}$	$-1.4*10^{-6}$

In addition to the border distortion that occurs from using wavelets, the velocity and concentration measurements themselves may contribute to the overall error. Note that the concentration measurements from the OBS and the velocity measurements from the velocimeter do not measure the same control volume, but rather are as much as 0.5 m distant from each other. On the time scale of the seiche or tide, average concentration and velocity is unlikely to vary between the two measurement volumes (large correlation length scale). However, instantaneous values of both the concentration and velocity are likely to differ over that length scale, both because individual turbulent motions are de-correlated at this separation distance and because high frequency waves (>0.5 Hz) are not completely correlated (see Chapter 4). Moreover, the OBS measurement volume (a cone on the order of several cm) averages out small scale, high frequency variations in sediment concentration (e.g., small wind waves). The results

presented here suggest that it is possible to measure the flux of sediments at the wave frequency, since the estimates for both an ocean swell dominated period (tide 5) and a wind-wave dominated period (tide 8) are above the noise floor. However, it is possible that net fluxes at higher frequencies (e.g. wind waves) are not measured, due to decorrelation of measurements.

In the rest of this chapter, we investigate the physical processes that lead to the non-zero fluxes at the wave, seiche, and tidal frequencies. In particular, a peculiar, persistent asymmetry occurs between the seiche velocity and seiche concentration, and is investigated in sections 6.3 and 6.4.

6.2.3: Variation on a tidal scale

Figure 6.1a shows the evolution of sediment concentration at a height of 0.05 m off the bed over four periods of inundation from April 13th, 2003 to April 15th, 2003. Over a tidal cycle, sediment concentrations are generally largest just after wetting, either due to advection from more exposed areas or from local erosion of unconsolidated upper layers of sediment by wind waves and/or tidal currents. As water deepens and the tide approaches slack water, this sediment settles out or is carried away (towards the tidal front) and the local concentration in suspension decreases. On the ebbing tide, increased flow energy results in another spike of sediment concentration; alternately, a front with sediment laden water passes the sensor during the ebb. However, the magnitude of sediment in the water column is less than during the flood tide for the

period of inundation under consideration (see figure 6.1a). Thus, the evolution of sediment concentration over a period of inundation follows the pattern seen at many other intertidal areas (e.g., Dyer, 1998, Dyer et al., 1999).

The transport rates in table 6.1 reflect asymmetric sediment concentrations between the flood and ebb measured at a height off the bed of 0.05 m during tides 5-8 in experiment #3. Similar patterns of sediment concentration persist at points higher than 0.05 m off the bed (e.g., at 0.19 m), albeit with smaller overall sediment concentrations. By contrast, tidal velocities at 0.155 m for both tide 5 and tide 8 are fairly symmetric, with the magnitude of the flood and the ebb currents in tide 5 and tide 8 approaching a maximum of ~ 0.1 m/s in each case (see figure 3.11 for comparison of tidal energy at 0.155 m; the square root of energy sets the velocity scale). Therefore, the net sediment flux is largely determined by the difference in time-integrated sediment concentrations between ebb and flood. In tide 5, sediment concentrations of greater than 500 mg/L are measured during the flood, and elevated concentrations persist over the first 150 minutes of wetting. By contrast, concentration increases during the ebb to only 300 mg/L. Therefore, the time-integrated sediment flux during the ebb tide is less than during the flood, and as a result sediment is imported onto the mudflat. During tide 8 (April 15th, 2003), the situation is exactly reversed: the time integrated sediment concentration is more during the ebb than during the flood, largely because sediment concentrations increase during the ebb from 100 mg/L to over 200 mg/L after about t~350 minutes.

Because the velocity profile over the tide is symmetric, the stress applied by the mean velocity cannot be the primary cause of the asymmetric sediment resuspension observed over these periods of inundation (though changing erosion thresholds may explain some of the asymmetry). Instead, the action of waves explains many of the differences observed in the evolution of sediment concentration over the four immersed periods shown in figure 6.1. For example, relatively large wind waves with an rms velocity of 0.1 m/s occur at the beginning of tide 5 (April 13th, 2003), then steeply decline. This is reflected in the sharp decline in sediment concentration over the same period (between 50 minutes and 150 minutes). Conversely, the rise in sediment concentration during the ebb in tide 8 (April 15th, 2003) follows the increase in wave orbital velocity due to an increase in local wind speed. This is visually demonstrated in figure 6.2, which shows a scatter plot of sediment concentration at a height of 0.19 m off the bed vs. the square of the maximum orbital velocity measured in one minute increments. The maximum shoreward velocity is calculated by finding regional maximums in the total, raw velocity signal over a minute, sorting the regional maximums in ascending order, and averaging the top three velocities.

Figure 6.2 follows a classic 'hockey stick' profile: sediment concentrations stay constant until a critical energy is reached, then increase upwards at an approximately constant slope. The goodness of fit parameter, R, is good (R=0.65), though scatter may be occurring due to changing conditions over the measurement period (e.g., depth, erosion threshold, tidal currents). From figure 6.2, a critical wave orbital energy of ~ 0.02-0.03 m^2/s^2 is surmised; thus, wind wave orbital velocities between 0.14-0.17 m/s

cause sediment erosion. Similar results are found when the rms wave energy is used instead of the maximum orbital velocity.

During periods with no large waves (rms wave velocity of less than 0.05 m/s) the relationship between waves and sediment concentration is less clear. The predominance of small waves (rms wave velocity of less than 0.05 m/s) from April 14^{th}-15^{th} (slack of tide 6, through the slack of tide 8) may explain the relatively suppressed sediment concentrations during the slack and ebb tides. However, the development of large sediment concentrations during the wetting period of tide 6 and tide 7, as well as the increase in sediment concentration after t=350 minutes in tide 5, suggest that other processes besides direct erosion by an applied wave stress are occurring. During ocean swell dominated conditions (e.g., the ebb of tide 5 and flood of tide 6), large shoreward orbital velocities occur when the depth is small, as the ocean swell becomes nonlinear (see chapter 3). However, as shown in figure 6.3, these large orbital velocities do not translate into increased sediment concentrations. In fact, the scatter plot of the square of maximum orbital velocity vs. sediment concentration at a height of 0.19 m off the bed shows no trend or pattern, as the small goodness of fit parameter (R=0.08) shows. Other parameters such as rms wave energy show no correlation as well. Therefore, it is not the magnitude of the orbital wave velocity that is controlling sediment concentration. Rather, some other phenomenon must explain the increase in sediment concentration observed during an ebb tide dominated by ocean swell (tide 5).

As described in Chapter 3, wave energy is a function of water depth, local meteorology, and ocean swell conditions. These interact dynamically with the bed to produce mean and instantaneous stresses that vary greatly over a tide (see chapter 5). Because of their larger accelerations, wind waves impart more instantaneous stress on the bed than ocean swell (see figure 5.9, which shows a graph of friction velocity due to waves). Thus, it is not surprising that a clear relationship is found between sediment concentration and wind-waves, but not ocean swell. Yet sediment concentration increases during the ebb of tide 5 during large swell conditions, despite no critical erosion threshold being exceeded. As will be shown later in the chapter, the interaction of ocean swell with bed-form ripples forms an alternate explanation for the increase of sediment concentration during the ebb of tide 5.

During calm periods with little or no wave energy, the mean tidal current may dominate the energy climate (see chapter 3), and therefore also the erosion of sediments. For example, figure 6.4 shows a tidal period in February 2001 in which waves are small ($V_{rms} < 0.05$ m/s), but the ebb current is intermittently large (> 0.25 m/s). The large ebb current at ~5 hours correlates with a large spike in the ADV and OBS backscatter signal, indicating increased sediment concentration. Interestingly, the wave velocity also picks up. Note that the large spike in current at ~ 5 hours may indicate that the channel is overtopping and flowing over the mudflat; as such, it is unclear whether the sediment is locally eroded or advected from the channel. However, the bed stress exceeds 0.75 Pa, as calculated using the Grant and Madsen (1986) algorithm. Typically, the critical stress for erosion in an intertidal area with both cohesive and

noncohesive sediments is lower than this value (see e.g. Partheniades, 1962), and therefore this current is large enough to erode sediments. Thus, suspended sediment concentration at the Richmond mudflat is not just affected by waves, but also by the mean current, particularly during periods of time when the ebb current is the largest source of energy. This occurs during spring tides or during large freshwater runoff events (see chapter 3). Correspondingly, during other periods the waves dominate the energy climate and suspended sediment characteristics (e.g., tide 5 and tide 8). Both wave climate and tidal currents depend on location, and therefore the dominant process is a function of both position and time.

6.2.4 Variation on a seiche time scale

The notable net transport of sediment at the seiche frequency during tide 5 (see table 6.1) suggests that there is a systematic, anomalous phasing occurring between sediment concentration and the seiche velocity. This anomalous phasing can be seen in figure 6.5, which shows acoustic backscatter (from ADV), sediment concentration (from OBS), bed stress, and velocity over a 100 minute interval during the ebb of tide 5. The stress is calculated using the log-linear profile (equation 5.2), and any stress that is greater than 0.1 N/m^2 is marked with a circle. The sediment concentration is measured using the OBS sensor at 0.19 m, while acoustic backscatter is measured at 0.15 m and presented in raw, uncalibrated form.

Figure 6.5 shows that both the optical backscatter and the acoustic backscatter are periodic over the 8 minute time scale of the seiche. However, no clear relationship exists between large stress and sediment concentration. In fact, as the light-colored circles show, the largest stresses ($\tau > 0.1$ N/m^2) occur during periods with the smallest sediment concentrations, except for a brief period at t~380 minutes. Thus, the anomalous phasing that is observed between bed stress and sediment concentration apparently subverts the model that increasing stress results in larger sediment concentrations.

The same anomalous phasing between sediment concentration and velocity at the seiche time scale occurs closer to the bed, as is shown in figure 6.6. In this figure, sediment concentration at 0.05 m is compared with the bed stress and velocity at 0.15 m over a 50 minute time period during the same ebb as figure 6.5. Times when the mean stress at the bed is greater than 0.2 N are marked with light colored circles; this threshold is a significant stress for estuarine sediments, and is the critical stress for erosion that Krone (1962) measured for San Francisco bay sediments. Theory suggests that at this threshold, erosion occurs and sediment concentrations in the water column should increase. Again, the phasing of concentration and stress is exactly opposite of the behavior expected by theory. The largest spikes in sediment concentration occur during times of low mean velocity and stress, while during periods of large stress ($\tau > 0.2$ N/m^2) the sediment concentration is suppressed. Moreover, the phenomenon occurs throughout the lower 0.35 m of the water column, and is not isolated to a particular location.

The periodic fluctuation in concentration at the seiche frequency leads to a net sediment transport. Because concentration is largest during the shoreward motion of the seiche, the net direction is shoreward. This explains the notable component of flux at tide 5 at the seiche frequency. Similarly, portions of the ebb during tide 6 and tide 8 show a similar asymmetry—large ebb velocities correlate with comparatively low sediment concentration, while reduced mean velocity correlates with increased sediment concentration (see figure 6.7). The seiche/concentration asymmetry appears to occur only during ebb tides, and has not been observed during the flood tides. Thus, the asymmetry between sediment concentration and the seiche velocity is systematic during the ebb and results in the net sediment transport displayed in table 6.1. In the next section we explore possible explanations for the observed behavior.

6.3. Fluctuations of Sediment Concentration at Seiche Frequency

Many possible mechanisms can explain the observed anomaly between sediment concentration and the seiche velocity. Shown in figure 6.8 is a cartoon depicting possible scenarios in which sediment concentration increases as velocity decreases (and vice versa). For example, patches of sediment may advect past the sensor, or vertical settling may periodically occur from a turbid upper layer. Another explanation is that waves preferentially eject sediments during the positive phase of the seiche, when the total fluid motion is more likely to reverse direction and eject sediment laden vortices into the water column. On the other hand, the observed asymmetry may indicate that

sediment is mixing into the water column with a time delay relative to the large stress events. Finally, the interaction of velocity and pressure with a permeable bed or fluid mud layer could potentially cause the observed sediment profiles. The most likely mechanism is the interaction of the flow with ripples. Before discussing this in section 6.4, we address the other theories and present why they are unlikely.

6.3.1: Advection

The fluctuating pattern of sediment concentration during the ebb tide may record the horizontal variation in sediment concentration. In other words, an alternating pattern of high and low concentration may exist upstream of the sensor (i.e., in the direction opposite the mean current). When the mean current flows by the sensor, it then carries a record of upstream patterns of sediment erosion and/or deposition. Sediment may be getting stirred over only portions of a wave. For example, when waves break at a predictable location, Okayasu et al. (2005) observed a continuous pattern of high sediment concentrations during low velocity offshore flow at a location seaward of the break.

Given an ebb velocity that typically varies between 0 m/s and 0.1 m/s, the flow is advecting up to 25 m of water past the sensor over the half cycle of the seiche. On the mudflat, the physical mechanism that would cause patches of large and small sediment concentration at this length scale is unclear; moreover, these patches are required to move past the sensor in a way that exactly reproduces the observed phasing of sediment

and seiche velocity (regardless of ebb velocity). Though the seiche period correlates with the sediment fluctuations in tide 5, its long wavelength of ~ 1500 m (see Ch. 3) means that velocity (and thus stress) varies little over 25 m. On the other hand, the large stratification that occurs after the storm of April 11^{th}-12^{th} may support baroclinic internal wave motions with much smaller wavelengths. Using the dispersion relation for a two layer stratified system (see e.g. Pond and Pickard,1983), the wavelength of a 500 second period internal wave with a step change in density of $\Delta\rho$ of 0.5-1 kg/m^3 at a depth of 0.5 m (total depth = 1 m) is between 17 m and 25 m. Thus, the length scale of an internal wave in the baroclinic mode is on the same order of magnitude as the length scale of water moved past the sensors by the ebb. Therefore, it is possible that sediment eroded upstream of the sensors during a high energy phase is advected to the experimental frame. However, one would expect the phasing of sediment relative to the seiche to change as ebb velocity varies; this does not occur. Moreover, the baroclinic mode of internal waves requires that the surface fluctuations at the wave frequency virtually disappear, which is inconsistent with the measured pressure signal. Thus, advection mediated by internal waves is unlikely. For similar reasons, it is unlikely that eddies or instabilities from the channel are advecting past the sensors; again, the consistent phasing between sediment concentration and the seiche velocity makes advection due to any mechanism unlikely.

6.3.2: Vertical structure with settling lag

When velocity is small, settling of inert particles occurs into lower layers of the water column. As velocity is increased, turbulent kinetic energy and mass diffusivity also increase (see Chapters 4 and 5). Therefore, sediment may mix over a larger portion of the water column, reducing the concentration of sediment near the bed (assuming no erosion). This pattern of settling and re-mixing potentially explains the anomalous phasing of sediment concentration and velocity (see figures 6.5-6.7). Instead of re-mixing, the sediment that has settled into lower parts of the water column may also be swept away by clean water with little sediment load.

As described in chapter 5, large stratification due to salinity is observed over the ebb tide on the order of ~0.5 kg/m^3 between the depths of 0.1 m and 0.5 m. Stratification tends to reduce mixing, and increases the time for a disturbance to propagate up the water column (see Chapter 5). Therefore, significant variation should be seen in the timing of maximum concentration for the sensors at 0.05 m, 0.19 m, and 0.35 m. However, sediment fluctuations at all heights are in phase with each other over the period of the seiche (see figure 6.9), suggesting that mixing and settling processes do not account for the observed variation in sediment concentration. In other words, if the vertical structure of sediment and settling lag were the mechanism, a phase lag would be required between instruments.

Another possibility is that an upper turbid layer of sediment is settling out at a relatively constant rate. During increased flow accumulation would be inhibited, as sediment is advected away. For the model to work, though, water with a low sediment concentration is required to constantly sweep past the sensors in the lower stratified layer. This is unlikely if the upstream water contains an upper turbid layer. Moreover, sediment concentrations do not increase with height. Therefore, this mechanism is also unlikely.

For the observed fluctuation in sediment concentration to occur (see figures 6.5-6.7), settling time of sediment must be small compared to the period of the seiche; otherwise, sediment ejected during the positive phase of the seiche would remain in suspension during the negative phase, and no variation would be observed. For cohesive sediments in suspension (see Chapter 2), settling velocity is typically modeled to be on the order of 1 mm/s (see e.g. Roberts et al., 2000). Thus, the settling time for the sensor at 0.05 m is on the order of 50 seconds, which is much smaller than the 8 minute period of the seiche. At the upper sensor at 0.35 m, settling time to the bed scales to about 350 seconds, which is on the order of the seiche period. However, the observed fluctuation in concentration at 0.35 m, which is approximately in phase with the concentration at 0.05 m (see figure 6.9), requires only that enough sediment settles out of the measurement volume of the sensor to explain the observed asymmetry between sediment concentration and velocity (see figures 6.5-6.7). A time scale of ~ 1 minute, as with the sensor at 0.05 m, is plausible.

Another condition for settling is that bed stress must be less than the critical shear stress for deposition. For reference, Krone (1962) gives a critical stress for deposition of about 0.06 N/m^2. Because sediment is ejected into the water column during times of overall low mean stress ($\tau < 0.06$ N/m^2; see figures 6.5-6.7), this condition is met—as long as settling occurs before stress exceeds the critical level. In fact, as the mean bed stress increases above 0.1 - 0.2 N/ N/m^2, the profile of sediment concentration stops decreasing and approaches background values (~ 25 mg/L in figure 6.5, ~ 120 mg/L in figure 6.6, and ~ 20 mg/L in figure 6.7). Therefore, the seiche likely determines when settling occurs or ceases. Again, the relative magnitudes of seiche and ebb are critical; for a more energetic ebb or less energetic seiche, the inferred pattern of settling will probably alter.

6.3.3: Critical Stress model with diffusion lag

The critical stress model for sediment erosion suggests that the large stresses produced during the offshore phase of the seiche should cause erosion during the ebb, particularly considering the added stress from waves and nonlinear wave-current interactions. The anomalous phasing of small sediment concentrations with large mean velocities (see figures 6.5-6.7) apparently contradicts this explanation of sediment erosion. It is possible, however, that sediment is indeed eroded during large stress periods but mixes slowly through the water column as turbulent energy produced at the bed propagates upwards. If the time to mix into the water column is on the order of half the wave cycle, large sediment concentrations will be measured precisely when the total velocity

(ebb + seiche) is at a minimum. Moreover, because the total (ebb + seiche) velocity is small during the positive phase, little erosion will occur. During this phase, sediment settles out, assuming that settling time is fast compared to the seiche motion and that the critical stress for deposition is not exceeded (see section 6.2.2). Hence, a packet of comparatively clean water propagates through the water column, showing up 180 degrees later as a decreased sediment concentration at the sensors. The question is, how long does it take for sediment to mix upwards through the water column, and how long does it take for the water column to clear?

The question of mixing time depends on the eddy (mass) diffusivity, which in turn varies with depth and the time dependant structure of turbulent kinetic energy. Figure 5.16 shows the propagation of turbulent energy of an idealized seiche wave over time and space calculated by GOTM (General Ocean Turbulence Model); as can be seen, turbulent motions produced at t=0 seconds propagate to 0.05 m in ~ 50 seconds, to 0.15 m in ~ 150 seconds, and to 0.25 m in ~ 250 seconds. The resulting structure of eddy diffusivity predicted by GOTM is shown in figure 6.10; not surprisingly, eddy viscosity greatly resembles the eddy viscosity displayed in figure 5.18. In the lower 0.2 m of the water column eddy diffusivity varies between ~$2*10^{-5}$ and ~$6*10^{-5}$ m^2/s over a seiche wave cycle for a 'large' seiche of ~ 0.06 m/s amplitude. Using the median diffusivity of D~$4*10^{-5}$ m^2/s, and estimating the time scale by L^2/D, the time for mass to propagate to 0.05 m is ~60 seconds, while the time to propagate to 0.15 m is 560 seconds—greater than the time scale of the seiche.

Thus, both turbulent kinetic energy and the suspended sediment signal are predicted to reach the sensors at 0.05 m, 0.19 m, and 0.35 m at greatly different times. However, as shown in figure 6.9, the concentrations of sediment at these heights are all in phase. There is no measured time delay, but rather just experimental noise; in fact, the phase at 0.19 m leads the sensor at 0.05 m and 0.35 m by ~30 seconds. Physically, a time shift must exist between the heights; however, because the sensor at 0.35 m is sampling once per minute, finer resolution is not possible. In any case, the measured fluctuation in sediment concentration suggest that turbulence—and mass—is propagating up through the water column more quickly than predicted by GOTM. In fact, the observed phasing of concentration in figure 6.9 is consistent with the ejection of sediment from the bed into the water column over a short (< 30 sec) time scale. Therefore, the anomalous phasing of sediment concentration and bed stress is likely not explained by the time it takes for a signal to propagate through the water column.

In practice, nonlinear interactions between waves (ocean swell and wind waves) and the 1-min mean current (seiche + tidal) increase the turbulent production at the bed, more than doubling the friction velocity of the mean current (see Chapter 5). In shallow water, contributions to mixing may occur from the upper boundary layer as well. Thus, GOTM may underestimate the turbulent kinetic energy and therefore the time to propagate upwards in the water column. Other results confirm that mixing is occurring more quickly than predicted; for example, the correlation presented in figure 6.2 is at a maximum at a zero lag, suggesting that mixing occurs quickly.

6.3.4: Interaction of fluid with bed structure

Fluid interactions with the sediment matrix—either by fluidization or subsurface flow—can affect suspended sediment concentrations which potentially vary with the seiche frequency. As described by Precht and Huettel (2004), the presence of ripples on the bed alters the flow structure of water and creates regions of high pressure (trough) and low pressure (ripple peak) on the bed. This results in a persistent pattern of infiltration into the porous bed at the trough, and exfiltration of water—and sediment--at the peak. A detailed analysis of this phenomenon and how it is affected by waves, seiching, and tidal currents is beyond the scope of this dissertation. Qualitatively, however, increasing flow during the ebb should increase the negative pressure over the ripple crest (by Bernoulli theorem), amplifying the pressure difference between the ripple peak and trough. Thus, if anything, more subsurface cycling should occur during the negative phase of the seiche, causing greater ejection of sediment into the water column. Again, this is opposite of the observed pattern, though subsurface cycling is likely not to occur instantaneously and there may be phase lag effects.

Fluid motions, in particular the cyclic loading of waves, can set up a layer of fluid mud at the soil/water interface, which is then periodically entrained into the water column (e.g. Mehta et al., 1989). Again, however, larger flow is likely to entrain more sediment into the water column—opposite of the observed phenomenon. Moreover, given that the bed consists mostly of small sand grains, fluidization is unlikely (see Chapter 2).

6.4. Interaction of turbulent eddies with ripples

In unidirectional flow over ripples, flow often separates from the ripple crest and creates a low pressure region in the lee region, and forms an eddy (vortices) that is moved downstream by the mean flow. As is shown in figure 6.11, sediment particles are continually streamed up the front of a ripple and are deposited on the lee side during bedload transport. When the direction of velocity is reversed, however, the eddy formed by separation is advected back into the lee side of the ripple. The eddy erodes the recently deposited particles from the lee side of the ripple and ejects them into the flow. Sleath and Wallbridge (2002) describe this mechanism of erosion and show that for waves in a wave tank, bursting of sediment into the water column occurs both at the maximum orbital velocities and when flow reverses over a ripple. The erosion at maximum flow is explained by the critical stress theory, while the ejection at reversal is due to turbulent vortices. Note that the observed phasing of concentration in tide 5 (see figure 6.9) is consistent with ejections of sediment into the water column.

For the ebb tides in consideration, the mean offshore flow is modulated by the seiche frequency, creating an alternating pattern of larger and smaller negative velocities. In figure 6.12, the measured waves are overlaid upon the mean (seiche + ebb) velocity over a 50 minute period. A point is displayed for every instance that the raw, measured velocity changes from negative to positive. Each so-called zero up-crossing is given a color coded symbol, depending on whether the seiche phase is positive (light colored circles) or negative (dark colored squares). Positive refers to onshore, northwards flow,

while negative denotes offshore, southwards flow. Clearly, the frequency of velocity reversal greatly increases when the seiche velocity is positive and shoreward. Thus, the frequency of reversal correlates well with the increase of sediment concentration that occurs during the positive seiche, and suggests that ejection of sediment by a reversal of velocity is a viable explanation.

Note that the frequency of velocity reversal depends critically upon the relative values of the seiche, the ebb flow, and the wave orbital velocities. For example, the wind waves that occur during the ebb of tide 8 are large enough to reverse the flow of velocity on both the positive and negative phases of the seiche (see figure 6.13). There is no visually apparent asymmetry in the frequency of zero crossings. However, the number of reversals per minute is still dependant on the phase of the seiching motion, as figure 6.14 shows. In the shoreward (+) direction, the number of zero up-crossings varies from 19-25 crossings/minute, while in the offshore (-) direction the number of zero up-crossings varies from 15-22 crossings/minute. This asymmetry of 3-5 crossings/minute occurs because small wind waves are not able to reverse the overall negative flow during an offshore phase of the seiche (ebb + seiche).

6.4.1: Concentration activity

When sediment is suspended by the action of waves, it is likely that sediment concentrations will be patchy at the time and length scales of the waves. These patches of high and low sediment are advected past the OBS sensors by the combined action of

waves, seiching motions, and tidal currents. The OBS record therefore contains a time history of how patchy the upstream sediment concentrations are. For very little erosion, the sediment concentration moving past the sensor should be approximately constant, and reflect only measurement error and the horizontal concentration gradient. A small component due to vertical orbital velocity also occurs. As sediment bursts upstream of the sensors become more frequent, the total variance in concentration is likely to increase, reflecting the patchiness in time and space of sediment erosion. We therefore define a concentration activity coefficient, ϕ_c:

$$\phi_c = \frac{\sigma_{c,w}}{C_T + C_s}, \tag{6.6}$$

where $\sigma_{c,w}$ = standard deviation of the component of concentration at the wave frequency, C_T = Sediment concentration at the tidal frequency, and C_S = concentration at the seiche frequency. We normalize the standard deviation of concentration by the total background concentration to avoid measuring changes in sediment activity that occurs purely from variation in the background concentration. This definition is now applied to the period of inundation on April 13th, 2003 and April 15th, 2003 (tide 5 and tide 8), and the results are shown in figure 6.15.

For tide 5, the minimum activity of concentration occurs during the negative stroke of the seiche between 0 and -0.05 m/s, indicating that the activity of concentration—and therefore sediment suspension processes—are relatively muted. On the other hand,

positive seiche velocity corresponds with an increase in sediment activity, which is consistent with erosion occurring due to waves. This asymmetry between positive and negative seiching velocities cannot be explained by differences in wave energy, which remains statistically constant over a seiching period. Rather, it indicates that erosion is likely occurring because velocity is reversing over the rippled bed, causing ejection of turbulent vortices laden with sediment.

The pattern in sediment activity observed during the ebb of tide 8 echoes the behavior observed in tide 5. As shown in figure 6.16, there is increased sediment activity during the positive, onshore phases at the seiche frequency, while patchiness decreases during the offshore phase. However, the relative difference in activity between positive and negative phases of the seiche is less; instead of a ~50 percent difference between positive and negative wave activities, there is only a ~15 percent difference. Moreover, the overall variance in sediment concentration is greater, likely because the wave climate is more energetic. Note that a large spike in patchiness at the wave frequency occurs at ~ -0.03 m/s. This suggests that the combination of waves, seiche, and ebb are enough to suspend sediment by exceeding a critical stress. This may explain the correlation between wave velocity (stress) and sediment concentration observed in figure 6.2. This magnitude of velocity (-0.03 m/s) is quite small, and points out how small changes in the energy climate can have nonlinear effects on the suspension of sediment.

6.5. Transport of sediment due to waves

The measured flux of sediment due to waves is small compared to variation on the tidal scale. However, the aggregate effect of the tidal and seiche asymmetries is not yet known for this site, as large fluxes over different periods of inundation may cancel each other (see e.g. tide 5 and tide 8, tidal frequency) or be an intermittent occurrence that is averaged over time (seiche). Thus, it is worthwhile to look at transport due to ocean swell and wind waves, and identify the mechanisms with which they are working.

6.5.1: Observations of backscatter signal

During the ebb of tide 5, the sediment concentration at a height of 0.05 m (figure 6.17a) is observed to fluctuate at the same frequency as the ocean swell (figure 6.17b). An obvious explanation is that the vertical orbital velocity is simply cycling lower, more sediment laden water and higher, cleaner water past the sensor in a periodic fashion. However, in theory the vertical orbital velocity at the top of the boundary layer at ~ 0.05 m should be nearly zero, assuming an impermeable bed. Moreover, the magnitude of the sediment fluctuation does not always correlate with the velocity of the wave; for example, the large wave at 484.4 minutes does not cause a large sediment fluctuation, whereas the small wave measured at 483.2 minutes is coincident with a large burst of sediment. Another explanation for the observed sediment fluctuations are that sediment is being periodically resuspended at ripple crests and settling into the troughs. In fact,

Sleath and Wallbridge (2002) and others note spatial patterns of high sediment in suspension over ripple crests.

By contrast, fluctuations at the wind wave frequency appear less often in the sediment signal during wind-wave dominated conditions (figure 6.18a). Rather, wind waves appear to cause a 'beat' in the concentration signal that parallels the passing of several large waves at once (termed a 'wave group'). For example, the large waves at 466 minutes, 465.5 minutes, and 465.9 minutes clearly increase sediment concentration for a period of 10-20 seconds each, after which the sediment concentration decreases to background levels. Therefore, wave groups likely dominate sediment resuspension for wind waves, and thus transport is likely to occur due to asymmetric phasing between sediment and the long waves that are bound to the groups (e.g. Shi and Larson, 1984). The long waves dominate in part because the boundary layer of wind waves is smaller than ocean swell (maximum 0.01 m vs. 0.04 m), and vortices are less likely to bring sediment laden water past the sensor at 0.05 m. Moreover, the excursion amplitude of wind waves is less than ocean swell, which increases the likelihood of mixing by turbulent eddies. Therefore, a diffusive process of sediment mixing is more likely. However, some of the observed differences may occur because of the measurement technique. As noted previously, the OBS samples a larger portion of the wind wave excursion amplitude, and averages over any phase differences.

6.5.2: Spikes in backscatter

The largest onshore motions of the asymmetric, non-linear swell during tide 5 result in large bursts of sediment that are measured by the OBS and shown in figure 6.17 (see for example t=485.3 min.). This pattern of sediment spikes during large ocean swell events is not isolated but occurs throughout the ebb tide, and can be measured statistically by correlating the ocean swell with the OBS sediment signal at 0.05 m during tide 5. When the entire ebb is compared, the maximum lagged correlation is only 0.25, indicating a weak correlation between OBS fluctuations and ocean swell. On the other hand, if only periods of time with wave amplitudes greater than 0.20 m/s are sampled, the correlation coefficient rises above 0.57 –indicating that large waves and spikes in OBS backscatter are indeed correlated. Note that this correlation was defined by setting all data not with-in three seconds of a wave peak to zero. At a height of 0.19 m the correlation of the sub-sampled data set is low (0.1). However, when only the negative (offshore) seiche is sampled, the correlation increases to 0.35. Thus, during more energetic mean current conditions, some pulses of sediment are carried to heights of 0.19 m in a matter of seconds. The correlation of the largest ocean swell with sediment spikes in the OBS record suggests that the non-linear waves are preferentially moving sediment onshore. This happens because the largest orbital velocity of ocean swell (see figure 3.14)—and therefore spikes in sediment concentration—are occurring during the shoreward stroke. This was also observed by Ribberink and Al Salem (1991), who found that non-linear waves in a laboratory move sediment in the direction of the largest orbital velocity.

The largest sediment transport at the wave frequency occurs during the period of inundation on April 15th, when large wind waves are whipped up during the ebb. By contrast with the ocean swell, wind driven waves rarely cause a large spike in the OBS signal at 0.05 m; during the ebb of tide 8, the correlation for the entire signal is 0.25, while a subsampling based on waves greater than 0.20 m/s yields virtually the same value—0.24. This indicates that sediment dynamics occur differently for wind waves and ocean swell. Because there is little correlation between the OBS signal and the high frequency wind waves, sediment transport must be occurring due to lower frequency, lower amplitude waves such as those bound to wave groups.

6.6. Discussion

Perhaps the most surprising result in this chapter is that erosion is occurring during times when the stress applied to the bed by the hydrodynamics is at its minimum. At first glance, this result contradicts the time-tested theory that erosion occurs when stress exceeds a critical shear stress. However, it is more instructive to look at the underlying process that causes erosion—namely, turbulent bursting processes that eject low velocity, high sediment concentration fluid into the water column. At its core, the critical shear stress theory simply expresses that on average turbulent bursting processes are sufficiently energetic enough to entrain sediment. Erosion is not only a constant upward flux of sediment that occurs above a critical shear stress, but also an aggregate

of individual, random, intermittent bursting events. Only on a time scale large compared to near bed turbulent motions does entrainment of sediment appear constant.

Sediment erosion by the reversal of velocity over a ripple occurs due to the interaction of a vortex with the lee side of a ripple. This is simply another way in which turbulent motion can interact with the bed, albeit one that does not depend upon the stress applied at the bed from waves and currents. The critical determining factor of sediment erosion is therefore not bed stress, but rather the formation of vortices and how they interact with the bed. Clearly, the formation and strength of vortices depends on the energy in the flow, which in turn affects erosion. As the mean wave energy increases, the magnitude of the concentration spike during the positive phase of the seiche also increases, indicating more turbulent erosion from the bed (see figure 6.1). But the energy of the vortex peeled from the ripple crest is not the only determining factor; in fact, theory holds that TKE should be larger during the negative phase of the seiche than the positive during an ebb tide. Rather, the asymmetry of the rippled bed provides the potential for asymmetric, unequal interaction of fluid motions with the bed. For example, even unidirectional flow creates an uneven pressure distribution over the ripple profile, making erosion more likely near the ripple crest. When the flow regime is not simply unidirectional or fluctuating in a constant manner, but depends on the superposition of multiple frequencies of motion, the potential for time varying interaction with the asymmetric bed exists.

In addition to producing a random wave climate that varies over many time scales, the multiple frequencies of motion move sediment in unique ways. Wind waves affect the sediment concentration through wave groups, while fluctuations of ocean swell and sediment occur at the same frequency. The characteristics of transport changes again at the seiche frequency, and depends critically on asymmetries in concentration that occur due to its interaction with both waves and the tidal frequency. Finally, tidally driven transport of sediment occurs primarily due to variation of the mean energy in waves, though the ebb/flood asymmetry in current sometimes plays a role as well (figures 6.1 and 6.4). Each type of wave is idiosyncratic, but sediment transport at this mudflat depends on the interaction of these different waves with each other. Clearly, these interactions must be well understood before aggregating upwards to larger time scales such as the spring-neap or annual cycles.

The time scales—and the timing—over which fluid motions occur has implications for sediment transport as well. Wind waves occur intermittently, and are tied to local conditions. These conditions often change over the course of the tide, and often determine whether sediment accretes or erodes during a period of immersion. In tide 5, wind is strong during the wetting phase of the tide, while in tide 8, wind is blowing during the ebb; not surprisingly, the net sediment fluxes are in opposite directions. An open question is whether instantaneous stress on the time scale of seconds or average stress applied over minutes is more important to sediment erosion and transport—whether convective motions by turbulent bursts (e.g., during velocity reversal) or the dispersion of turbulence through the water column by longer scale motions (e.g., tidal

currents). This feeds directly into the question about whether vertical sediment movement is a convective or diffusive process. The results presented here suggest that both are important. Thus, the intertidal environment is dominated by asymmetry and non-linearity—asymmetric sediment concentrations forced by non-linear waves, non-linear wave-current interactions, advection by turbulent vortices, and step changes in sediment concentration as either the flow direction is reversed or a critical erosion threshold is exceeded.

6.7. Figures

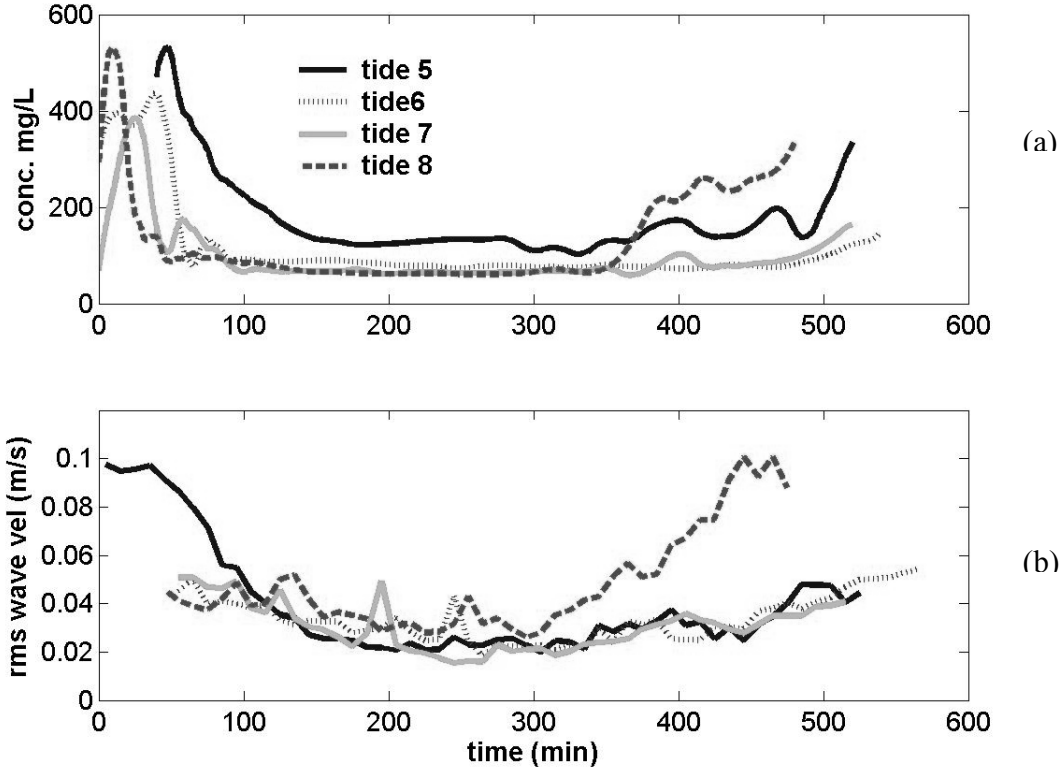

Figure 6.1: Profiles of the tidal component of sediment concentration (C_{tidal} ,on panel 'a') and root mean square (rms) of the wave component of velocity (V_{wave}, on panel 'b') over tides 5-8 on April 13th-April 15th, 2003. The begin and end time of each period of inundation is defined in table 6.1, while C_{tidal} and V_{wave} are defined by equations 6.3 and 6.4.

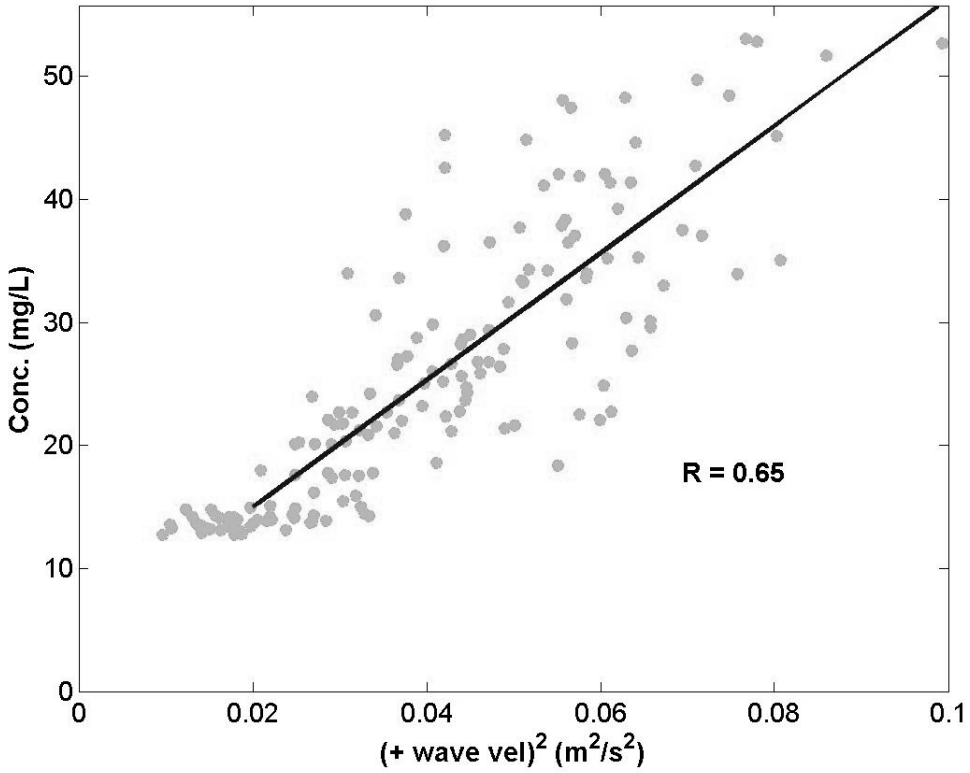

Figure 6.2: Scatter plot of wave energy at a height of 0.155 m with sediment concentration at 0.19 m over an ebb tide on April 15th, 2003 (tide 8). Concentration is determined using a 1-min mean. The wave energy is the square of the maximum orbital velocity in the positive, onshore direction, determined by finding the average of the three largest waves over each 1 minute segment.

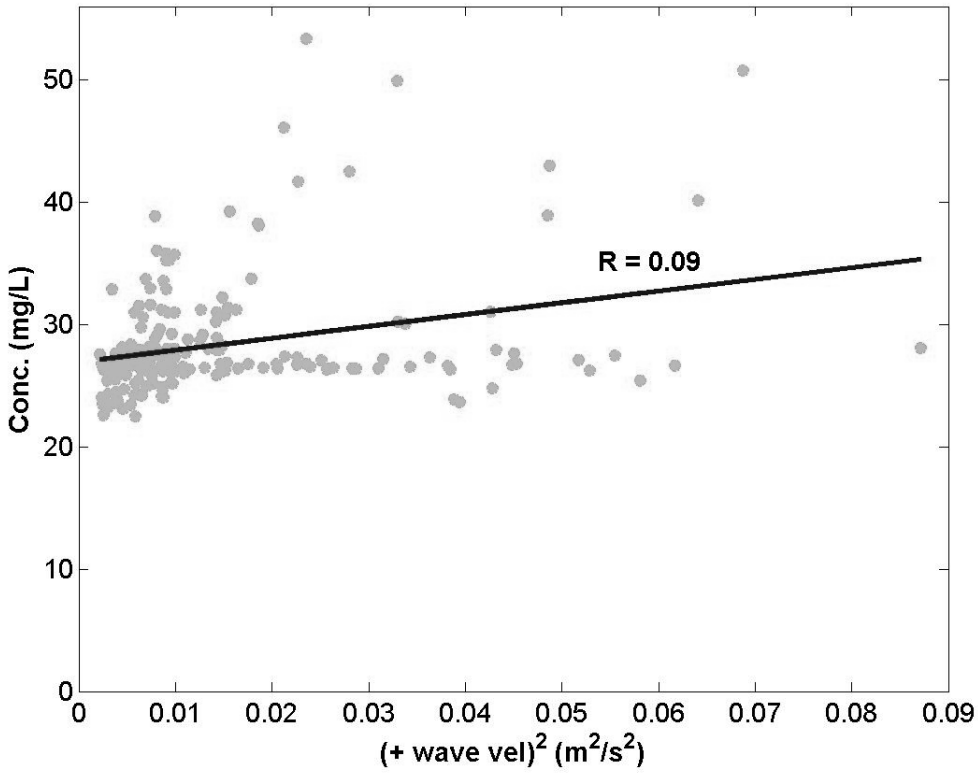

Figure 6.3: Scatter plot of wave energy at 0.155 m with sediment concentration at 0.19 m over an ebb tide on the morning of April 14th, 2003 (tide 5). Concentration is determined using a 1-min mean. The wave energy is the square of the maximum orbital velocity in the positive, onshore direction, determined by finding the average of the three largest waves over each 1 minute segment.

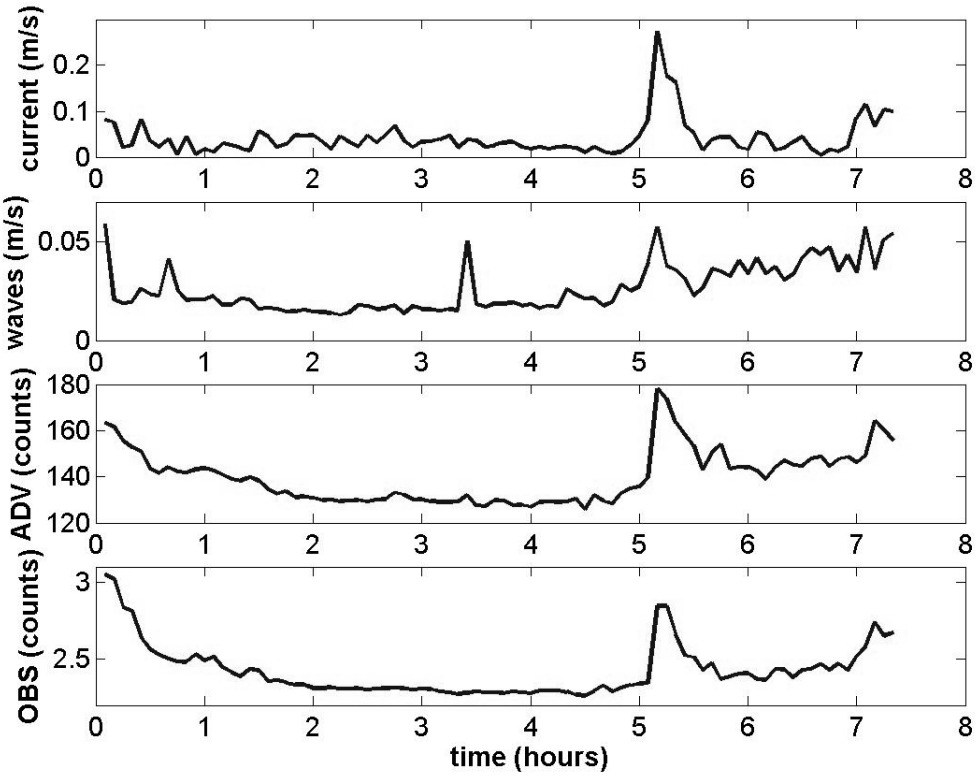

Figure 6.4: Comparison of the energy climate and both acoustic and optical backscatter over an immersed period beginning at 12:10 pm on February 12, 2001. As can be seen, the large increase in current after t=5 hours correlates with an increase in both acoustic (ADV) and optical (OBS) backscatter.

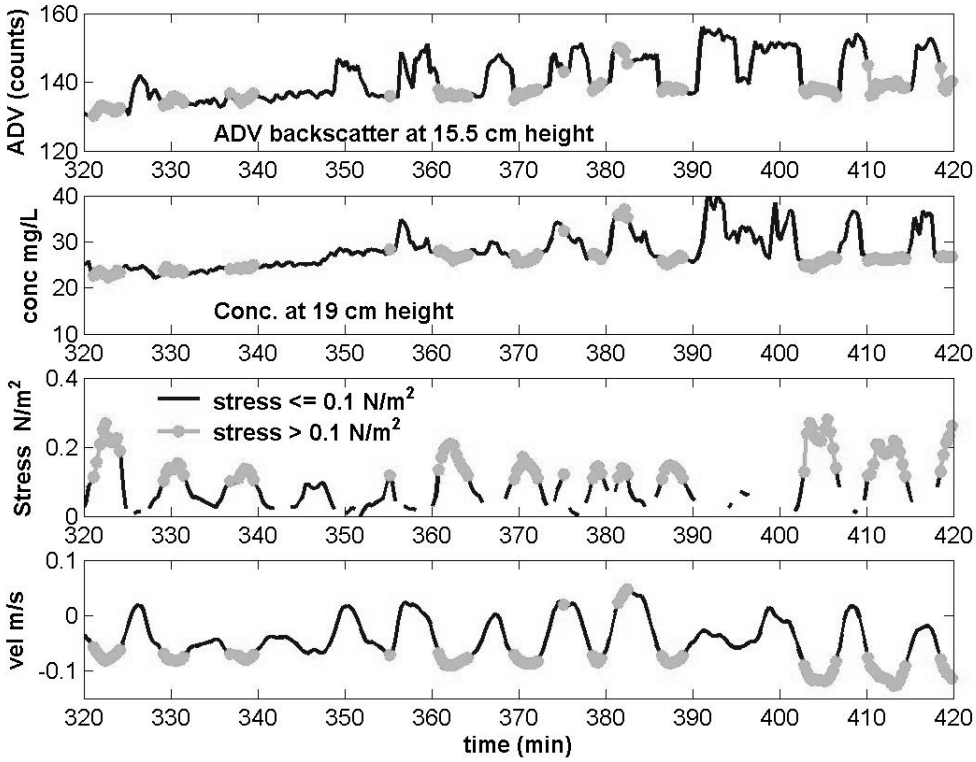

Figure 6.5: Comparison of sediment concentration (measured from OBS) and acoustic backscatter with the bed stress and velocity over an ebb period on the morning of April 14th, 2003 (tide 5). Times in which stress is greater than 0.1 N/m^2 is depicted in light color over all plots, while dark lines depict times of low stress. The OBS and ADV data are measured at 0.19 m and 0.155 m, respectively. Velocity, concentration, and acoustic (ADV) backscatter are 1 minute averages, while bed stress is found using a log-linear fit (equation 5.2).

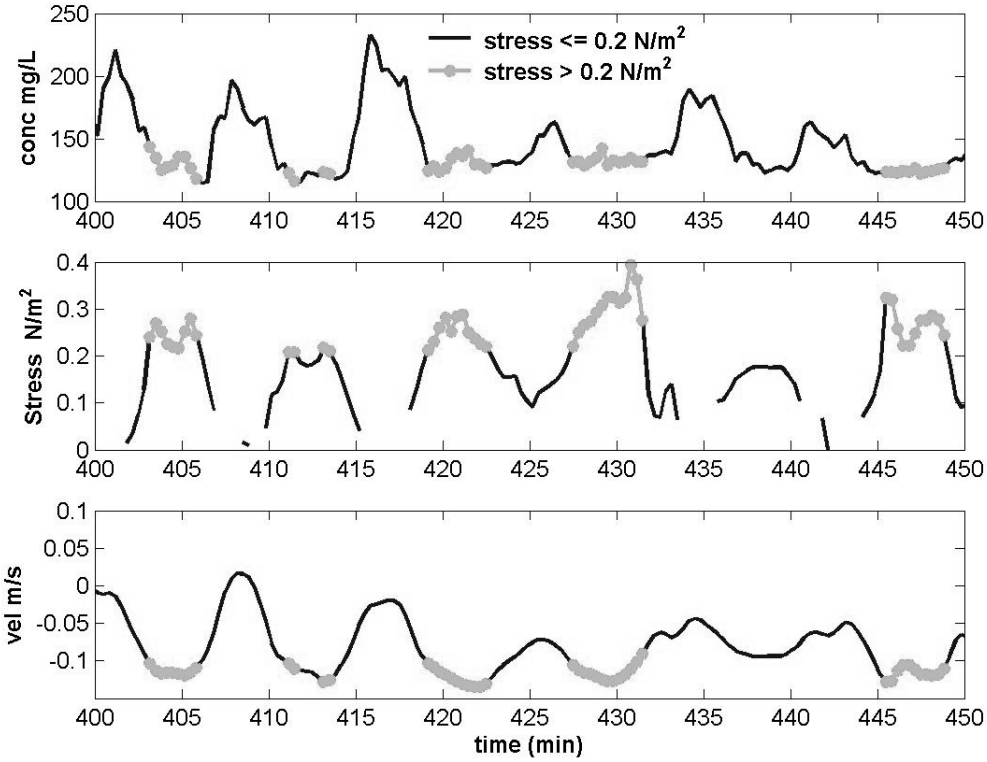

Figure 6.6: Comparison of sediment concentration (measured from OBS) and acoustic backscatter with the bed stress and velocity over an ebb period on the morning of April 14th, 2003 (tide 5). Times in which stress is greater than 0.2 N/m^2 is depicted in light color over all plots, while dark lines depict times of low stress. The OBS and ADV data are measured at 0.05 m and 0.155 m, respectively. Velocity, concentration, and acoustic (ADV) backscatter are 1 minute averages, while bed stress is found using a log-linear fit (equation 5.2).

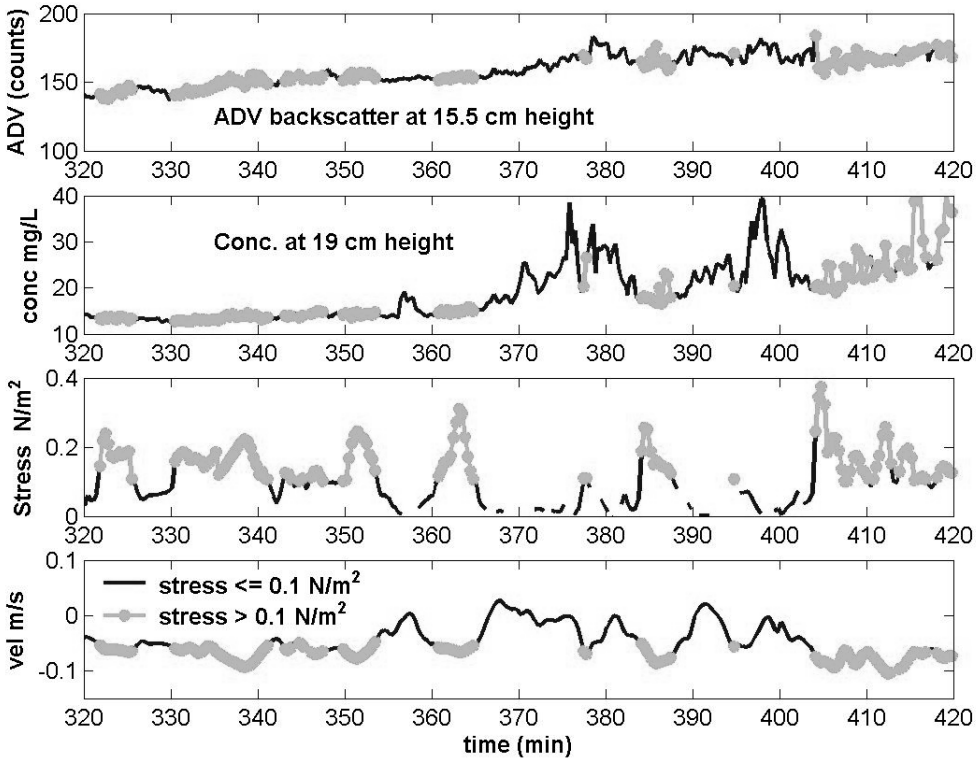

Figure 6.7: Comparison of sediment concentration (measured from OBS) and acoustic backscatter with the bed stress and velocity over an ebb period on the afternoon of April 15th, 2003 (tide 8). Times in which stress is greater than 0.1 N/m^2 is depicted in light color over all plots, while dark lines depict times of low stress. The OBS and ADV data are measured at 0.19 m and 0.155 m, respectively. Velocity, concentration, and acoustic (ADV) backscatter are 1 minute averages, while bed stress is found using a log-linear fit (equation 5.2).

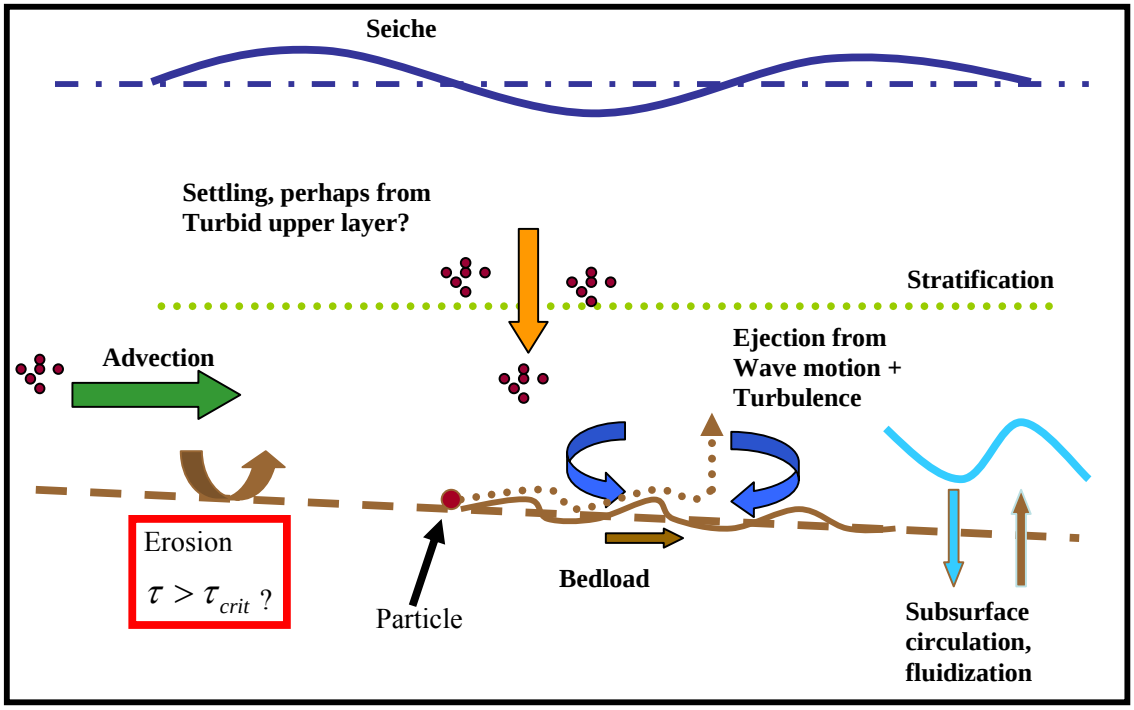

Figure 6.8 Schematic of potential reasons for the anomalous phasing between seiche and sediment concentration.

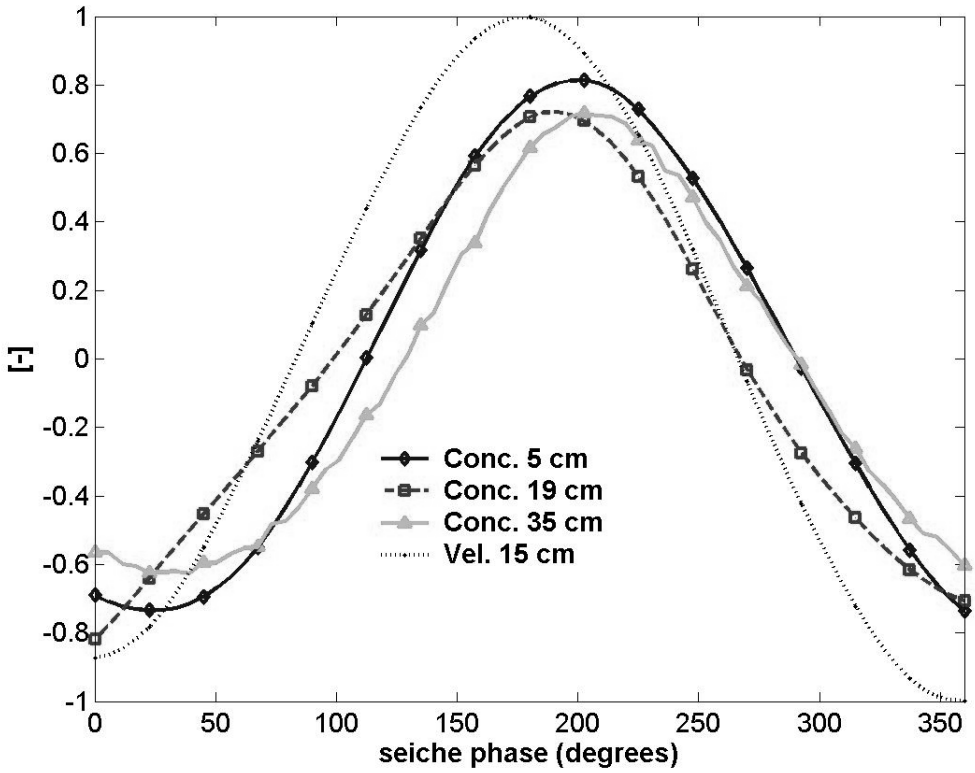

Figure 6.9: Phasing of concentration fluctuations at the seiche frequency (C_{seiche}) relative to the seiche velocity (V_{seiche}), measured over an ebb tide on April 13th, 2003 (tide 5). Note that each profile is averaged from multiple profiles that are normalized by the maximum concentration (or velocity) in each particular seiche instance.

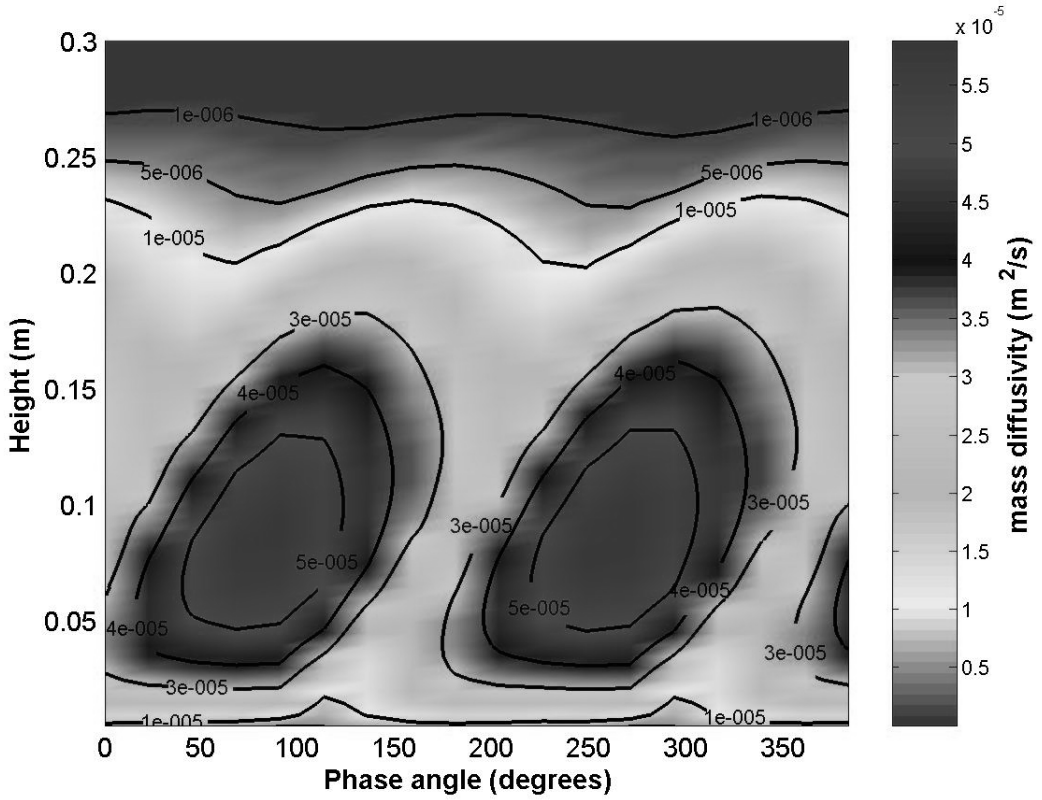

Figure 6.10: Mass diffusivity predicted by GOTM over a 480 second seiche wave as a function of height for the stratified case. Zero degrees is defined as the maximum, offshore (negative) seiching motion. Note that unstratified conditions yield a similar behavior.

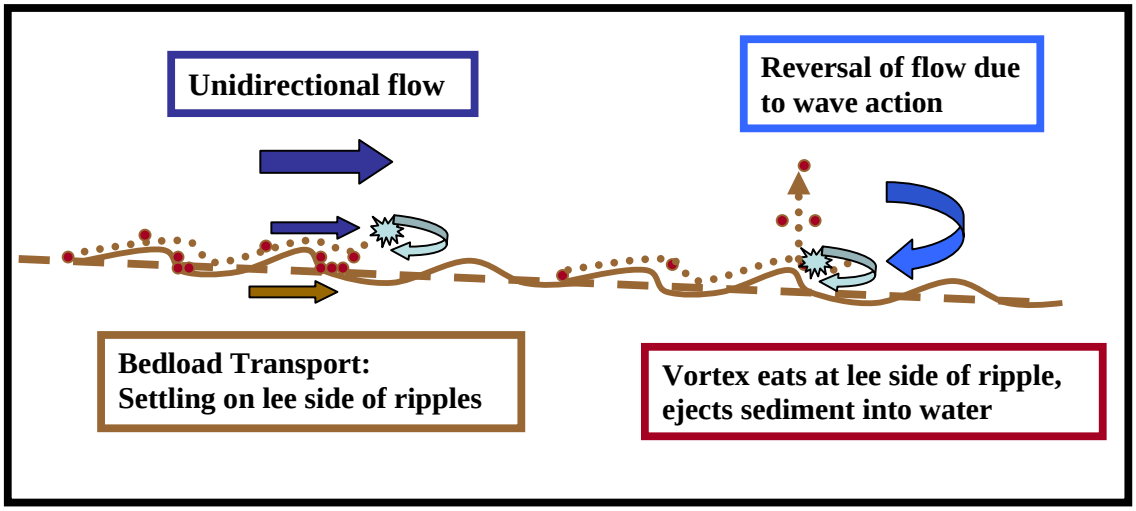

Figure 6.11: Schematic describing sediment erosion due to the reversal of velocity mechanism. Follows observations of Sleath and Wallbridge, 2002.

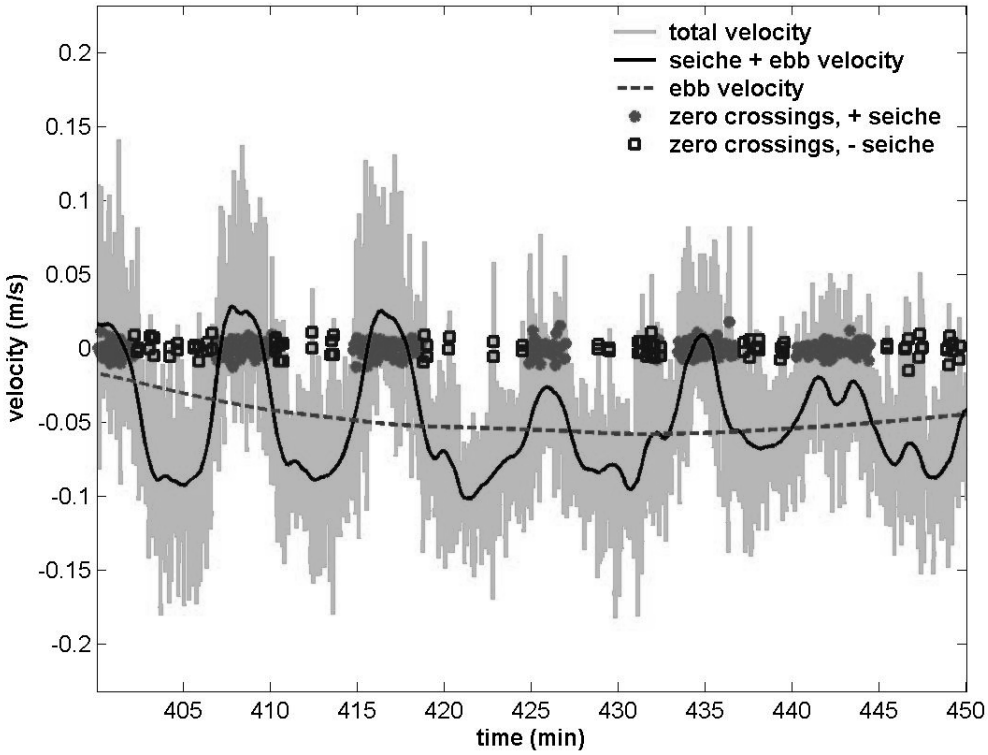

Figure 6.12: Zero crossings as a function of the phase of the seiche during an ebb period dominated by ocean swell during the early morning of April 14th, 2003 (tide 5). The total mean velocity (seiche + ebb) velocity is given by a solid dark line, while the ebb velocity is a dashed line. The total measured velocity (seiche + ebb + waves) is shown as a solid light line. Solid circles indicate a zero crossing during the positive, onshore phase of the seiche, while zero crossings during the negative, offshore phase of the seiche are depicted by squares. Zero crossings are much more frequent during the positive phase of the seiche than over the negative phase

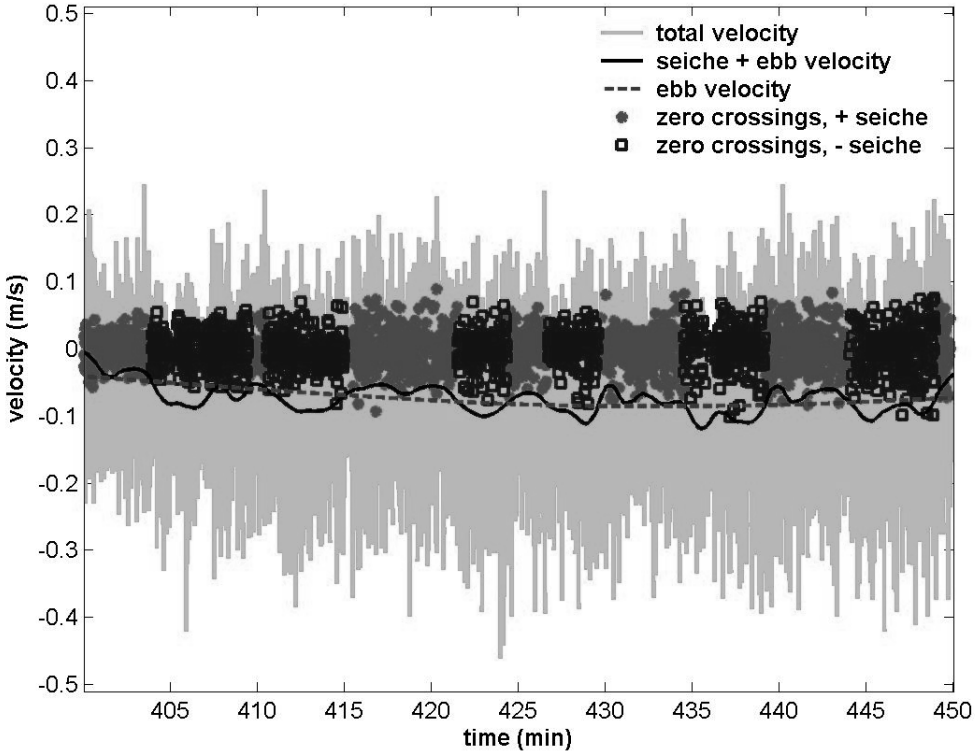

Figure 6.13: Zero crossing as a function of the phase of the seiche during an ebb period dominated by locally driven wind waves on April 15th, 2004 (tide 8). The total mean velocity (seiche + ebb) velocity is given by a solid dark line, while the ebb velocity is a dashed line. The total measured velocity (seiche + ebb + waves) is shown as a solid light line. Solid circles indicate a zero crossing during the positive seiche, while zero crossings during the negative seiche are depicted by squares. There is no readily apparent difference in zero crossings between the positive and negative phases of the seiche.

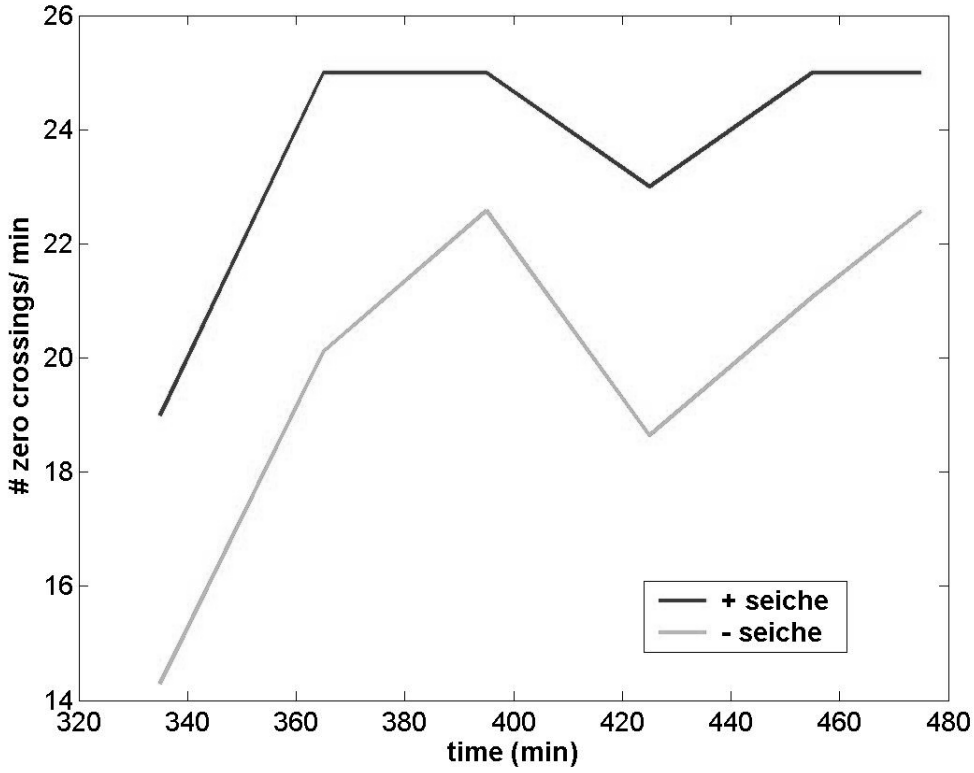

Figure 6.14: Number of zero crossings from the negative to positive direction per minute over the ebb tide in wind wave dominated conditions on April 15th, 2003 (tide 8).

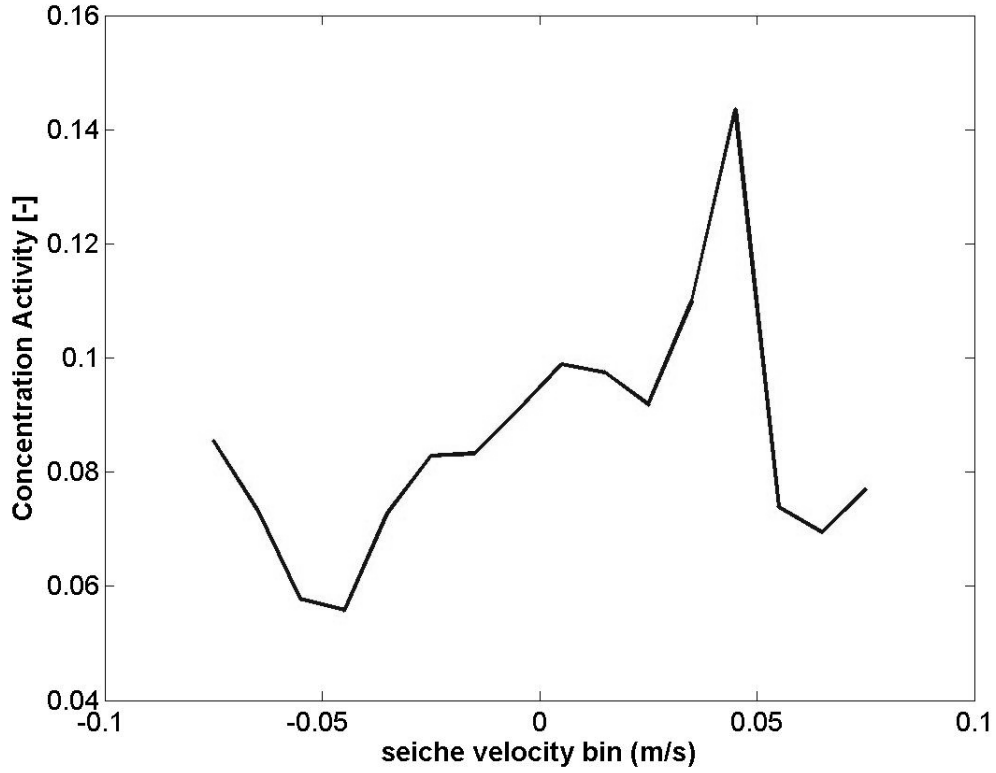

Figure 6.15: Sediment activity during an ebb dominated by ocean swell on April 13th, 2003 (tide 5), binned by seiche velocity. Concentration data are separated into bins of the seiche velocity that vary in blocks of 0.01 m/s. The concentration activity is then determined according to equation 6.6.

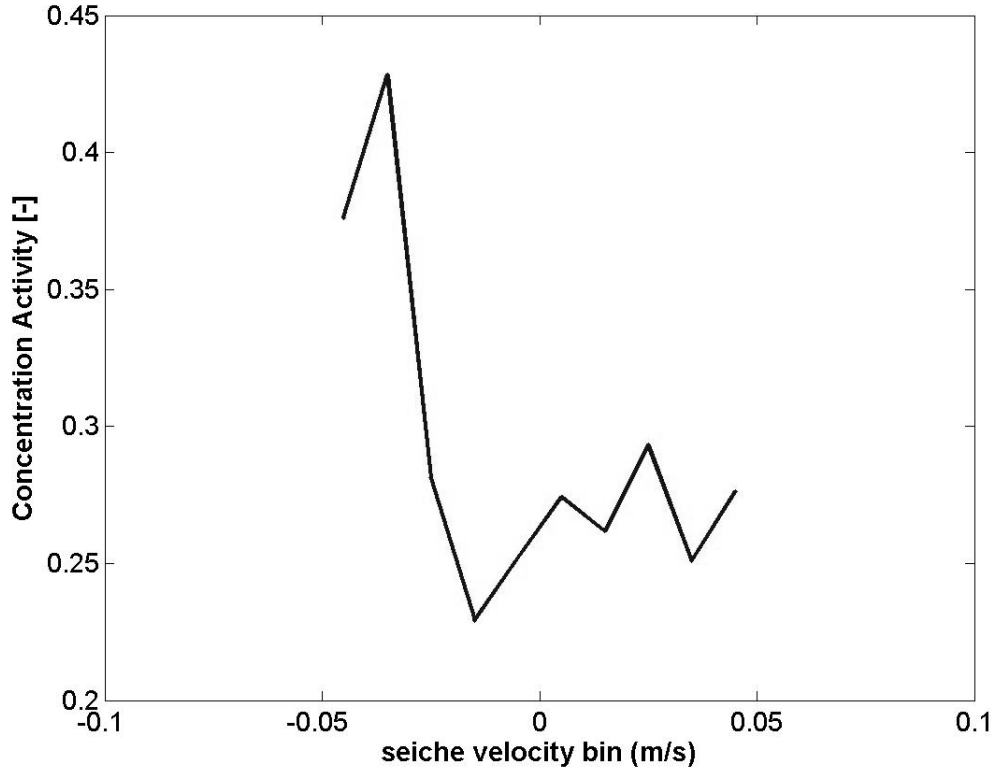

Figure 6.16: Sediment activity during the ebb period dominated by wind waves on April 15th, 2003 (tide 8) as a function of seiche velocity. Concentration data are separated into bins of the seiche velocity that vary in blocks of 0.01 m/s. The concentration activity is then determined according to equation 6.6.

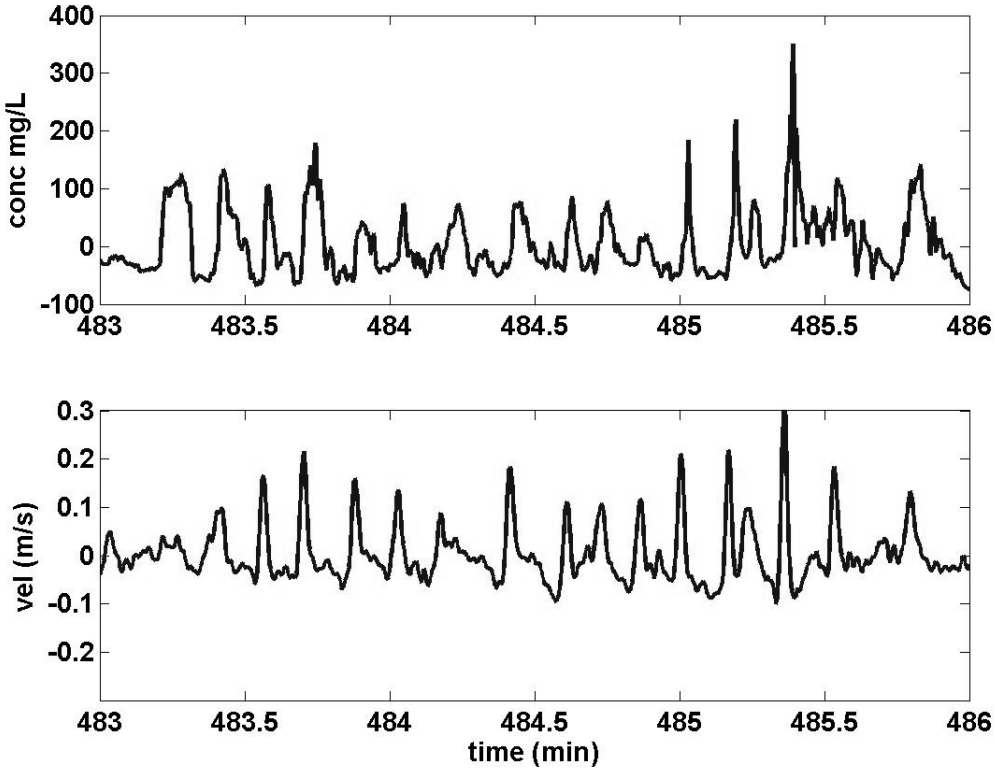

Figure 6.17: The wave component of sediment concentration and velocity (C_{wave} and V_{wave}) over a 3 minute period during an ebb tide dominated by ocean swell on the morning of April 14th, 2003 (tide 5). Sediment concentration is measured at 0.05 m, while velocity is measured at 0.155 m.

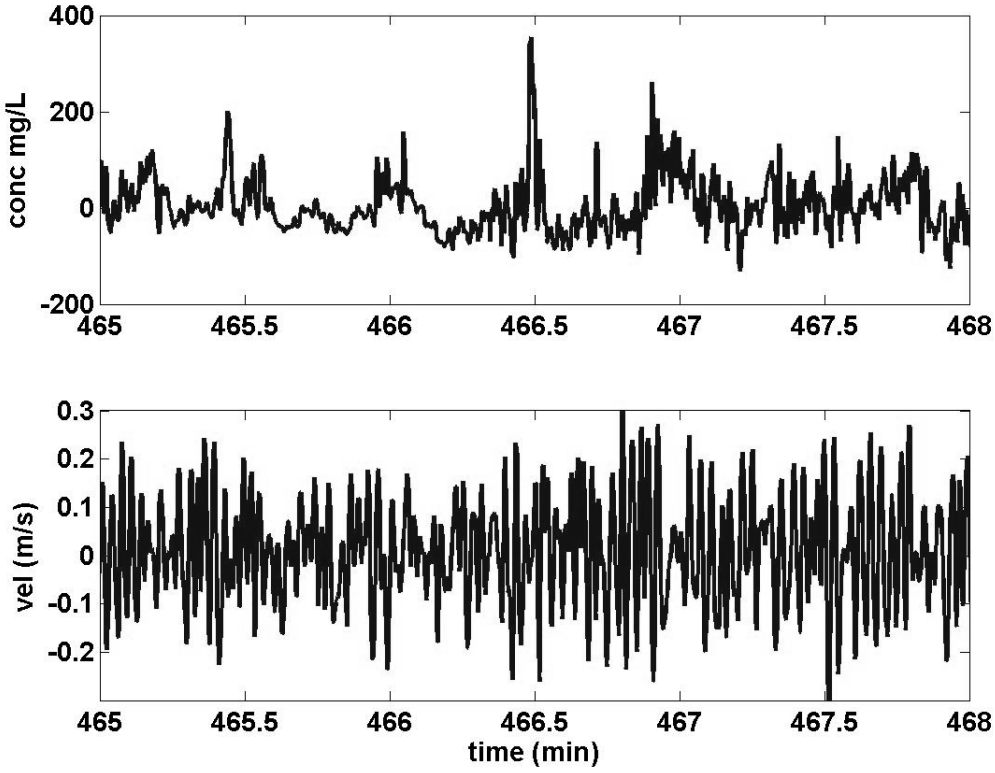

Figure 6.18: The wave component of sediment concentration and velocity (C_{wave} and V_{wave}) over a 3 minute period during an ebb tide dominated by locally driven wind waves on the afternoon of April 15th, 2003 (tide 8). Sediment concentration is measured at 0.05 m, while velocity is measured at 0.155 m.

Chapter 7: Conclusions and Future Directions

The hydrodynamic processes on an intertidal mudflat, as described in this dissertation, are complex and vary over multiple time scales that often interact in surprising ways. A major theme throughout is to highlight the effects of ocean swell and seiching motions, which are often neglected in this environment. In many ways, the wave climate of an intertidal, estuarine mudflat environment is analogous to open shore beaches, just scaled with smaller waves and less violent forces. Wave boundary layers are formed and destroyed; sediment is suspended by ejection over ripples; ocean swell arrives in wave groups and follows a Rayleigh distribution; and other processes such as shoaling, wave breaking, refraction, rip currents, edge waves, etc. are likely to occur. On the other hand, estuaries are semi-enclosed basins and thus subject to the seiching, wind wave processes, and circulation patterns that occur for example in lakes. The intersection of these paradigms makes a unique environment. Wind produces stress on the upper surface and creates wind waves, storms create fresh water flow and stratification, tides continually modulate the depth and the mean currents, and interaction of flow with the bed produces turbulence, causes sediment erosion, and forms ripples. In short, the mudflat is an ideal scale model in which to investigate multiple hydrodynamic processes over widely different conditions as depth, stratification, wind waves, ocean swell, seiching, and tidal currents vary. This dissertation isolates these processes and analyzes them separately, for example by investigating the boundary layer structure of the seiche using a numerical model or by describing the characteristics of ocean swell as depth changes. After highlighting the differences, we integrate the physical processes

by observing the patterns of turbulent kinetic energy, bed stress, and sediment transport that occur and explain how all the frequencies of motion interact to create the unique mudflat environment.

7.1. Major Conclusions

The major results described in the dissertation are summarized below.

1. Multiple scales of variability are found at an intertidal mudflat in the Central San Francisco Bay. Within a tidal period, we have isolated locally driven wind-waves (~ 2 second period), ocean swell (~10-15 second period), and seiching (~500 second period). Tides vary diurnally and on a spring-neap time scale. These multiple frequencies superpose together to form a complex hydrodynamic environment in which the frequency of motion that dominates varies over time. Ocean swell is typically not considered in estuarine intertidal areas, though the results presented here suggest that ocean swell is widely distributed throughout the central bay region and is likely a feature of other estuaries. Similarly, seiching motions are features of all enclosed basins, but are not considered in models of intertidal sediment transport.

2. Wind waves and ocean swell are fundamentally different in how they need to be modeled on a mudflat. Wind waves are driven by local meteorological events (summer breezes, storms) and geography, and can change greatly over an hour

as conditions change. Over a tide, the distribution of wind wave orbital velocity does not follow a predictable, repeatable distribution. By contrast, ocean swell are created in the ocean by non-local disturbances and follow a Rayleigh distribution that changes over multiple hours or days. For a given wave height, ocean swell goes non-linear and breaks before similarly sized wind waves; this has implications for bed stress and sediment resuspension. While all but the largest wind waves can be modeled by linear wave theory, ocean swell is better represented by the cnoidal wave. Finally, the orbital velocity of wind waves at the bed is noticeably attenuated during slack water, while ocean swell is not affected.

3. I apply several different methods of estimating turbulent kinetic energy (TKE) and dissipation in the intertidal environment, and compare these methods with a hybrid approach that is presented here for the first time. In the intertidal environment, separating waves from turbulence is critical because these motions occur at the same frequencies (> 0.1 Hz). However, the presence of several wave types (ocean swell and wind waves) complicates the separation. The Soulsby method requires identifying and removing the wave peak in the power spectrum, which is ill defined when multiple peaks occur, particularly as depth decreases and high frequency wind waves and higher harmonics of ocean swell occur. The Trowbridge and hybrid methods require that instruments be separated by distances at which turbulent motions are decorrelated; practically, in the intertidal environment, this means that high frequency (> 0.5 Hz) wave

motions are also decorrelated. However, after removing low frequency wind waves and ocean swell, the remaining wave energy is easily removed using the Soulsby technique. Overall, the hybrid and Trowbridge techniques are less error prone than the Soulsby method, though all three methods produce TKE and dissipation results that are consistent with each other over a tidal period.

4. The variability of TKE and dissipation is characterized over a tidal period, and follows a pattern similar to the tides and waves: During the flood and ebb, TKE and dissipation are relatively large, while during the slack tide measured values decrease by 2-3 orders of magnitude. The variability is caused by changes in waves and currents, which also vary by 1-2 orders of magnitude over a tide (see figure 3.10 and figure 3.11). Therefore, the energy climate in the intertidal zone—which depends on multiple types of motion and varies over many time scales—is essential to understanding water column processes (e.g., turbulent mixing). In general, the measured TKE intensity is a small proportion of the mean velocity or rms velocity, and is on the order of ~ 10 percent. Note that the average ratio of TKE intensity to mean velocity is less than the ratio predicted for open channel flow, particularly as the bed is approached (e.g., Nezu and Nakagawa, 1993; see figure 4.10). A likely cause is the unsteadiness in the flow, which causes large scatter in the data.

5. Over a tidal period, bed stress is estimated by fitting a logarithmic profile and a log-linear profile to the mean velocity in the water column. Though the logarithmic profile is typically assumed in estuarine studies, only ~20 percent of profiles over a typical period of inundation were found to be logarithmic. Instead, the log-linear model (which adds a linear correction to the logarithmic profile) fits the observed water column profiles quite well. However, the physical interpretation of the log-linear model remains problematic. Though both stratification and acceleration can cause deviations from the logarithmic profile, neither explained the observed profiles. The probable cause is that the time for the acceleration and stratification corrections to occur (i.e., through mixing), as currently modeled, is large compared to the variability in the mean flow. Thus, though the log-linear model is a good curve fitting techniques for finding the shear stress, it is not a viable model in an intertidal zone with intra-tidal variations in the mean velocity (e.g., the seiche).

6. Using the Grant and Madsen (1986) model, we show that ocean swell and wind waves greatly increase the mean bed stress by a factor greater than 2x through non-linear wave-current interactions. The increased bed stress agrees more closely to the measured logarithmic and log-linear results than with stress estimated using current only (i.e., using a friction factor). The non-linear model predicts that ocean swell has a greater affect on the mean current profile than wind waves of the same size, with a greater increase in both friction velocity and the virtual roughness height. In fact, the roughness measured by the log-linear

model correlates well with the roughness predicted by non-linear interaction between ocean swell and current. By contrast, only the largest wind waves (> 0.20 m/s) cause virtual roughness that is near the measured result. Thus, ocean swell likely dominates the virtual roughness that is seen by the tidal current in typical (non-storm) conditions.

7. The boundary layer of the seiching motion on the intertidal mudflat is modeled using an analytical wave boundary layer model (Smith 1977), the log-linear current model, and a κ-ε turbulence closure model (General Ocean Turbulence Model, GOTM). These results are compared to a normalized boundary layer profile that is an aggregate of all the seiche wave forms measured on the mudflat. The seiching motion is isolated from the other scales of motion using a bandpass filter. Results show that the log-linear model is a good curve fit to the data but is difficult to interpret physically (see discussion of tidal boundary layer in chapter 5). The Smith model, which is based on the assumption of a linearly varying eddy viscosity, overestimates the magnitude of the overshoot region and the height of the boundary layer. On the other hand, GOTM more closely represents the shape of the boundary layer structure of velocity, though deviation occurs during some phases of the seiche. In general, the height of the boundary layer and magnitude of the overshoot region is well predicted by the numerical model, in particular when the measured stratification is included.

8. The numerical model predicts that TKE is diffused slowly through the boundary layer; as the wave reverses velocity, TKE produced during the maximum velocity has only propagated to a height of ~0.10 - 0.15 m. Eddy viscosity, which depends on the turbulent energy and eddy length scale, therefore is a function of both time and depth. As a result, the predicted profile of velocity has several inflection points, which become particularly apparent as the wave reverses velocity. This behavior is consistent with the measured boundary layer, and increases our confidence in both the numerical model and the results (though with only four points in the boundary layer, no definite conclusion can be made). In summary, GOTM provides a more sophisticated model of the seiche boundary layer, and is necessary to model the affects of stratification and time-varying eddy viscosity.

9. The simple analytical model for the wave boundary layer (Smith, 1977) correctly models the observed boundary layer structure of ocean swell. Because only two measured points are consistently in the boundary layer, the rms profiles are compared. Nonetheless, both the decay towards zero at the roughness height and the magnitude and height of the overshoot region are well modeled by the Smith model. Thus, the assumption of a linearly varying eddy viscosity works for ocean swell and likely wind waves.

10. The largest component of sediment transport occurs due to variation in sediment concentration on a tidal scale, which in turn depends on the timing of waves and

currents over the tide. For example, large wind waves during the flood lead to onshore transport, while wind events during the ebb lead to the export of sediment. During times when wind waves are small, sediment concentration increases due to ocean swell and mean currents during the flood and ebb. Because ocean swell are more persistent in time and change less over a tide, they are less likely to cause large asymmetries in the tidal component of sediment concentration. The aggregate affect of wind waves over many tides is yet unknown, though some cancellation of fluxes is likely.

11. During the ebb period, high concentrations of sediment are observed during the shoreward phase of the seiche, when total mean velocity is at a minimum. By contrast, the lowest sediment concentration is observed during the offshore phase of the seiche, when the mean velocity is largest. This asymmetric phasing induces a net shoreward transport that is an important component of the net sediment transport budget. We hypothesize that the action of waves during the positive phase of the seiche are acting to reverse the direction of velocity, which causes turbulent vortices and sediment to be ejected into the water column. During the negative seiching motion, waves are not large enough to reverse the combined effect of ebb and seiche, and sediment tends to settle. Evidence for erosion by this mechanism is observed in the variation of zero up-crossings and the activity of concentration as a function of seiche velocity. When the seiche is directed onshore, more up-crossings occur and sediment fluctuations in the water column are comparatively more active (indicating greater erosion, despite

reduced shear stress). Sediment concentration is observed to be in phase between 0.05 m and 0.35 m, which is consistent with sediment being ejected from the bed in a burst. Because high concentrations occur at small stress, the only plausible ejection mechanism is the reversal of velocity.

12. In addition to the velocity reversal mechanism, erosion still occurs when a critical stress is exceeded. At a location near the channel, large ebb currents are observed to cause increases in sediment concentration during times of small wave activity. Moreover, during a period of wind dominated conditions, wind wave energy is found to correlate with sediment concentration during both onshore and offshore seiching motions. In addition, the activity (or patchiness) of sediment concentration is observed to increase when the ebb velocity is largest, suggesting direct erosion. Thus, we find evidence of erosion above a critical stress. However, this dissertation suggests that the anomalous phasing of observed sediment concentrations at the seiche frequency is caused by fluctuations in the likelihood of reversing velocity. As a result, numerical models of intertidal areas cannot simply use the critical erosion threshold as a parameter, but must also include more complex processes such as the ejection of sediment (and turbulent eddies) from the lee side of bedforms. Thus, the vertical advection of sediment by large turbulent eddies—in addition to diffusive processes by smaller scale mixing—is important in the intertidal boundary layer.

13. Residual sediment transport by waves is found to occur during immersed periods with significant wave energy, and is directed onshore over the 4 immersed periods studied. Transport of sediment by waves is small compared to transport based on tidal asymmetries. However, because the results are averaged over thousands of wave instances, they are more robust than the tidal transport estimates. Because wind waves and ocean swell have different properties (see conclusion # 2), they produce differences in the sediment concentration signal at the wave time-scale. Ocean swell often induces fluctuations in concentration at its frequency, while variations in sediment due to wind waves more typically fluctuate with wave groups. The largest ocean swell velocities (> 0.20 m/s) cause large bursts of sediment to be ejected into the water column, regardless of the phase of the seiche. This causes an asymmetry in the sediment flux term $C_{wave} * V_{wave}$, and explains some of the observed onshore transport. By contrast, no sediment bursting due to wind waves was observed. Other mechanisms of transport surely occur at the wave frequency (e.g., radiation stresses, wave groups) but are difficult to diagnose in the field.

7.2. New Directions

The conclusions reached with this research lead to many questions that would be interesting to explore in the future. These vary from short to long time scales, from understanding turbulent bursting processes to characterizing the long-term morphological change of the mudflat. Processes such as the non-linear interactions

between multiple frequencies of motion (e.g., ocean swell, wind waves, seiching, etc.) are poorly understood, but vitally important. In general, understanding how processes of different time scales interact with each other—how short term processes affect long term change, and vice-versa--is an open area of research. Moreover, feedback mechanisms occur across disciplines as well; for example, the cycling of biota, nutrients, and contaminants in the intertidal environment over different time and spatial scales involves hydrodynamics, biology, and chemistry.

7.2.1 Short term variation

The estimates of turbulent energy, stress, and dissipation measured from the hydrodynamic data are inherently averaged quantities. These are vital for estimating the erosion and mixing of scalars on time scales large compared to waves and turbulence. However, as suggested throughout the dissertation, instantaneous processes are likely important for eroding sediments and transporting them through the water column and along the bed. In particular, the interaction of flow with ripples, and the creation and ejection of sediment laden vortices in an environment with multiple forcing frequencies, is critical for understanding the production of turbulence and therefore the dissipation of energy in the mudflat environment.

The methods outlined in chapter 4 of separating waves from currents using either the Trowbridge method or the hybrid method shows promise for creating a data set with little wave contamination. Used carefully, this turbulent data set can then be used to

measure turbulent bursts, for example by the VITA technique (see e.g. Nezu and Nakagawa, 1993). However, because turbulent motions are small compared to waves, residual contamination from waves makes estimation of turbulent bursts difficult. Thus, better instruments are needed in the field, perhaps something similar to the Particle Imaging Velocimetry (PIV) methods that are currently used in laboratories to measure 2-D or 3-D turbulent motions.

Better instrumentation might help measure the progression of the ocean swell boundary layer in shallow water as a function of phase angle (which proved to be beyond the capabilities of our instruments and experimental setup). Detailed phase measurements for small amplitude ocean swell and wind waves would give valuable information on shear stresses, bursting processes, and the erosion of sediment by both the critical shear stress mechanism and the velocity reversal mechanism.

7.2.2 Sediment dynamics over longer time scales

The characterization of the multiple scales of motion and their effect on sediment transport over the time scale of a tide sets the groundwork for understanding longer term processes on the scale of the spring-neap cycle, seasonal patterns, and even longer-term morphological change. Over the winter season, the timing of wind due to storm events relative to the tides will be random, and the net sediment flux that occurs due to any asymmetric phasing of waves—and hence sediment concentration—should equal out. In summer, however, afternoon breezes consistently flow from the ocean towards

warm inland areas. Since the tides vary by approximately an hour each day over the spring-neap cycle, the timing of wind relative to tidal phase shifts as well; thus, during the summer months there is likely to be a spring-neap cycle of onshore/offshore transport, mediated by variation in tidal velocity and variation in the strength and timing of wind events.

The conditions of ocean swell change less radically over a period of inundation than wind waves, and therefore are less likely to cause asymmetry in sediment concentration on a tidal scale. On an annual scale, however, ocean swell is largest between December and April, and diminishes during the summer months. During the winter, storm events dominate the energy climate, though tidal action and ocean swell can be large during otherwise calm periods. In the summer, the daily cycle of wind, coupled to the tides, likely dominates. Therefore, the energy climate shifts over the year, likely with non-trivial interactions with mudflat morphology. For example, beaches are known to erode during the winter when ocean swell is largest, with sand deposited offshore. During the calmer summer months, sand migrates back to the beach. Might there be cycling and migration of sediment on intertidal flats that occurs on an annual scale, mediated not only be wind waves but also ocean swell? Moreover, what role does sediment input from either the estuary or the upland watershed have on long-term change at the mudflat? These and other questions are critically important for the long-term evolution of the mudflat and the fate and transport of the contaminated sediments which are buried near the experimental site, and can be attacked by a mixture of field work and numerical modeling.

7.2.2 Interactions of hydrodynamics with biology

The biology on intertidal mudflats is critically dependant on the hydrodynamic forcing, which brings the nutrients—and contaminants—to the biota but also creates both large and small disturbances as the bed is continually reworked. The spatial and temporal variation of the hydrodynamics is thus critical to understanding the biology on the mudflat. For example, the timing and frequency of turbulent bursting greatly affects the likelihood that larvae can settle and attach to the substrate without being resuspended. Over the time scale of a tide, filter feeders and deposit feeders greatly rework the bed in the process of burrowing and feeding, causing known—but largely unquantified—affects on sediment transport. On the scale of days and weeks, benthic diatoms avoid being eroded by secreting polysaccharides that bind the sediment and increase the erosion threshold. Finally, aggregate processes occurring over much larger time scales may be important to species such as clams which can survive for several decades. This small subsampling of biological processes shows how intertwined hydrodynamics, sediment transport, and biological endpoints are. The mechanisms of interaction between fluid flow and biology are still being discovered; thus, predictive capability through modeling is still in its infancy and is a ripe area of investigation.

7.2.4 Non-linear interaction between multiple boundary layers

As described in Chapter 5, non-linear interaction is known to occur between waves and currents. The primary premise of this paradigm, however, is that turbulent motions from the boundary layer of one motion interact with the turbulent motions produced by the other, creating enhanced friction in both types of motion. In an environment with multiple frequencies, it stands to reason that each is interacting with the others. Modeling this interaction through coupled equations of motions using simple assumptions (such as a linearly varying eddy viscosity) is perhaps possible, though results suggest that the seiche boundary layer is ideally modeled with more complex, time varying eddy viscosity. A numerical model that fully predicts turbulent motions over multiple time and length scales would be ideal (though currently not realistic). At the very least, non-linear wave-current interaction models can be applied separately to each wave and current frequency, yielding order of magnitude results (as in this dissertation). Another option is to treat ocean swell, for example, as quasi-steady compared to wind waves and apply current formulations of nonlinear wave-current interaction. However, ocean swell/wind wave interaction is likely to be more complex than such a simple model. In any case, this area remains open for both theoretical and experimental exploration.

7.2.5 Miscellaneous

Though this dissertation focused on waves, current, and sediment transport, many other physical processes are under-described in the intertidal environment. This includes stratification due to sediments or temperature variation, variation of wave energy over spatial gradients due to diffraction and refraction, the presence of edge waves, rip currents, etc. These processes could be investigated experimentally, or in numerical models. For example, further exploration with GOTM includes adding horizontal salinity gradients, wind stress, and sediment, to make the model more realistic.

References

Amos, C.L., Brylinksi, M., Sutherland,T.F., O'Brien, D., Lee, S. and Cramp, C. 1996. The stability of a mudflat in the Humber estuary, South Yorkshire, UK 25-43. *In*: Black, K.S., Paterson, D.M. and Cramp, A. (eds) *Sedimentary Processes in the Intertidal Zone.* Geological Society, London, Special Publications, **139** 25-43.

Anderson, F.E., 1981. The Northern muddy intertidal: seasonal factors controlling erosion and deposition—a review. *Canadian Journal of Fisheries and Aquatic Science* **40** (Suppl. 1), 143-159.

Anderson, F.E., Howell, B.A.., 1984. Dewatering of an unvegetated muddy tidal flat during exposure: desiccation or drainage? *Estuaries* **7-3**, 225-232.

Batchelor, G.K.,1953. *The Theory of Homogenous Turbulence*. Cambridge University Press, 197 pp.

Bendat, J.S. and Piersol, A. G., 1966. *Measurement and analysis of random data.* Wiley, New York.

Benilov, A.Y. and Filyuskin, B.N., 1970. Application of methods of linear filtration to an analysis of fluctuations in the surface layer of the sea. *Izv., Atmospheric and Oceanic Physics*, **6**, 810-819.

Booij, N., Ris, C., and Holthuijsen, L.H., 1999. A third generation wave model for coastal regions 1. Model description and validation. *Journal of Geophysical Research* **104**, 7649-7666.

Bowden, K.F., and White, R.A., 1966. Measurement of the orbital velocities of sea waves and use in determining the directional spectrum. *Geophysical Journal*, **12**, 1.

Bricker, J.D., 2003. Bed Drag Coefficient Variability under wind waves in a tidal estuary: Field Measurements and Numerical Modeling. *Ph.D., Stanford University*.

Burchard, H., and Baumert, H., 1995. On the performance of a mixed-layer model based on the k- ε turbulence closure. *Journal of Geophysical Research*, **100**, C5, 8523-8540.

Chriss, T.M. and Caldwell, D.R., 1982. Evidence for the influence of form drag on bottom boundary layer flow. *Journal of Geophysical Research*, **89**, 6403-6414.

Burnett, W.C., Bokuniewicz, H., Huettel, M., Moore, W.S., and Taniguchi, M., 2003. Groundwater and pore water inputs to the coastal zone, *Biogeochemistry* **66**, 3-33.

Cheng, R.T., Casulli, V. and Gartner, J.W., 1993. Tidal, residual and intertidal mudflat (TRIM) model and its applications to San Francisco Bay, California. *Estuarine Coastal Shelf Science,* **36**, 235-280.

Christie, M.C., and Dyer, K.R., 1998. Measurements of the turbid tidal edge over the Skeffling mudflats. In: Black, K.S., Patterson, D.M., and Cramp, A (eds.), *Sedimentary Processes in the Intertidal Zone*. Geological Society, London, Special Publications, **139**, 45-55.

Christie, M.C., Dyer, K.R., and Turner, P., 1999. Sediment Flux and Bed Level Measurements from a Macro Tidal Mudflat, *Estuarine, Coastal and Shelf Science* **49**, 667-688.

Cloern, J.E., 1982. Does the benthos control phytoplankton biomass in South San Francisco Bay? *Mar. Ecol. Prog. Ser.* Vol. **9**: 191-202.

Collins, M.B., Ke, X., and Gao, S. 1998. Tidally-induced Flow Structure Over Intertidal Flats, *Estuarine, Coastal and Shelf Science*, **46**, 233-250.

Connor, C.S. and DeVisser, A.M. 1992. A Laboratory Investigation of Particle Size Effect on an Optical Backscatterance Sensor. *Marine Geology* **108**: 151-159.

Couperthwaite, J.S., Mitchell, S.B., West, J.R., and Lawler, D.M., 1998. Cohesive Sediment Dynamics on an Inter-tidal Bank on the Tidal Trent, UK. *Marine Pollution Bulletin* **37**, 144-154.

Davey, J.T., and Partridge, V.A., 1998. The macrofaunal communities of the Skeffling muds (Humber estuary), with special reference to bioturbation. *In*: Black, K.S., Paterson, D.M. and Cramp,A. (eds) *Sedimentary Processes in the Intertidal Zone.* Geological Society, London, Special Publications, **139**, 115-124.

De Lange, W. and Healy, T., 1990. Wave Spectra for a Shallow Meso-Tidal Estuarine Lagoon: Bay of Plenty, New Zealand. *Journal of Coastal Research*, **6**, 1, 189-199.

Dyer, K. R., 1989. Sediment Processes In Estuaries: Future Research Requirements. *Journal of Geophysical Research*, **194**, No. C10, pp. 14,327-14,339.

Dyer, K. R., 1998. The typology of intertidal mudflats. Black, K.S., Patterson, D.M., and Cramp, A. (eds.), *Sedimentary Processes in the Intertidal Zone*. Geological Society, London, Special Publications, **139**, 11-24.

Dyer, K.R., Christie, M.C., Feates, N., Fennessy, M.J., Pejrup, M., and van der Lee, W., 2000. An Investigation into Processes Influencing the Morphodynamics of an Intertidal Mudflat, the Dollard Estuary, The Netherlands: I. Hydrodynamics and Suspended Sediment. *Estuarine, Coastal and Shelf Science*, **50**, 607-625.

Fenton, J.D., 1979. A high-order cnoidal wave theory, *Journal of Fluid Mechanics*, **94**, part 1, 129-161.

Flick, R.E, Guza, R.T., and Inman, D.L., (Year?) Elevation and velocity measurements of laboratory shoaling waves, *Journal of Geophysical Research*, **86**, 4149-4160.

Fredsoe, J., 1993. Modelling of non-cohesive sediment transport processes in the marine environment. *Coastal Engineering*, **21**, 71-103.

Fredsoe,J., Anderson, K.H., Sumer, B.M., 1999, Wave plus current over a ripple-covered bed, *Coastal Engineering*, 38 177-221.

Foster, D.L., Beach, R.A., and Holman, R.A., 2000. Field observations of the wave bottom boundary layer. *Journal of Geophysical Research*, **105**, C8, 19,631-19,647.

George, R., Flick, R.E., and Guza, R.T. (1994). Observations of turbulence in the surf zone. *Journal of Geophysical Research,* **99**, C1, 801-810.

Gilbert, G.K., 1917. Hydraulic-mining debris in the Sierra Nevada: *U.S. Geological Survey Professional Paper 105*.

GoalsProject, 1999. Baylands Ecosystem Habitat goals. A report of habitat recommendations prepared by the San Francisco Bay Area Wetlands Ecosystem Goals Project. Joint Publication of the U.S. Environmental Protection Agency, San Francisco, California, and San Francisco Bay Regional Water Quality Control Board, Oakland, CA.

Grant, J., Bathmann, U.V. and Mills, E.L., 1986. The interaction between benthic diatom films and sediment transport. *Estuarine, Coastal and Shelf Science*, **23**, 225-238.

Grant, W. D. and Madsen, O.S., 1979. Combined Wave and Current Interaction with a Rough Bottom. *Journal of Geophysical Research* **84**, C4, 1797-1808.

Grant, W.D. and Madsen, O.S., 1986. The Continental Shelf Boundary Layer, *Annual Review of Fluid Mechanics*, **18**, 265-305.

Grant, W.D., Williams, A.J, and Glenn, S.M., 1983. Bottom Stress Estimates and their Prediction on the Northern California Continental Shelf during CODE-1: The Importance of Wave-Current Interaction. *Journal of Physical Oceanography*, **14**, 506-527.

Green, M.O. and MacDonald, I.T., 2001. Processes driving estuary infilling by marine sands on an embayed coast. *Mar. Geol.* **178**, 11-37.

Gross, T.F., and Nowell, A.R.M, 1985. Spectral Scaling in a Tidal Boundary Layer. *Journal of Physical Oceanography*, **15**, 496-508.

Gross, T.F., Williams, A.J., and Terray, E.A., 1994. Bottom boundary layer spectral dissipation estimates in the presence of wave motions. *Continental Shelf Research*, **14**, No. 10/11, 1239-1256.

Holland, A.F., Zingmark, R.G., and Dean, J.M. 1974. Quantitative evidence concerning the stabilization of sediments by marine benthic diatoms. *Marine Biology*, **17**, 191-196.

Horne, A. J. and Goldman, C. R., 1994. *Limnology*, McGraw-Hill, Inc., New York.

Houwing, E. J., 1999. Determination of the Critical Erosion Threshold of Cohesive Sediments on Intertidal Mudflats Along the Dutch Wadden Sea Coast. *Estuarine, Coastal and Shelf Science*, **49**, 545-555.

Huntley, D.A., 1988. A modified inertial dissipation method for estimating seabed stresses at low Reynolds numbers, with application to wave/current boundary layer measurements. *Journal of Physical Oceanography* **18**, 339-346.

Inman, D.L. and Bowen, A.J., 1962. Flume experiments on sand transport by waves and currents. In: *Proce. 8th Conf. Coastal Eng*., Mexico City, p 137-150.

Janssen-Stelder, B., 2000. The effect of different hydrodynamic conditions on the morphodynamics of a tidal mudflat in the Dutch Wadden Sea. *Continental Shelf Research* **20**, 1461-1478.

Jing, L. and Ridd, P.V., 1996. Wave-current bottom shear stresses and sediment resusupension in Cleveland Bay, Australia. *Coastal Engineering* **29**, 169-186.

Kawanisi, K., 2004. Structure of Turbulent Flow in a Shallow Tidal Estuary, *Journal of Hydraulic Engineering*, **130**, 4, 360-370.

Kim, S.C., Friedrichs, C.T., Maa, J.P., and Wright, L.D., 2000. Estimating Bottom Stress in Tidal Boundary Layer From Acoustic Doppler Velocimeter Data. *Journal of Hydraulic Engineering*, **126**, 6, 399-406.

Knaapen, M.A.F., Holzhauer, H., Hulscher, S.J.M.H., Baptist, M.J., de Vries, M.B., van Ledden, M., 2003. On the modeling of biological effects on morphology in estuaries and seas. In (Ed.), *Proceedings third IAHR Symposium on River, Coastal, and Estuarine Morphodynamics*, 773-783.

Kolmogorov, A.N., 1941. The local structure of turbulence in incompressible viscous fluid for very large Reynolds numbers. *C.R. Acad. Sci. URSS* 30:301.

Komar, P.D., 1976. *Beach Processes and Sedimentation.* Prentice-Hall, New York.

Kornman, B.A. and De Deckere, E.M.G.T. 1998. Temporal variation in sediment erodibility and suspended sediment dynamics in the Dollard estuary. *In*: Black, K.S., Paterson, D.M. and Cramp, A. (eds) *Sedimentary Processes in the Intertidal Zone.* Geological Society, London, Special Publications, **139**, 231-241.

Krone, R.B., 1962. Flume studies of the transport of sediments in estuarial shoaling processes. *Final Rep., Hydraulic Engineering Laboratory and Sanitary Engineering Research Laboratory*, University of California, Berkeley.

Kuo, A.Y., Shen, J., and Hamrick, J.M, 1996. Effect of Acceleration on Bottom Shear Stress in Tidal Estuaries. *Journal of Waterway, Port, Coastal, and Ocean Engineering* **122,** No. 2 75-83.

Lee, G.H., Dade, W.B., Friedrichs, C.T., and Vincent, C.E., 2003. Spectral estimates of bed shear stress using suspended-sediment concentrations in a wave-current boundary layer. *Journal of Geophysical Research***, 108,** C7.

Le Mehaute, B., 1976. An Introduction to Hydrodynamics and Water Waves. *Springer Verlag*, Dusseldorf.

Lhermitte,R. 1983. Doppler sonar observation of tidal flow. *Journal of Geophysical Research.* **88** C1 725-742.

Li, Y., and Parchure, T.M., 1998. Mudbanks of the Southwest Coast of India. VI: Suspended Sediment Profiles. *Journal of Coastal Research*. **14** (4), 1363-1372.

Le Normant, C., 2000. Three-dimensional modeling of cohesive sediment transport in the Loire estuary. *Hydrological Processes*, **14**, 2231-2243.

Lippman, T.C., Holman, R.A., and Bowen, A.J., 1997. Generation of edge waves in shallow water. *Journal of Geophysical Research*, **102**, C4, 8663-8679.

Longuet-Higgins, M.S., 1952. On Statistical Distribution of the Heights of Sea Waves. *J. Mar. Res*. **11**: pp. 245-266.

Lumley, J.L. and Terray, E.A., 1983. Kinematics of turbulence convected by a random wave field. *Journal of Physical Oceanography*, **13**, 2000-2007.

Mathisen, P.P., Madsen, O.S., 1996. Waves and currents over a fixed rippled bed 1. Bottom Roughness experienced by waves in the presence and absence of currents, *Journal of Geophysical Research*, **101**, No. C7, 16533-16542.

Matlab Help, 2002. The Mathworks, Inc., Version 6.5, release 13.

Meadows, A., Meadows, P.S., and McLaughlin, P., 1998. Spatial heterogeneity in an intertidal sedimentary environment and its macrobenthic community. . *In*: Black, K.S., Paterson, D.M. and Cramp, A. (eds) *Sedimentary Processes in the Intertidal Zone.* Geological Society, London, Special Publications, **139** 367-388.

Mehta, A.J., and Maa, P.Y., 1986. Waves over mud: Modeling erosion. *Proceedings 3rd International Symposium on River Sedimentation, Vol III*, Univ. of Miss., 558-601.

Mehta, A.J., Hayter, E.J., Parker, W.R., Krone,R.B., Teeter, A.M., 1989. Cohesive Sediment Transport. I. Process Description, *Journal of Hydraulic Engineering*, **115**, No. 8.

Mellor, G., 2002. Oscillatory Bottom Boundary Layers, *Journal of Physical Oceanography*, **32**, 3075-3088.

Melville, W.K., 1994. Energy Dissipation by Breaking Waves. *Journal of Physical Oceanography*. **24** 2041-2049.

Meyer, Y. 1990. *Ondelettes et opérateurs, Tome 1*, Hermann Ed. (English translation: Wavelets and operators, Cambridge Univ. Press. 1993.)

Monin, A.S., and Yaglom, A.M., 1971. *Statistical fluid mechanics: Mechanics of Turbulence*, vol. 1, 425-442, MIT press, Cambridge, Mass.

Nezu, I., and Nakagawa, H., 1993. *Turbulence in Open Channel Flows*. International Association for Hydraulic Research, Monograph Series, A.A. Balkema Publishers, Rotterdam, Netherlands.

Okayasu, A., Suzuki,T., Cox, D., Katayama,H., Mori,N., 2005. Field Observations of the Generation of Sediment Clouds. *Submitted to Marine Geology*.

Oppenheim, A. V. and Schafer, R.W., 1989. *Discrete Time Signal Processing*. Prentice Hall. Englewood Cliffs, New Jersey.

Partheniades, E., 1962. *A study of erosion and deposition of cohesive soils in salt water*. PhD Thesis, University of California at Berkeley, 182 pp.

Paterson, D.M. 1997 Biological mediation of sediment erodibility: ecology and physical dynamics. In *Cohesive Sediments* (Burt, N., Parker, R., and Watts, J. eds). John Wiley and Sons, London, 215-229.

Pond, S. and Pickard, G., 1983. Introductory Dynamical Oceanography, 2nd Edition. *Butterworth-Heinemann*, Oxford OX2 8DP.

Potsma, H., 1961. Transport and accumulation of suspended matter in the Dutch Wadden Sea. *Netherland Journal of Sea Research* **1**, 148-190.

Ralston, D.K. 2005. Hydrodynamics and scalar transport in subtidal channels through intertidal mudflats. *Ph.D., University of California, Berkeley.*

Ribberink,J.S., and Al-Salem, A., 1991. Near-bed sediment transport and suspended sediment concentrations under waves. In: *Int. Symp. On the Transport of Suspended Sediments and its Mathematical Modeling*, IAHR, Florence, 375-388.

Riethmueller, R., Hakvoort, J.H.M, Heineke, M., Heymann, K., Kuehl, H., and Witte, G., 1998. Relating Erosion shear stress to tidal flat surface color. In: Black, K.S., Patterson, D.M., and Cramp, A. (eds.), *Sedimentary Processes in the Intertidal Zone*. Geological Society, London, Special Publications, **139**, 283-293.

Richardson, L. F., 1926. Atmospheric Diffusion shown on a distance-neighbor Graph. *Proc. R. Soc. London, Ser. A.* **110,** 709-737.

Roberts, W., Le Hir, P., and Whitehouse, R.J.S., 2000. Investigation using simple mathematical models of the effect of tidal currents and waves on the profile shape of intertidal mudflats. *Continental Shelf Research*, **20**, 1079-1097.

Ruhl, C.A., and Schoellhamer, D.H., 2004. Spatial and temporal variability of suspended-sediment concentration in a shallow estuarine environment. *San San Francisco Estuary and Watershed Science* [online serial]. **Vol. 2,** Issue 2, Article 1.

Ryan, N.M. and Cooper, J.A.G 1998. Spatial variability of tidal flats in response to wave exposure: examples from Strangford Lough, Co. Down, Northern Ireland. In: Black, K.S., Patterson, D.M., and Cramp, A. (eds.), *Sedimentary Processes in the Intertidal Zone*. Geological Society, London, Special Publications, **139**, 221-230.

Sanford, L.P, 1994. Wave-Forced Resuspension of Upper Chesapeake Bay Muds. *Estuaries,* **17**, No. 18, 148-165.

Sanford, T.B., and Lien, R.C., 1999. Turbulent properties in a homogenous tidal bottom boundary layer, *Journal Geophysical Research*, **104,** 1245-1257.

Schoellhamer, D.H., 1996. Factors affecting suspended-solids concentration in South San Francisco Bay, California. *Journal of Geophysical Research* **101** (C5): 12087-12095.

Shanmugan, K., and Breiphol, A. M., 1998. *Random Signals: Detection, Estimation, and Data Analysis*. John Wiley and Sons, New York.

Shaw, W.J., and Trowbridge, J.H., 2001. The Direct Estimation of Near-Bottom Turbulent Fluxes in the Presence of Energetic Wave Motions. *Journal of Atmospheric and Oceanic Technology*, **18**, 1540-1557.

Shi, N.C., Larsen, L.H., 1984. Reverse sediment transport induced by amplitude-modulated waves. *Marine Geology* **54**, 181-200.

Sleath, J.F.A., 1984. Sea Bed Mechanics, *John Wiley and Sons*, New York.

Sleath, J.F.A., 1990 Seabed Boundary Layers. *The Sea,* B. Le Mehaute and DM Hanes, Eds., Ocean Engineering Science, Vol. 9, Wiley and Sons 239-292.

Sleath, J.F.A. and Wallbridge, S., 2002. Pickup from Rippled Beds in Oscillatory Flow. *Journal of Waterway, Port, Coastal and Ocean Engineering*, **128**, 6, 228-237.

Simpson, J.H., Brown, J., Matthews, J., Allen, G., 1990. Tidal Straining, Density Currents and Stirring in the Control of Estuarine Stratification. *Estuaries* **13** No. 2, 125-132.

Smith, J.D., 1977. Modeling of sediment transport on continental shelves. In: Goldeberg, E.D., (Ed.), *The Sea*, vol. 6. Wiley, New York, 539-577.

Smith, W.A.M.N., Atsavapranee, P., Katz, J., Osborn, T.R., 2002. PIV measurements in the bottom boundary layer of the coastal ocean. *Experiments in Fluids*, **33**, 962-971.

Smyth, C., Hay, A.E., and Zedel, L., 2002. Coherent Doppler Profiler measurements of near-bed suspended sediment fluxes and the influence of bed forms, *Journal of Geophysical Research*, **107,** No. C8, 19-1—19-20.

SonTek ADV Acoustic Doppler Velocimeter, Technical Documentation, 2001. SonTek Inc., San Diego, CA.

Soulsby, R.L., and Dyer, K.R., 1981. The Form of the Near-Bed Velocity Profile in a Tidally Accelerating Flow. *Journal of Geophysical Research*, **86,** C9, 8067-8074.

Soulsby, R.L and Wainright, B.L.S.A., 1987. A criterion for the effect of suspended sediment on near-bottom velocity profiles, *Journal of Hydraulic Research* 25(3) 341-356.

Soulsby, R.L.,1983. The bottom boundary layer of shelf seas, in B.Johns (ed.), *Physical Oceanography of Coastal and Shelf Seas*, Elsevier Science Pub., Amsterdam, 189-266.

Soulsby, R.L., Humphery, J.D., 1989. Field observations of wave-current interaction at the sea bed. In: Torum, A., Gudmestad, O.T. (eds), *Proceedings of NATO Advanced*

Research Workshop on Water Wave Kinematics, Molde, Norway, 22-25 May 1989, Kluwer Academic Publishers, Dordrecht, Netherlands, 413-428.

Soulsby, R.L., Hamm, L., Klopman, G., Myrhaug, D., Simons, R.R., and Thomas, G.P., 1993. Wave-current interaction within and outside the bottom boundary layer. *Coastal Engineering,* **21**, 41-69.

Sultan, N.J., Ting, F.C.K., 1993. Experimental study of undertow and turbulence intensity under irregular waves in the surf zone. *Proc. 2nd Int. Symposium on Ocean Wave Measurement and Analysis, New Orleans.* ASCE, New York, 602-613.

Stacey, M.T., and Ralston, D.K., 2005. The Scaling and Structure of the Estuarine Bottom Boundary Layer. *Journal of Physical Oceanography*, **35,** 55-71.

Taylor, G.I., 1938. The Spectrum of Turbulence. *Proc. Roy. Soc. London*, **A164**, 476-490.

Teisson, C., Ockenden, M., Le Hir, P., Kranenburg, C., and Hamm, L., 1993. Cohesive sediment transport processes. *Coastal Engineering* **21** 129-162.

Tennekes, H., and Lumley, J.L., 1972. *A First Course in Turbulence*. MIT Press, Cambridge, Massachusetts.

Thais, L., and Magnaudet, J., 1996. Turbulent structure beneath surface gravity waves sheared by the wind.

Thwaites, F.T. and Williams, A.J. III, 2001. BASS Measurements of Currents, Waves, Stress, and Turbulence in the North Sea Bottom-Boundary Layer. *IEEE Journal of Oceanic Engineering,* **26**, 2, 161-170.

Ting, F.C.K., 2001. Laboratory study of wave and turbulence velocities in a broad-banded irregular wave surf zone. *Coastal Engineering* **43**, 183-208.

Trowbridge, J.H., 1998. On a Technique for Measurement of Turbulent Shear Stress in the Presence of Surface Waves. *Journal of Atmospheric and Oceanic Technology*, **15**, 290-298.

Trowbridge, J.H., Geyer, W.R., Bowen, M.M., and Williams, A.J., 1999. Near-bottom turbulence measurements in a partially mixed estuary: Turbulent energy balance, velocity structure, and along-channel momentum balance, *Journal Physical Oceanography,* **29**, 3056-3072.

URS, 2000, Field Sampling and Analysis Results, University of California, Berkeley Richmond Field Station/Stege Marsh Richmond California, Final Report prepared for University of California, Environment, Health, and Safety

Van der Lee, W.T.B., 1998. The impact of fluid shear and the suspended sediment concentration on the mud floc size variation in the Dollard estuary, The Netherlands. In: Black, K.S., Patterson, D.M., and Cramp, A. (eds.), *Sedimentary Processes in the Intertidal Zone*. Geological Society, London, Special Publications, **139**, 187-198.

Wells, J. T. and Kemp, P.G., 1986. Interaction of Surface Waves and Cohesive Sediments: Field Observations and Geologic Significance. In: Mehta, A.J. (Ed.), *Estuarine Cohesive Sediment Dynamics, Lecture notes on Coastal and Estuarine Studies N^{o}14*. Springer, Berlin, 43-65.

Whitehouse, R.J.S., and Mitchener, H.J., 1998. Observations of the morphodynamic behavior of an intertidal mudflat at different timescales. In: Black, K.S., Patterson, D.M., and Cramp, A. (eds.), *Sedimentary Processes in the Intertidal Zone*. Geological Society, London, Special Publications, **139**, 255-271.

Whitehouse, R.J.S., Bassoullet, P., Dyer, K.R., Mitchener, H.J., Roberts, W., 2000. The influence of bedforms on flow and sediment transport over intertidal mudflats. *Continental Shelf Research* **20** 1099-1124.

Widdows, J., Brinsley, M., and Elliott, M., 1998. Use of in-situ flume to quantify particle flux (biodeposition rates and sediment erosion) for an intertidal mudflat in relation to changes in current velocity and benthic macrofauna. In: Black, K.S.,

Patterson, D.M., and Cramp, A. (eds.), *Sedimentary Processes in the Intertidal Zone*. Geological Society, London, Special Publications, **139**, 85-97.

Williamson, H.J., and Ockenden, M.C., 1996. ISIS: An instrument for measuring erosion shear stress in-situ. *Estuarine, Coastal and Shelf Science* **42**, 1-18.

Winterwerp, H., 1999. On the dynamics of high-concentrated mud suspensions. *Communications on Hydraulic Engineering*, Delft University of Technology, Report 99-3.

Winterwerp, J.C., 2001. Stratification effects by cohesive and noncohesive sediment, *Journal of Geophysical research*, **106**, C10, 22559-22574.

Wolf, J., 1999. The estimation of shear stresses from near-bed turbulent velocities for combined wave-current flows. *Coastal Engineering* **37**, 529-543.

Wood, R.G., Black, K.S., Jago, C.F, 1998. Measurements of preliminary modeling of current velocity over an intertidal mudflat, Humber estuary, UK. In: Black, K.S., Patterson, D.M., and Cramp, A. (eds.), *Sedimentary Processes in the Intertidal Zone*. Geological Society, London, Special Publications, **139**, 167-175.

Wood, R. and Widdows, J., 2002. A model of sediment transport over an intertidal transect, comparing the influences of biological and physical factors. *Limnology and Oceanography* **47**(3), 848-855.

Wright, L.D., Boon, J.D., Xu, J.P., and Kim,S.C., 1992. The bottom boundary layer of the Bay Stem Plains environment of lower Chesapeake Bay. *Estuaries, Coastal, and Shelf Science* **35**, 17-36.

Wright, S.A. and Schoellhamer, D.H., 2004. Trends in the sediment yield of the Sacramento River, California, 1957-2001. *San Francisco Estuary and Watershed Science* [online serial]. **Vol. 2,** Issue 2, Article 2.

Zhang, S. and Jin, J., 1996. *Computation of Special Functions*, Wiley and Sons, New York.

Zhen-Gang, J., Morton, M.R., Hamrick, J.M., 2000. Modeling hydrodynamic and sediment processes in Morro Bay. In: Spaulding, M.L. and Butler, H.L. (eds.), *Estuarine and coastal modeling; proceedings of the sixth international conference*, **6**, 1035-1054.